

ŁÓDŹ UNIVERSITY OF TECHNOLOGY
&
UNIVERSITY OF STRATHCLYDE

Numerical model of the flow phenomena
preceding surge in the centrifugal blower
and assessment of its applicability
in designing anti-surge devices

Author:

Grzegorz LIŚKIEWICZ

Supervisors:

Longin HORODKO, DSc, PhD

Krzysztof SOBCZAK, PhD

Matthew STICKLAND, PhD

*A thesis submitted in fulfilment of the requirements
for the degree of Doctor of Philosophy*

in the

Department of Mechanical Engineering

Łódź University of Technology

&

Department of Mechanical and Aerospace Engineering

University of Strathclyde

March 27, 2014

mojej kochanej Babci

Abstract

The dissertation is devoted to analysis of unstable phenomena in the centrifugal blower. These phenomena are known to be a source of serious threat to safety of the machine and the piping system connected to it. The complexity of centrifugal impellers causes that instabilities therein can have various forms and locations and have been subject of interest for over 60 years. The dissertation consists of two main parts: one of them being a result of the experimental investigations, the other one describing an outcome of the numerical simulations.

In the experimental part, three methods of data analysis were applied: static, dynamic and a novel approach referred to as the quasi-dynamic one. The blower was examined in two configurations of the outlet pipe corresponding to different outlet plenum volumes. The results were presented in a form of a performance curve, amplitude plots, scalograms, phase trajectories and spectral maps. The machine was found to operate in four different regimes, namely: the stable regime, the inlet recirculation, the transient phase and the deep surge. The inlet recirculation was identified as the earliest instability present in the inlet zone. It was characterized by strong pressure jumps and a spectral structure of broadband noise. In the transient phase, the pressure oscillation amplitude grew by one order of magnitude and appeared in all points analyzed. In the deep surge, strong pressure oscillations appeared, with one frequency component close to the Helmholtz frequency. A new factor that can be used for real-time monitoring and early detection of unstable flow phenomena was developed as a result of signal phase trajectory analysis. The second part presents results of the transient numerical simulations conducted with FLUENT and then compared to the experimental data. The full impeller geometry was simulated together with the diffuser, the volute and large volumes of the inlet and outlet pipes. Computations were run at different combinations of the boundary conditions corresponding to different operational points. Simulations with a reduced plenum volume were also conducted analogously to the experimental study. The machine was found to operate in four working regimes: stable regime, pre-surge (impeller instability), pre-surge (inlet recirculation) and the deep surge. An overview on the machine performance was provided together with a detailed description of particular flow structures. The results were compared to the experimental data by means of, a performance curve, phase trajectories and frequency spectra and were found to be in reasonable agreement. The numerical study introduced a possibility of a detailed analysis of unstable flow structures such as the inlet recirculation, the impeller instability, a the deep surge cycle.

The study confirmed that computational methods introduce an opportunity to understand the unstable flow structures in detail and provide a missing link between real flow phenomena and mathematical surge and stall models, which is essential for effective anti-surge protection.

Contents

Contents	vii
List of Figures	ix
List of Tables	xv
Abbreviations	xvii
Nomenclature	xx
1 Theoretical background	1
1.1 Introduction	1
1.2 Classification of unstable flow structures	2
1.3 Surge	3
1.3.1 Greitzer model	4
1.3.2 Calculation of the stability limit	8
1.3.3 The surge cycle	13
1.4 Rotating stall	14
1.4.1 Progressive impeller rotating stall	16
1.4.2 Vaneless diffuser rotating stall	18
1.4.3 Abrupt impeller rotating stall	20
1.5 Inlet recirculation	22
1.6 Numerical analyses of the unstable flow phenomena	22
1.7 Aim of study	24
1.7.1 Motivation	24
1.7.2 Thesis of dissertation	24
2 Experimental study	27
2.1 Test stand description	27
2.1.1 Signal Collection and Analysis	29
2.2 Results of the experimental investigation	37
2.2.1 Static analysis	37
2.2.2 Dynamic analysis	40
2.2.3 Quasi-dynamic analysis	48
2.2.4 Influence of the plenum volume on system dynamics	58
2.3 Summary	68
3 Numerical study	71
3.1 Task description	71
3.1.1 Blower configuration	71
3.1.2 Computational mesh	72

3.1.3	Simulation definition	75
3.1.4	Solver monitoring	82
3.1.5	Mesh size study	83
3.1.6	Turbulence model study	85
3.1.7	Method of comparison with the experimental data	87
3.2	Results	89
3.2.1	Blower performance curve	89
3.2.2	Representation of the flow structures - stable working conditions and pre-surge	92
3.2.3	Representation of the flow structures - the deep surge	103
3.3	Comparison with experimental results	113
3.3.1	Spectral analysis	113
3.3.2	Influence of the outlet plenum volume	120
3.3.3	Representation of signals in the phase space	123
3.4	Summary	127
4	Closing remarks	131
4.1	Main achievements of the present study	131
4.2	Answer to the thesis	132
4.3	Future work	133
	Bibliography	143
	A Differential spectral maps	145
	B Frequency spectra	149
B.1	$\dot{m} = 0.1 \frac{kg}{s}$	149
B.2	$\dot{m} = 0.1 \frac{kg}{s}$ with reduced plenum	152
B.3	$\dot{m} = 0.3 \frac{kg}{s}$	155
B.4	$\dot{m} = 0.5 \frac{kg}{s}$	158
B.5	$\dot{m} = 0.8 \frac{kg}{s}$	161

List of Figures

1.1	Cross-section of the compressing machine with its main dimensions	1
1.2	Typical performance curves of the compressing machine (blue) and the system characteristics (brown)	2
1.3	Localisation of unstable flow structures according to classification applied in this study	3
1.4	Compressing machine in Greitzer model	4
1.5	Static stability limit	10
1.6	Static stability limit	11
1.7	Response of system on perturbation in a function of $\lambda = \alpha \mp i\omega$ [122] . . .	12
1.8	Influence of \mathcal{B} -factor on the surge limit cycle in the axial compressor [39]; C_x - axial flow velocity, u - mean rotor velocity	13
1.9	Comparison of the Greitzer model with the experimental pressure signal obtained in a low speed centrifugal compressor [88]; solid line - Greitzer model, dashed line - experimental result	13
1.10	Time dependence of pressure signals registered during the first surge cycle [118]	14
1.11	Trajectory of the operational point at onset of the deep surge [51]	15
1.12	Rotating stall cells and their influence on pressure signal	15
1.13	Influence of PIRS and AIRS on the compressing machine performance curve	16
1.14	Mechanism of propagation of the PIRS [72]	16
1.15	Variation of the PIRS cell speed with flow coefficient [89]	17
1.16	Scheme of the rotating stall cells observed in the axial compressor [35] . .	17
1.17	Flow in vaneless diffuser in conditions of mass flow rate smaller than at design conditions	18
1.18	Separated flows in vaneless diffusers at different mass flow rates [100] . .	19
1.19	Influence of diffuser width and length on angle α_r [106]	19
1.20	Experimental (upper plots) and calculated (lower plots) velocity and pressure fluctuations during the VDRS [119]	20
1.21	Influence of number of stall cells on vaneless diffuser flow stability [6] . . .	21
1.22	Variation of the impeller outlet velocity and its influence on the impeller inlet [121]	21
1.23	Inlet recirculation observed in the centrifugal pump [15]	22
1.24	Number of patents on the compressor surge in general (solid black), surge avoidance (grey) and surge detection (dashed black) [124]	25
2.1	Cross-section of the DP1.12 blower in configuration used in this study with the most important dimensions	27
2.2	Cross-section of the DP1.12 blower in the configuration used in this study with positions of the pressure gauges	29
2.3	Overview of the test stand and the data acquisition system	30

2.4	Gauge characteristics obtained in one of the calibrations	31
2.5	Inlet profile obtained in one series of the static experimental analysis . . .	31
2.6	Integration over area S	32
2.7	Pressure registered at gauge p_{s-imp1} in one of dynamic tests	33
2.8	Scheme demonstrating the methodology used in dynamic tests	34
2.9	Scheme demonstrating the methodology used in dynamic tests	35
2.10	Normalized inlet pressure profile at the highest and the lowest value of TOA	36
2.11	Value of A and B dynamic pressure profile parameters at different TOA .	37
2.12	Dependency between throttle opening and measured mass flow rate	38
2.13	Performance curve of the blower $PR(\dot{m})$	38
2.14	Performance curve of the blower $\psi(\phi)$	39
2.15	Performance curve obtained with pre and post calibrations	39
2.16	Pressure signal at the gauge p_{s-in} and its CWT scalogram	41
2.17	Pressure signal at the gauge p_{s-out} and its CWT scalogram	41
2.18	Pressure signal at gauge p_{s-imp1} and its CWT scalogram	42
2.19	Pressure signal at gauge p_{s-imp2} and its CWT scalogram	42
2.20	Pressure signal at gauge p_{s-imp3} and its CWT scalogram	42
2.21	Phase trajectory of the pressure signals registered by gauge p_{s-in} and its projections	43
2.22	Phase trajectory of the pressure signals registered by gauge p_{s-out} and its projections	44
2.23	Phase trajectory of the pressure signals registered by gauge p_{s-imp1} and its projections	45
2.24	Phase trajectory of the pressure signals registered by gauge p_{s-imp2} and its projections	45
2.25	Phase trajectory of the pressure signals registered by gauge p_{s-imp3} and its projections	46
2.26	RDF factor obtained at pressure tappings in dynamic tests and suggested threshold value ($RDF_t = 3$)	47
2.27	Block diagram of the controller for a real-time RDF measurement	48
2.28	Pressure min-to-max plots registered at different positions of the throttling valve; RDF values registered at different positions of the throttling valve .	49
2.29	Static pressure frequency spectra obtained for different throttle values at the blower inlet (p_{s-in})	52
2.30	Static pressure frequency spectra obtained for different throttle values at the blower outlet (p_{s-out})	53
2.31	Static pressure frequency spectra obtained for different throttle values at the blower shroud before leading edge at $-0.2L$ (p_{s-imp1})	53
2.32	Static pressure frequency spectra obtained for different throttle values at the blower shroud over impeller at $0.4L$ (p_{s-imp2})	54
2.33	Static pressure frequency spectra obtained for different throttle values at the blower shroud over impeller at $0.9L$ (p_{s-imp3})	55
2.34	XY scatter plots of FFT power spectra obtained within inlet zone (p_{s-imp1}) at characteristic values of the throttling corresponding to different working conditions	56
2.35	Phase portraits of the pressure signals registered at gauge p_{s-in} at TOA values corresponding to different working regimes	57

2.36	Phase portraits of the pressure signals registered at gauge p_{s-imp1} at TOA values corresponding to different working regimes	58
2.37	Pressure min-to-max plots registered at different positions of the throttling valve in the case of reduced plenum volume; RDF values registered at different positions of the throttling valve in the case of reduced plenum volume	59
2.38	Static pressure frequency spectra obtained for different throttle values at the blower inlet (p_{s-in})	61
2.39	Static pressure frequency spectra obtained for different throttle values at the blower outlet (p_{s-out})	62
2.40	Static pressure frequency spectra obtained for different throttle values at the blower shroud before leading edge at $-0.2L$ (p_{s-imp1})	63
2.41	Static pressure frequency spectra obtained for different throttle values at the blower shroud over impeller at $0.4L$ (p_{s-imp2})	63
2.42	Static pressure frequency spectra obtained for different throttle values at the blower shroud over impeller at $0.9L$ (p_{s-imp3})	64
2.43	Frequency spectra at p_{s-out} at the deep surge $TOA = 5\%$	65
2.44	Frequency spectra at p_{s-imp3} at the deep surge $TOA = 5\%$	66
3.1	Geometry of the fluid domain. Impeller shroud was not included in the display	71
3.2	Selected elements of the CAD geometry of the experimental stand	72
3.3	Wedge-shaped block resulting from the necessity of joining block vertices	73
3.4	Inlet domain	74
3.5	Rotor domain	74
3.6	Outlet domain (not full outlet pipe section is shown)	74
3.7	Computational domain used in the study with the main boundary conditions and interfaces outlined	78
3.8	Comparison of velocity profiles obtained in the simulation and in the experiment at the pipe cross-section containing gauges p_{s-in} , p_{t-in1} and p_{t-in2} ($\dot{m} = 0.8 \frac{\text{kg}}{\text{s}}$)	79
3.9	Interfaces defined in the study between two domains	81
3.10	Interfaces defined in the study in particular domains	82
3.11	Positions and labels of the monitoring points and surfaces	82
3.12	Example of the simulation final result establishment	83
3.13	Results of the mesh size study conducted close to the design conditions ($\dot{m} = 0.8 \frac{\text{kg}}{\text{s}}$)	84
3.14	Results of the turbulence model study	87
3.15	TOA values in quasi dynamic analysis that were chosen for comparison with the mass flow rate applied in the simulation	88
3.16	Frequency spectra obtained from full experimental signal ($2^{21} = 2097152$ samples) and experimental signal after trimming (65995 samples)	89
3.17	Compressor performance curve $PR(\dot{m})$ obtained in the experiment and the numerical study	90
3.18	Compressor performance curve $\psi(\phi)$ obtained in the experiment and the numerical study	90
3.19	Operational point traces obtained in the simulation compared to the experimental performance curve	91

3.20	Flow within impeller and diffuser	93
3.21	Circumferentially mass flow averaged velocity in the meridional cross-section of the vaneless diffuser	94
3.22	Circumferentially mass flow averaged flow angle from the normal direction in the meridional cross-section of the vaneless diffuser	94
3.23	Mass flow averaged pressure rise along the diffuser	95
3.24	Velocity distribution in the volute cross-section located opposite to the tongue; arrows correspond to the velocity component tangential to the surface, color map corresponds to the velocity component normal to the surface	96
3.25	Overview on flow at $\dot{m} = 0.5 \frac{\text{kg}}{\text{s}}$	97
3.26	Velocity color maps at $t = \tau$ on blade to blade surfaces located at different spanwise positions, where 0% corresponds to the hub and 100% to the shroud	98
3.27	Migration of stagnation cells from shroud to hub	99
3.28	Axial velocity component at cross-section containing point p_{s-imp1} at $\dot{m} = 0.3 \frac{\text{kg}}{\text{s}}$	101
3.29	Region affected by the inlet recirculation at $\dot{m} = 0.3 \frac{\text{kg}}{\text{s}}$	102
3.30	Pressure color map of inlet zone at different mass flow rates	102
3.31	Time-variation of flow parameters at the control surfaces during the surge cycle	103
3.32	Pressure ratio during the surge cycle	104
3.33	Pressure distribution at consecutive moments of the surge cycle	105
3.34	Surge cycle at $t = 0.0000 \text{ s}$	107
3.35	Surge cycle at $t = 0.0176 \text{ s}$	108
3.36	Surge cycle at $t = 0.0352 \text{ s}$	109
3.37	Surge cycle at $t = 0.0528 \text{ s}$	110
3.38	Surge cycle at $t = 0.0704 \text{ s}$	111
3.39	Surge cycle at $t = 0.0880 \text{ s}$	112
3.40	Recirculation at the impeller outlet at $t = 0.0704 \text{ s}$	113
3.41	Comparison of signals obtained at p_{s-in} in the quasi dynamic experiment conducted at $TOA = 41\%$ and in the simulation at $\dot{m} = 0.8 \frac{\text{kg}}{\text{s}}$	114
3.42	Comparison of signals obtained at p_{s-out} in the quasi dynamic experiment conducted at $TOA = 41\%$ and in the simulation at $\dot{m} = 0.8 \frac{\text{kg}}{\text{s}}$	115
3.43	Variation of the mass flow averaged pressure signals at the surface <i>insurf</i> for different boundary conditions	116
3.44	Comparison of pressure signals obtained at p_{s-imp1} in the quasi dynamic experiment conducted at $TOA = 18\%$ and in the simulation at $\dot{m} = 0.5 \frac{\text{kg}}{\text{s}}$	117
3.45	Comparison of pressure signals obtained at p_{s-imp1} in the quasi dynamic experiment conducted at $TOA = 8\%$ and in the simulation at $\dot{m} = 0.3 \frac{\text{kg}}{\text{s}}$	118
3.46	Comparison of signals obtained at p_{s-in} in the quasi dynamic experiment conducted at $TOA = 5\%$ and in the simulation at $\dot{m} = 0.1 \frac{\text{kg}}{\text{s}}$	119
3.47	Comparison of pressure signals obtained at p_{s-out} in the quasi dynamic experiment conducted at $TOA = 5\%$ and in the simulation at $\dot{m} = 0.1 \frac{\text{kg}}{\text{s}}$	120
3.48	Comparison of pressure signals obtained at p_{s-in} in the quasi dynamic experiment conducted at $TOA = 5\%$ and in the simulation at $\dot{m} = 0.1 \frac{\text{kg}}{\text{s}}$ with reduced plenum volume	121

3.49	Comparison of pressure signals obtained at p_{s-out} in the quasi dynamic experiment conducted at $TOA = 5\%$ and in the simulation at $\dot{m} = 0.1 \frac{\text{kg}}{\text{s}}$ with reduced plenum volume	122
3.50	Phase portrait of the pressure signals in the control point p_{s-in} at \dot{m} values corresponding to different working regimes	124
3.51	Comparison of the phase portrait projections of the pressure signals in the control point p_{s-in} at $\dot{m} = 0.1 \frac{\text{kg}}{\text{s}}$ and $TOA = 5\%$	124
3.52	Phase portrait of the pressure signals obtained in the simulation in the control point p_{s-out} at \dot{m} values corresponding to different working regimes	125
3.53	Comparison of the phase portrait projections of the pressure signals in the control point p_{s-out} at $\dot{m} = 0.1 \frac{\text{kg}}{\text{s}}$ and $TOA = 5\%$	125
3.54	Phase portrait of the pressure signals obtained in the simulation in the control point p_{s-imp1} at \dot{m} values corresponding to different working regimes	126
3.55	Comparison of the phase portrait projections of the pressure signals in the control point p_{s-imp1} at $\dot{m} = 0.1 \frac{\text{kg}}{\text{s}}$ and $TOA = 5\%$	126

List of Tables

1.1	Summary of different alterations of the surge model; ΔN_s - model includes rotor speed variations; Impeller type: A - axial, C - centrifugal; RS - model includes the rotating stall	7
2.1	Characteristic frequencies observed in the dynamic analysis; abbreviations: N-present at a unstable regime, B-present at all TOA	40
2.2	Working regimes identified during dynamical tests	40
2.3	Working regimes identified during quasi-dynamic tests	49
2.4	Characteristic frequencies observed in the study; wide peaks are marked with \approx sign; abbreviations: S-present at the stable regime ($TOA > 20\%$), N-present at the unstable regime ($TOA < 20\%$), B-present at all TOA	51
2.5	Characteristic frequencies observed in the study in the SP case; wide peaks are marked with \approx sign; abbreviations: S-present at the stable regime ($TOA > 20\%$), N-present at the unstable regime ($TOA < 20\%$), B-present at all TOA	61
2.6	Surge amplitudes and frequency in the SP and the LP cases	62
2.7	Surge amplitudes and frequency in SP and LP case	67
3.1	Parameters of the computational mesh used in this study	76
3.2	Meshes used in the mesh size study	83
3.3	Models of turbulence used in the study	85
3.4	Working regimes identified during the simulations	91
3.5	Characteristic frequencies observed in the numerical study; abbreviations: S-present at the stable regime ($\dot{m} \geq 0.8 \frac{\text{kg}}{\text{s}}$); N-present at the pre-surge and the surge regime ($\dot{m} \leq 0.5 \frac{\text{kg}}{\text{s}}$), B-present under both: stable and unstable conditions	114
3.6	Characteristic frequencies observed at the deep surge in the numerical study with the reduced plenum volume	120
3.7	Surge amplitudes and frequencies in the SP and the LP cases	123

Abbreviations

AIRS	A brupt I mpeller R otating S tall
CFD	C omputational F luid D ynamics
CNC	C omputer N umerical C ontrol
FFT	F ast F ourier T ransform
IR	I nlet R ecirculation
IT	I nstitute of T urbomachinery
LP	L arge P lenum - corresponds to the experimental stand with a long outlet pipe
LSM	L east S quare M ethod
TUL	Ł ódź U niversity of T echnology
ODE	O rdinary D ifferential E quation
PIRS	P rogressive I mpeller R otating S tall
PIV	P article I mage V elocimetry
RANS	R eynolds A veraged N avier S tokes
RDF	R ate of D errivative F luctuation
RS	R otating S tall
SP	S mall P lenum - corresponds to the experimental stand with a short outlet pipe
TOA	T hrottle O pening A rea
US	U niversity of S trathclyde
VDRS	V aneless D iffuser R otating S tall

Nomenclature

α	diffuser flow angle measured from the normal direction
α_{cr}	critical diffuser inlet flow angle for the VDRS onset measured from the normal direction
α_r	diffuser inlet flow angle for recirculation of the boundary layer measured from the normal direction
$\delta = 0.8 \text{ mm}$	blade tip clearance
ϵ	turbulent dissipation rate
$\phi = \frac{\dot{m}}{\pi D_2 b_2 \rho u_{tip}}$	dimensionless mass flow rate coefficient
$\lambda_{1,2}$	system eigenvalues
λ_c	number of the stall cells
μ	dynamic viscosity
ω	turbulent specific dissipation
$\psi = \frac{2(p_{out}-p_{in})}{\rho u_{tip}^2}$	dimensionless pressure rise coefficient
ρ	medium density
A, B	dimensionless parameters describing the empirical dynamic pressure profile $\frac{p_d}{p_{dmax}} = A \left[1 - \left(\frac{r}{R} \right)^2 \right]^B$
$A_{p-in} = 823 \text{ mm}^2$	cross-section area of the passage at the impeller inflow
$A_{p-out} = 676 \text{ mm}^2$	cross-section area of the passage at the impeller outflow
$\mathcal{B} = \frac{u_{tip}}{2c} \sqrt{\frac{V_p}{S_c L_c}} = \frac{u_{tip}}{2L_c \omega_H}$	\mathcal{B} factor in Greitzer model
$b_1 = 38.9 \text{ mm}$	blade height at the leading edge
$b_2 = 14.5 \text{ mm}$	blade height at the trailing edge
$\frac{b}{R_2} = \frac{2b_2}{D_2} = 0.087$	relative diffuser length
$c = 340 \frac{\text{m}}{\text{s}}$	speed of sound in the air at 25 °C
$D_{1hub} = 86.3 \text{ mm}$	diameter of the hub at the leading edge
$D_2 = 330.0 \text{ mm}$	diameter of the impeller at the trailing edge
$D_3 = 476 \text{ mm}$	diameter of the diffuser outlet
$D_{in} = 300 \text{ mm}$	diameter of the inlet pipe
$D_{out} = 150 \text{ mm}$	diameter of the outlet pipe
$f_{BP} = 2.3 \text{ kHz}$	blade passing frequency
f_c	frequency of the stall cell rotation
f_H	frequency of the Helmholtz resonator

$f_{H-LP} = 11$ Hz	frequency of the Helmholtz resonator in the case of large plenum volume
$f_{H-SP} = 17$ Hz	frequency of the Helmholtz resonator in the case of small plenum volume
f_n	frequency of phenomena present at unstable operation
$f_{rot} = 100$ Hz	impeller rotation frequency (100Hz)
f_s	frequency of phenomena present at stable operation
$\mathcal{G} = \frac{S_c L_t}{S_t L_c}$	\mathcal{G} factor in Greitzer model
k	turbulent kinetic energy
L	dimensionless parameter describing gauge position along the blade
$L_{c/t}$	length of the compression/throttling duct in Greitzer model
$L_p = 154$ mm	average length of a passage
\dot{m}	mass flow rate
$\dot{m}_{c/t}$	mass flow rate in the compression/throttling duct in Greitzer model
p	static pressure
p_c	pressure in the compressor duct in Greitzer model
p_d	dynamic pressure
p_p	pressure in the plenum in Greitzer model
PR	pressure ratio
p_{s-impX}	signal representing static pressure at the impeller shroud ($X \in \{1, 2, 3\}$)
p_{s-in}	signal representing static pressure at the blower inlet
p_{s-out}	signal representing static pressure at the blower outlet
p_t	pressure in the throttle duct in Greitzer model
$p_{t-in1-2}$	signal representing total pressure at the blower inlet
$S_{c/t}$	area of the compression/throttling duct in Greitzer model
u	velocity
u'	velocity fluctuation
u_{avg}	average flow velocity
u_τ	shear velocity
$u_{tip} = 103 \frac{m}{s}$	impeller tip speed
$V_{LP} = 0.0968$ m ³	volume of the outlet plenum in the case of long pipe configuration
V_p	plenum volume in Greitzer model
$V_{SP} = 0.0435$ m ³	volume of the outlet plenum in the case of short pipe configuration
y^+	dimensionless wall distance
$z = 23$	number of blades

Theoretical background

1.1 Introduction

Figure 1.1 presents the cross-section of the centrifugal compressor, fan or blower (referred to as the compressing machine further on) with definitions of its main dimensions. Performance of the compressing machine is traditionally represented by a plot with pressure ratio $PR = \frac{p_{out}}{p_{in}}$ on the ordinate and mass flow rate \dot{m} $\left[\frac{\text{kg}}{\text{s}}\right]$ on the abscissa. Alternatively, a non-dimensional parameters are used. A non-dimensional mass-flow rate coefficient ϕ is calculated using formula 1.1 and a non-dimensional pressure rise coefficient ψ is calculated using formula 1.2.

$$\phi = \frac{\dot{m}}{\pi D_2 b_2 \rho u_{tip}} = \frac{\dot{m}}{\pi^2 D_2^2 b_2 \rho_2 f_{rot}} \quad (1.1)$$

$$\psi = \frac{2(p_{out} - p_{in})}{\rho u_{tip}^2} = \frac{2p_{in}(PR - 1)}{\pi^2 D_2^2 \rho_2 f_{rot}^2} \quad (1.2)$$

where $u_{tip} = \pi D_2 f_{rot}$ corresponds to entrainment velocity of the blade trailing edge and ρ_2 corresponds to density of compressed medium at the impeller outlet. Non-dimensional coefficients allow to eliminate dependency of the performance curve on the peripheral parameter u_{tip} and ρ . A given compressing machine at different f_{rot} , but at the same ϕ and ψ has the same inlet flow angle, hence in absence of compressibility effects (low Mach numbers) and neglecting the diffusion losses, the outlet flow angle is also the same.

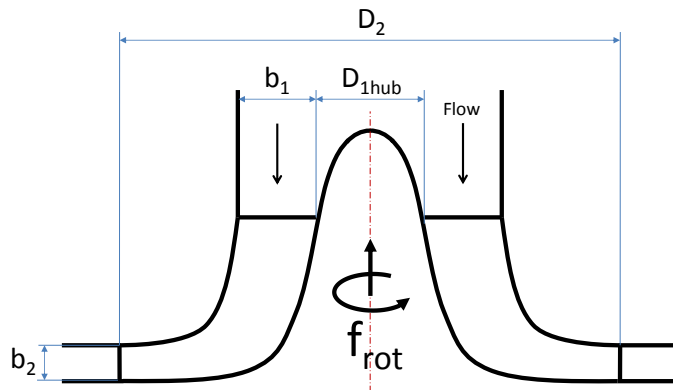


FIGURE 1.1: Cross-section of the compressing machine with its main dimensions

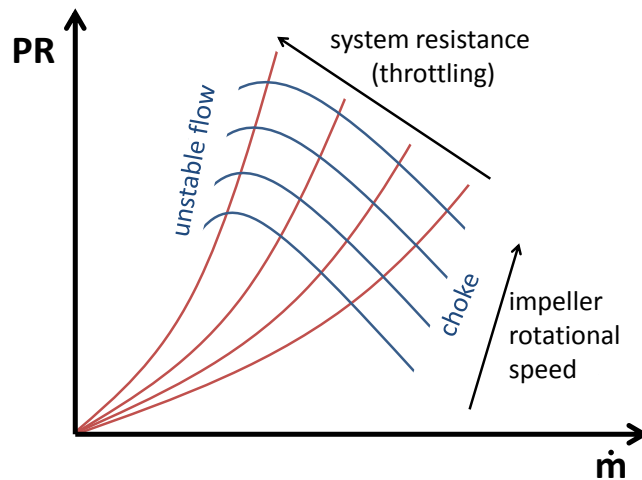


FIGURE 1.2: Typical performance curves of the compressing machine (blue) and the system characteristics (brown)

Neglecting the Reynolds number variation effects one can conclude that also the efficiency is the same [22].

Typical performance curves of the compressing machine are presented together with typical system resistance characteristics in figure 1.2 [68]. A family of machine performance curves is obtained by variation of rotational speed f_{rot} . A family of the system resistance curves can be obtained by variable throttling. At the experimental stand this is usually done by different positions of the outlet throttling valve. Intersection of curves attained at given f_{rot} and system resistance defines the operating point of the system. At high mass flow rates the machine operational range is limited by phenomenon known as choke [122]. At low mass flow rates the machine operational range is limited by unstable phenomena which are examined in this study. Description of known unstable flow structures is provided in section 1.2. At high Mach numbers the distance between surge and choke becomes smaller [102].

1.2 Classification of unstable flow structures

As it was presented, whenever a compressing machine operates at a given rotational speed and the flow is continuously reduced, there is usually a moment after which the stage will no longer operate in a stable manner. Therefore, it is very important to accurately predict the point at which instabilities are likely to occur. However, there are many mechanisms and regions of appearance of unstable flow structures and it is very difficult to predict the conditions of their occurrence. The most common words used in reference to unstable working conditions are the **surge** and the **stall**. Although they are different phenomena, these words are commonly used, or misused, to describe the same phenomenon or unstable operating conditions in general. This section is intended to provide brief classification of the unstable flow phenomena which was used in this study. It was based on definitions given in different textbooks including Japikse [60, 61], Pampreen [98], van den Braembussche [122], Greitzer [41] and Kryłowicz [68].

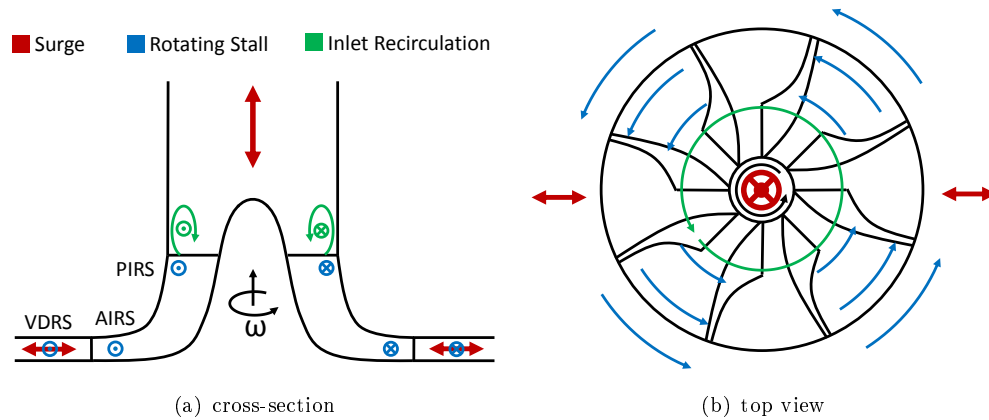


FIGURE 1.3: Localisation of unstable flow structures according to classification applied in this study

Each unstable flow structure is associated with oscillations of flow parameters which are propagating in certain direction. Direction of disturbance propagation can be treated as a good distinguishing mark for each class of unstable flow structures. Instability can be global, i.e. influence the whole machine together with the inlet and the outlet piping or appear locally. In the case of local instabilities the place of occurrence is also important for classification. Each part of the compressing machine is characterized by different flow structures and consequently different unstable phenomena can be triggered therein. Figure 1.3 illustrates flow structures divided according to presented criteria. It includes:

- **Surge** - global flow fluctuations in the axial direction.
- **Rotating Stall (RS)** - local circumferential flow fluctuations. Depending on the place of occurrence it can be classified as:
 - **Progressive Impeller Rotating Stall (PIRS)** - appearing in the inducer zone. This structure is usually connected with gradual drop of the machine pressure ratio, hence the name "progressive".
 - **Abrupt Impeller Rotating Stall (AIRS)** - appearing close to the impeller outlet. This structure is usually connected with sudden drop of the machine pressure ratio, hence the name "abrupt".
 - **Vaneless Diffuser Rotating Stall (VDRS)** - appearing in the diffuser.
- **Inlet Recirculation (IR)**, also known as the inducer recirculation or inducer back-flow) - local flow structure upstream of the impeller. This phenomenon has a form of toroidal flow structure that can be present around the whole circumference.

1.3 Surge

According to [23], the surge phenomenon can be divided into four stages:

- Mild Surge - minor oscillations of the pressure, a reverse flow is not observed.
- Classic Surge - non-linear oscillations, a reverse flow is not observed.

- Modified Surge - classic surge together with the rotating stall (see section 1.4).
- Deep Surge - pressure oscillations are large enough to reverse the flow direction periodically.

In fact, it is usually difficult to distinguish between these types and it is common to simplify the division into the mild and the deep surge only [114]. The deep surge corresponds to situation, when oscillations reach the scale leading to global inversion of a flow direction during some part of the cycle. Surge phenomenon was firstly recognized in the 1950s and has been a subject of extensive research thereafter. The first non-stable phenomena in centrifugal units were identified and analysed by Emmons et al. [26]. In 1976 Greitzer developed a mathematical model of surge onset [38] and confirmed it by the experiment [39]. This model, in spite of being originally developed for axial compressing units, was proven to work well in case of the centrifugal machine [44, 87, 129]. Second Greitzer model, which was developed to describe the time-evolution of developed flow instability [91, 92] was successfully applied only in the case of axial compressors.

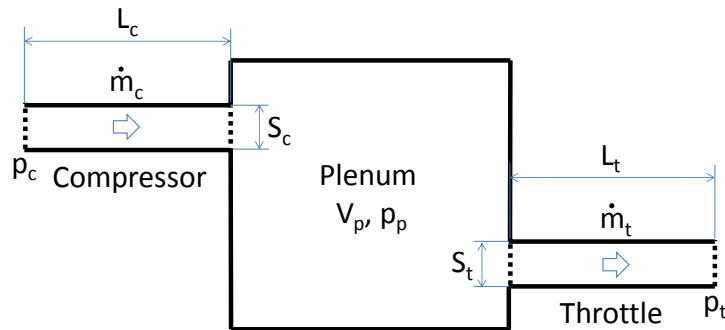


FIGURE 1.4: Compressing machine in Greitzer model

1.3.1 Greitzer model

1.3.1.1 Model assumptions

Figure 1.4 presents a scheme of a compressing system applied by Greitzer. The compressor is represented by a characteristic function generator (that can be also interpreted as the moving actuator disc) and a constant area pipe. In this region the fluid has significant kinetic energy. Length of the inlet duct L_c and area of its cross-section S_c are specified in a way assuring the same dynamics in conditions of variable mass flow rate. Similarly, the parameters of the throttle valve L_t and S_t are chosen. The plenum of volume V_p is considered as large capacity reservoir with negligible kinetic energy of the fluid inside, but its variable pressure p_p [122]. Model assumptions are summarized below [50]:

- Flow within pipes is incompressible, inviscid and one dimensional, hence \dot{m}_c and \dot{m}_t are constant along the ducts.
- Compression in the plenum is isentropic.
- Temperature in the whole compression system is constant.

- Pressure in the whole plenum is uniform.
- Valve is quasi-static.
- Gravity forces are neglected.

One can see that this model is very basic. Also, the assumption of isentropic compression contradicts the assumption of a constant temperature. Nevertheless, the Greitzer model is considered as milestone in the field of surge modelling and is widely used till now.

The derivation of lumped parameter surge model was based on two fundamental equations of the fluid mechanics. Due to assumption of no kinetic energy in the plenum the energy equation became trivial and derivation was based on mass and momentum conservation. The mass conservation equation is given below [127]:

$$\frac{1}{\rho} \frac{D\rho}{Dt} + \nabla \cdot \mathbf{u} = 0 \quad (1.3)$$

Second is the momentum conservation of inviscid fluid:

$$\rho \frac{D\mathbf{u}}{Dt} = -\nabla p + \rho \mathbf{g} \quad (1.4)$$

Where \mathbf{g} corresponds to gravitational force vector. The Hamilton operator $\nabla = \left(\frac{\partial}{\partial x}, \frac{\partial}{\partial y}, \frac{\partial}{\partial z} \right)$ in one dimension simplifies to:

$$\nabla = \frac{\partial}{\partial x} \quad (1.5)$$

Similarly the Stokes operator $\frac{D}{Dt} = \frac{\partial}{\partial t} + \mathbf{u} \cdot \nabla$ in one dimension simplifies to:

$$\frac{D}{Dt} = \frac{\partial}{\partial t} + u \frac{\partial}{\partial x} \quad (1.6)$$

1.3.1.2 Compressor and throttle duct

For an incompressible flow the term $\frac{1}{\rho} \frac{D\rho}{Dt}$ can be neglected. In absence of gravitational forces $\rho \mathbf{g}$ can be also neglected. Equations 1.3 and 1.4 simplify to:

$$\begin{cases} \nabla \cdot \mathbf{u} &= 0 \\ \rho \frac{D\mathbf{u}}{Dt} &= -\nabla p \end{cases}$$

After combining those two equations and applying formulas 1.5 and 1.6 one obtains:

$$\rho \frac{\partial u}{\partial t} = -\frac{\partial p}{\partial x}$$

One can introduce $\dot{m}_c = \rho u S_c$, which according to the incompressibility assumption is constant along the whole pipe:

$$d\dot{m}_c = -\frac{\partial p}{\partial x} S_c dt$$

Relation $p_c(\dot{m}_c)$ is given by the compressor performance curve. A change Δp_c induces certain change of Δp_p . Therefore, the global change of pressure along the inlet duct is

given by $\frac{\partial p}{\partial x} = \frac{\Delta p_p - \Delta p_c}{L_c}$. The instantaneous change in mass flow in the compressor can be described by:

$$dm_c = (\Delta p_c - \Delta p_p) \frac{S_c}{L_c} dt \quad (1.7)$$

For the throttle duct, the same approach yields:

$$dm_t = (\Delta p_p - \Delta p_t) \frac{S_t}{L_t} dt \quad (1.8)$$

1.3.1.3 Plenum

Speed of sound in a certain medium is given by a partial derivative of pressure over density at constant entropy [28]:

$$c^2 = \left(\frac{\partial p}{\partial \rho} \right)_s$$

From assumption of isentropic transformation in the plenum one can write:

$$\frac{\partial \rho}{\partial t} = \frac{1}{c^2} \frac{\partial p}{\partial t}$$

The rate of change of the mass flow rate in the plenum $\frac{d\dot{m}}{dt}$ is simply equal to difference of mass flow rates in both ducts $\dot{m}_c - \dot{m}_t$. Therefore, one can write:

$$\dot{m}_c - \dot{m}_t = \frac{d(\rho V_p)}{dt} = V_p \frac{1}{c^2} \frac{dp_p}{dt} \quad (1.9)$$

1.3.1.4 Model equations

Equations in Greitzer model are usually presented in non-dimensional form with ϕ and ψ parameters and time scale τ

$$\tau = 2\pi f_H t$$

where f_H represents frequency of the Helmholtz resonator [41]:

$$f_H = c \sqrt{\frac{S_c}{V_p L_c}} \quad (1.10)$$

Then, equations 1.7, 1.8, 1.9 transform to

$$\frac{d\phi_c}{d\tau} = \mathcal{B}(\psi_c - \psi_p) \quad (1.11)$$

$$\frac{d\phi_t}{d\tau} = \frac{\mathcal{B}}{\mathcal{G}}(\psi_p - \psi_t) \quad (1.12)$$

$$\frac{d\psi_p}{d\tau} = \frac{1}{\mathcal{B}}(\phi_c - \phi_t) \quad (1.13)$$

Mass flow coefficient ϕ and pressure rise coefficient ψ were defined by equations 1.1 and 1.2 respectively. Coefficients \mathcal{G} and \mathcal{B} are given by:

$$\mathcal{G} = \frac{S_c L_t}{S_t L_c}$$

$$\mathcal{B} = \frac{u_{tip}}{2c} \sqrt{\frac{V_p}{S_c L_c}} = \frac{u_{tip}}{2L_c \omega_H} \quad (1.14)$$

Hence, instead of five parameters (S_c , S_t , L_c , L_t , V_p), there are only two significant parameters that control the system dynamics. In fact, \mathcal{G} factor has small influence on the system dynamics. It is often assumed that L_t is very small and consequently also \mathcal{G} becomes insignificant [29, 129]. The most important parameter, that influences the system dynamics is the Greitzer factor \mathcal{B} .

Greitzer originally supplemented the model with fourth equation describing the rotating stall and the time-lag in reaching certain value of pressure that is caused by process of formation of this phenomenon:

$$\frac{d\psi_c}{d\tau} = \frac{1}{\eta}(\psi_{c,ss} - \psi_c); \quad \eta = N_s \frac{\pi D_2}{2\mathcal{B}L_c} \quad (1.15)$$

where N_s is the number of impeller rotations needed for the rotating stall to form. Nevertheless, this equation was proven to be a source of many problems in case of the centrifugal impellers [50]. Greitzer himself applied different values [39] including $N_s = 2$, $N_s = 0$ and pointed out that this parameter has different values for different positions on the machine performance curve. Hansen et al. [44] obtained good agreement with experiment for $N_s = 0.5$, Meuleman [87] applied $N_s = 2$. In fact, as it will be presented in section 1.4 the phenomenon of the rotating stall in the centrifugal compressing machines can have many different forms and locations. Therefore, according to the contemporary knowledge (see section 1.4), it can be stated that equation 1.15 does not describe complexity of this phenomenon in case of the centrifugal impellers. Moreover, it is introduced for a price of additional parameter η depending on N_s which is difficult to be established without empirical data.

TABLE 1.1: Summary of different alterations of the surge model; ΔN_s - model includes rotor speed variations; Impeller type: A - axial, C - centrifugal; RS - model includes the rotating stall

Authorship	Year	Equations	ΔN_s	Impeller type	RS
Greitzer [38]	1976	1D Incompressible	✗	A	✗
Hansen et al. [44]	1981	1D Incompressible	✗	C	✗
Elder and Gill [25]	1985	1D Compressible	✗	C	✗
Fink et al. [29]	1992	1D Incompressible	✓	C	✗
Gravdahl and Egeland [37]	1997	1D Incompressible	✓	C	✗
Willems [129]	2000	1D Incompressible	✗	C	✗
Meuleman [87]	2002	1D Incompressible	✗	C	✗
Helvoirt [124]	2007	1D Incompressible	✗	C	✗
Yoon et al. [131]	2011	1D Incompressible	✗	C	✗
Macdougall and Elder [81]	1983	1D Compressible	✗	AC	✗
Botros [13]	1994	1D Compressible	✓	AC	✗
Badmus et al. [9]	1995	Quasi-1D Compressible	✗	AC	✗
Moore and Greitzer [91]	1986	2D Incompressible	✗	A	✓
Gravdahl and Egeland [36]	1997	2D Incompressible	✓	A	✓
Feulner et al. [27]	1996	1D/2D Compressible	✗	A	✓
Ishii and Kashiwabara [57]	1996	2D Compressible	✗	A	✓
Spakovszky [112]	2001	2D Compressible	✗	A	✓

1.3.1.5 Another surge models

Numerous researchers analysed Greitzer model in attempt to introduce another factors that are known to be important for the surge onset and the surge cycle. Table 1.1 contains list of papers considering different surge models and their alterations. Table was created by Willems and de Jager [130] and supplemented with more recent works.

Greitzer model from 1976 was originally developed for low-speed axial units. Hansen et al. confirmed that 1976 Greitzer model is applicable for centrifugal impellers and improved the model by introducing a higher-order polynomial to approximate the compressor performance curve $\psi_c(\phi_c)$. Badmus et al. [9] also applied a higher-order performance curve, Fink et al. [29] introduced influence of the rotor speed variation. Gravdahl and Egeland determined a second-order approximation of $\psi_c(\phi_c)$ based on compressor geometry and energy considerations. They also included influence of the impeller rotational speed. Elder and Gill [25] modelled sections of the impeller separately (inducer, impeller tip, space between impeller and vaned diffuser, vaned diffuser). Meuleman [87] proposed correction that included the unsteady character of the laminar flow and provided better agreement with the experimental amplitudes of fluctuation. Willems in his book [129] analysed two-equation (equations 1.11 and 1.13) Greitzer model that considered also the valve dynamics. In fact, most of recent developments of Greitzer model consider the two-equation version and the emphasis is put on the valve $\psi_t(\phi_t)$ and machine $\psi_c(\phi_c)$ characteristics. Van Helvoirt [124] developed a closed-loop surge model that was based on two-equation Greitzer model with additional parameter F being a measure for the ratio of the plenum volume and the return piping volume. Yoon et al. [131] examined a two-equation Greitzer model supplemented with empirical throttle characteristics.

Macdougall and Elder [82] used relations for a polytropic compression process in combination with principles of conservation of mass, momentum and energy. This method was followed by Badus et al. [9] and Botros [14] including variation of the impeller speed. These three models can be applied to both axial and centrifugal compression systems, nevertheless, they are quite complex.

In 1986 Greitzer together with Moore developed a model that included the time-evolution of the developed instability. This model was also created for axial impellers. In fact, all models that followed this method and included influence of the rotating stall were confirmed to be valid only for the axial impellers [27, 36, 57, 112].

1.3.2 Calculation of the stability limit

Stability limit is calculated in the same manner as it was presented by Van Den Braembussche [122]. Two-equation Greitzer model is a system of differential equations 1.11 and 1.13 that contains two independent variables ϕ_c and ψ_p . Variable ϕ_t can be then treated as a parameter which depends on ψ_t according to the valve characteristics $\phi_t(\psi_t)$. Similarly ψ_c can be treated as a parameter that depends on ϕ_c according to the compressor performance curve $\psi_c(\phi_c)$. Including above conclusions, the system of equations 1.11 and 1.13 has a form:

$$\begin{aligned}\frac{d\phi_c}{d\tau} &= \mathcal{B}(\psi_c(\phi_c) - \psi_p) \\ \frac{d\psi_p}{d\tau} &= \frac{1}{\mathcal{B}}(\phi_c - \phi_t(\psi_t))\end{aligned}$$

After linearisation around the point (ϕ_c, ψ_p) system transforms to:

$$\frac{d\Delta\phi_c}{d\tau} = \mathcal{B} \left(\frac{\partial\psi_c}{\partial\phi_c} \Delta\phi_c - \Delta\psi_p \right) \quad (1.16)$$

$$\frac{d\Delta\psi_p}{d\tau} = \frac{1}{\mathcal{B}} \left(\Delta\phi_c - \frac{\partial\phi_t}{\partial\psi_t} \Delta\psi_t \right) \quad (1.17)$$

Component $\frac{\partial\psi_c}{\partial\phi_c}$ can be interpreted as slope of the machine performance curve and therefore can be written as $\psi'_c(\phi_c)$. Similarly $\frac{\partial\psi_t}{\partial\phi_t}$ can be interpreted as slope of the valve resistance curve and can be written as $\psi'_t(\phi_t)$. From the assumption of constant pressure within the plenum ψ_p and negligible L_t one can conclude that $\Delta\psi_t \approx \Delta\psi_p$. Including above comments, system of equations 1.16-1.17 can be presented in the matrix form:

$$\begin{bmatrix} \frac{d\Delta\phi_c}{d\tau} \\ \frac{d\Delta\psi_p}{d\tau} \end{bmatrix} = \begin{bmatrix} \mathcal{B}\psi'_c(\phi_c) & -\mathcal{B} \\ \frac{1}{\mathcal{B}} & -\frac{1}{\mathcal{B}\psi'_t(\phi_t)} \end{bmatrix} \cdot \begin{bmatrix} \Delta\phi_c \\ \Delta\psi_p \end{bmatrix} \quad (1.18)$$

To solve such a system of ODE's one has to determine the characteristic polynomial $\det[M - \lambda I] = 0$, where M represents matrix of coefficients in equation 1.18, λ - eigenvalues of M , I - identity matrix:

$$\begin{aligned} \det(M - \lambda I) &= (\mathcal{B}\psi'_c(\phi_c) - \lambda) \left(-\frac{1}{\mathcal{B}\psi'_t(\phi_t)} - \lambda \right) - \left(\frac{-\mathcal{B}}{\mathcal{B}} \right) \\ &= \lambda^2 + \lambda \left(\frac{1}{\mathcal{B}\psi'_t(\phi_t)} - \mathcal{B}\psi'_c(\phi_c) \right) + 1 - \frac{\psi'_c(\phi_c)}{\psi'_t(\phi_t)} = 0 \end{aligned} \quad (1.19)$$

Therefore the characteristic equation has a form of the second order polynomial with coefficients:

$$\begin{aligned} a &= 1 \\ b &= \frac{1}{\mathcal{B}\psi'_t(\phi_t)} - \mathcal{B}\psi'_c(\phi_c) \\ c &= 1 - \frac{\psi'_c(\phi_c)}{\psi'_t(\phi_t)} \\ \Delta &= \left(\frac{1}{\mathcal{B}\psi'_t(\phi_t)} - \mathcal{B}\psi'_c(\phi_c) \right)^2 - 4 \left(1 - \frac{\psi'_c(\phi_c)}{\psi'_t(\phi_t)} \right) \\ &= \left(\frac{1}{\mathcal{B}\psi'_t(\phi_t)} + \mathcal{B}\psi'_c(\phi_c) \right)^2 - 4 \end{aligned}$$

and two solutions $\lambda_1 = \frac{1}{2}(-b - \sqrt{\Delta})$ and $\lambda_2 = \frac{1}{2}(-b + \sqrt{\Delta})$ such as:

$$(\lambda - \lambda_1)(\lambda - \lambda_2) = 0 \quad (1.20)$$

Substitution $\lambda = \frac{d\Delta\phi_c}{d\tau}$ or $\lambda = \frac{d\Delta\psi_p}{d\tau}$ gives two particular solutions of $\Delta\phi_c(\tau)$ and $\Delta\psi_p(\tau)$:

$$\begin{aligned} \Delta\phi_c &= \widehat{\phi}_{c1,2} e^{\lambda_{1,2}\tau} = \widehat{\phi}_{c1,2} e^{\alpha_{1,2} + i\omega_{1,2}\tau} \\ \Delta\psi_p &= \widehat{\psi}_{p1,2} e^{\lambda_{1,2}\tau} = \widehat{\psi}_{p1,2} e^{\alpha_{1,2} + i\omega_{1,2}\tau} \end{aligned}$$

where $\widehat{\phi}_{c1,2}$ and $\widehat{\psi}_{p1,2}$ are corresponding amplitudes, $\alpha_{1,2}$ and $\omega_{1,2}$ represent real and imaginary parts of $\lambda_{1,2}$ respectively. General solution is a simple sum of both particular solutions $e^{\lambda_{1,2}\tau}$. If at least one of them is unstable, then the general solution is also

unstable. Therefore, for a given point (ϕ_c, ψ_p) one needs to analyse the exponents $\lambda_{1,2}$ to specify if the machine operation at this point can be regarded as stable.

1.3.2.1 Static stability limit ($\Delta > 0$)

At $\Delta > 0$ the characteristic equation has two real solutions, hence the system stability is maintained as long as $\lambda_1 \leq 0$ and $\lambda_2 \leq 0$. The first solution that can become positive is $\lambda_2 = \frac{1}{2}(-b + \sqrt{\Delta})$. Therefore, the system becomes unstable when:

$$\begin{aligned}
 0 &\leq \lambda_2 \\
 \frac{1}{\mathcal{B}\psi'_t(\phi_t)} - \mathcal{B}\psi'_c(\phi_c) &\leq \sqrt{\left(\frac{1}{\mathcal{B}\psi'_t(\phi_t)} - \mathcal{B}\psi'_c(\phi_c)\right)^2 - 4\left(1 - \frac{\psi'_c(\phi_c)}{\psi'_t(\phi_t)}\right)} \\
 0 &\leq -4\left(1 - \frac{\psi'_c(\phi_c)}{\psi'_t(\phi_t)}\right) \\
 \psi'_t(\phi_t) &\leq \psi'_c(\phi_c)
 \end{aligned} \tag{1.21}$$

Interpretation of this condition is presented in figure 1.5. At the right hand side of the compressing machine performance curve, its slope is negative $\psi'_c(\phi_c) < 0$ and the system curve is always positive $\psi'_t(\phi_t) > 0$. This assures fulfilment of static stability condition 1.21 and both roots of characteristic equation 1.19 are real negative numbers. In such a circumstance the system operational point is located in the local energy minimum and each random disturbance from operational point is damped.

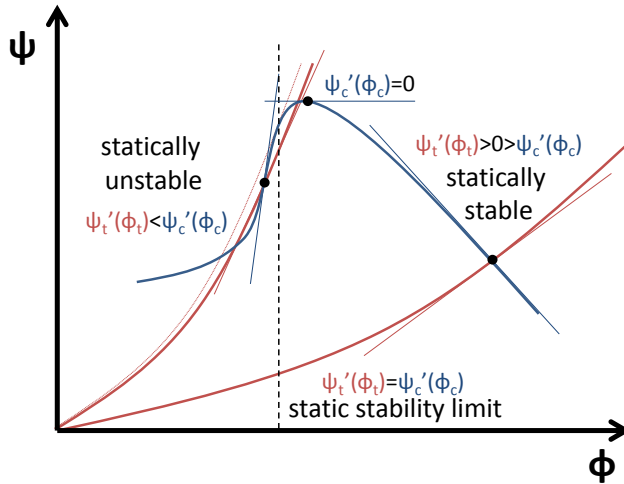


FIGURE 1.5: Static stability limit

At the left hand side of the slope of the compressing machine performance curve, both curves have positive slopes and condition 1.21 may be fulfilled. The stability limit may be obtained by finding a hypothetical system resistance curve that is tangent to ψ_c at one point. The mass flow rate ϕ at which such a situation is possible can be defined as the stability limit. All lower mass flow rates can be regarded as unstable. In this instance, one root of characteristic equation 1.19 becomes a positive real number. This means that stable equilibrium point transforms into saddle point and the equilibrium becomes unstable, i.e. every minor disturbance can cause loss of stability.

1.3.2.2 Dynamic stability limit ($\Delta < 0$)

At $\Delta < 0$ the characteristic equation has two solutions:

$$\lambda_{1,2} = \frac{1}{2}(-b \mp \sqrt{\Delta}) = -\frac{1}{2} \left(\frac{1}{\mathcal{B}\psi'_t(\phi_t)} - \mathcal{B}\psi'_c(\phi_c) \right) \mp i \sqrt{\frac{1}{4} \left(\frac{1}{\mathcal{B}\psi'_t(\phi_t)} + \mathcal{B}\psi'_c(\phi_c) \right)^2 - 1} \quad (1.22)$$

Both solutions are complex conjugates $\lambda_{1,2} = \alpha \mp i\omega$. The Euler trigonometric formula allows to associate ω with frequency of the oscillations [16], while α is responsible for the system stability. Similarly to the previous case, system is stable if the real part of both roots is negative, i.e. if $\alpha \leq 0$. Therefore, the system becomes unstable when:

$$\begin{aligned} 0 &\leq -\frac{1}{2} \left(\frac{1}{\mathcal{B}\psi'_t(\phi_t)} - \mathcal{B}\psi'_c(\phi_c) \right) \\ \frac{1}{\mathcal{B}^2\psi'_t(\phi_t)} &\leq \psi'_c(\phi_c) \end{aligned} \quad (1.23)$$

Interpretation of this condition is presented in figure 1.6. At the right hand side of the compressing machine performance curve, its slope is negative $\psi'_c(\phi_c) < 0$ and the system resistance curve is always positive $\psi'_t(\phi_t) > 0$, hence $\frac{1}{\mathcal{B}^2\psi'_t(\phi_t)} > 0$. This assures fulfilment of dynamic stability condition 1.23 and real parts of both roots of characteristic equation 1.19 are negative. In such a circumstance the system operational point is located in the local energy minimum and each random disturbance from operational point is damped.

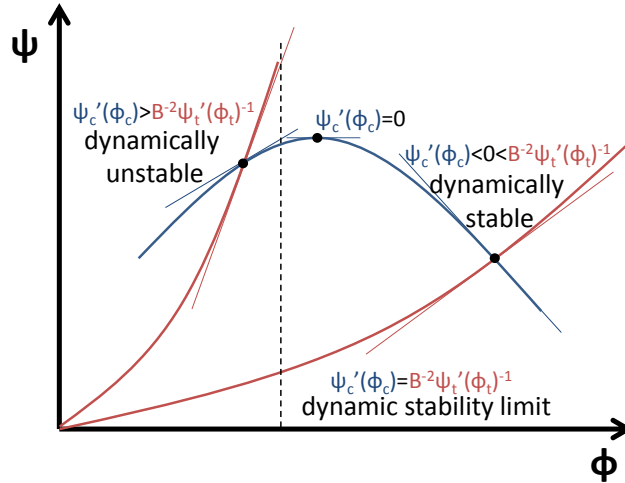


FIGURE 1.6: Static stability limit

At the left hand side of the compressing machine performance curve, both curves have positive slopes and condition 1.23 may be fulfilled. In fact, this condition is much more likely to be achieved than the condition 1.21 and the dynamic stability limit can be treated as the overall stability limit of the machine, i.e. the surge onset point. This condition also gives indication of the possible ways of increasing the machine stability.

First, trivial, can be achieved by opening the throttling valve which results in decrement of $\psi'_t(\phi_t)$. The machine stability can be also increased through decreasing the Greitzer \mathcal{B} -factor. This can be achieved by re-design of the machine or change of the plenum volume (see equation 1.14).

Assuming linear oscillations at the surge one can calculate the frequency of oscillations f from imaginary part of roots of the characteristic polynomial $\lambda_{1,2}$ given by equation 1.22:

$$f = f_H \sqrt{\frac{1}{4} \left(\frac{1}{\mathcal{B}\psi'_t(\phi_t)} + \mathcal{B}\psi'_c(\phi_c) \right)^2 - 1}$$

Assuming, that the surge onset appears at the dynamical stability limit:

$$f = f_H \sqrt{1 - \frac{\mathcal{B}\psi'_c(\phi_c)}{2}} = f_H \sqrt{1 - \frac{1}{2\mathcal{B}\psi'_t(\phi_t)}}$$

this equation allows to treat the Helmholtz resonator frequency f_H as the natural frequency of the surge. The real frequency of oscillations is slightly lower due to damping. This approximation, however, is based on assumption of linear behaviour of the surge which is not true. In fact, this phenomenon is usually characterized by very strong oscillations which are non-linear. Some researchers observed good agreement of the experimental data with f_H [103], while in some experiments it was totally different [29]. Possible reason lies in the fact, that formula 1.10 contains parameters such as L_c and A_c and there is no universal rule to estimate them. The source of discrepancy may also lay in the model assumptions listed in section 1.3.1.1.

Figure 1.7 presents summary of the system response to a small perturbation depending on the real and imaginary parts of $\lambda = \alpha \mp i\omega$. As mentioned above α is responsible for damping of the oscillations, while ω describes the oscillation frequency. Points located on the horizontal axis, i.e. for $\omega = 0$ correspond to the static stability criterion. All other points correspond to the dynamic stability criterion. From dynamical point of view, vertical axis $\alpha = 0$ can be treated as the Hopf bifurcation from the stable operation into the limit cycle [8, 74]. In such an interpretation α plays a role of Lyapunov exponent [79].

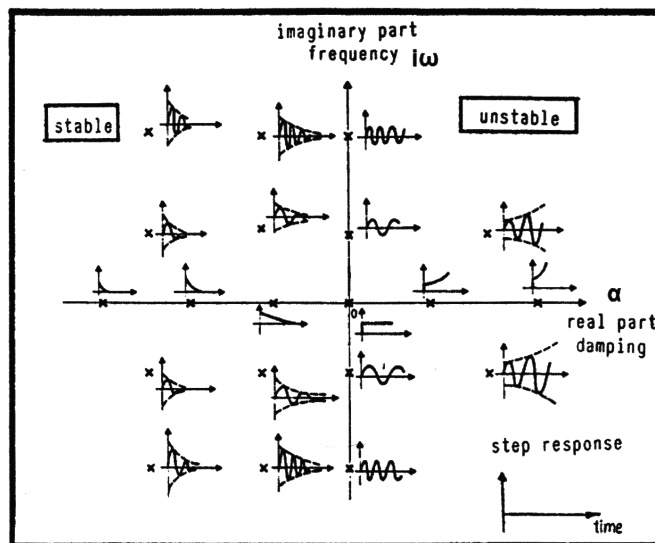


FIGURE 1.7: Response of system on perturbation in a function of $\lambda = \alpha \mp i\omega$ [122]

1.3.3 The surge cycle

The surge cycle was illustrated by Greitzer [39] for the axial compressor. Study included configurations corresponding to different \mathcal{B} -factors. Figure 1.8 presents the surge cycles obtained in cases corresponding to $\mathcal{B} = 0.65$ (figure 1.8(a)) and $\mathcal{B} = 1.00$ (figure 1.8(b)). One can observe that the amplitude of the surge oscillations was strongly dependent on \mathcal{B} . However, the onset point was very similar in both cases. The surge onset was preceded by slight pressure fluctuations which were referred to as the mild surge by Greitzer.

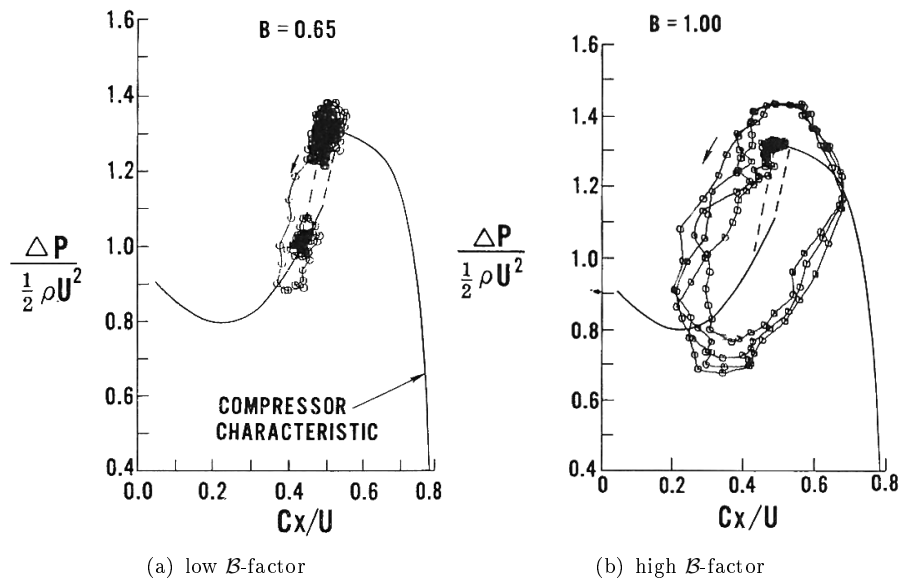


FIGURE 1.8: Influence of \mathcal{B} -factor on the surge limit cycle in the axial compressor [39]; C_x - axial flow velocity, u - mean rotor velocity

The fact, that Greitzer model is applicable also in the case of centrifugal compressing machines was proven by numerous researchers [29, 44, 51, 67, 125, 129, 131] including Greitzer himself [41]. Figure 1.9 presents comparison of two-equation Greitzer model (including equations 1.11 and 1.13) with experiment conducted by Meuleman [87]. One can observe, that the model slightly under-predicted the surge frequency. The oscillations amplitude was predicted reasonably well in presented case. This was achieved after some modifications in the compressor characteristic used in the model. The first attempts revealed strong under-prediction of the amplitude. This study has proven that the Greitzer model describes the surge cycle with reasonable accuracy in the case of low-speed compressing machines.

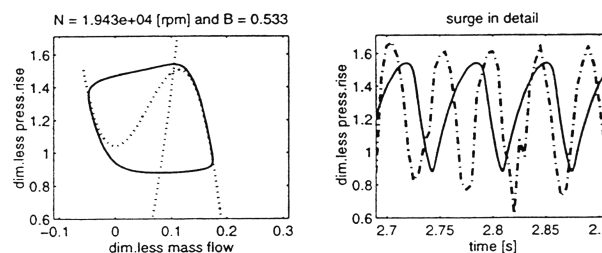


FIGURE 1.9: Comparison of the Greitzer model with the experimental pressure signal obtained in a low speed centrifugal compressor [88]; solid line - Greitzer model, dashed line - experimental result

Refined experimental analysis of the surge cycle in the centrifugal compressor was conducted by Toyama et al. [118]. Figure 1.10 presents pressure signals recorded in different locations versus time. One can observe sudden onset of the surge cycle. Contrary to data obtained by Meuleman et al. this cycle was very non-linear. Toyama divided it into two stages: the backflow period and the recovery period. Each of them started with very strong pressure change and some time of pressure stabilisation. Oscillations in the plenum were very weak. This was caused by the fact, that the analysed plot contained only the first surge cycle. The frequency of oscillations was of the order of 10 Hz which was close to frequency of the Helmholtz resonator.

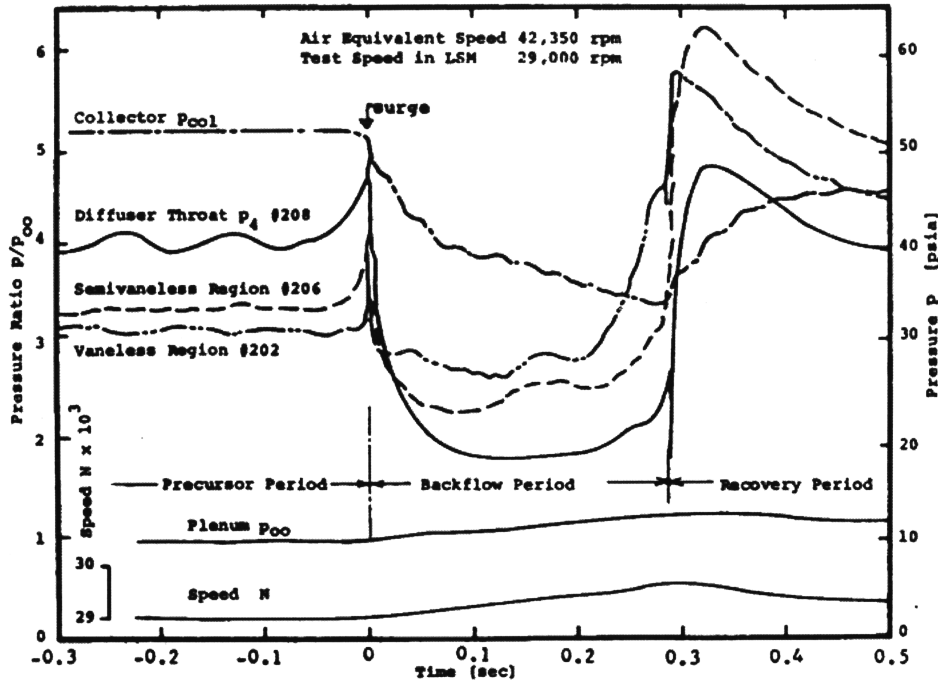


FIGURE 1.10: Time dependence of pressure signals registered during the first surge cycle [118]

Figure 1.11 presents the process of surge onset along the performance curve measured dynamically by Horodko in the centrifugal blower. Bold line represents the compressor performance curve. One can observe that the process of entering a wide limit cycle was preceded by slight fluctuations corresponding to the mild surge, similarly as it was observed by Greitzer in the axial compressor (see figure 1.8). Then, the parameters started oscillating around the onset point and the size of the cycle was growing. After reaching the limit cycle the system was oscillating repetitively.

1.4 Rotating stall

The term **rotating stall (RS)** refers to circumferential variation of flow parameters (pressure and velocity). It can be generated by destabilisation of the impeller flow or by unsteady interaction between the impeller and the diffuser. Different triggering mechanisms result in different forms and locations of the rotating stall. In all cases fluctuations

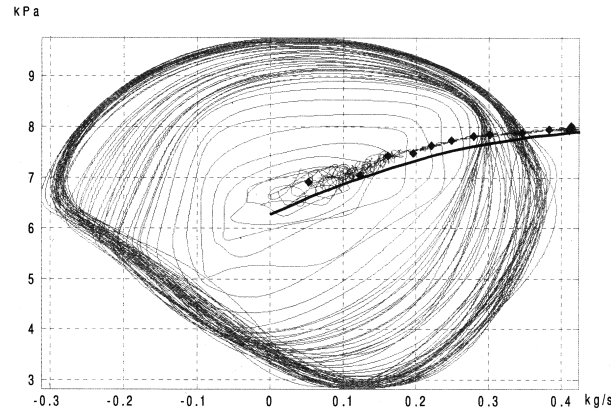


FIGURE 1.11: Trajectory of the operational point at onset of the deep surge [51]

are characterized by two parameters: a number of stall cells λ_c and a frequency of their rotation which is usually presented as a fraction or percentage of the impeller frequency f_{rot} [73]. Figure 1.12 presents scheme of the RS structure with three stall cells $\lambda_c = 3$. A stall cell is characterized by lower pressure which results in recurrent pressure drops registered in the pressure signal by a fixed transducers. Different numbers of stall cells can be observed, usually between 1 and 4 [65, 117]. However, some researchers, including Ljevar et al. [78] and Izmaylov [58] registered rotating stall with 8 cells.

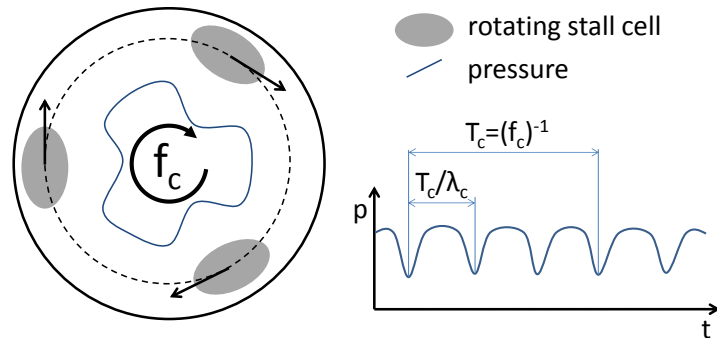


FIGURE 1.12: Rotating stall cells and their influence on pressure signal

The mechanism of rotating stall in centrifugal impeller is slightly different from the classic scheme known in the case of axial machines presented in the literature [112]. Frigne and Van den Braembussche examined flow patterns obtained in a centrifugal compressor at different positions of the inlet vanes [33]. Comparison of their experiment with previous papers allowed to distinguish three main rotating stall patterns:

- **diffuser rotating stall** (in case of vaneless diffuser referred to as **VDRS**) caused by a strong interaction between the boundary layer and the inviscid core flow in the vaneless diffuser. The number of stall cells can vary. Their frequency is low $f \leq 0.2f_{rot}$.
- **abrupt impeller rotating stall (AIRS)** appearing due to strong interaction between the impeller and the diffuser flows. The number of stall cells increases with decreasing mass flow rate. Their frequency is in the range $0.2f_{rot} \leq f \leq 0.4f_{rot}$.

- **progressive impeller rotating stall (PIRS)** caused by gradual flow separation in the impeller. The number of stall cells remains constant. Their frequency is in the range $0.5f_{rot} \leq f \leq 0.8f_{rot}$.

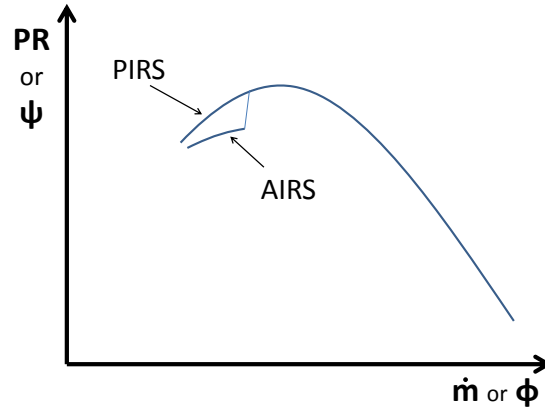


FIGURE 1.13: Influence of PIRS and AIRS on the compressing machine performance curve

Izmailov [58] introduced a more complex classification resulting from examination of different diffuser shapes. However, one can observe certain similarities. According to Izmailov and Seleznev the diffuser rotating stall cell speed was also small (or even zero if the diffuser was vanned), and could be characterized by high number of cells (up to 8). Impeller cells travelled faster and did not exhibit such a wide range of possible number of stall cells. It has to be noted that location and character of the RS depends also on the impeller rotational velocity [65, 88]. Cells may have different sizes which is observed by a fixed pressure gauge as non-symmetrical pressure variation [30, 73]. Haupt et al. noted that it is possible for different modes to occur concurrently [46].

The distinction between the PIRS and the AIRS was motivated by the same reason as in case of the axial unit [56, 98]. Figure 1.13 presents how both phenomena affect performance curve of the compressing machine. Appearance of PIRS causes gradual decrement of the pressure ratio, while AIRS results in its sudden drop.

1.4.1 Progressive impeller rotating stall

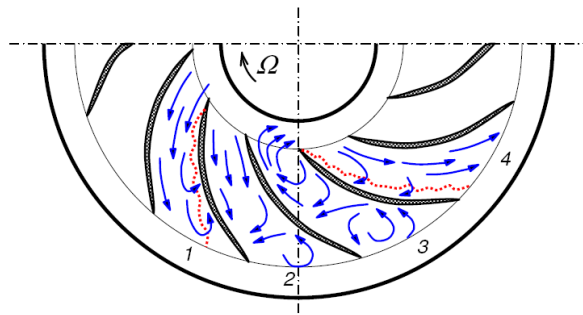


FIGURE 1.14: Mechanism of propagation of the PIRS [72]

Figure 1.14 presents mechanism of propagation of the PIRS. It was first visualized by Lennemann and Howard [72] with the use of hydrogen bubbles. Channel 1 operates in normal conditions with the first signs of flow separation. According to the two-zone flow theorem described by Dean and Senoo [24], separation occurs firstly in a wake region which can start from the leading edge of the blade. A separation bubble grows in size and if it reaches suction side of the next blade the flow blockage appears (channel 2). Then, the flow direction reverses (channel 3). This initiates the second separation on the blade suction side. Growth of the bubble induces return of the regular flow in the channel and finishes the cycle (channel 4). That sequence repeats continuously through all blades and creates an impression of separation "travelling" with frequency f_c ($f_c < f_{rot}$). In the frame of reference rotating with the rotor, the rotating stall is travelling in the direction opposite to the direction of the frame rotation.

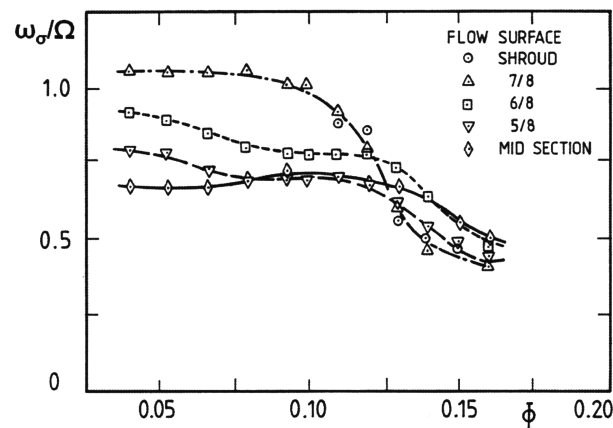


FIGURE 1.15: Variation of the PIRS cell speed with flow coefficient [89]

Mizuki et al. analyzed how f_c of PIRS depended on mass flow rate [89]. Figure 1.15 presents that the cell speed increased with decrement of ϕ . This gave explanation to the fact, that PIRS caused gradual decrement of the machine performance. Both centrifugal and axial compressing machines can be affected by a wide range of forms and shapes of the observed stall cells. Graham et al. conducted exhaustive analysis of how the stall cell shape evolved in case of the axial impeller [35]. The main distinction was introduced between full span and part span cells (figure 1.16). Part-span cells were observed in high numbers (up to 8) very close to the machine design operational point. Full span cells were observed in smaller numbers (up to 4) at much smaller mass flow rates. In all cases, a regular flow was maintained in some channels. Therefore, from the point of view of the whole machine, the flow could be considered as stable. Nevertheless, the biggest problem of PIRS and RS in general is that it is very difficult to predict f_c and λ_c and possible resonance of the machine components with pressure fluctuations, which can be a source of serious damage [11].

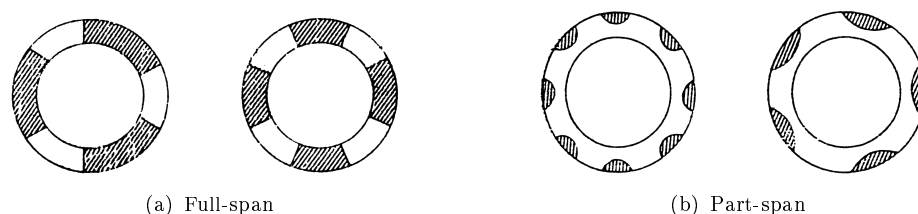


FIGURE 1.16: Scheme of the rotating stall cells observed in the axial compressor [35]

1.4.2 Vaneless diffuser rotating stall

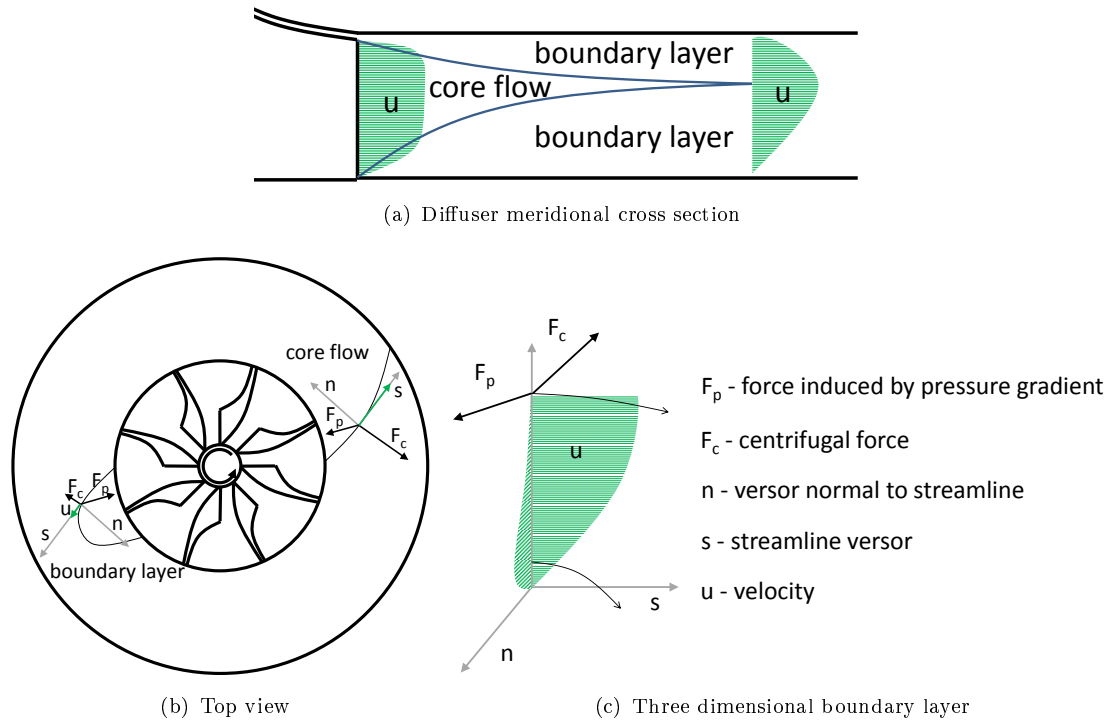


FIGURE 1.17: Flow in vaneless diffuser in conditions of mass flow rate smaller than at design conditions

Due to different character of pressure fluctuations another model was formulated to describe the rotating stall in the diffuser. A two dimensional model was created by Jansen [59], who proved that a circumferential distortion of the diffuser flow conditions in certain conditions is not damped. Afterwards, the model was developed by Senoo and Kinoshita [105, 106] who corrected the stability limit. Frigne and Van den Braembussche [34] confirmed the destabilizing effect of the boundary layer that can lead to the VDRS which is presented in figure 1.17. Figure 1.17(a) illustrates a typical velocity profile in the diffuser meridional cross-section in conditions of smaller mass flow rate than at the design point. In such circumstances the profile is non-symmetrical. The boundary layer at the diffuser front wall (impeller shroud) is thinner than at the diffuser back wall (impeller hub). Thicker boundary layer at the diffuser back wall is, therefore, more prone to the boundary layer separation. As the flow propagates, both boundary layers are developing and if the diffuser is long enough, the flow becomes fully developed and more stable. Figure 1.17(b) demonstrates the force diagrams of elementary flow volumes located in the core flow and in the boundary layer. In the core flow the centrifugal force acts together with the force induced by pressure gradient in the diffuser. The resultant force direction is opposite to direction of streamline and particle is decelerating. In the case of boundary layer flow velocity is much smaller. Therefore, the centrifugal force is not big enough to compensate the force caused by adverse pressure gradient and flow is bent towards the impeller. This difference in flow directions results in creation of so-called 3-dimensional boundary layer presented in figure 1.17(c) [122]. In the boundary layer region, velocity component perpendicular to initial flow direction grows and causes a risk of flow recirculation.

Figure 1.18 presents separations observed in the vaneless diffuser by Rebernik [100] in the

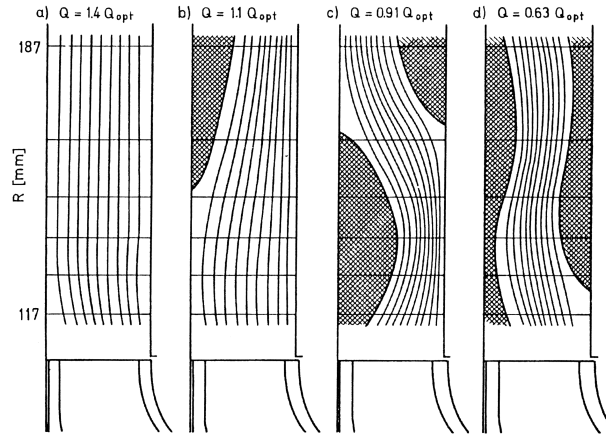


FIGURE 1.18: Separated flows in vaneless diffusers at different mass flow rates [100]

case of radial pumps. As the mass flow rate decreases, the average velocity is smaller and the probability of separation and recirculation increases. The recirculating flow interacts with the core flow and loss of stability becomes possible. Senoo and Kinoshita [105] defined the critical conditions at which recirculation of the boundary layer leads to the VDRS:

$$\frac{90^\circ - \alpha_{cr}}{90^\circ - \alpha_r} = 0.88 \quad (1.24)$$

where α_{cr} is the critical angle at which the VDRS appears, α_r - angle at which flow in

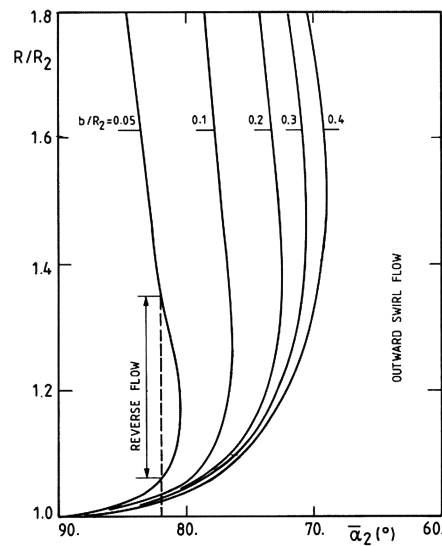


FIGURE 1.19: Influence of diffuser width and length on angle α_r [106]

the boundary layer starts to reverse. α_{cr} and α_r depend on relative diffuser length which is defined as ratio of the diffuser height b to its inner radius R_2 . Figure 1.19 presents influence of average flow angle at the diffuser inlet $\bar{\alpha}_2$ on the region of reversed flow. One can observe, that for $\bar{\alpha}_2 > 72^\circ$ there was no reversed flow in all analysed diffusers. Dashed line corresponds to case of $\bar{\alpha}_2 = 82^\circ$ and $\frac{b}{R_2} = 0.05$. One can observe that in this case reversed flow can be expected at a considerable distance. Equation 1.24 shows that the VDRS appears at slightly lower angle i.e. when reversed flow occupies certain length of the diffuser. However, as it was presented by Shen et al. the VDRS onset depends also on shape of the diffuser inlet profile [108]. The shape of fully developed VDRS was

presented by Tsujimoto et al. [119]. Figure 1.20 presents experimental and calculated velocity and pressure fluctuations obtained in their study. One can observe that in this case $\lambda_c = 4$, however, the number of the VDRS stall cells can be higher [76].

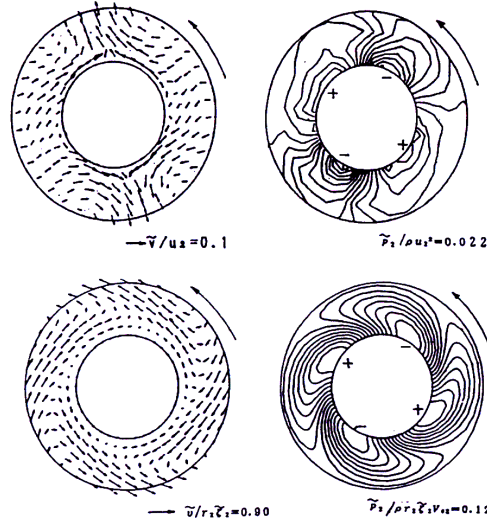


FIGURE 1.20: Experimental (upper plots) and calculated (lower plots) velocity and pressure fluctuations during the VDRS [119]

1.4.3 Abrupt impeller rotating stall

Stability of the vaneless diffuser flow was analysed by Abdelhamid [6] in a similar way to Jansen [59], but taking into account possible circumferential distortion of the inlet flow. A constant static pressure was imposed at the diffuser exit and the diffuser inlet conditions were calculated from interaction between the diffuser and the impeller. They were characterized by:

$$Z_p = \frac{dp}{du}$$

$$Z_u = \frac{du}{du_r}$$

Where u represents velocity, p - pressure, u_r - radial velocity. At a given time instant, direction of du is the same as direction of $d\dot{m}$, hence negative Z_p could be associated with negative slope of the performance curve, positive Z_p with positive slope of the performance curve. Z_u depends mainly on blade angle at the trailing edge. Impellers with radial or backward leaning blades have negative Z_u . Positive Z_u is more likely to occur in forward leaning blades, but can also happen even in backward leaning blades in presence of strong local flow perturbations. In case of reversed flow direction Z_u changes sign. Figure 1.21 presents regions of stable and unstable flow as a function of Z_p , Z_u and λ_c calculated by Abdelhamid. Results for negative Z_u were in agreement with observations presented for the VDRS in section 1.4.2. Cells were characterized by small rotational velocity, number of stall cells was small and loss of stability appeared at ϕ_{cr} which was analogous to α_{cr} defined by Jansen [59], Senoo and Kinoshita [105] and Frigne and Van den Braembussche [34]. Study of Abdelhamid also shown that the VDRS is possible, but less likely, for positive Z_p (figure 1.21) i.e. at the positive slope side of the compressing machine performance curve.

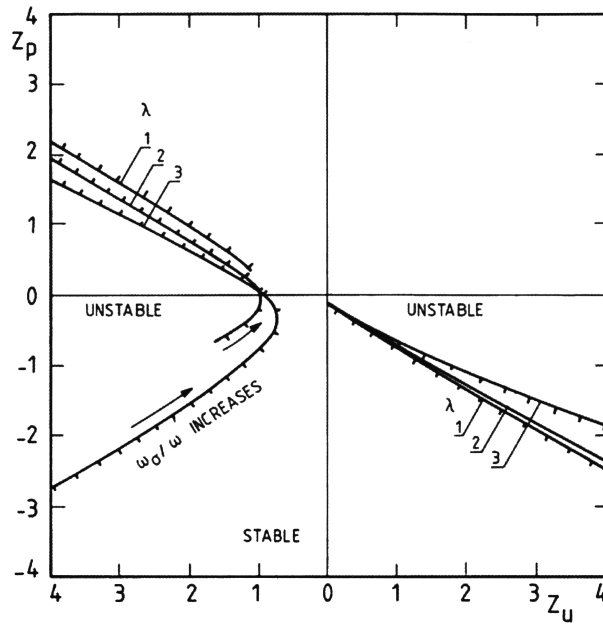


FIGURE 1.21: Influence of number of stall cells on vaneless diffuser flow stability [6]

At positive Z_u another unstable region can be observed. It corresponds to a situation when strong impeller-diffuser interaction results in flow distortion referred to as the abrupt impeller rotating stall (AIRS). As it was mentioned, positive Z_u is most likely to occur in forward leaning or radial blades at the impeller outlet. In the case of backward leaning blades, positive Z_u can also occur in presence of the reversed flow. In such a situation distortion in the impeller outlet can propagate upstream and cause distortion even at the impeller inlet [111]. Figure 1.22 presents distortion in the diffuser measured by Uchida et al. [121] that triggered the AIRS. The volute working under off-design conditions is known to produce a non-uniform pressure distribution at the diffuser outlet [113] and this distortion can also influence the impeller outlet [110, 119]. A strong impeller-diffuser interaction created conditions for appearance of the AIRS which propagated upstream to the impeller inlet. This phenomenon appeared after exceeding critical conditions and immediately resulted in a drop of the compressor performance.

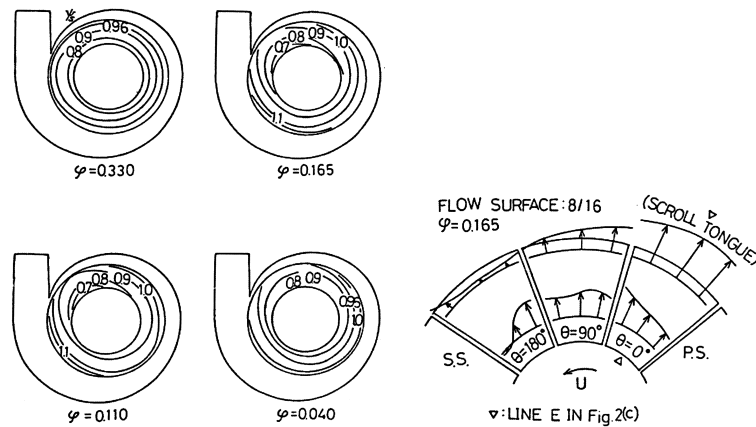


FIGURE 1.22: Variation of the impeller outlet velocity and its influence on the impeller inlet [121]

1.5 Inlet recirculation

Knowledge about this phenomenon in centrifugal compressors is moderate compared to the rotating stall and the surge. This can be explained by the fact, that the inlet recirculation (IR) is not considered as dangerous for the machine. Nevertheless, its detection can be crucial for identification of incoming onset of another unstable flow structures [48, 67, 83]. Most of papers devoted to this phenomenon consider centrifugal pumps, where IR has much stronger influence on the machine performance [31, 61]. Figure 1.23 presents the IR observed by Breugelmans and Sen [15]. It can be described as a torus-like backflow which is observed in the close vicinity of the shroud at the impeller inlet. Initially, machine working conditions remain stable but with reduced efficiency [67]. However, if the recirculation zone continues to increase in size, it can trigger another instabilities which propagate towards the impeller and even the diffuser [116].

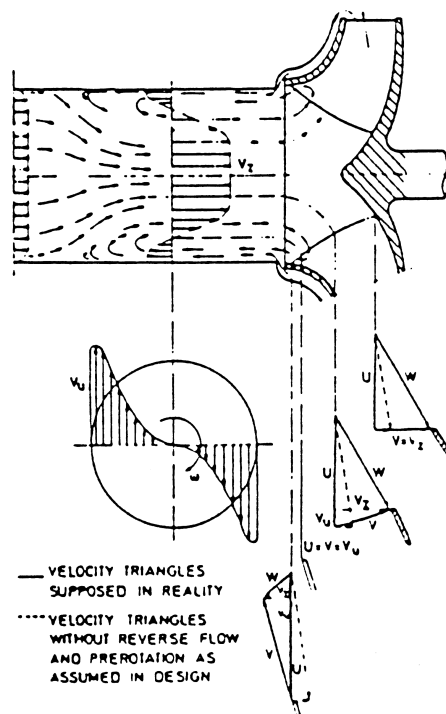


FIGURE 1.23: Inlet recirculation observed in the centrifugal pump [15]

Inlet recirculation can be suppressed by application of casing bleed system. Such a solution for centrifugal compressors was studied by Hunziker et al. [55], Tamaki [115] and resulted in shifting the instability limit towards smaller mass flow rate. Horodko [52] described possibility of using this phenomenon for an early surge detection. McKee et al. suggested [84] and patented [83] such a system based on detection of the inlet recirculation.

1.6 Numerical analyses of the unstable flow phenomena

There are still not many examples of using CFD for analysis of unstable flows in the centrifugal compressing machines. Recent years have introduced some improvement in

that field, mainly due to higher availability of high computational power.

In [120] Turunen-Saaresti and Larjola examined non-stationary phenomena in the centrifugal compressor. The domain included the impeller, the inlet channel, the volute and part of the outlet channel. Such a large domain allowed fluid to fluctuate freely without interfering with the boundary conditions. The impeller had 7 blades and 7 splitters. The mesh consisted of 618496 elements per whole machine. No mesh independence study was presented. FINFLO solver was used with $k - \epsilon$ turbulence model. Fourier transform of the inlet and the outlet pressures were used to compare the results with the experiment. The main surge peak obtained in both methods was in reasonable agreement.

Huang et al. [54] conducted investigations of a centrifugal compressor with 19 blades and a vaned diffuser (15 blades). There was no information provided whether the inlet and outlet channel were simulated as well. The mesh consisted of 2 million elements. FLUENT solver was applied with $k - \epsilon$ model of turbulence. Analysis included 9 points located at the shroud along the channel. In the highest mass flow rate pressure was fluctuating only with the blade passing frequency uniformly along the whole channel. At slightly smaller mass flow rate two weaker components appeared. Under the smallest mass flow rate very significant fluctuation component appeared at a frequency of 85 percent of the impeller frequency. This fluctuation was present mainly in the inducer zone. Guo et al. [43] presented results of the numerical and experimental analyses of the compressor having 6 full and 6 splitting blades. The mesh consisted of around 2.4 millions of elements and included the rotor and the volute. In order to allow for temporary fluid oscillations, the adequate outlet condition was applied, which simulated presence of the outer plenum with the assumptions of an isentropic, spatially uniform flow. This allowed for the temporary changes of static pressure at the housing outlet according to the formulae derived by the authors. The simulation was performed with the use of ANSYS CFX solver and $k - \epsilon$ turbulence model. The simulation results were compared to the experimental data only in terms of compressor stage performance (total pressure ratio and efficiency) and stationary simulations. They agreed well in the region of the compressor design point. At off-design, some discrepancy appeared. The authors have detected a standing pressure wave within the volute which was amplified by interaction with rotating stall in the rotor. This induced local backflows in the outlet plenum, which are characteristic for surge.

Technical report of Chen et al. [18] contains description of numerical analysis of the rotating stall control technology based on steady tip injection. Computations were conducted by TURBO code that was developed with support of the National Aeronautics and Space Administration, the United States Department of Defense and industry with intention of creating a high-fidelity multiphysics solver for multistage turbomachinery problems [19]. Solver uses two-equation turbulence model developed at Glenn Research Center which was proven to accurately simulate flows in turbomachinery [107]. No information was provided about the mesh size and size of the computational domain. Calculation was conducted on 315 processors which suggests significant mesh refinement. However, presented plots suggest that it included the rotor domain only. Analysed compressor CC3 had 15 blades and 15 splitters and was followed by 24 diffuser vanes. Simulations showed slight disagreement with experiment in prediction of the moment of the rotating stall onset. However, the influence of injection shifted the stability limit in both cases. Presented work stood out as the successful attempt of simulating local flow instability. However, it was achieved with the use of substantial computational resources.

Interesting works describing numerical simulations of the isolated diffuser flow were published by Ljevar et al. [77, 78] and Ljevar individually in her monograph [76]. Mentioned works describe 2D flow simulations of the VDRS structures depending on the assumed

inlet boundary conditions. Computations were calculated in FLUENT assuming laminar flow. Work showed substantial amount of data that stayed in agreement with state of the art in the field of the VDRS (see section 1.4.2), however, the important aspect of 3-dimensional boundary layer formation was not included in this study.

1.7 Aim of study

1.7.1 Motivation

Unstable flow structures are known to be a source of serious damage of the compressing system. On the other side, these structures can appear very close to the maximum of the machine performance curve. Therefore, each modern compressing installation should be equipped with anti-surge device that is reliable and provides wide operational range. Figure 1.24 presents number of patents devoted to the anti-surge devices registered in years 1974-2006. One can observe a clear increasing trend, especially in the last years. This shows that there is still need for design of better devices that protect against unstable flow structures. This can be achieved through better understanding of the flow phenomena appearing at different stages of unstable machine operation.

Contemporary knowledge about instabilities in centrifugal compressing machine was shaped in almost 6 decades starting from 1955 [26]. In last 20 years further development was decelerated by limitations of experimental methods that can provide selective information about time-evolution of parameters at certain points (measuring probes) or surfaces (PIV methods). Section 1.6 presented emergence of new trend of application of CFD methods for this purpose. This approach is believed to provide deeper understanding of fundamental flow physics that provides a link between mathematical models and real flow dynamics [18].

1.7.2 Thesis of dissertation

CFD methods can provide description of surge and pre-surge flow phenomena in the centrifugal blower. In further perspective, it can lead to construction of efficient anti-surge devices.

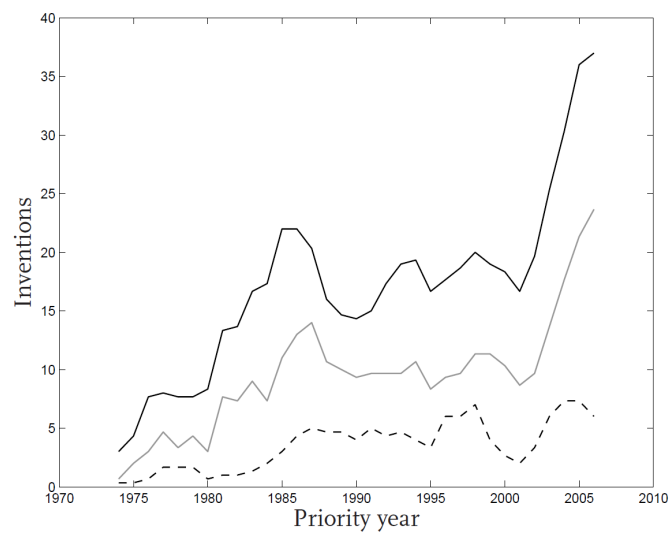


FIGURE 1.24: Number of patents on the compressor surge in general (solid black), surge avoidance (grey) and surge detection (dashed black) [124]

Experimental study

2.1 Test stand description

A single stage centrifugal blower DP1.12 was the object of investigation. The initial test rig constructed by Magiera [80] was modified in order to be fully adapted to requirements of presented study. Figure 2.1 presents the cross-section of the blower and its main dimensions.

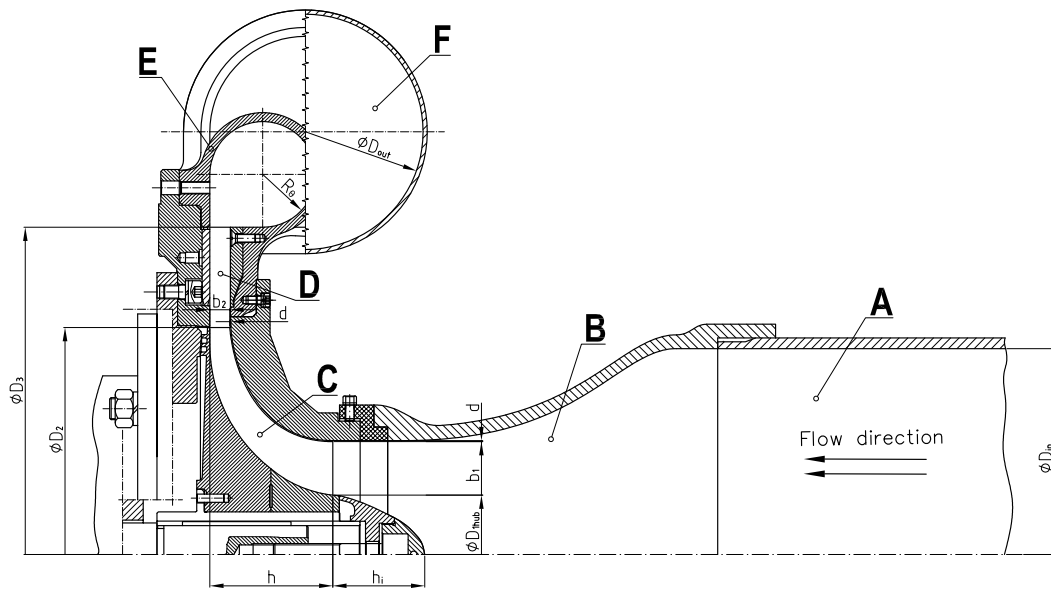


FIGURE 2.1: Cross-section of the DP1.12 blower in configuration used in this study with the most important dimensions

The flow entered the rig through the inlet pipe (A) of diameter $D_{in} = 300$ mm. Then, it was accelerated in the Witoszynski nozzle [70] (B) and directed towards the impeller (C). The rotor inlet diameter at the hub equalled $D_{1hub} = 86.3$ mm and the inlet span $b_1 = 38.9$ mm. At the outlet, the diameter and the span equalled $D_2 = 330.0$ mm and $b_2 = 14.5$ mm respectively. The gap between the blade tip and the shroud maintained constant value $\delta = 0.8$ mm along the whole blade. The length of a single impeller passage varied from 174 mm at hub to 134 mm at the shroud giving an average $L_p = 154$ mm. The area of the passage cross-section at the impeller inlet was $A_{p-in} = 823$ mm² and $A_{p-out} = 676$ mm² at the outlet. Downstream of the rotor, air entered the vaneless diffuser (D). The diffuser outlet diameter was equal to $D_3 = 476$ mm. Afterwards,

flow entered the circular volute (E) of radius R_θ . The radius was gradually increasing streamwise from the volute tongue gap of 5 mm towards the outlet pipe of diameter $D_{out} = 150$ mm. The outlet pipe contained two straight sections connected with the right-angle elbow. The section joining the volute and the elbow was 250 mm long, section behind the elbow was 3750 mm long. A throttling valve was mounted at the end of the outlet pipe.

The rotor was driven by an asynchronous AC motor (400V/15kVA). The blower was designed to operate at ambient inlet conditions. The design point was attained at $f_{rot} = 120$ Hz, $\dot{m} = 0.8 \frac{\text{kg}}{\text{s}}$ and $PR = 1.12$. However, in this study, in order to avoid a risk of the impeller damage at surge, the unit was run with slightly lower rotational speed of $f_{rot} = 100$ Hz with nominal flow rate of $\dot{m}_n = 0.75 \frac{\text{kg}}{\text{s}}$ and pressure ratio $PR = 1.08$. Rotational speed yielded the impeller tip speed equal to $u_{tip} = 103 \frac{\text{m}}{\text{s}}$. The impeller had $z = 23$ blades, hence the blade passing frequency was equal to $f_{BP} = 2.3$ kHz.

2.1.0.1 Pressure measurement

Stand overview The test stand was equipped with 7 dynamic subminiature Kulite transducers connected to an Iotech Wavebook 516/E data acquisition system. Five of the transducers were mounted flush to the shroud walls to measure the static pressure, two were built into Pitot tubes located in the inlet pipe. Gauge positions are presented in figure 2.2. The list below contains the notation and position of each gauge:

- p_{s-in} - static pressure at the inlet pipe upstream of the Witoszynski nozzle;
- p_{s-out} - outlet static pressure at the volute outlet;
- p_{s-imp1} - static pressures at the impeller shroud, in the inlet zone ($L = -0.2$);
- p_{s-imp2} - static pressures at the impeller shroud, at the mid-chord ($L = 0.4$);
- p_{s-imp3} - static pressures at the impeller shroud, near the trailing edge ($L = 0.9$);
- p_{t-in1}, p_{t-in1} - total pressure at the inlet pipe upstream of the Witoszynski nozzle;
- p_{t-in2} - total pressure at the inlet pipe upstream of the Witoszynski nozzle.

Longitudinal position of the static tappings at the impeller shroud was described by the L dimensionless parameter. It was set to be equal to $L = 0$ at the rotor leading edge and $L = 1$ at the rotor trailing edge.

The assembled experimental rig is presented in figure 2.3. Picture 2.3(a) presents the overview of the whole stand with indication of positions of the gauges. Mass flow rate was controlled by the the outlet valve 2.3(b). Total pressure profile was measured by two Pitot tubes located in the inlet pipe (2.3(c)). The static pressure gauges were mounted flush to the walls (figures 2.3(d) - 2.3(f)). The static and total pressure gauges were connected to star collector (figure 2.3(g)) which was connected to Druck DPI610HC pressure calibrator presented in figure 2.3(h). During experiments pressure signals were transferred to Wavebook 516/E and stored in binary file.

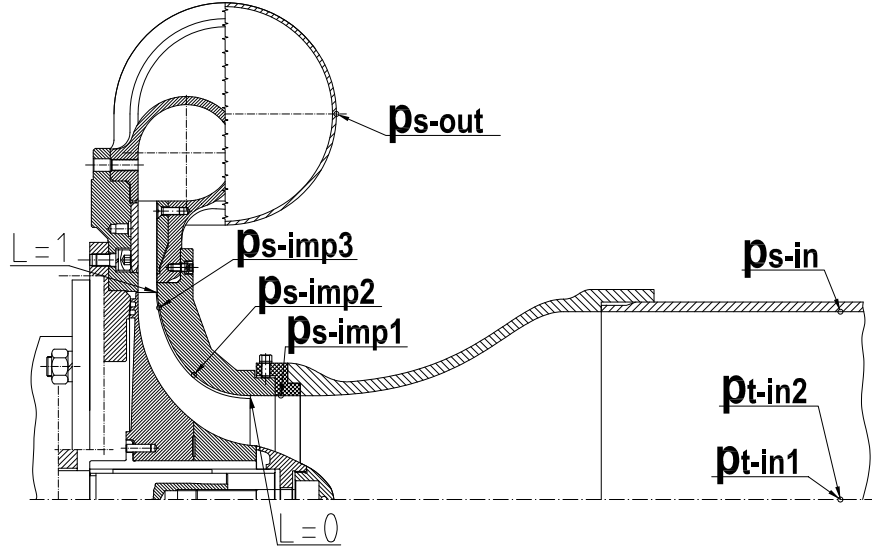


FIGURE 2.2: Cross-section of the DP1.12 blower in the configuration used in this study with positions of the pressure gauges

2.1.0.2 Two variants of the plenum volume

In order to examine the influence of the outlet plenum volume on dynamics of unsteady phenomena all measurements were conducted for two configurations of the outlet pipe. In the first campaign the volume of the outlet pipe was equal to $V_{LP} = 0.0968 \text{ m}^3$. According to Fink et al. [29], this volume can be treated as the volume of a Helmholtz resonator. The Helmholtz frequency is given by equation 1.10:

$$f_{H-LP} = \frac{c}{2\pi} \sqrt{\frac{A_{p-out}}{L_p V_{LP}}} = 11 \text{ Hz} \quad (2.1)$$

In the second campaign the experiments were repeated with a shorter outlet pipe giving the total volume of the plenum $V_{SP} = 0.0435 \text{ m}^3$. According to formula 1.10 this results in higher Helmholtz frequency:

$$f_{H-SP} = \frac{c}{2\pi} \sqrt{\frac{A_{p-out}}{L_p V_{SP}}} = 17 \text{ Hz} \quad (2.2)$$

2.1.1 Signal Collection and Analysis

Data was acquired in three runs: Static, Dynamic and Quasi-dynamic. Prior to each measurement the system was running for at least one hour in order to stabilize the temperature of the machine and gauges. After warming up, the atmospheric pressure, and the ambient temperature were measured. These parameters were controlled throughout the whole experimental campaign and corrected if significant change was noted. Afterwards, the calibration was performed with the use of Druck pressure calibrator DPI610HC. The reference pressure was set to the opposite side of the membrane of each gauge by star-collector presented in figure 2.3(g). Each calibration was conducted on the basis of three measurements: negative and positive gauge pressure and the atmospheric pressure

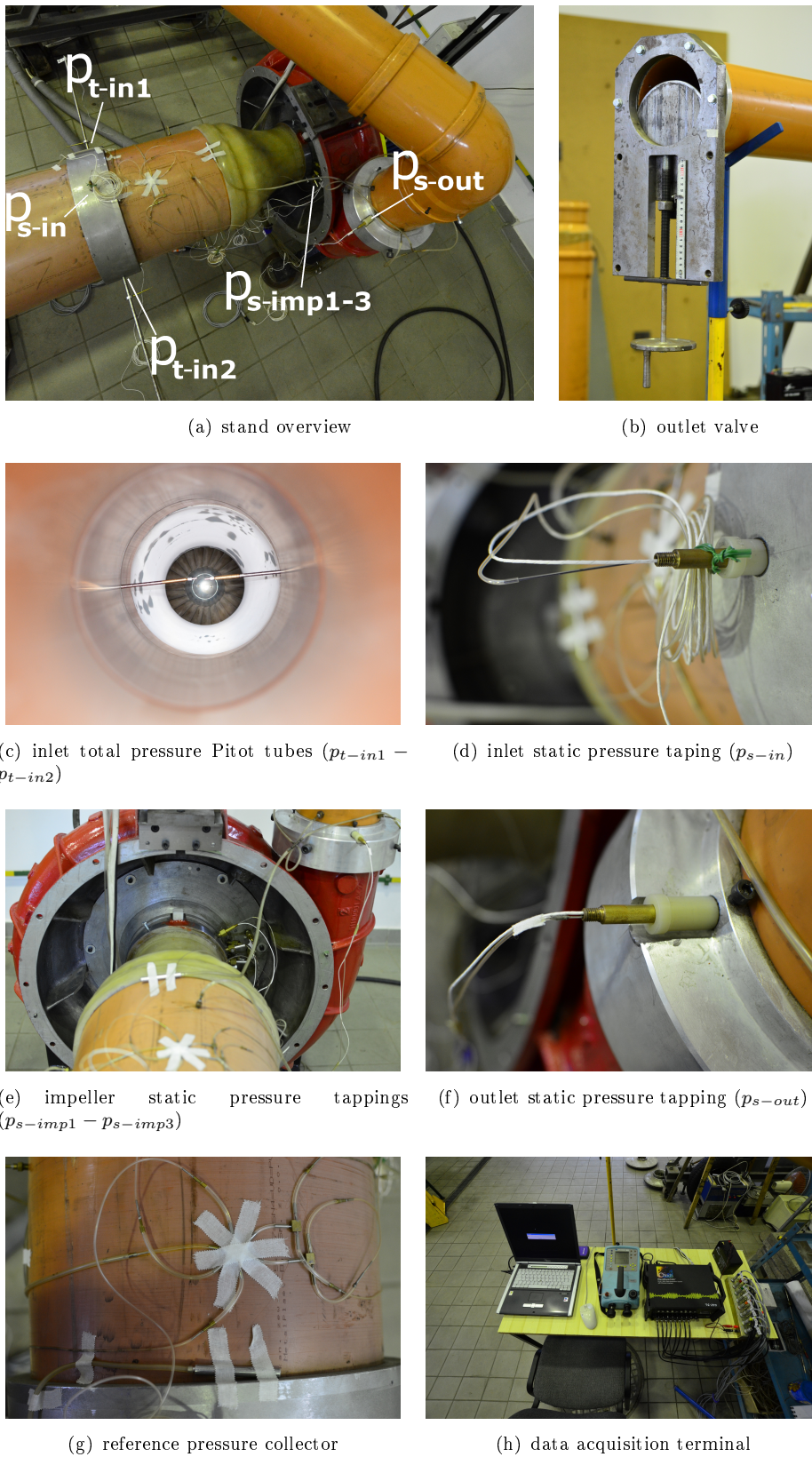


FIGURE 2.3: Overview of the test stand and the data acquisition system

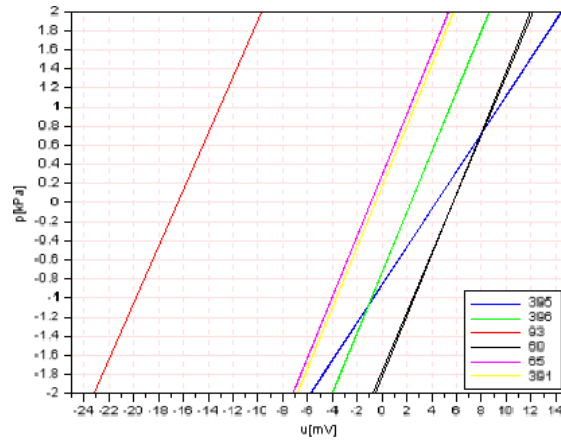
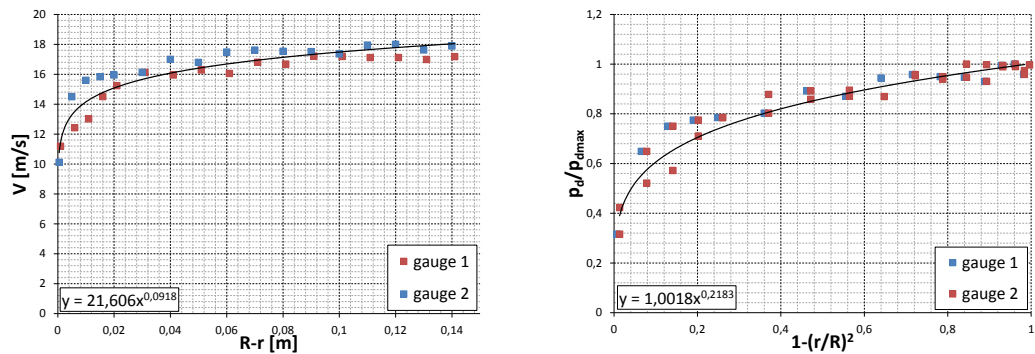


FIGURE 2.4: Gauge characteristics obtained in one of the calibrations

(p_{atm}). The transducer characteristic was assumed to be linear, hence two points were necessary for its establishment. However, in order to examine the hysteresis effect, two characteristics were drawn for each gauge: the first with positive gauge and atmospheric pressures, the other with negative gauge and atmospheric pressures. As a result a set of 14 lines was obtained: 2 per each gauge. In all calibrations, the hysteresis was not observed. Figure 2.4 presents results of one of the calibrations. Two lines obtained for the same gauge are drawn in the same colour. It could be noted that the discrepancies are minimal which confirms the aforementioned fact of negligible hysteresis. The calibration procedure was conducted before and after each measurement series. Based on the calibration curves the signal was converted from volts into pascals. The registration time and sampling rate depended on the type of analysis and is noted in their description.

2.1.1.1 Static analysis



(a) Velocity versus radial position

(b) Normalized dynamic pressure versus normalized radial position

FIGURE 2.5: Inlet profile obtained in one series of the static experimental analysis

Static analysis aimed at determination of the blower performance curve. Each series of measurements was conducted for a fixed valve position and included static pressures p_{s-in} , p_{s-out} and total pressures p_{t-in1} , p_{t-in2} at 16 different positions of the Pitot tubes. Each measurement contained $2^{13} = 8192$ samples gathered at a frequency of 1 kHz. Therefore, the signal was recorded continuously over 8.192 s which corresponded

to more than 800 rotor revolutions. The average values were treated as the final readings. Calibration of transducers was performed before and after each series in order to avoid possible change of their characteristics. Dynamic pressure was calculated as a difference of total pressure measured by Pitot tube and corresponding static pressure measured on the wall at the same inlet cross-section. Figure 2.5 presents the profiles obtained in the selected series. In each series 2×16 measurements were taken which provided good representation of the total pressure profile. Close to the wall the spatial density of measurements was higher due to high velocity gradients in the boundary layer. The mass flow rate was calculated based on normalized dynamic pressure profile presented in figure 2.5(b). In figure 2.5(a) one can observe the velocity profile registered at both sides of the pipe.

Calculation of mass flow rate: The approximation curve obtained with LSM in plot 2.5(b) has a form:

$$y = Ax^B \quad (2.3)$$

where abscissa is given by:

$$x = 1 - \left(\frac{r}{R}\right)^2; 0 < x < 1 \quad (2.4)$$

and ordinate:

$$y = \frac{p_d}{p_{dmax}}; 0 < y < 1$$

The relation between these two parameters comes from the power-law velocity profile equation [93]. Values of A and B were calculated for each profile and used to calculate the gross mass flow rate. The calculations below show how this aim was achieved. The relation between dynamic pressure and velocity gives

$$u = \sqrt{\frac{2p_d}{\rho}} = \sqrt{\frac{2p_{dmax}A}{\rho}} \sqrt{x^B} \quad (2.5)$$

The total mass flow rate over cross-section is given by the formula:

$$\dot{m} = \rho u S$$

for the infinitesimal area $dS = 2\pi r dr$ (see figure 2.6):

$$d\dot{m} = \rho u dS = \rho u 2\pi r dr$$

Substituting equation 2.5 one obtains:

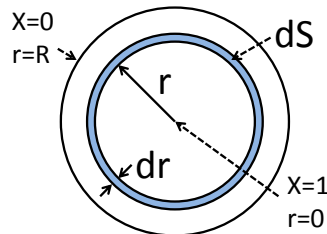


FIGURE 2.6: Integration over area S

$$d\dot{m} = 2\pi\sqrt{2p_{dmax}A\rho}\sqrt{x^B}rdr$$

From equation 2.4 one can conclude that $dx = -2\frac{r}{R^2}dr$ and consequently

$$d\dot{m} = 2\pi\frac{-R^2}{2}\sqrt{2p_{dmax}A\rho}\sqrt{x^B}dx$$

To obtain total mass flow rate over pipe cross section one has to integrate $d\dot{m}$.

$$\dot{m} = -\pi R^2\sqrt{2p_{dmax}A\rho}\int_1^0\sqrt{x^B}dx$$

The limits come from the fact that $x \rightarrow 1$ for $r \rightarrow 0$ and $x \rightarrow 0$ for $r \rightarrow R$. Knowing that $\int x^{\frac{B}{2}}dx = \frac{2x^{\frac{B}{2}+1}}{B+2}$ one obtains:

$$\dot{m} = 2\pi R^2\sqrt{2p_{dmax}A\rho}\frac{1}{B+2}\left[\frac{\text{kg}}{\text{s}}\right] \quad (2.6)$$

Equation 2.6 was used to calculate the mass flow rate from dimensionless parameters A and B determined empirically. The mass flow rate together with the pressure ratio obtained at different positions of the throttling valve allowed to obtain the empirical compressor performance curve presented in section 2.2.1.

Equation 2.6 depended on the air density which was determined indirectly. After warming-up period the ambient temperature and pressure were registered and controlled throughout the whole experimental campaign. Density was calculated from ideal gas formula:

$$\rho = \frac{p}{RT}\left[\frac{\text{kg}}{\text{m}^3}\right] \quad (2.7)$$

2.1.1.2 Dynamic analysis

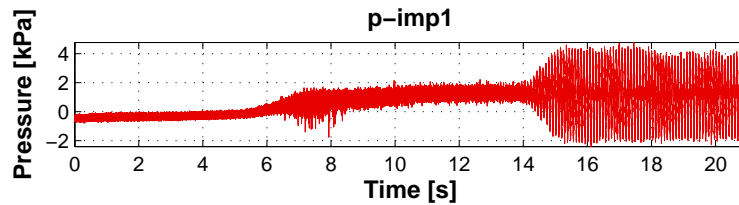


FIGURE 2.7: Pressure registered at gauge p_{s-imp1} in one of dynamic tests

Dynamic tests are a very popular way of examining surge onset in compressing machines. Such a method was applied in many papers including [17, 48, 71, 90]. In this methodology, the mass flow rate was gradually decreased during signal collection. This is usually obtained by increase of throttling which in the case of presented work was done by gradual closure of the throttling valve presented in figure 2.3(b). Figure 2.7 presents typical pressure signal registered during such a procedure. The signal itself allowed to identify certain stages of entering unstable regime. One can observe that the stable working regime was followed by a period $t \in (6 \text{ s}, 9 \text{ s})$ characterized by increased pressure amplitude accompanied with separate peaks. Then the peaks disappeared, but the amplitude and average value of pressure remained higher. Finally, around $t = 14 \text{ s}$ the onset of high-amplitude oscillations was observed.

Dynamic signals were often subject to post-processing. Bulot et al. applied low-pass filter [17]. Also Lawless and Fleeter [71] used band-pass filter. In this work, the signal was transformed into time-frequency space by means of CWT with Morlet wavelet. This method was proven to be a very valuable tool in analysis of dynamic signals. All scalograms were obtained with code implemented in MATLAB by Horodko [48–51]. The

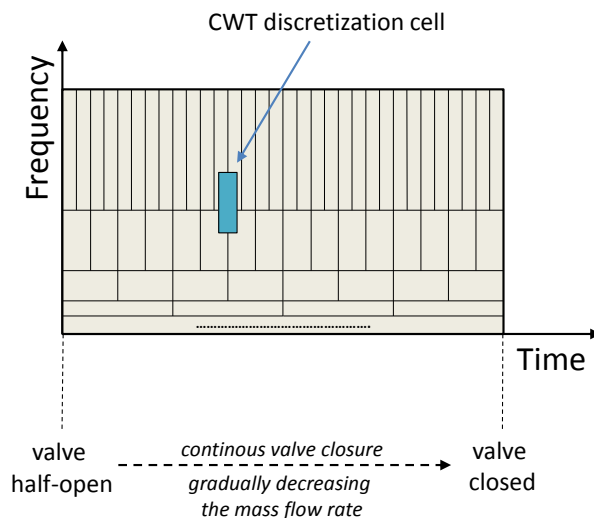


FIGURE 2.8: Scheme demonstrating the methodology used in dynamic tests

measurement contained $2^{21} = 2097152$ samples gathered with a frequency of 100 kHz. The signal was recorded continuously over 20.97 s which corresponded to more than 2000 rotor revolutions. The structure of CWT scalogram is presented in figure 2.8. During signal collection the throttling valve was being closed continuously, hence the signal represented the process of abrupt stall onset. The dimensions of the time window varied with the frequency as it is presented in figure 2.8. The dynamic method with application of CWT is one of the best approaches for analysis of surge and pre-surge pressure signals. However, one has to be aware of limitations of such a methodology:

- Due to Heisenberg-Gabor uncertainty principle, the size of time window was limited [86].
- Resolution in time and frequency domain changed which made it difficult to specify the uncertainty of the results.
- Phenomena could be associated with the time of appearance only. It would be much more valuable to specify the mass flow rate at which they occurred.
- Similarly to forced and damped harmonic oscillator, pressure fluctuations could consist of two types of components: permanent and diminishing with time. Dynamic analysis registered both and it was not possible to distinguish them. Therefore, some phenomena registered in the experiment could have small importance due to the fact, that they were damped in very short time.

Results of dynamic analysis are presented in section 2.2.2.

2.1.1.3 Quasi-dynamic analysis

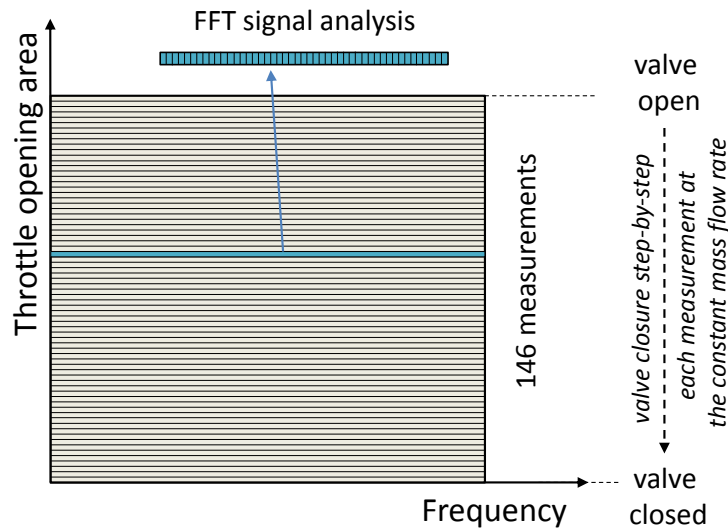


FIGURE 2.9: Scheme demonstrating the methodology used in dynamic tests

As a response to some doubts raised in the previous section, the original method was developed [75]. The idea of this methodology is illustrated in figure 2.9. The main aim of this approach was to find a way of measurement of the progressive instability onset by very slow changes in throttling. Each measurement was conducted at constant valve position and contained $2^{21} = 2097152$ samples gathered at a frequency of 100 kHz. The difference between valve positions in consecutive signal registrations was very small and the whole range was covered by as many as 146 measurements. Moreover, in order to assure disappearance of temporary pressure oscillations the settling time of 20 s was provided prior to each measurement therefore this kind of measurement was called **quasi-dynamic**. All the signals were assumed to be deterministic and the Fourier transformation (by means of FFT algorithm) was used to obtain their frequency spectra. The amplitude spectra (absolute values of the Fourier transformation) of the signals, acquired at different positions of the throttling valve, were presented in the form of 2D maps (figures 2.30-2.33 in section 2.2.3.2). Similar spectral maps were used by Raitor and Neise [99] for noise analysis and by Hellmich and Seume in the case of the axial high speed compressor [47]. This work, however, apart from applying the method for different type of machine and different gauge locations was featured by high resolution of positions of the throttling valve that allowed to identify the moment of appearance of the unstable phenomena.

If the underlying assumption about the deterministic character of the signals was false, the pressure spectra maps would be disordered without any regular patterns. In such a case, a method of spectral density estimation of a random signal should have been applied. The obtained results proved that the random components of the signals were rather weak. It can be explained considering the fact that the signal gathering period was very long and covered over 2000 rotations. In such a long period all the repeating phenomena were observed at least several times and the recorded signals were a good representations of the flow phenomena. On the other hand, the sampling frequency should be compared with the blade passing frequency ($f_{BP} = 2.3$ kHz). The ratio $\frac{100}{2}$ assured, that every significant flow structure appeared couple of times.

2.1.1.4 Representation of signals in the phase space

Plotting the signals in the phase space was proven to be a valuable tool for analysis of unstable phenomena in centrifugal compressors [42, 66, 94]. Observation of phase portrait allowed to obtain the information about the attractor which gave the information about character of the phenomenon (stable/unstable, periodic/quasi-periodic/non-periodic/chaotic etc.). Moreover, it provided very convenient method for comparison of signals obtained in the experiment and the simulation due to the fact, that the phase shift did not influence the phase portrait if the signal contained more than one oscillation period. Therefore, it was possible to obtain comprehensive comparison of signals without necessity of time-correlation.

Phase trajectory was created in a way presented by Packard et al.[97]. Phase space contained three dimensions: pressure p_x , its first derivative $\overline{p_x}$ describing the changes of signal monotonicity and its second derivative $\overline{\overline{p_x}}$ describing the changes of signal concavity. It can be also intuitively understood as the acceleration of the pressure changes.

Usually, the biggest problem in creation of phase trajectory is caused by noise being an inevitable component of the signal. Gu et al. [42] and Komatsubara and Mizuki [66] applied Singular Value Decomposition method to reduce its influence. Mutou et al. [94] reconstructed the signal equations using the frequency spectrum with the method proposed by Noack et al. [95]. Each of presented methods allow to remove the noise component efficiently from the signal at the post-processing stage. In other words, noise removal can be done with complete signal only. However, in order to introduce the possibility of application of the method to monitoring of compressing units, the aim of this work was to provide a method that can be performed efficiently in real time. Also, the preference was to choose a method which did not require extensive computations and could be done by simple circuits. Therefore, the phase trajectory included the signals and derivatives in original units (Pa , $\frac{\text{Pa}}{\text{s}}$, $\frac{\text{Pa}}{\text{s}^2}$). Each of them was smoothed by the moving average using the Gaussian filter. The value of standard deviation of the window was set to $\sigma = 50$ samples. This value provided the averaging window of the range comparable to the period of the blade passing frequency $f_{BP} = 2.3$ kHz. It allowed to smooth the noise to an extent much lower than the main flow fluctuations observed in the experiment.

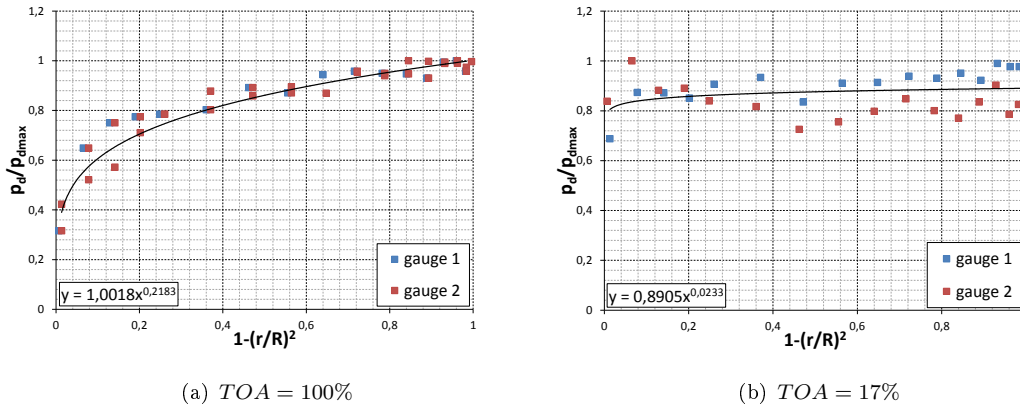


FIGURE 2.10: Normalized inlet pressure profile at the highest and the lowest value of TOA

2.2 Results of the experimental investigation

2.2.1 Static analysis

In this work throttling is described by the dimensionless parameter describing the percentage of valve which was left open and referred to as the throttling opening area or TOA . As mentioned in section 2.1.1.1, the dimensionless inlet dynamic pressure profile was approximated by the curve which was assumed to be described by formula 2.3. The profile was changing together with TOA . Figure 2.10 shows normalized profiles obtained at two extreme throttling values. At full opening of the valve (figure 2.10(a)) the velocity profile was fully developed. Figure 2.10(b) presents that at the verge of measurability ($TOA = 17\%$) the boundary layer become almost indistinguishable. The profile became almost perfectly flat which was reflected in very small value of the exponent B . This was caused by the fact that the process of boundary layer formation was interrupted by local velocity fluctuations in the inlet zone.

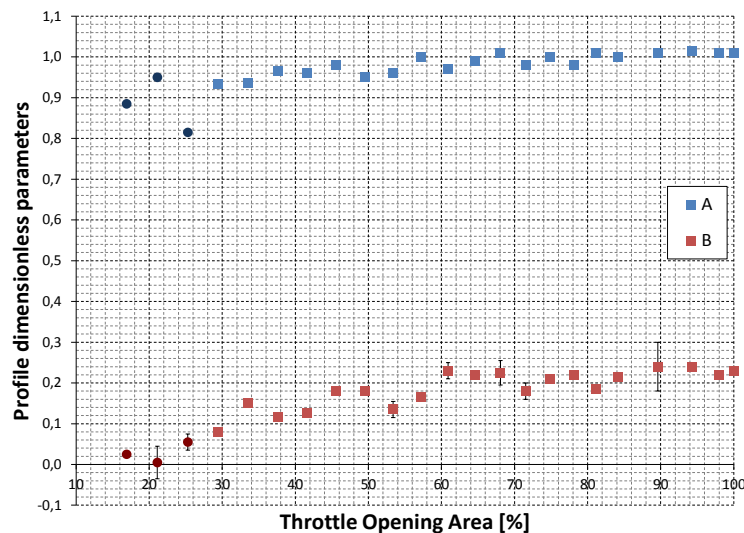


FIGURE 2.11: Value of A and B dynamic pressure profile parameters at different TOA

Figure 2.11 presents values of A and B determining dynamic pressure profiles obtained at different throttling. As it was mentioned in 2.1.1.1 the calibration procedure was conducted before and after each measurement series. The average of these two indications was treated as the final reading and the difference was presented in the form of error bars. The uncertainty of TOA was much smaller than the size of points presented in figure. Three points at $TOA < 27\%$ were considered as not fully representative for stable analysis due to the fact, that the measurements in this region were affected by the instabilities present in the inlet zone. According to equation 2.3, parameter A can be interpreted as the ratio $\frac{p_d(r=0)_{profile}}{p_{dmax}}$ where $p_d(r=0)_{profile}$ is the maximal value of dynamic pressure in the approximated profile and p_{dmax} is the maximal measured dynamic pressure. Therefore, value close to 1 was expected. One can observe, that in all cases it was close to this value, with the only exception of two points which were located in the region $TOA < 27\%$. The B parameter depended on thickness of the boundary layer. One can observe, that this parameter was changing from $B \approx 0.2$ at high TOA to values close to zero at small values of TOA . Figures 2.10(a) ($B \approx 0.2$) and 2.10(b)

($B \approx 0$) illustrate the influence of B on the profile shape.

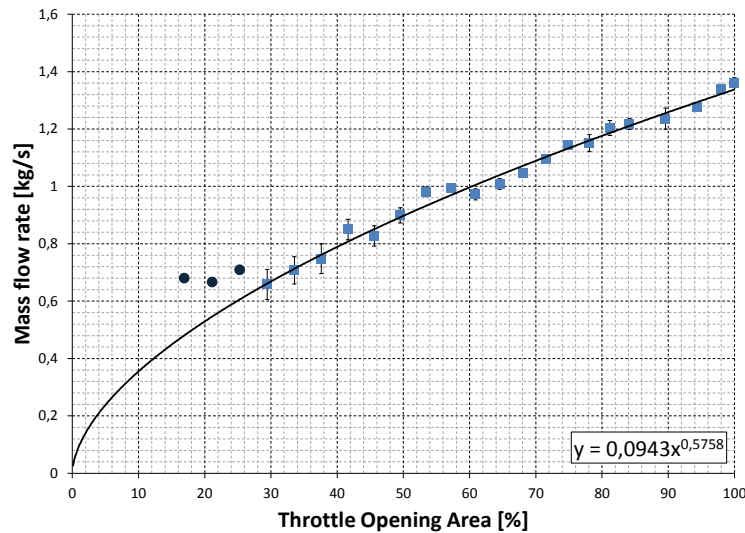


FIGURE 2.12: Dependency between throttle opening and measured mass flow rate

Figure 2.12 illustrates relation between throttle opening area and measured mass flow rate. The dependency can be described as nearly linear for $TOA > 30\%$. Below $30\%TOA$ the mass flow rate tended to become constant (dark round points). Therefore, these points were not included in calculation of the approximated empirical curve expressing the dependency between mass flow rate and TOA . This curve was obtained by means of least square method with assumption that at $TOA = 0\%$ the mass flow rate was equal to $\dot{m} = 0 \frac{\text{kg}}{\text{s}}$. Curve was used to choose the signal that was compared with numerical simulation conducted at given mass flow rate. Its shape at $TOA < 30\%$ cannot be regarded as certain. However, for described purpose such an approach was satisfactory.

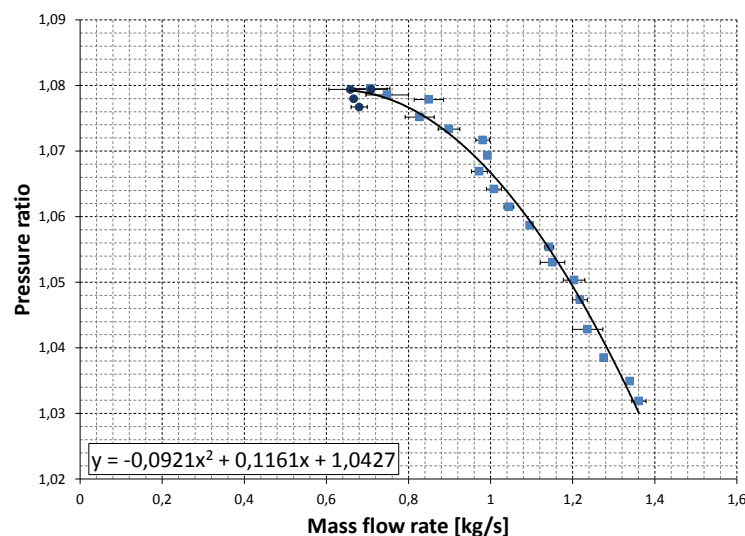


FIGURE 2.13: Performance curve of the blower $PR(\dot{m})$

Figure 2.13 presents the blower performance chart. Horizontal error bars represent the aforementioned uncertainty of the mass flow rate measurement associated with changing

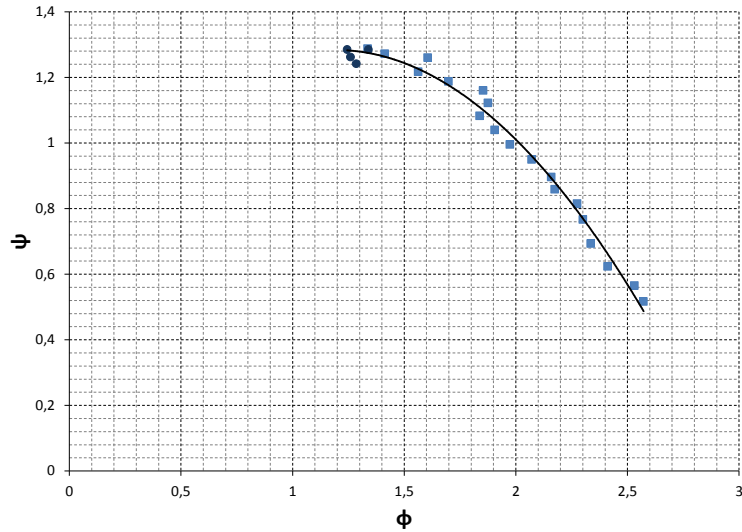


FIGURE 2.14: Performance curve of the blower $\psi(\phi)$

characteristics of the pressure transducers. The pressure uncertainty was smaller than the size of the points presented in figure. One can observe that the measurements represented a trend that could be closely approximated by the performance curve which was obtained with least squares method. Dark circles represent measurements done for $TOA < 27\%$. It can be also noted that all of them were located in similar location. This suggested that the moment of entering unstable operation was preceded by quite wide range of throttle opening areas ($17\% < TOA < 30\%$), where its pressure head was relatively constant. At $TOA = 17\%$ instabilities emerged to such a level that further measurements were impossible. The region of unstable work is thoroughly examined by means of the dynamic analysis in section 2.2.2 and the quasi-dynamic analysis in section 2.2.3. Figure 2.14 presents the performance curve in non-dimensional space $\psi(\phi)$.

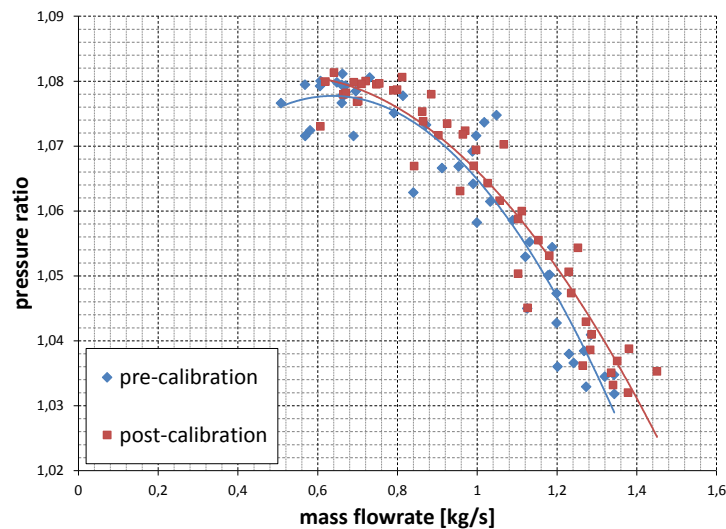


FIGURE 2.15: Performance curve obtained with pre and post calibrations

Figure 2.15 shows comparison of results calculated with the use of pre-calibration and

post-calibration and performance curves obtained from both by means of least square method. One can observe, that application of pre calibration resulted in lower position of the performance curve. This suggested that the measurements were affected by systematic error which was not constant. In fact it is a well known phenomenon that the gauges were slightly changing their characteristics under the influence of temperature rise caused by the stand operation. This phenomenon was minimised by application of the warm-up period which lasted at least one hour before the measurements were initiated. However, slight error was inevitable due to the fact, that each series lasted more than half an hour. Therefore, two calibrations were the best way to estimate the scale of discrepancy. The average value presented in figure 2.13 minimised the error that would be present if only one calibration was performed and the actual error was smaller than the size of bars presented in figures 2.11, 2.12 and 2.13.

TABLE 2.1: Characteristic frequencies observed in the dynamic analysis; abbreviations: N-present at a unstable regime, B-present at all *TOA*

notation	frequency Hz	Type	Gauges	Amplitude kPa	Name
f_{BP}	2300	B	$p_{s-imp2-3}$	various	blade passing frequency
f_{BP_h}	4600	B	$p_{s-imp2-3}$	various	blade passing frequency (second harm.)
f_{dn1}	10.8	N	all	≈ 1	main surge frequency
f_{dn2}	22	N	$p_{s-imp2-3}$	various	
f_{dn3}	30 – 100	N	all	$\approx 10^{-1}$	
f_{dn4}	100 – 200	N	p_{s-in}, p_{s-out}	$\approx 10^{-1}$	
f_{dn5}	300 – 1000	N	p_{s-imp1}	$\approx 10^{-1}$	inlet recirculation

2.2.2 Dynamic analysis

2.2.2.1 Time-frequency analysis

This section is devoted to examination of figures 2.16-2.20 presenting the CWT scalograms. The characteristic frequencies detected in the analysis are summarised in table 2.1. Characteristic working regimes are listed in table 2.2.

TABLE 2.2: Working regimes identified during dynamical tests

Time range	Stability	Gauges	Name
$t < 6$ s	stable	all	nominal work
$t \in (6$ s, 9 s)	transient	p_{s-imp1}	inlet recirculation
$t \in (9$ s, 14 s)	unstable	all	transient phase
$t > 14$ s	unstable	all	deep surge

Figure 2.16 presents the signal registered by the inlet static pressure gauge p_{s-in} . At the beginning, pressure exhibited only slight fluctuations around the atmospheric pressure which did not leave any trace on the CWT scalogram. This region is referred to as the **stable regime** henceforth. As the time advanced, the throttling valve was closed continuously. One can observe slight increment in the size of pressure fluctuations at $t \approx 9$ s. It was confirmed by the CWT scalogram that exhibited a slight increment in the amplitude

at a wide spectrum of frequencies below and over $f_{rot} = 100$ Hz. This region is referred to as the **transient phase** henceforth. Fluctuations appearing in this regime belonged to ranges $f_{dn3} = 30 - 100$ Hz and $f_{dn4} = 100 - 200$ Hz. Very weak fluctuations appeared also around $f_{dn1} = 10.8$ Hz and $f_{dn2} = 22$ Hz. At $t \approx 14$ s the fluctuations increased by one order of magnitude. This was represented on the scalogram by two distinct pressure peaks that appeared clearly at $f_{dn1} = 10.8$ Hz and $f_{dn2} = 22$ Hz. Smaller fluctuations at $f_{dn2} = 30 - 100$ Hz remained present. This region is referred to as the **deep surge** henceforth. At all circumstances, weak oscillations were observed at frequencies higher than 10 kHz. Their presence was caused by the signal noise and remained unchanged regardless of the system working regime.

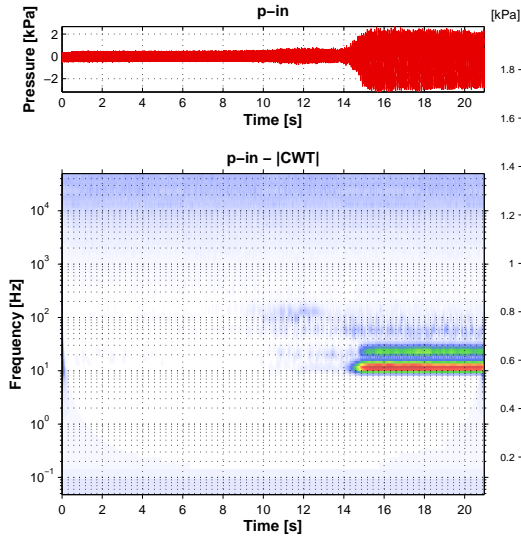


FIGURE 2.16: Pressure signal at the gauge p_{s-in} and its *CWT* scalogram

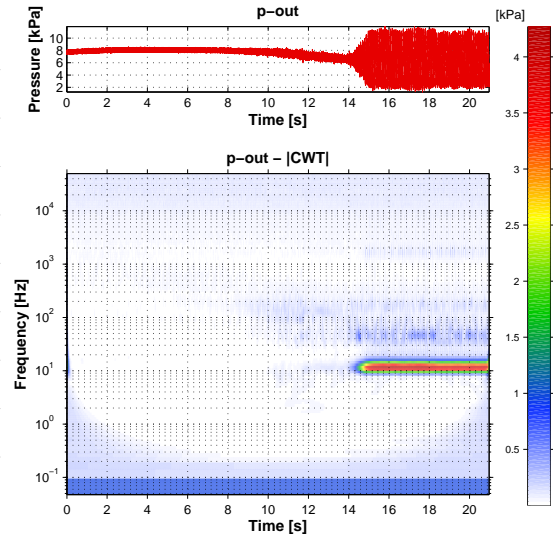


FIGURE 2.17: Pressure signal at the gauge p_{s-out} and its *CWT* scalogram

The outlet pressure gauge p_{s-out} registered similar behaviour which is reflected in signal amplitude plot and its *CWT* scalogram (figure 2.17). The main difference came from the dependency of pressure head on mass flow rate. This resulted in gradual change of pressure at the outlet. One can observe that the pressure signal resembled the performance curve of the compressor at $t < 14$ s. This variation of the average outlet pressure resulted in high amplitude at the frequency 10^{-1} Hz observed on the scalogram. When the system entered the deep surge at $t \approx 14$ s one strong pressure peak appeared at $f_{dn1} = 10.8$ Hz. Fluctuations were also observed at $f_{dn3} = 30 - 100$ Hz, $f_{dn4} = 100 - 200$ Hz and at the blade passing frequency $f_{BP} = 2.3$ kHz. This suggested that the blade traces were still not fully mixed behind the volute. In comparison to p_{s-in} , the peak $f_{dn2} = 22$ Hz was not observed at the outlet.

The inlet zone static pressure gauge p_{s-imp1} exhibited the same behaviour as the p_{s-in} at $t < 6$ s which can be observed in figure 2.18. At $t \in (6 \text{ s}, 9 \text{ s})$ fluctuations were observed in a wide range $f_{dn5} = 300 - 1000$ Hz. Pressure signal showed that very strong single pressure jumps were also noted during this period. Non-periodic character of these peaks was responsible for the broadband noise observed in the scalogram. Localisation and character of this phenomenon allows to claim that it represented the **inlet recirculation** which was firstly discovered in the centrifugal pump [32]. At the transient phase $f_{dn3} = 30 - 100$ Hz and $f_{dn4} = 100 - 200$ Hz appeared. At the deep surge strong peaks were observed at $f_{dn1} = 10.8$ Hz and $f_{dn2} = 22$ Hz which were accompanied by weaker oscillations in the range $f_{dn3} = 30 - 100$ Hz.

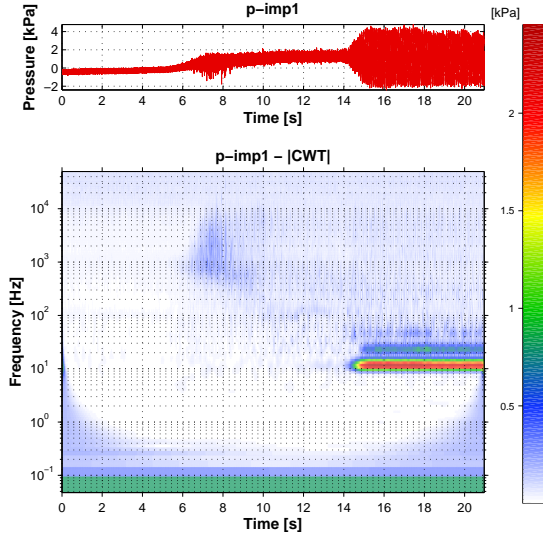


FIGURE 2.18: Pressure signal at gauge p_{s-imp1} and its *CWT* scalogram

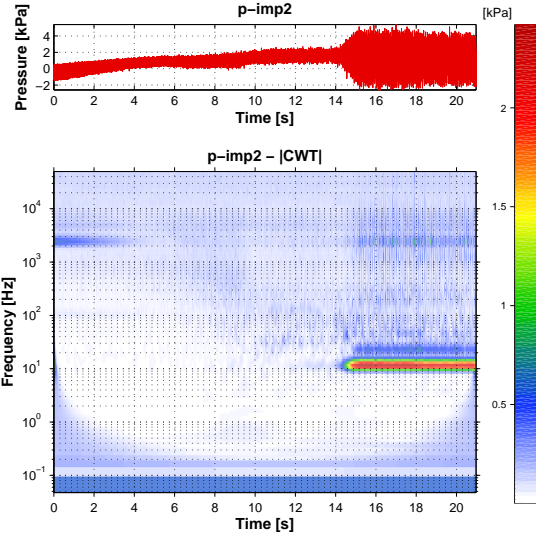


FIGURE 2.19: Pressure signal at gauge p_{s-imp2} and its *CWT* scalogram

At gauge p_{s-imp2} (figure 2.19) the inlet recirculation was also present, but to smaller extent than in the inlet zone. Around $t \approx 9$ s the system entered the transient phase, where the oscillations of frequencies characteristic for the inlet recirculation ($f_{dn5} = 300 - 1000$ Hz) were weaker. Concurrently, fluctuations appeared at $f_{dn3} = 30 - 100$ Hz and $f_{dn4} = 100 - 200$ Hz. At the deep surge, two strong peaks appeared at $f_{dn1} = 10.8$ Hz (main surge frequency) and $f_{dn2} = 22$ Hz. At high frequencies one can observe the peak at the blade passing frequency $f_{BP} = 2.3$ kHz which was caused by pressure drop over blade tips. Weak peak was also observed at its second harmonic frequency $f_{BP_h} = 4.6$ kHz. Both maxima diminished at the inlet recirculation and the transient phase.

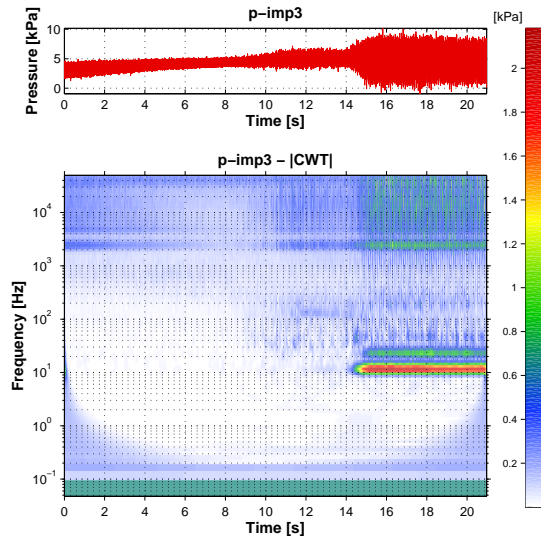


FIGURE 2.20: Pressure signal at gauge p_{s-imp3} and its *CWT* scalogram

Gauge p_{s-imp3} was located very close to the blade trailing edge. One can observe in figure 2.20, that this location was not affected by the inlet recirculation, as the fluctuations at $t \in (6 \text{ s}, 9 \text{ s})$ did not exhibit character similar to p_{s-imp1} and p_{s-imp2} . At the transient

phase, fluctuations were present only at $f_{dn3} = 30 - 100$ Hz and $f_{dn4} = 100 - 200$ Hz. At the deep surge, peaks $f_{dn1} = 10.8$ Hz and $f_{dn2} = 22$ Hz appeared as well as wider fluctuations at $f_{dn3} = 30 - 100$ Hz and $f_{dn4} = 100 - 200$ Hz. Moreover, during the whole test peaks at $f_{BP} = 2.3$ kHz and $f_{BP_h} = 4.6$ kHz were noticeable.

2.2.2.2 Representation of signals in the phase space

Figures 2.21-2.25 present the pressure signals in 3 dimensional phase spaces and their three projections on all two dimensional subspaces. For the sake of clarity the 3-dimensional representations contained only the points registered at $t > 14$ s, i.e. at deep surge. All 2-dimensional projections contained the signal registered during the full test, but each phase distinguished in table 2.2 was marked in different colour. The procedure of drawing the phase trajectory was described in section 2.1.1.4.

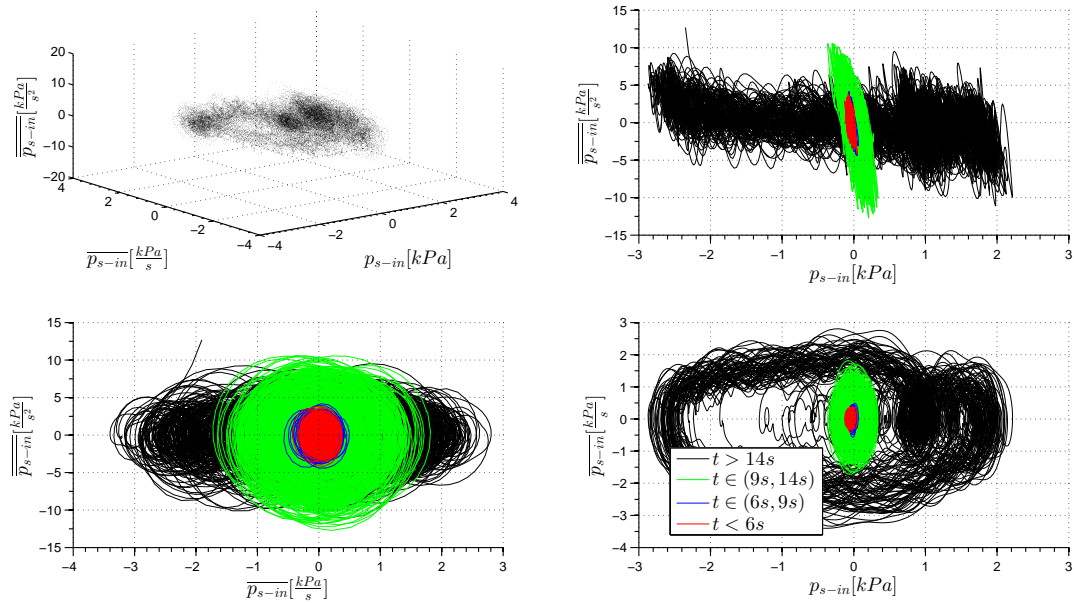


FIGURE 2.21: Phase trajectory of the pressure signals registered by gauge p_{s-in} and its projections

Figure 2.21 presents the phase trajectory of the pressure signal gathered at the inlet. At stable working conditions the signal oscillated in narrow range around $(0,0,0)$. It had a form of flat elliptical disc. Higher values of the second derivative were a constant tendency and were caused by the rising influence of noise with the order of derivation. Nevertheless, the scale of oscillations was limited and the phase attractor at $t < 6$ s had undoubtedly a form of a point which meant that the system was dynamically stable. At $t \in (6 \text{ s}, 9 \text{ s})$ the fluctuations of derivatives were only slightly higher. The system appeared to remain dynamically stable from the point of view of phase portrait of the signal p_{s-in} .

At $t \in (9 \text{ s}, 14 \text{ s})$ the scale of oscillations increased. Growth of p_{s-in} was observed. However, the relative growth of both derivatives was much higher and the derivatives were noticeably fluctuating around zero which can be observed in projection $\overline{\overline{p_{s-in}}} - \overline{p_{s-in}}$. This observation allowed to formulate a new parameter indicating appearance of the unstable phenomena. Section 2.2.2.3 is devoted to this matter. At the deep surge situation

changed dramatically. The projection $\overline{\overline{p_{s-in}}} - \overline{p_{s-in}}$ showed that the range of fluctuation of the first derivative increased, while the second maintained at the same level of fluctuation. The phase trajectory reached the limit cycle which was much more complicated than a simple ellipse. This reflected a non-linear character of the oscillations. Projection $\overline{p_{s-in}} - p_{s-in}$ exhibited that the origin was very loosely occupied by the points. Therefore, the trajectory was encircling the point of stable operation.

Briefly speaking, the process of entering surge can be described as gradual loss of stability reflected in increment in fluctuation of both derivatives. At the surge onset, bifurcation appeared from stable attractor located at the point $(0, 0, 0)$ to the limit cycle corresponding to the deep surge. After bifurcation, the pressure started to oscillate noticeably.

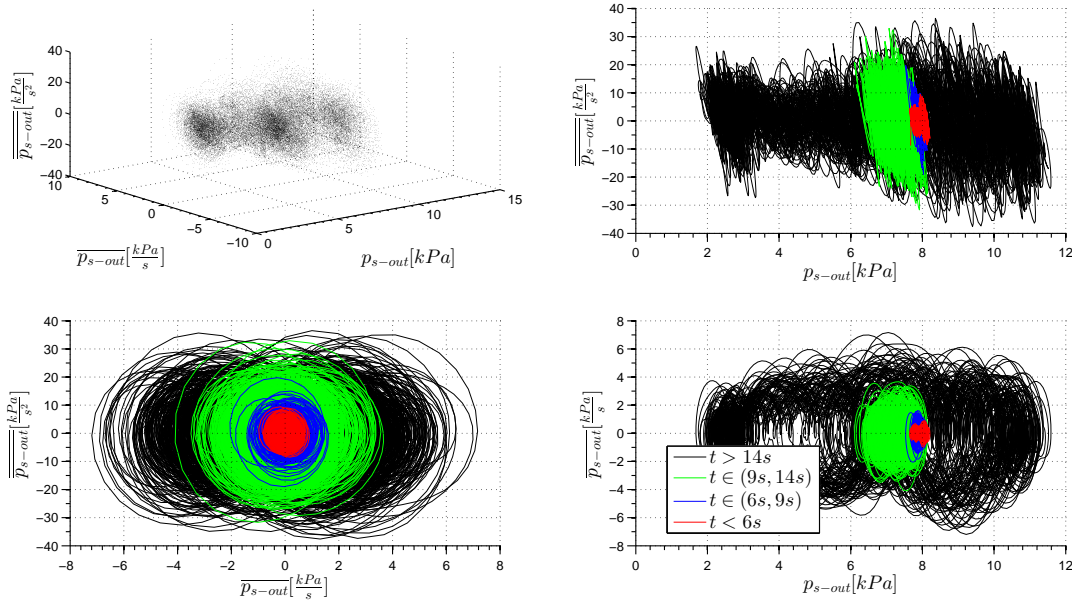


FIGURE 2.22: Phase trajectory of the pressure signals registered by gauge p_{s-out} and its projections

Phase trajectory of the outlet pressure signal p_{s-out} presented in figure 2.22 exhibited some similarities to the previous one. At stable regime slight oscillations around the stationary point were observed. One can observe that the phase portrait at $t < 6$ s was characterized by small fluctuations of both derivatives. Pressure change was caused by change in the blower pressure head and it could be expected that for fixed working conditions the phase portrait had a shape of ellipsoid. This statement was confirmed by phase portraits obtained in quasi-dynamic analysis described in section 2.1.1.4. At $t \in (6 \text{ s}, 9 \text{ s})$ the derivatives fluctuations became slightly higher and at the transient phase they increased again. At the deep surge, the range of fluctuation of the first derivative became higher, while the second derivative maintained at the same level of fluctuation. The pressure p_{s-out} oscillated between 2 kPa and 11 kPa and the limit cycle was observed. Figure 2.23 shows the phase trajectory of the pressure signal registered at the shroud in close vicinity of the impeller leading edge. At $t < 6$ s the phase portrait had a form of ellipsoid which was moving along the p_{s-imp1} axis. One can observe that at the nominal point the pressure was negative due to suction zone formed upstream of the compressor. Afterwards the suction effect diminished and the system entered the inlet recirculation $t \in (6 \text{ s}, 9 \text{ s})$ where the rate of derivatives fluctuation increased. The projection $\overline{\overline{p_{s-imp1}}} - \overline{p_{s-imp1}}$ clearly showed the scale of growth of fluctuation of both derivatives

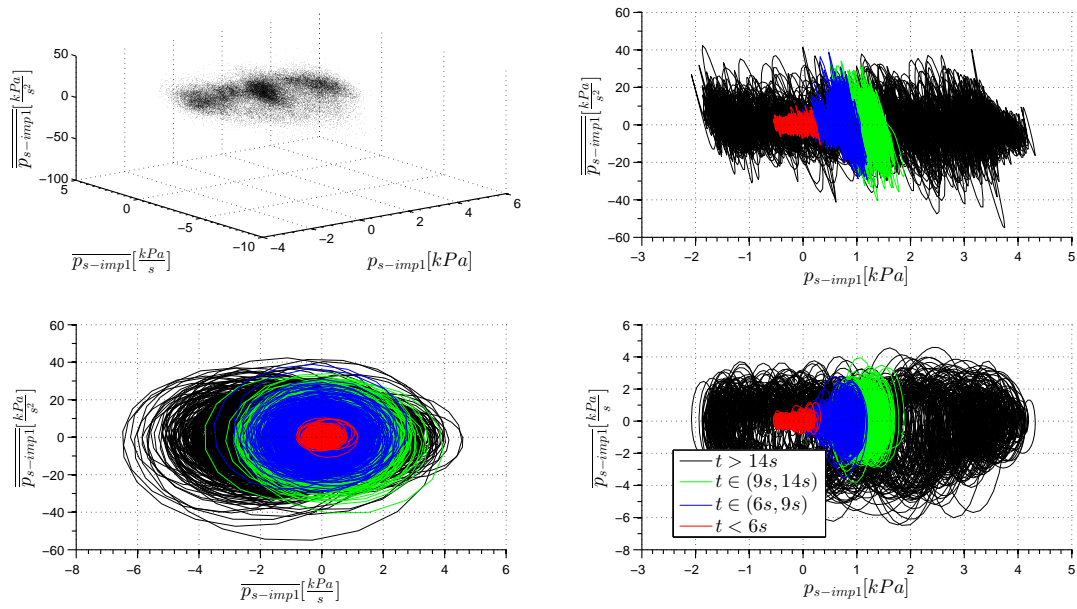


FIGURE 2.23: Phase trajectory of the pressure signals registered by gauge p_{s-imp1} and its projections

which was much higher than in previous cases. This confirmed that the instability appeared much earlier in this location. According to numerous researchers [48, 67, 90] the onset of instabilities of blowers and low-head compressors can be expected in the inlet zone. At the transient phase, pressure p_{s-imp1} gradual decrement was continued whereas the derivatives kept constant rate of fluctuation. At the surge the system entered a large limit cycle enclosed between -2 kPa and 4 kPa.

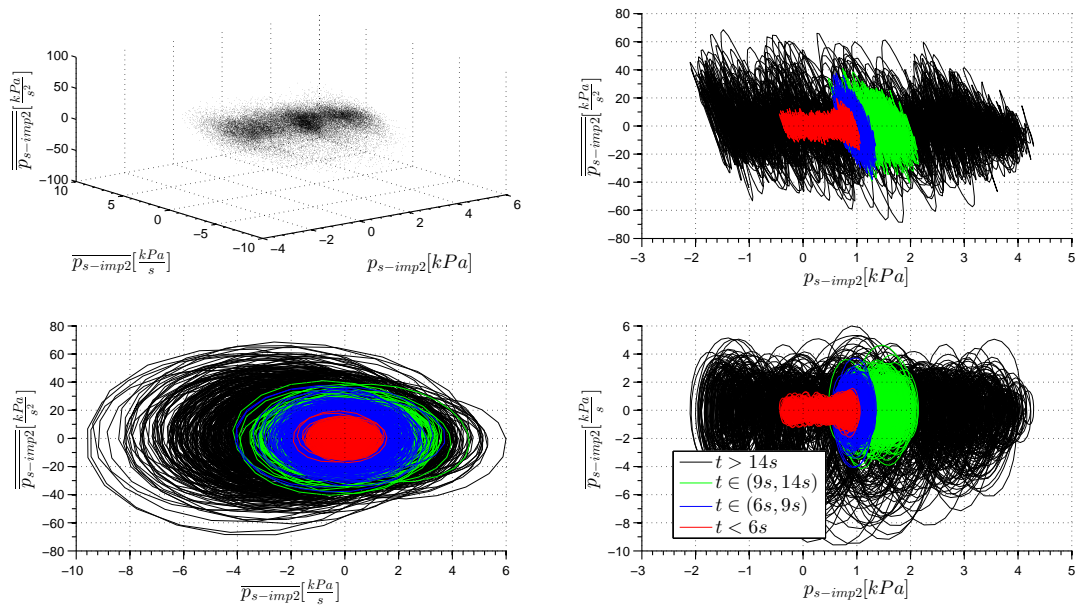


FIGURE 2.24: Phase trajectory of the pressure signals registered by gauge p_{s-imp2} and its projections

The signal at p_{s-imp2} was registered at the blade mid-span (figure 2.24). Therefore it was expected that the phase trajectory plotted for this location was very similar to the previous one. Again, in this case high fluctuations of derivatives were observed in the inlet recirculation regime, i.e. at $t \in (6 \text{ s}, 9 \text{ s})$. Then the rate of fluctuations remained constant till the deep surge onset. At the deep surge, the pressure oscillated between -2 kPa and 4 kPa .

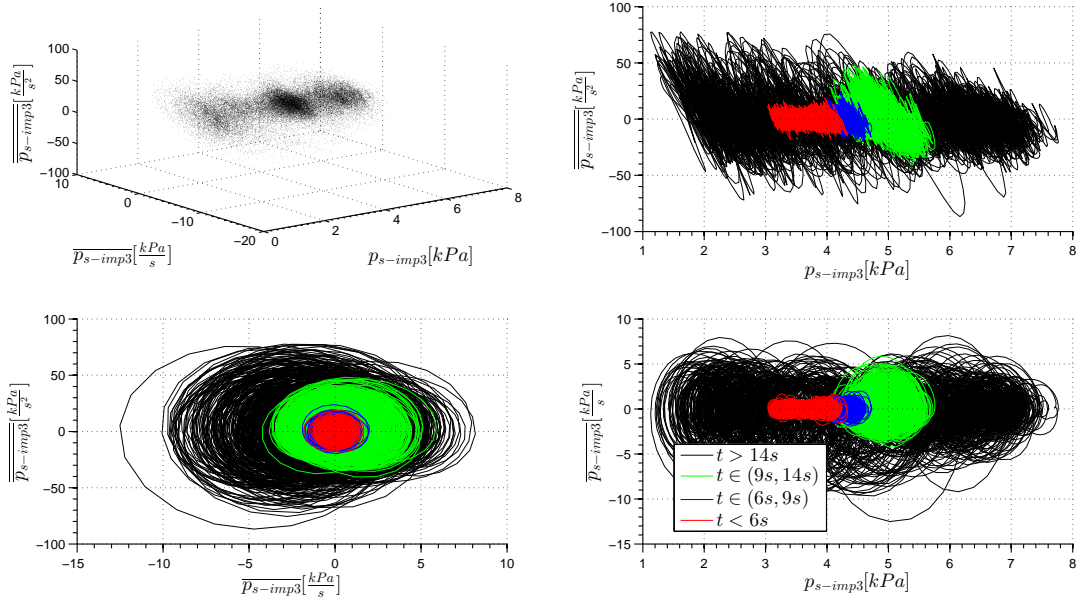


FIGURE 2.25: Phase trajectory of the pressure signals registered by gauge p_{s-imp3} and its projections

The phase portrait of dynamic signal at p_{s-imp3} is presented in figure 2.25. It can be observed that it showed no trace of the inlet recirculation. At $t \in (6 \text{ s}, 9 \text{ s})$ the rate of fluctuation of the derivatives remained unchanged. The phase portrait had a form of ellipsoid moving along p_{s-imp3} axis. At the transient phase the rate of fluctuation of derivatives was increasing and then slightly decreased just before entering the deep surge. At the deep surge the system entered a large limit cycle enclosed between 1 kPa and 8 kPa .

In all presented cases amplitude of fluctuation of both derivatives depended on the regime in which the blower operated. All projections $\overline{\overline{p_x}} - \overline{p_x}$ confirmed this statement. Phase portrait at $t < 6 \text{ s}$ had a form of an ellipse around $(0, 0)$. As the system left the stable working conditions, ellipse radii corresponding to directions $\overline{\overline{p_x}}$ and $\overline{\overline{p_x}}$ increased. At the deep surge oscillations had more complex structure. Nevertheless, the distance from the point $(0, 0)$ in both directions did not decrease. This observation allowed to define the *RDF* parameter (section 2.2.2.3), that may play an important role in the early surge detection.

2.2.2.3 RDF factor

Basing on findings presented in section 2.2.2.2 it was concluded that the instability can be measured by the following factor:

$$RDF = \frac{1}{\sqrt{2}} \sqrt{\frac{\left(\frac{dp}{dt}\right)^2}{\left(\frac{dp}{dt}\right)_D^2} + \frac{\left(\frac{d^2p}{dt^2}\right)^2}{\left(\frac{d^2p}{dt^2}\right)_D^2}} \quad (2.8)$$

This factor is referred to as the **Rate of Derivative Fluctuation**, or shorter *RDF*. The main advantage of the *RDF* lied in fact, that this parameter can be calculated at given moment of time based on the smoothed signal. Hence, it can be used for real-time monitoring. $(\cdot)_D$ in equation 2.8 indicates the average value determined at the design conditions. In the case of compressing system it can be measured separately. In this experiment, the $(\cdot)_D$ values were calculated from the first second of the experiment. The normalization constant $\frac{1}{\sqrt{2}}$ came from the fact, that each of the elements of the sum was normalized to one and in the nominal working conditions the *RDF* attained the value of $\sqrt{1+1}$.

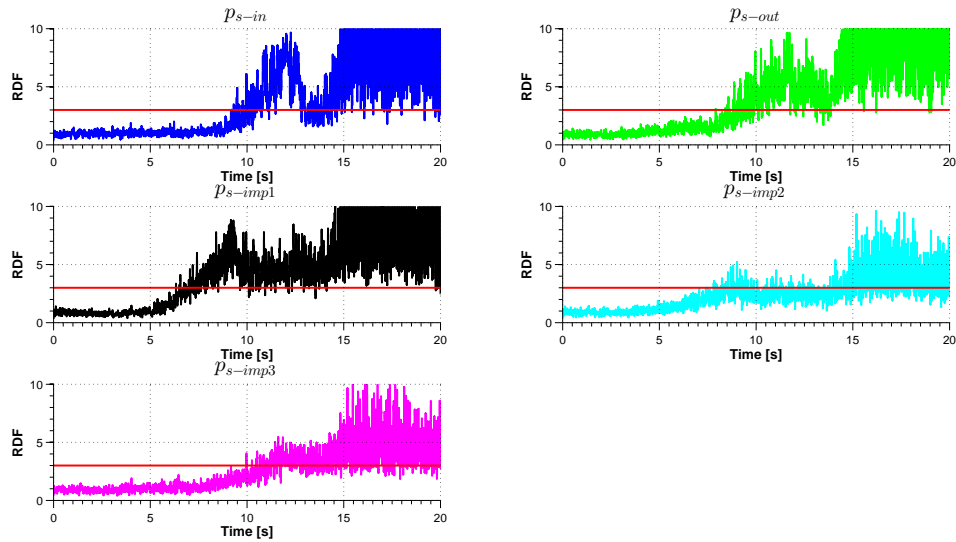


FIGURE 2.26: *RDF* factor obtained at pressure tapplings in dynamic tests and suggested threshold value ($RDF_t = 3$)

Figure 2.26 presents the values of *RDF* obtained at analysed pressure tapplings. In order to assure better readability all plots were smoothed with the Gaussian moving average filter. At the stable working conditions the *RDF* slightly oscillated around 1 at all gauges. Every permanent increment indicated that the rate of fluctuation of derivatives increased and the unstable structures appeared. Therefore, it was possible to define the threshold value RDF_t above which the anti-surge system could be activated. Too small value of the threshold may cause some false alarms, while too high would cause a delay in detection of dangerous unstable working conditions. Values around $RDF_t = 3$ seemed to be a reasonable compromise. *RDF* at the gauge p_{s-imp1} allowed to detect the inlet recirculation as early as in 7th second of the recorded signal. At p_{s-out} and p_{s-in} the value of 3 was reached around 9th and 10th second respectively. Both corresponded to

the transient phase. Gauges p_{s-imp1} and p_{s-imp2} are not recommended for detection of instabilities due to the risk of unintentional warning that may be caused by pressure fluctuations caused by the flow over blade tips.

The *RDF* can be monitored by a real-time controller. A Schematic block diagram of such a controller is presented in figure 2.27, where source signal is smoothed in order to reduce the noise. Then it is split into two branches and goes through single/double differentiating block. Afterwards, in each branch the signal is squared and multiplied by the normalization factor obtained at the design conditions. Next, signal is summed, goes through the square root block and $\frac{1}{\sqrt{2}}$ gain. Final smoothing block can be added to avoid activation caused by incidental and short instability. Finally, as a result of this simple signal transformation, the *RDF* is obtained. If it exceeds the threshold value, the anti-surge system can be activated.

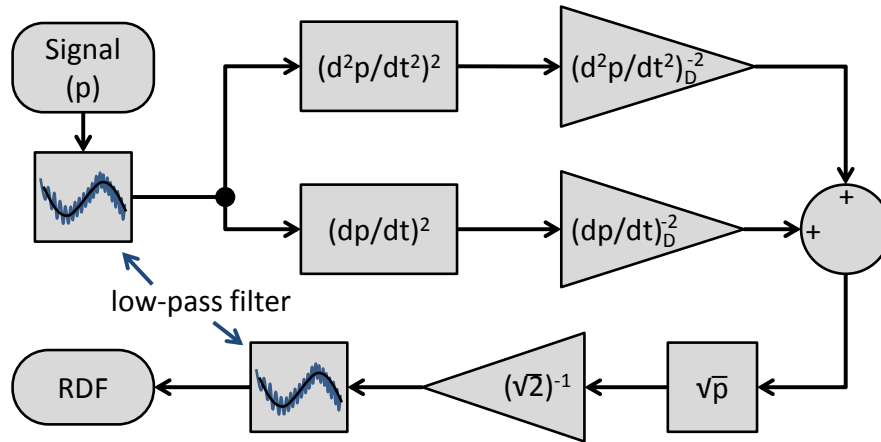


FIGURE 2.27: Block diagram of the controller for a real-time *RDF* measurement

2.2.3 Quasi-dynamic analysis

2.2.3.1 Amplitude of pressure fluctuations

In order to achieve a wider view of the phenomena appearing at a particular valve position, a quasi-dynamic analysis was conducted. It was possible to continue the measurements to a valve opening area as small as $TOA = 5\%$, where the machine was evidently operating at the deep surge. Measurements below this TOA were stopped due to large oscillations of the blower and the experimental rig. Some findings presented in this section were published in paper [75].

Amplitude of pressure variation In the quasi-dynamic analysis each signal was recorded at constant position of the throttling valve. Figure 2.28 presents average pressures attained at different TOA together with the range in which it oscillated. Table 2.3 presents the flow regimes identified at different values of the throttling. Plot 2.28(f) presents the values of the *RDF* factor calculated according to formula 2.8. The normalization was done in such a way, that *RDF* was equal to one at $TOA = 30\%$.

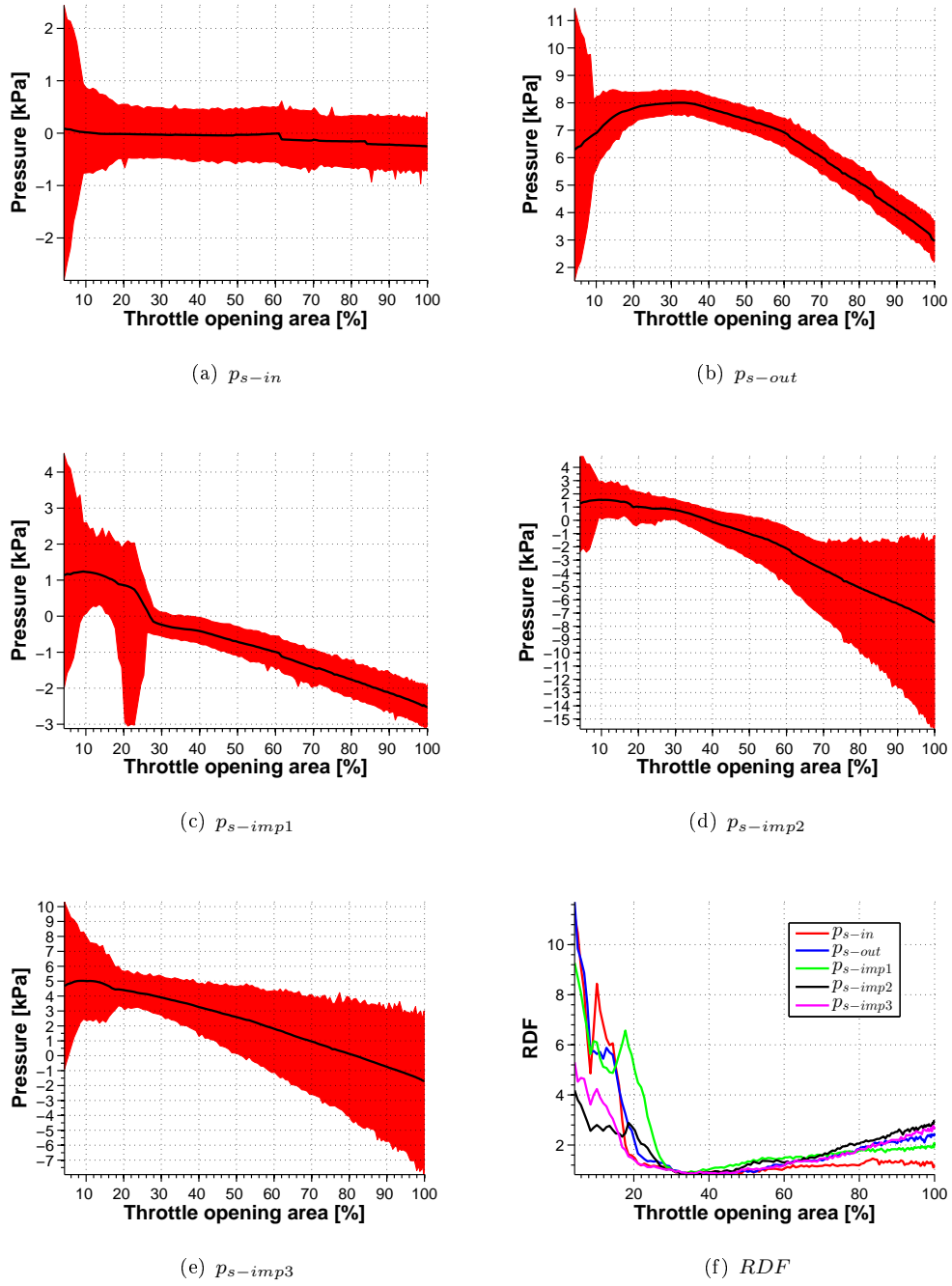


FIGURE 2.28: Pressure min-to-max plots registered at different positions of the throttling valve; RDF values registered at different positions of the throttling valve

TABLE 2.3: Working regimes identified during quasi-dynamic tests

TOA	Stability	Gauges	Name
$TOA > 27\%$	stable	all	nominal work
$TOA \in (17\%, 27\%)$	transient	p_{s-imp1}, p_{s-imp2}	inlet recirculation
$TOA \in (10\%, 17\%)$	unstable	all	transient phase
$t < 10\%$	unstable	all	deep surge

Figure 2.28(a) presents range of oscillation of the mean inlet static pressure p_{s-in} . The pressure average value and oscillations amplitude remained constant at the **stable regime** at $TOA > 17\%$. At the **transient phase** for $10\% < TOA < 17\%$ the amplitude of oscillation increased steadily. At $TOA = 10\%$ the amplitude of oscillation increased rapidly and it was evident that the system entered the **deep surge**.

It can be observed in figure 2.28(b) that the amplitude of pressure oscillation at the outlet p_{s-out} was characterized by similar behaviour to p_{s-in} , with the exception of the mean pressure which was changing due to changing machine pressure ratio. One can notice that the average pressure reflected the shape of the blower performance curve. The drop of mean pressure at $TOA < 27\%$ also well illustrated drop of blower pressure ratio which was beyond the measurable range of the static analysis (see section 2.2.1). The maximum value of the mean pressure was attained at $TOA \approx 30\%$, then it tended to decrease which was accompanied by a gradual increase in the pressure oscillation amplitude. It can be also noted that peak to peak pressure oscillation at the outlet at the surge was close to 10 kPa which was approximately two times higher than the amplitude of the pressure oscillation at the inlet.

Gauge p_{s-imp1} (fig. 2.28(c)) was located within the inlet zone upstream of the blade leading edge and appeared to be mostly affected by phenomena preceding the surge. The pressure fluctuation amplitude was constant at large throttle openings similar to the pressures at p_{s-in} and p_{s-out} . At TOA of approximately 27% the pressure oscillations rapidly increased and reached a level of 5 kPa peak-to-peak. The growth of the pressure oscillation amplitude was accompanied by an increase of the mean pressure. This was associated with the **inlet recirculation** [67].

At high TOA strong pressure oscillations were observed at both shroud gauges situated over the impeller: p_{s-imp2} and p_{s-imp3} . This pressure oscillation was associated with flows over the impeller blades. The gauge p_{s-imp2} located at $0.4L$, exhibited a slight influence of the inlet recirculation at $17\% < TOA < 27\%$, also a slight increase of the oscillation amplitude in region of the transient phase $10\% < TOA < 17\%$ and an increase of pressure oscillation to approximately 7 kPa at the deep surge. Gauge p_{s-imp3} located at $0.9L$ noted the highest amplitude amongst all the examined locations in the region of the transient phase ($10\% < TOA < 17\%$). Then, at the deep surge, it increased to the same extent as it was noted at the outlet gauge p_{s-out} . It can be suspected, therefore, that the highest amplitude of pressure oscillations at the deep surge was attained in the space between diffuser and the valve, i.e. in the plenum.

Figure 2.28(f) shows the values of RDF in the pressure data obtained at all gauges. Large values of pressure oscillations at p_{s-imp2} and p_{s-imp3} at large TOA were associated with pressure fluctuations associated with flow over the impeller blades. This showed that the RDF parameter can be used not only for detection of the pre-surge phase, but also the near-choke conditions. As TOA decreased the local maximum in the rate of derivative fluctuation was attained first at p_{s-imp1} and p_{s-imp2} at $TOA = 19\%$ and then at another gauges. That showed that first symptoms of the instability appeared firstly at the inlet recirculation zone (gauge p_{s-imp1}), then propagated through the middle of the impeller (p_{s-imp2}) towards the trailing edge (p_{s-imp3}) and confirmed the findings obtained by Tamaki [115] and, by means of CWT, by Horodko [48, 49]. Also, very strong increment of the RDF at p_{s-in} was observed around $TOA = 10\%$, just before entering the deep surge.

TABLE 2.4: Characteristic frequencies observed in the study; wide peaks are marked with \approx sign; abbreviations: S-present at the stable regime ($TOA > 20\%$), N-present at the unstable regime ($TOA < 20\%$), B-present at all TOA

notation	frequency Hz	Type	Gauges	Amplitude kPa	Name
f_{rot}	100	B	all	$\approx 10^{-2}$	impeller frequency
f_{BP}	2300	B	$P_{s-in}, p_{s-imp1-3}$	various	blade passing frequency
f_{BP_h}	4600	B	$p_{s-imp2-3}$	various	blade passing frequency (second harm.)
f_{sb1}	20000	B	P_{s-in}, p_{s-out}	$\approx 10^{-3}$	
f_{ss1}	≈ 16	S	all	$\approx 10^{-3}$	
f_{ss2}	≈ 50	S	$p_{s-in}, p_{s-imp1,3}$	$\approx 10^{-3}$	
f_{sn1}	10.8	N	all	≈ 1	main surge frequency
f_{sn2}	≈ 33	N	$p_{s-imp2-3}, p_{s-out}$	$\approx 10^{-2}$	
f_{sn3}	44	N	$p_{s-imp2-3}, p_{s-out}$	$\approx 10^{-2}$	
f_{sn4}	≈ 56	N	p_{s-in}, p_{s-out}	$\approx 10^{-2}$	

2.2.3.2 Spectral maps

Signal recording period and sampling frequency listed in section 2.1.1.3 implied an effective spectral analysis in frequency band equal to 0.05 Hz – 50 kHz with resolution of 0.05 Hz. Such a range of frequencies allowed to analyse a wide range of phenomena, appearing within the blower with characteristic frequency ranging between $0.001f_{rot}$ to $500f_{rot}$ and $43.4 \cdot 10^{-6}f_{BP}$ to $22f_{BP}$. Results obtained at different valve positions were combined into the frequency maps presented in figures 2.29-2.33. Due to wide range of orders of magnitude of the amplitude and the frequency, the horizontal axis and color bar were drawn in the logarithmic scale. Frequencies smaller than 1 Hz did not bring any useful information and were removed. Characteristic frequencies appearing on more than one gauge are listed in table 2.4. Some local maxima of the pressure spectra appeared as very narrow lines on the plots, and may be hardly visible in the figure due to the size limitations. They were caused by mechanical phenomena: rotational frequency and frequency of passing blades or natural vibration of the transducer. One of them $f_{sb1} = 20$ kHz cannot be satisfactory explained in this study. Other local peaks were wider. These correspond to flow phenomena and are the main subjects of interest.

In figure 2.29 one can see that, at large valve openings, inlet pressure p_{s-in} contained several dominant frequencies. Apart from the maxima present at $f_{rot} = 100$ Hz and $f_{BP} = 2.3$ kHz there were also another peaks at $f_{sb1} = 20$ kHz and 25 kHz. Nevertheless, all of them existed at all TOA values and were not affected by the unstable flow phenomena. Between 10 Hz and 200 Hz a different behaviour in the spectrum was observed for low throttle openings. In the stable regime, for $TOA > 27\%$, there were three dispersed peaks: $f_{ss1} \approx 16$ Hz, $f_{ss2} \approx 50$ Hz and also one at 85 Hz. At the deep surge ($TOA < 10\%$) some peaks were very high (up to 1.5 kPa) and sharp at $f_{sn1} = 10.8$ Hz and its 2nd harmonic at 21.8 Hz, some a bit wider and lower (around 10^{-2} kPa) at $f_{sn3} = 44$ Hz and $f_{sn4} \approx 56$ Hz. The transient phase ($10\% < TOA < 17\%$) was characterized by dispersed maxima in the same regions.

Frequency $f_{sn1} = 10.8$ Hz was in very good agreement with the one estimated with the assumption of the system acting as a Helmholtzian resonator according to equation 2.1. On the other hand, Fink et al. [29] found, that the Helmholtzian resonator frequency f_H was several times higher than the surge frequency. Possibly, the difference came from the fact that the machine analysed in their study had a much higher rotational speed and

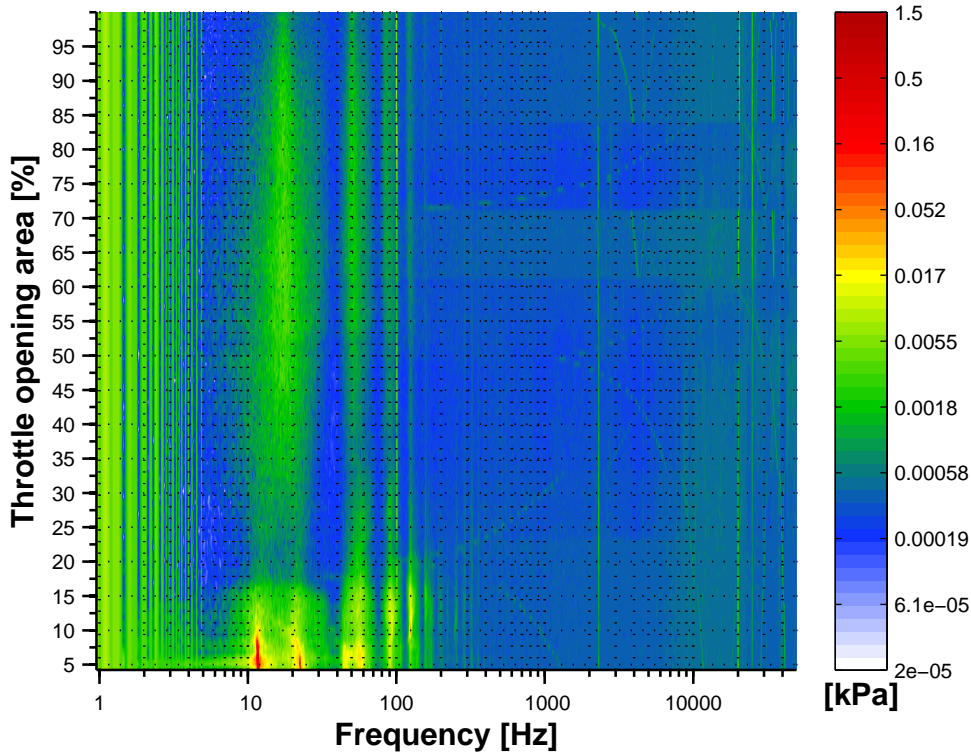


FIGURE 2.29: Static pressure frequency spectra obtained for different throttle values at the blower inlet (p_{s-in})

pressure ratio. Another possible reason lied in the choice of reference area and length for Helmholtzian frequency. In this study, the length of the channel mid-section was used, and its outlet area. The values of parameters applied by Fink are unknown.

When the TOA decreased, stable harmonics decayed slightly, and then grew to the form of sharp peaks. $f_{ss1} \approx 16$ Hz was situated in between $f_{sn1} = 10.8$ Hz and its second harmonic at 21.6 Hz, $f_{ss2} \approx 50$ Hz was situated in between $f_{sn3} = 44$ Hz and $f_{sn4} \approx 56$ Hz. The peak at ≈ 85 Hz grew up to an extent much higher than it was observed in the stable circumstances. The proximity of frequencies of phenomena present at the stable and the unstable regimes was in agreement with the general explanation proposed by Greitzer: the unstable fluctuation modes may also be present in stable circumstances, but in damped and dispersed form [38].

A spectral map of the outlet static pressure (fig. 2.30) also showed a peak at the impeller frequency $f_{rot} = 100$ Hz but it was slightly weaker at $TOA < 50\%$. What is worthy to note is that the volute effectively dissipated fluctuations associated with the blade passing frequency, as no peak was observed at $f_{BP} = 2.3$ kHz. In the stable regime $f_{ss1} \approx 16$ Hz and $f_{ss2} \approx 50$ Hz were hardly noticeable. Structure at the transient phase ($10\% < TOA < 17\%$) was very similar to what was observed in the inlet zone. At the deep surge: $f_{sn1} = 10.8$ Hz attained amplitude as high as 3.4 kPa. Another dominating peak was noted at $f_{sn3} = 44$ Hz with the amplitude weaker by two orders of magnitude.

A spectral map created for gauge placed in the impeller inlet zone p_{s-imp1} (figure 2.31) had a clear ridge at $f_{rot} = 100$ Hz and a weaker ridge at $f_{BP} = 2.3$ kHz at all throttle positions. At the deep surge, peaks were observed at frequency $f_{sn1} = 10.8$ Hz and its second harmonic. At the the transient phase ($10\% < TOA < 17\%$) the spectrum was

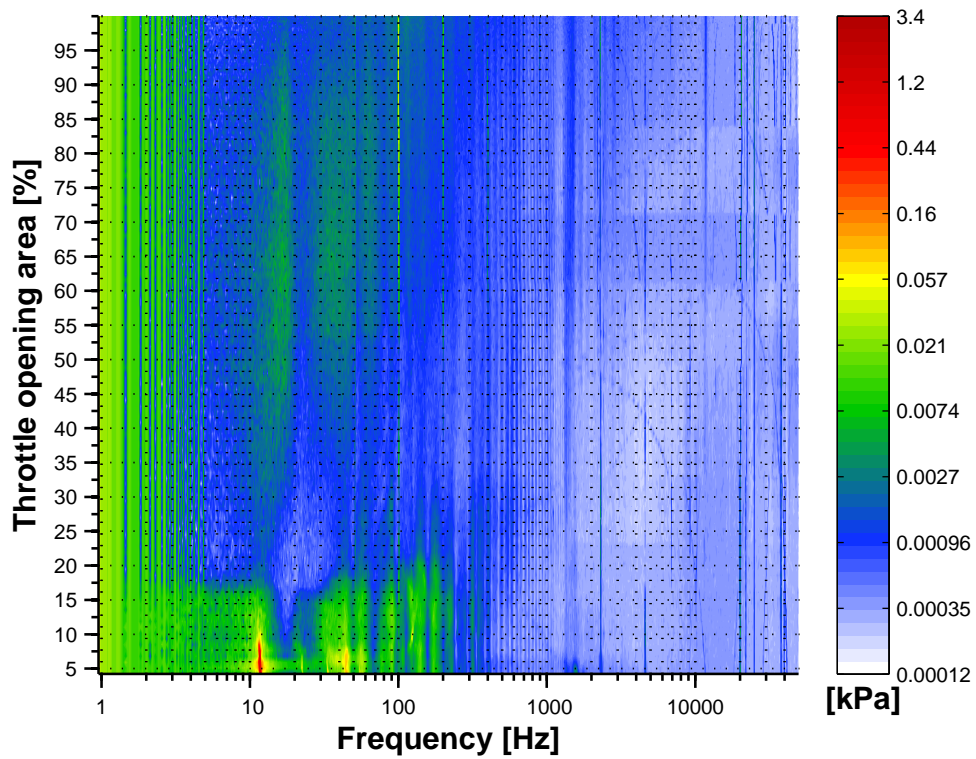


FIGURE 2.30: Static pressure frequency spectra obtained for different throttle values at the blower outlet (p_{s-out})

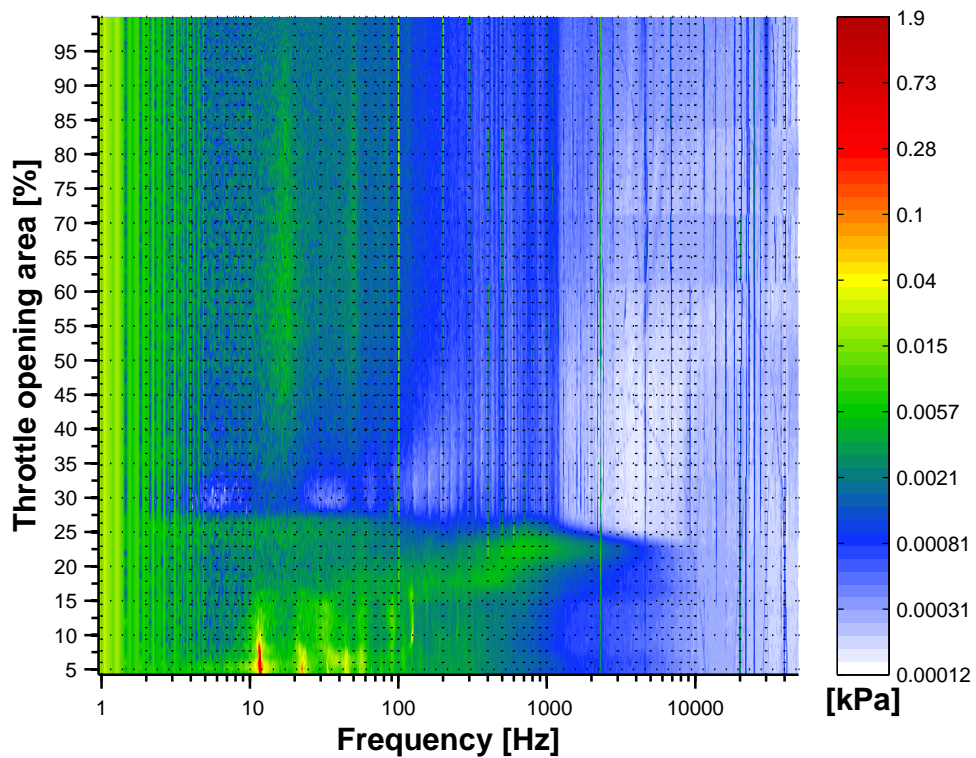


FIGURE 2.31: Static pressure frequency spectra obtained for different throttle values at the blower shroud before leading edge at $-0.2L$ (p_{s-imp1})

dispersed with some weak frequencies (including $f_{sn1} = 10.8$ Hz and $f_{sn2} \approx 33$ Hz). At the inlet recirculation ($17\% < TOA < 27\%$), the broadband noise was observed with no dominating frequencies. At the inlet recirculation, recurrent pressure drops were observed. Spectral analysis revealed that these drops were not periodic and, therefore, resulted in appearance of the broadband noise.

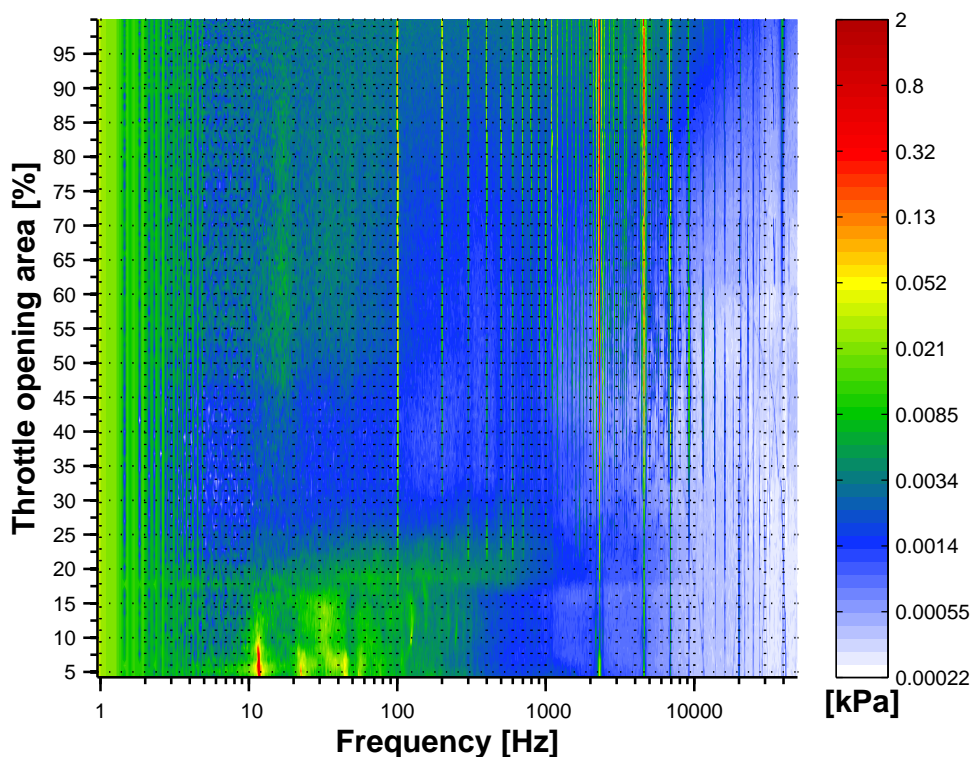


FIGURE 2.32: Static pressure frequency spectra obtained for different throttle values at the blower shroud over impeller at $0.4L$ (p_{s-imp2})

As expected, gauges located over the impeller (p_{s-imp2} in figure 2.32 and p_{s-imp3} in figure 2.33) had strong and sharp ridges associated with $f_{BP} = 2.3$ kHz, $f_{rot} = 100$ Hz and their several harmonics. At p_{s-imp2} weak influence of the inlet recirculation was also visible at $17\% < TOA < 27\%$. Spectra at the transient phase and the deep surge were very similar to that present at p_{s-imp1} . At p_{s-imp3} peaks at blade passing frequency $f_{BP} = 2.3$ kHz became wider in the region of the transient phase $10\% < TOA < 17\%$. Possible reason of this widening lied in the growth of the diffuser or the impeller instabilities. Simultaneously, broadband noise was generated at frequencies up to 300 Hz and its amplitude was the most significant compared to another gauges. One gentle peak around $f_{sn2} \approx 33$ Hz was observed. High amplitudes of instabilities in this location can be associated with structures such as VDRS, PIRS or another flow structures in the impeller and the diffuser. At the deep surge $TOA < 10\%$, additionally to $f_{sn1} = 10.8$ Hz and its second harmonic, ridges appeared around $f_{sn3} = 44$ Hz. At large TOA , p_{s-imp3} recorded high levels of noise which were not observed on the other gauges.

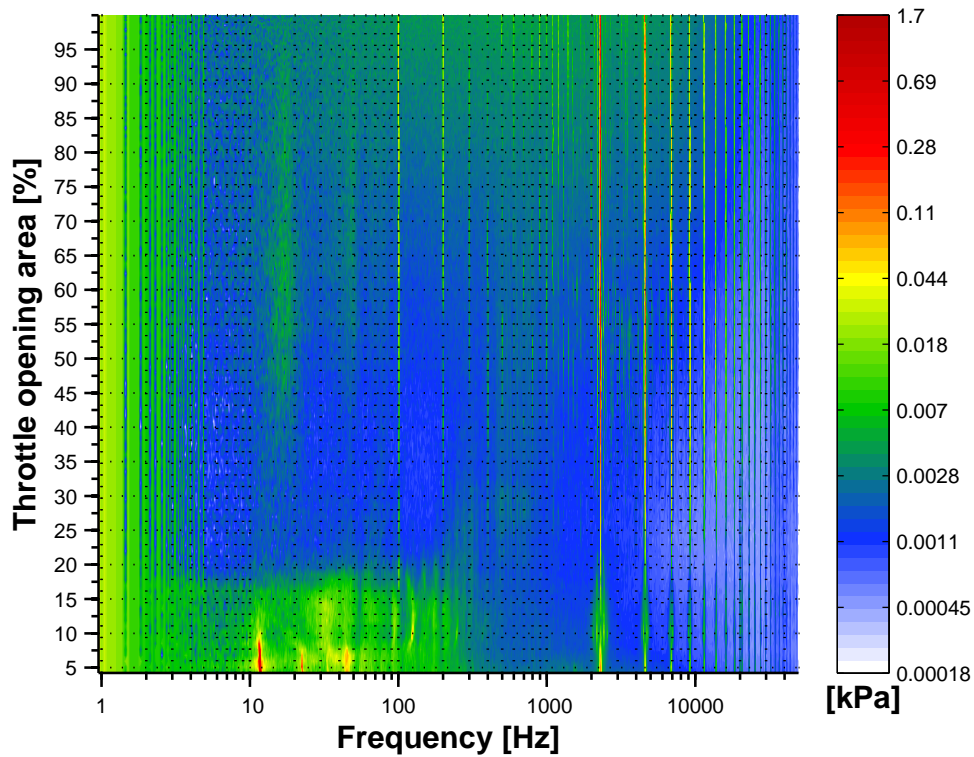


FIGURE 2.33: Static pressure frequency spectra obtained for different throttle values at the blower shroud over impeller at $0.9L$ (p_{s-imp3})

2.2.3.3 Conclusions regarding the onset of unstable structures

This section summarizes all the information gathered about the first indicators of the compressor surge. First significant fluctuations were recorded by the gauge located at the shroud above the impeller inlet p_{s-imp1} (figures 2.28(c) and 2.31). Undoubtedly, pressure fluctuations in this region and rise of the average pressure were the first indicators of instability that appeared at $TOA = 27\%$. Figure 2.34 presents the frequency spectra in the form of xy plots. Plots above $TOA = 27\%$ (figure 2.34(a)) and below $TOA = 27\%$ (figure 2.34(b)) show the difference in signal structures more clearly. At $TOA > 27\%$ the signal spectrum below 600 Hz had higher amplitude with one significantly stronger peak at $f_{rot} = 100$ Hz. At $TOA < 27\%$ all of them disappeared, with the only exception of $f_{rot} = 100$ Hz. However, the overall oscillation amplitude rose forming a broadband noise at frequencies up to 600 Hz. As observed in figure 2.31 the flow structure generating broadband noise remained present down to $TOA = 17\%$. Its disappearance was concurrent with the formation of new flow structures represented by periodic instabilities in the other zones.

Looking back to the results of the static analysis, one could associate the dark points from figure 2.12 and 2.13 with the range of presence of the inlet recirculation. This meant that, as long as the inlet recirculation was present, the operating point did not cross the surge limit. This may be described by the following mechanism: as the mass flow rate was decreasing the recirculation started to appear [67, 90]. As the TOA was reduced the recirculation grew and tended to move towards the impeller which was visible as noise on the p_{s-imp2} spectral map (fig. 2.32) and the position of local maxima of the RDF (figure 2.28(f)). Around a critical valve position, $TOA = 17\%$, the inlet recirculation

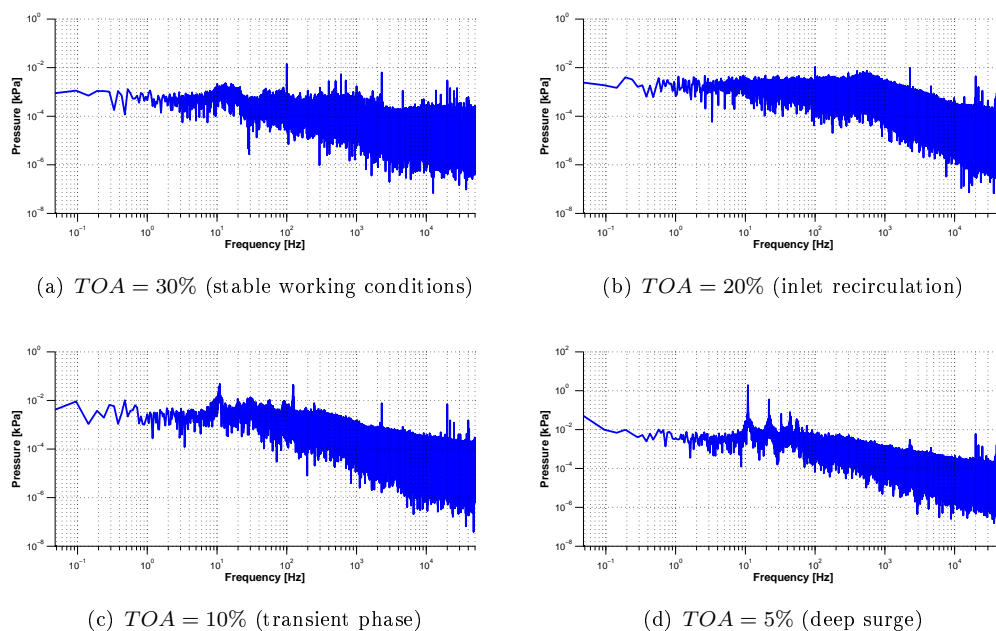


FIGURE 2.34: XY scatter plots of FFT power spectra obtained within inlet zone (p_{s-imp1}) at characteristic values of the throttling corresponding to different working conditions

vanished and unsteady flow structures started to appear throughout the machine. At the same moment further stationary analysis was impossible due to appearance of significant pressure oscillations in the whole machine. Before the deep surge, the instability is located close to the p_{s-imp3} gauge.

Literature did not devote much attention to the inlet recirculation. It is much more difficult to record the inlet recirculation in the dynamic analysis where the valve is continuously closed and it may take place for a very short period of time. However, in some cases the inlet recirculation was noticed. Tamaki reported presence of a similar structure in a compressor with much higher rotational speed [115]. Frigne and Van den Braembussche stated that the stall pattern onset took place in the impeller inlet zone (named as progressive stall) [33]. Kämmer and Rauten [65] noticed that the stall initiation at the impeller is common at low rotational speeds, while Oakes and Lawless [96] showed that the region of disturbance onset depends on the rotational speed of the rotor. They noted that in a low speed compressor, the rotating stall appears in mid-chord, while in the case of a high-speed unit stall appears in the diffuser. However, in both cases the stall could be preceded by the inlet recirculation which was not analysed in these studies. It can be suspected that the impeller stall patterns were preceded by disturbances in the close vicinity of the leading edge, which needs to be examined in a further research. If this structure commonly appears in centrifugal compressing machines, it will be possible to introduce improvements in existing anti-surge schemes. The sensors could be located in the region where the inlet recirculation is expected and could be used to identify a sudden pressure jumps. Such a system would be very safe, since it detects a flow structure that precedes the surge. The first trials of such a scheme conducted by McKee et al. [84] showed promising results.

2.2.3.4 Representation of signals in the phase space

Quasi dynamic analysis gave the possibility of drawing 'frozen' phase portraits that were attained at given TOA , which corresponded to a particular working regime. Figures below present the phase portraits attained at four values of throttling:

- $TOA = 30\%$ - the stable working regime
- $TOA = 20\%$ - the inlet recirculation
- $TOA = 10\%$ - the transient phase
- $TOA = 5\%$ - the deep surge

All TOA values are distinguished on 2 dimensional projections. For clarity, the 3 dimensional phase portrait contains the phase portrait at the deep surge only, similarly as it was presented in the case of the phase trajectories obtained in the dynamic test. The analysis includes comparison of quasi-static phase portraits with dynamic phase portraits presented in figures 2.21-2.25. As it was mentioned in section 1.4 according to Pampreen [98], there are two ways of entering the unstable working conditions: abrupt and progressive. The dynamic test created conditions which are most likely to induce the abrupt instabilities due to fast valve closure. On the other hand, the quasi-dynamic procedure incorporated throttling changes that were done progressively: very slowly and with small steps. Therefore, observed differences in phase portraits may give some information on how the unstable regimes depended on the way in which the system entered them. Due to many similarities between static and dynamic phase portraits only two examples are shown in order to illustrate the main differences.

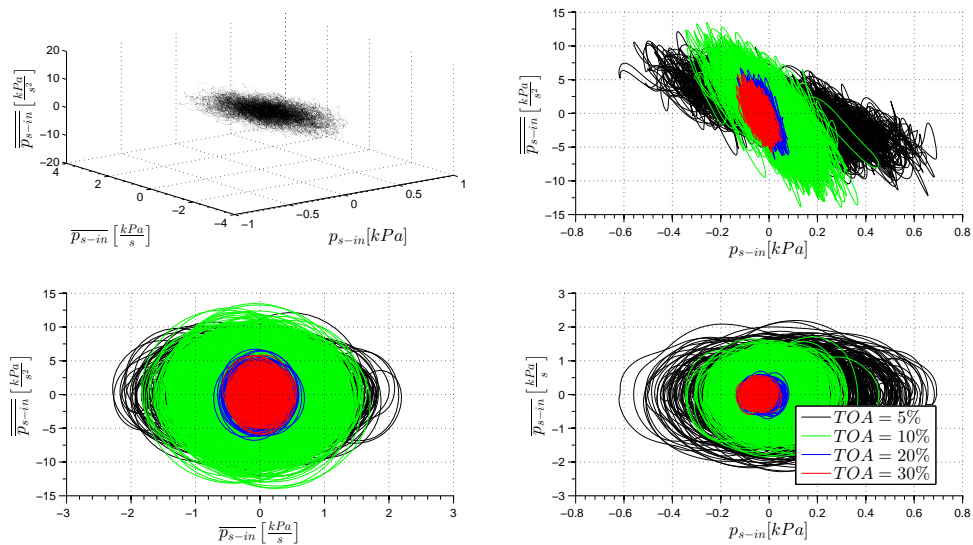


FIGURE 2.35: Phase portraits of the pressure signals registered at gauge p_{s-in} at TOA values corresponding to different working regimes

Figure 2.35 contains the phase portraits of the signal p_{s-in} and is analogous to 2.21 drawn for the dynamic test. In both cases the shape of phase cycles was very similar. The stable working conditions and the inlet recirculation did not exhibit any dependence

on the type of the analysis. The transient phase appeared to have a higher rate of derivatives fluctuation in the quasi-dynamic test. Therefore, it can be concluded that in the dynamic test limited amount of time did not allow the transient phase to obtain a fully developed form. On the other hand, at the deep surge the limit cycle appeared to be slightly bigger in the case of the dynamic test. Moreover, the gap in the middle of projection $\overline{p_{s-in}} - p_{s-in}$ (figure 2.21) was also bigger which suggested regular and stronger fluctuations of the pressure. However, one has to take into account the fact, that the quasi-dynamic tests were conducted up to $TOA = 5\%$ due to safety requirements, while the dynamic analysis was continued to fully closed throttling valve.

Signal p_{s-imp1} was chosen to construct the other characteristic phase portraits (figure 2.36). One can observe, that again the transient phase presented higher rate of fluctuation in the quasi-dynamic test. The same phenomenon was observed in the case of the inlet recirculation. It had much more developed form in case of quasi dynamic (i.e. progressive) way of entering the unstable regime. Similarly, the transient phase represented more developed form in case of the quasi-dynamic test at all other gauges. At all other control points the inlet recirculation was not observed both in the dynamic and the quasi-dynamic tests.

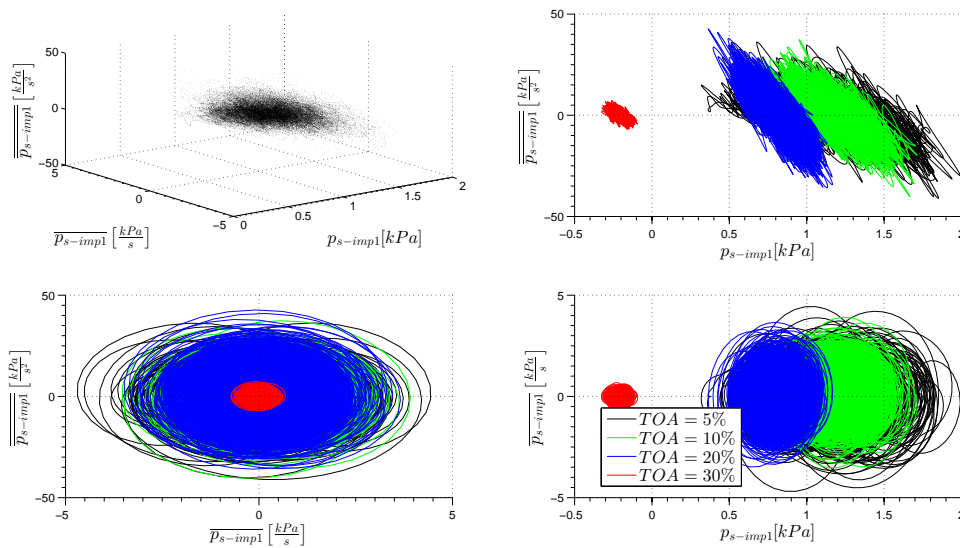


FIGURE 2.36: Phase portraits of the pressure signals registered at gauge p_{s-imp1} at TOA values corresponding to different working regimes

2.2.4 Influence of the plenum volume on system dynamics

This section presents results of the quasi-dynamic analysis conducted on the experimental stand with shorter outlet pipe resulting in reduced plenum volume. For sake of clarity, the cases of the large and the small pressure volume are denoted as **LP** and **SP** respectively. Corresponding Helmholtz frequencies were calculated from formulas 2.1 and 2.2 and constituted 11.45 Hz (LP case) and 17.09 Hz (SP case). The discussion is conducted in the form of comparison of results obtained at control points in the SP case to the LP case presented in section 2.2.3. Some of results presented in this section were published in [62].

2.2.4.1 Amplitude of pressure fluctuation

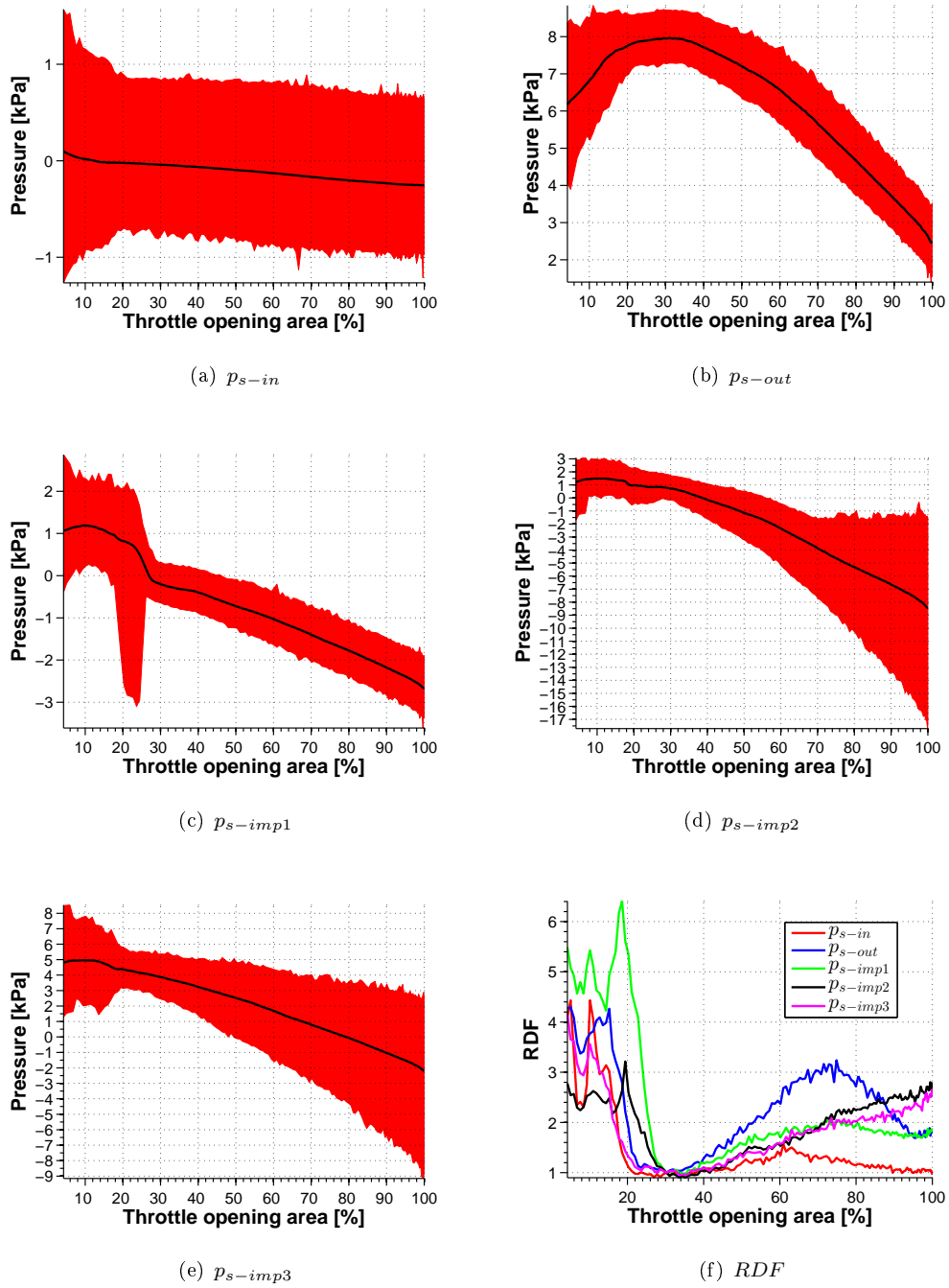


FIGURE 2.37: Pressure min-to-max plots registered at different positions of the throttling valve in the case of reduced plenum volume; RDF values registered at different positions of the throttling valve in the case of reduced plenum volume

Figure 2.28 presents the min-to-max plots and values of RDF obtained in the quasi-dynamic analysis for the LP case. Figure 2.37 contains analogous plots obtained in the case of the reduced plenum volume. Comparison between these allowed to draw the conclusions regarding influence of the plenum volume on the blower dynamics. The most important of them are listed below:

- The plenum volume did not influence the *TOA* at which particular flow regimes appeared. Hence, table 2.3 remained valid for this test campaign.
- Pressure fluctuation amplitude at the deep surge was smaller at all control points in the SP case. This was caused by smaller amount of the working medium that oscillated in the plenum (outlet pipe).
- The inlet recirculation registered at p_{s-imp1} and p_{s-imp2} was independent of the plenum volume. This included: its onset and disappearance moment, size of pressure fluctuations and the extent of average pressure rise (around 1 kPa).
- The amplitude of pressure fluctuation at p_{s-out} was about two times higher in the SP case, especially for values of *TOA* between 50% and 90%. This could be caused by the close proximity of the outlet valve to this gauge.

Some interesting conclusions can be also drawn from comparison of the *RDF* plot 2.37(f) of the SP case compared to the *RDF* plot of the LP case 2.28(f):

- *RDF* attained much smaller values at the surge in the SP case. As mentioned above, this was caused by smaller volume of the plenum.
- The value of *RDF* at the inlet recirculation at gauges p_{s-imp1} and p_{s-imp2} was the same in both cases: SP and LP. Due to less developed form of the surge in the SP case, the value of *RDF* at the inlet recirculation was higher than the value of *RDF* at the same gauge at the deep surge. This confirmed a very important finding that contrary to the transient phase and the deep surge, the inlet recirculation was totally independent of the plenum volume. This meant that the inlet recirculation was a structure that depended on the machine design only. Hence any anti-surge system based on the inlet recirculation detection is universal for all piping systems.
- Gauge p_{s-out} registered different behaviour of *RDF* in the SP and the LP cases at values of *TOA* between 50% and 90%. In the SP case it was significantly higher and attained local maximum equal to 3 at *TOA* = 70% and then decreased to a level similar to the LP case. As it was already mentioned, higher fluctuations at p_{s-out} in the SP case could be caused by the close proximity of the outlet valve. This was also reflected in higher *RDF*.

2.2.4.2 Spectral maps

Figures 2.38-2.42 contain spectral maps computed from data registered in the test campaign in the SP case. Table 2.5 summarises the amplitudes registered at all pressure tappings at the surge. Since the moments of onset and disappearance did not depend on the plenum volume, the names of flow regimes presented in table 2.2 are valid also in this section. For better readability of differences between both cases, differential spectral maps were constructed and are presented in appendix A.

Figure 2.38 illustrates the pressure fluctuation spectrum obtained at the gauge p_{s-in} in the SP case which can be compared to the LP case presented in figure 2.29. In both instances a high-frequency amplification was observed around $f_{sb1}^{SP} = 20$ kHz. As can be observed, this phenomenon was common for all signals at all circumstances and was not associated with any particular phenomenon. At *TOA* > 27% wide peaks were observed at frequency $f_{ss1}^{SP} \approx 16$ Hz. In this case, the fluctuation magnitude was almost

TABLE 2.5: Characteristic frequencies observed in the study in the SP case; wide peaks are marked with \approx sign; abbreviations: S-present at the stable regime ($TOA > 20\%$), N-present at the unstable regime ($TOA < 20\%$), B-present at all TOA

notation	frequency Hz	Type	Gauges	Amplitude kPa	
f_{rot}	100	B	all	$\approx 10^{-2}$	impeller frequency
f_{BP}	2300	B	$P_{s-in}, p_{s-imp1-3}$	various	blade passing frequency
f_{BPh}	4600	B	$p_{s-imp2-3}$	various	blade passing frequency (second harm.)
f_{sb1}^{SP}	20000	B	P_{s-in}, p_{s-out}	$\approx 10^{-3}$	
f_{ss1}^{SP}	≈ 16	S	all	$\approx 10^{-3}$	
f_{ss2}^{SP}	≈ 50	S	all	$\approx 10^{-3}$	
f_{sn1}^{SP}	14	N	all	$\approx 10^{-2}$	deep surge
f_{sn2}^{SP}	41	N	$p_{s-out}, p_{s-imp1-3}$	≈ 1	
f_{sn3}^{SP}	53	N	p_{s-in}, p_{s-out}	$\approx 10^{-1}$	

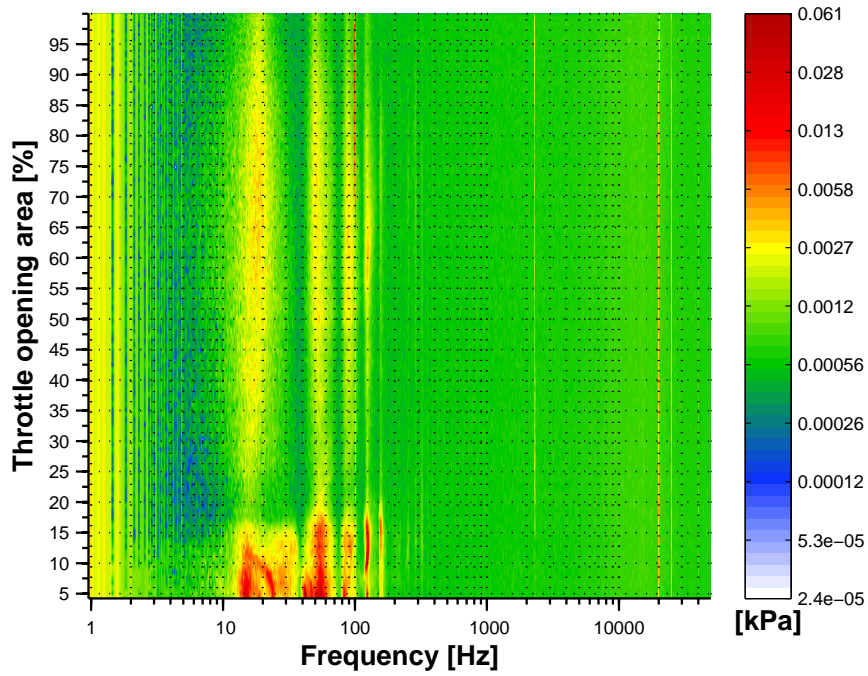


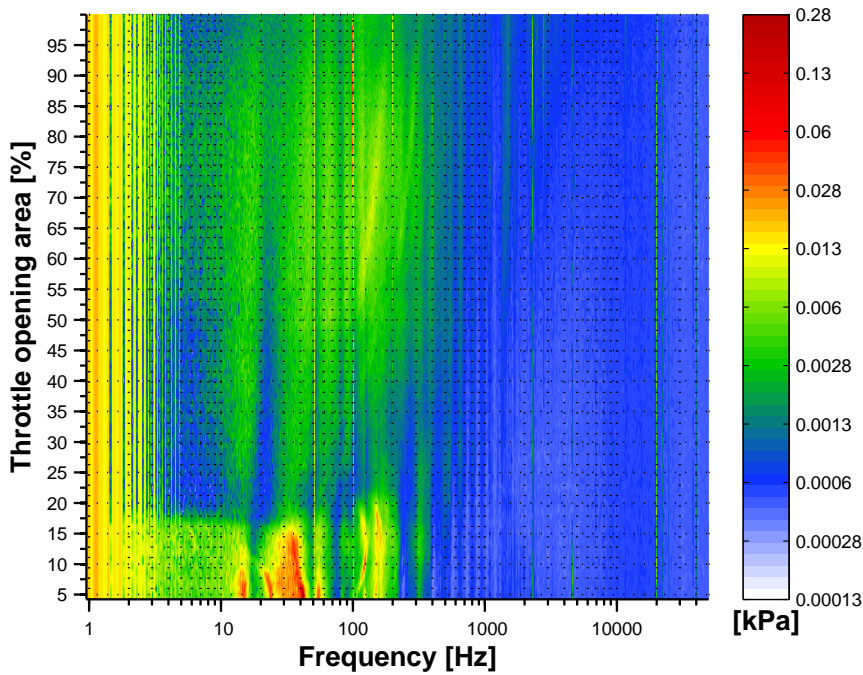
FIGURE 2.38: Static pressure frequency spectra obtained for different throttle values at the blower inlet (p_{s-in})

independent of the outlet volume and was close to 4 Pa. Similar amplifications were present around $f_{ss2}^{SP} \approx 50$ Hz, 80 – 90 Hz and in the SP case at 120 – 130 Hz. At very high frequencies the noise level was slightly higher in the SP case. In both cases, increment of amplitudes by one order of magnitude was observed at the transient phase at $TOA = 17\%$. At deep surge $TOA < 10\%$ the amplitude increased again by one (SP) or two (LP) orders of magnitude. The highest pulsation magnitude in LP equalled to 1500 Pa, which was 25 times higher than in the SP case. The oscillation amplitudes recorded at the strongest peaks are listed in table 2.6. $\frac{p_{max}}{p_{min}}$ represents ratio of highest to lowest surge amplitude registered at the analysed control points.

The pressure spectral map at the volute outlet shown in figures 2.39 (SP) and 2.30 (LP) appeared to be only slightly dependent on the plenum volume at the stable working

TABLE 2.6: Surge amplitudes and frequency in the SP and the LP cases

	Short pipe	Long pipe	Ratio
Frequency of the strongest peak	41 Hz	10.8 Hz	-
p_{s-in}	60 Pa	1500 Pa	25.0
p_{s-imp1}	70 Pa	1900 Pa	27.1
p_{s-imp2}	90 Pa	2000 Pa	22.2
p_{s-imp3}	370 Pa	1700 Pa	4.6
p_{s-out}	280 Pa	3400 Pa	12.1
$\frac{p_{max}}{p_{min}}$	9.0	2.3	

FIGURE 2.39: Static pressure frequency spectra obtained for different throttle values at the blower outlet (p_{s-out})

conditions. As in the previous case, fluctuations appeared to be stronger in the LP case. At the mild surge ($< 10\%TOA < 17\%$) several significant differences in the spectrum might be noted. Firstly, a fall in noise amplitude was observed in the region $18 \text{ Hz} < f < 20 \text{ Hz}$ (SP). In the LP case the fall was more significant and settled down between 15 Hz and 30 Hz. As the blade traces have already mixed inside the diffuser and the volute, the $f_{BP} = 2.3 \text{ kHz}$ peak was no longer present at this point. The discrepancy in the dominating surge amplitude noticed at the inlet pressure tapping stayed present at the machine outlet. The SP peak frequency was $f_{sn2}^{SP} = 41 \text{ Hz}$, the magnitude was around 280 Pa. In the LP case, the amplitude peak reached 3400 Pa and oscillated with frequency $f_{sn1} = 10.8 \text{ Hz}$. The amplitude ratio equalled to 12.1 which was lower compared to the signal at the gauge installed at the inlet.

Pressure fluctuation spectra at p_{s-imp1} shown in figures 2.40 (SP) and 2.31 (LP) look similar to the ones discussed above within the stable operational range $TOA > 27\%$. The difference was observed at $17\% < TOA < 27\%$, where the broadband noise appeared.

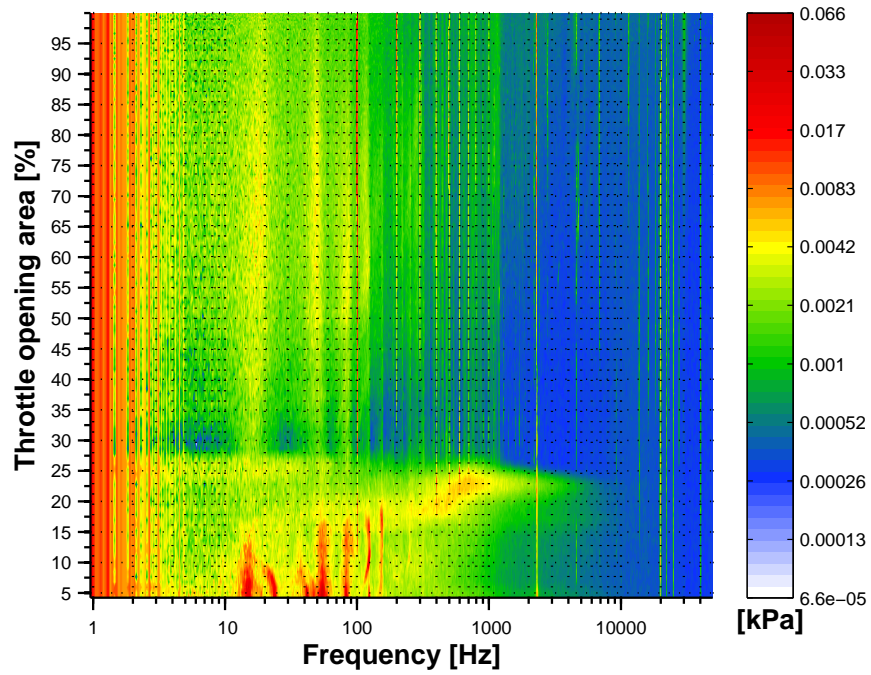


FIGURE 2.40: Static pressure frequency spectra obtained for different throttle values at the blower shroud before leading edge at $-0.2L$ (p_{s-imp1})

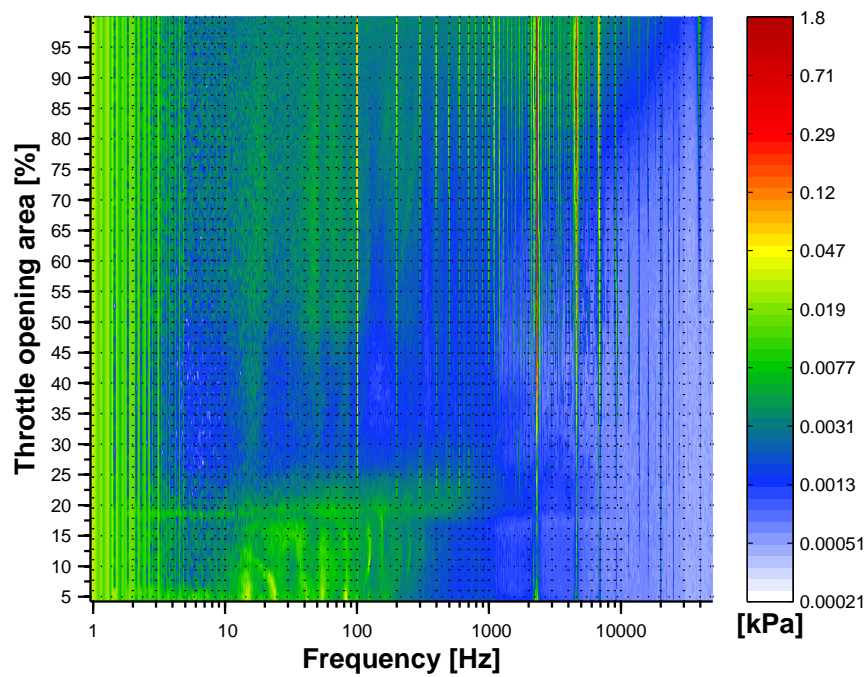


FIGURE 2.41: Static pressure frequency spectra obtained for different throttle values at the blower shroud over impeller at $0.4L$ (p_{s-imp2})

Pulsations had chaotic character and were almost independent of the plenum volume. As described in section 2.2.3 these instabilities were induced by the inlet recirculation. This study showed that moment of the inlet recirculation onset, end and its spectral structure did not depend on the plenum volume. The amplitude at surge in this region was equal to 70 Pa in the SP case and 1900 Pa in the LP case. The relative ratio in surge dominating amplitudes grew up to 27.1.

Figures 2.41 (SP) and 2.32 (LP) present the spectral maps at the rotor mid-chord p_{s-imp2} . In both cases the influence of the inlet recirculation was still visible at this point at $17\% < TOA < 27\%$, however, to a much smaller extent. It was confirmed by smaller amplitude and smaller frequency range $100 \text{ Hz} < f < 1000 \text{ Hz}$ of the broadband noise. Peaks connected with the blade passing frequency $f_{BP} = 2.3 \text{ kHz}$, the impeller frequency $f_{rot} = 100 \text{ Hz}$ and their harmonics were present in both cases.

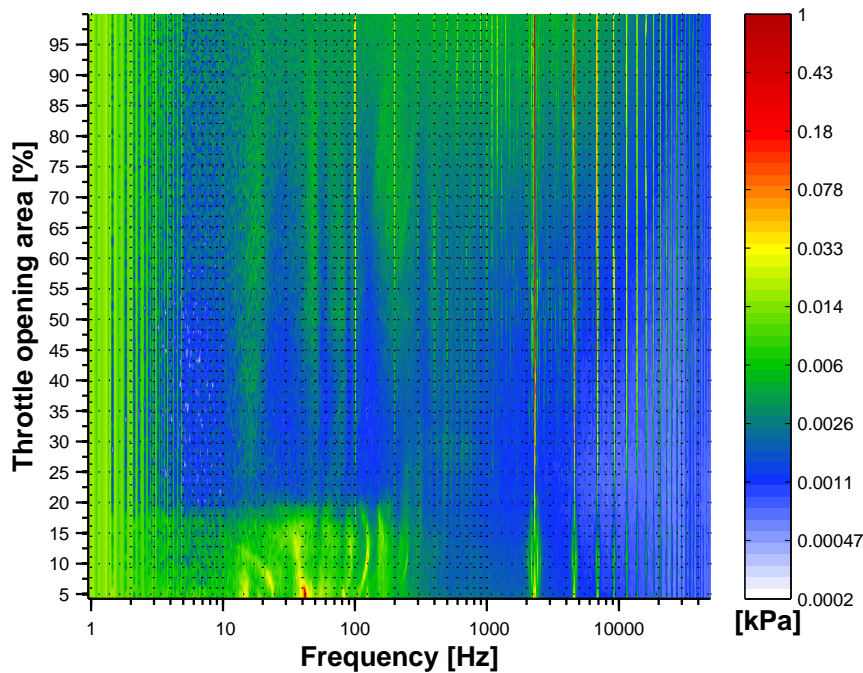
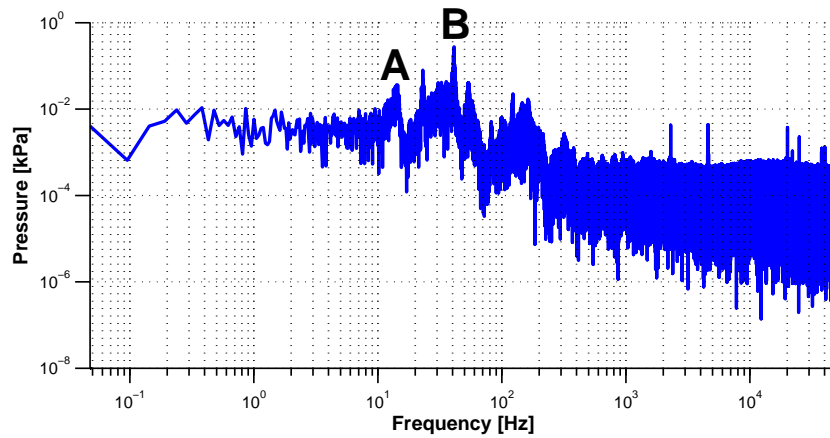


FIGURE 2.42: Static pressure frequency spectra obtained for different throttle values at the blower shroud over impeller at $0.9L$ (p_{s-imp3})

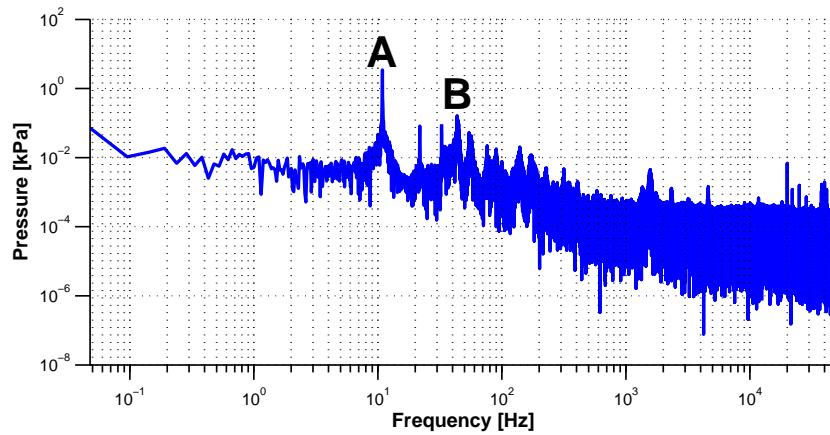
At the impeller outlet pressure tapping p_{s-imp3} (figures 2.42 for the SP case and 2.33 for the LP case), the inlet recirculation was not observed regardless of the plenum volume. The amplitude peaks at the deep surge kept the same frequencies as previously. In both cases the fourth (9200 Hz) and further harmonic frequencies of the $f_{BP} = 2.3 \text{ kHz}$ were present more explicitly than at p_{s-imp2} . The SP surge peak amplitude had increased to 370 Pa. Compared to p_{s-imp2} it rose around 4 times. What is interesting, it was also higher than at the p_{s-out} by a factor of 1.3. In the LP case, the highest amplitude was observed at the outlet.

2.2.4.3 Analysis of the deep surge dominating frequencies

For more detailed analysis of the unstable phenomena present for different plenum volumes, selected Fourier spectra are presented in the form of xy plots. Figures 2.43 and



(a) Small plenum volume



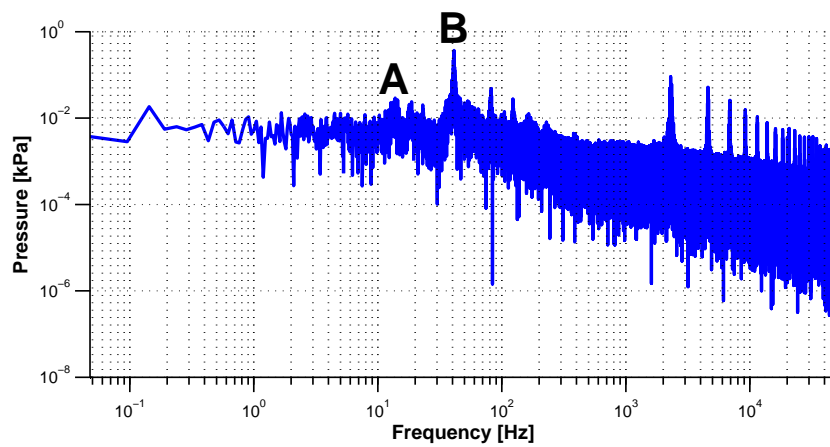
(b) Large plenum volume

FIGURE 2.43: Frequency spectra at p_{s-out} at the deep surge $TOA = 5\%$

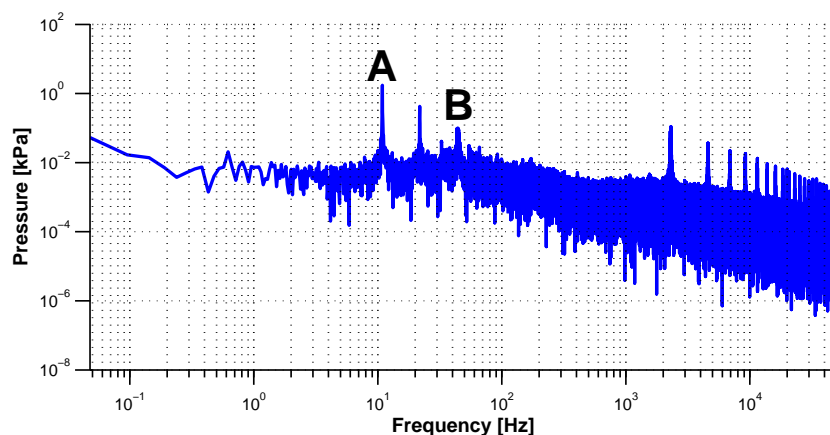
2.44 show the pressure frequency spectra of the signals attained at p_{s-out} and p_{s-imp3} respectively. In both figures, peaks at frequencies $f_A \approx 12$ Hz $\in [f_{sn1}, f_{sn1}^{SP}]$ and $f_B \approx 43$ Hz $\in [f_{sn3}, f_{sn2}^{SP}]$ were noticed. Peaks located close to f_A are referred to as **peak A** henceforth. Peaks located close to f_B are referred to as **peak B** henceforth.

Frequency of peaks A and B was only slightly affected by change of the plenum volume. Nevertheless, their change in amplitude was much more interesting. In the LP case oscillations were dominated by peak A which had the amplitude of 3400 kPa at the outlet. In the SP case, the highest A peak was also noted at the outlet gauge, but it reached no more than 40 Pa. On the other hand, f_B peak was dominating in the SP case. It attained 370 Pa at the gauge p_{s-imp3} . This suggested, that the source of peak B was located in the diffuser or in the volute. In the LP case the highest peak B was observed at p_{s-out} , where it reached 140 Pa. However, a very similar value of 100 Pa was noted at the p_{s-imp3} . Bigger amplitude at the outlet may have been caused by the fact, that frequency f_B was very close to the 4-th harmonic frequency of very strong peak A. Therefore, it was possible that the amplitude of f_B at the outlet plenum could be amplified by the resonance with peak A.

Information about peaks f_A and f_B is summarized in table 2.7. It contains amplitudes of the peaks at p_{s-out} (peak A), p_{s-imp3} , p_{s-out} (peak A). In each case, amplitude at



(a) Small plenum volume



(b) Large plenum volume

FIGURE 2.44: Frequency spectra at p_{s-imp3} at the deep surge $TOA = 5\%$

p_{s-in} was also presented, due to the fact that it was the most distant location from both p_{s-out} and p_{s-imp3} . Ratios $\frac{p_{s-out}}{p_{s-in}}$ for peak f_A and $\frac{p_{s-imp3}}{p_{s-in}}$ for peak f_B were calculated in order to illustrate spatial influence of the phenomenon associated with given peak. In both cases the ratio calculated for f_A peak was lower than for f_B peak. This suggested, that the A peak was associated with phenomenon affecting the whole machine, while the B peak was most likely associated with local flow phenomenon. Table also contains the corresponding Helmholtz frequencies of the system calculated according to formulas introduced in section 2.2.4.3. It can be observed that frequencies f_A were located very close to the frequency of the Helmholtz resonator. This suggested that the A peak could be associated with pressure oscillations in the plenum which was acting as the Helmholtz resonator.

It can be observed that peak A frequencies presented in table 2.7 were slightly lower compared to corresponding Helmholtzian frequency. The possible reason of this lied in the fact, that the shape of the outlet pipe acting as the plenum was different from ideal shape of the Helmholtz resonator. Therefore, the air fluctuations in the plenum were disturbed by local flow structures such as swirl behind the elbow or stagnation zones in the volute. Therefore, the effective amount of oscillating air was smaller than the

TABLE 2.7: Surge amplitudes and frequency in SP and LP case

Small plenum ($V = 4.35 \cdot 10^{-2} \text{ m}^3$)			
		Experiment	Helmholtz resonator
Peak A	Frequency	14 Hz	17 Hz
	Amplitude p_{s-in}	23 Pa	
	Amplitude p_{s-out}	36 Pa	
	Ratio $\frac{p_{s-out}}{p_{s-in}}$	1.57	
Peak B	Frequency	41 Hz	—
	Amplitude p_{s-in}	61 Pa	
	Amplitude p_{s-imp3}	370 Pa	
	Amplitude p_{s-out}	280 Pa	
	Ratio $\frac{p_{s-imp3}}{p_{s-in}}$	6.07	
Large plenum ($V = 9.68 \cdot 10^{-2} \text{ m}^3$)			
		Experiment	Helmholtz resonator
Peak A	Frequency	11 Hz	12 Hz
	Amplitude p_{s-in}	1500 Pa	
	Amplitude p_{s-out}	3400 Pa	
	Ratio $\frac{p_{s-out}}{p_{s-in}}$	2.27	
Peak B	Frequency	44 Hz	—
	Amplitude p_{s-in}	29 Pa	
	Amplitude p_{s-imp3}	100 Pa	
	Amplitude p_{s-out}	140 Pa	
	Ratio $\frac{p_{s-imp3}}{p_{s-in}}$	3.45	

measured plenum volume.

Peak f_B represented frequency $\frac{f}{f_{rot}} = 0.4$. Location of p_{s-imp3} suggested that it may refer to the impeller rotating stall or the vaneless diffuser rotating stall. According to Fringe and Van den Braembussche [33] this frequency lied close to regions characteristic for the PIRS ($0.5 < \frac{f}{f_{rot}} < 0.8$) and AIRS ($0.2 < \frac{f}{f_{rot}} < 0.4$). This type of oscillations was also reported in another studies [69, 72, 89]. According to Fringe and Van den Braembussche the VDRS can be observed in the range $0 < \frac{f}{f_{rot}} < 0.2$. Izmaylov in his work [58] put this limit even lower $0 < \frac{f}{f_{rot}} < 0.1$. Therefore, if the observed oscillation was caused by the diffuser rotating stall, it contained more than one stall cell.

2.3 Summary

In presented study the blower was found to operate in four different regimes:

1. stable working regime - the amplitude of pressure oscillations was negligible with the exception of the region over the impeller blades. Frequency of pressure oscillation was either connected with frequencies characteristic for the machine ($f_{rot} = 100$ Hz or $f_{BP} = 2.3$ kHz) or formed very wide and low ridges with no relevance for machine stability.
2. inlet recirculation - observed in the rotor inlet zone and, to a smaller extent, at the blade mid-span. The spectral structure of the pressure signals did not reveal any dominating frequency, oscillations had a form of the broadband noise. The regime may be considered as stable from the viewpoint of the overall machine since the unstable structure had local character.
3. transient phase - noticeable flow oscillations without strong dominating frequency components. This structure was regarded as unstable since it affected the whole volume of the machine.
4. deep surge - very strong pressure oscillations appeared in the whole compressing system that induced vibrations of the blower and the system of pipes. The machine vibrations were clearly visible and accompanied by a large noise emission. During a single period of the oscillation there was a range of time, when flow reversed (depressurization). Deep surge was extremely dangerous for the machine.

All findings are grouped into three main areas of interest. First, the conclusions regarding the onset of unstable phenomena are presented:

- Pressure transducers located in the vicinity of the impeller inlet recorded the inlet recirculation in the form of recurrent pressure drops. This phenomenon appeared before instabilities in any other zone (section 2.2.3.1).
- The inlet recirculation was associated with an almost tenfold growth of the range of the static pressure variation and a significant increase of its average value (section 2.2.3.1).
- This structure was preserved over a wide range of throttle opening areas between 17% and 30% and as long as it was observed, the instabilities were not observed in another regions. Hence, the inlet recirculation can be regarded as dynamically stable from the point of view of global machine working conditions. However, due to the fact, that the inlet recirculation can be treated as the starting point for the flow structures which were globally unstable, this regime can be treated as the pre-surge indicator in the anti-surge systems (section ex:sec:recirculation).
- When the inlet recirculation decayed, another unstable structures appeared in the impeller. As the valve continued to close, the pressure fluctuations propagated towards the plenum (section 2.2.3.3).
- Spectral map showed no dominating frequency of the inlet recirculation, hence, this disturbance had a very complicated structure that may be chaotic. This fitted well

to the state of the art where the inlet recirculation was described as random pressure jumps caused by a torus-like recirculating structure [15, 20, 32, 51, 67, 84, 116] (section 2.2.3.2).

- It was observed that some frequencies characteristic for the unstable working conditions were present in the stable working regime in the form of widely dispersed ridges. This phenomenon agreed with fundamentals of the Greitzer theorem, that unstable structures may be also present in a damped form at conditions regarded as stable. This observation gives an opportunity of prediction of the deep surge frequency without entering unstable regime (section 2.2.3.2).

Conclusions regarding the influence of the plenum volume:

- The points of instabilities onset did not reveal dependency on the plenum volume. This applied to all unstable structures: the inlet recirculation, the transient phase and the deep surge (section 2.2.4).
- The range of pressure variation during the inlet recirculation, its onset and disappearance point were exactly the same in both examined cases of the plenum volume. This feature is of great importance for possible anti-surge schemes based on detection of this phenomenon. The character of the inlet recirculation did not depend on the outlet piping system, hence such an anti-surge scheme would be universal for all systems connected to the blower (section 2.2.4).
- A stronger surge pressure pulsation was detected in the case of the large plenum volume. The pulsation was found to have 3.5 times lower frequency and 5~8 times higher amplitude compared to the small plenum volume (section 2.2.4).
- In both cases the main surge frequency was located close to frequency of the Helmholtzian resonator. In both instances the Helmholtz formula overestimated the result (section 2.2.4.3).
- In the case of small plenum volume, the frequency of strongest pressure oscillation component was different from the one associated with the Helmholtz resonator. The highest oscillations were observed at the impeller outlet. Fluctuations in another zones were much weaker which suggested local reach of instability in this case (section 2.2.4.3).

Conclusions regarding the phase portraits:

- The stable working regime was represented on the phase space by an ellipsoid reflecting moderate oscillations around one point. Therefore, the system attractor was represented by a point. The oscillations were caused partly by signal noise and partly by minor local flow fluctuations (section 2.2.3.4).
- Analysis of the fluctuation of pressure derivatives allowed to introduce the RDF factor which had a form presented in equation 2.8. When factor exceeded defined threshold, the anti-surge scheme should be activated. The proposed value of the threshold RDF was equal to 3 (section 2.2.2.3).
- At the transient phase, the phase portrait transformed into elliptical disc which resulted in significant increment in the RDF (section 2.2.2.2).

-
- The *RDF* increment appeared much earlier at the gauge located in the rotor inlet zone and the rotor mid-span due to the inlet recirculation. Oscillations had linear character (section 2.2.2.2).
 - At deep surge, the phase portrait transformed into more complicated shape reflecting non-linear character of oscillations. At the inlet and the outlet gauges phase portrait had a form of limit cycle, while at the impeller gauges it had a shape of very wide ellipsoids. Compared to the transient phase the *RDF* increase was moderate. However the rate of pressure fluctuation increased significantly (section 2.2.2.2).
 - Comparison of phase portraits obtained in the dynamic and quasi-dynamic tests allowed to conclude that the transient phase initiated progressively resulted in much higher *RDF* (section 2.2.3.4).

Numerical study

3.1 Task description

3.1.1 Blower configuration

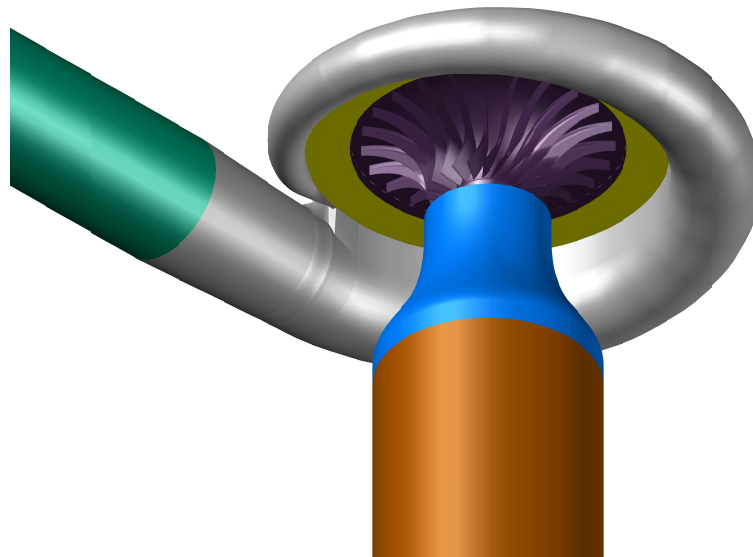


FIGURE 3.1: Geometry of the fluid domain. Impeller shroud was not included in the display

CAD model of the experimental test stand was developed on the basis of the documentation verified by on-site measurements. It consisted of several distinctive elements. Colours in parentheses correspond to figure 3.1.

- Inlet pipe (brown). The length of the pipe was set in such a way that the volume of the inlet pipe was equal to the outlet pipe volume. This was motivated by the fact, that equal volumes minimised the influence of the boundary conditions on air fluctuations at the deep surge.
- Witoszyński nozzle (blue). Its geometry corresponded to the element developed at the test stand design stage (see section 2.1).

- Blower impeller (violet). In this case the shroud shape was carefully examined at the test stand and some corrections with reference to previous numerical studies [80] were introduced. Figure 3.2(a) presents the numerical model of the impeller used in the study.
- Diffuser (yellow). Dimensions were taken from the documentation of previous experimental investigations of the machine by Magiera [80].
- Volute (grey). This part design was developed from cross-sections drawn based on the test stand documentation. Cross-sections presented in figure 3.2(b) were used to generate swept surface that created the volute model shown in figure 3.2(c).
- Outlet pipe (green). The outlet pipe consisted of two straight sections and the right-angle elbow. Dimensions were taken from on-site measurements. The position of the pipe outlet was analogous to the position of the valve at the experimental stand.

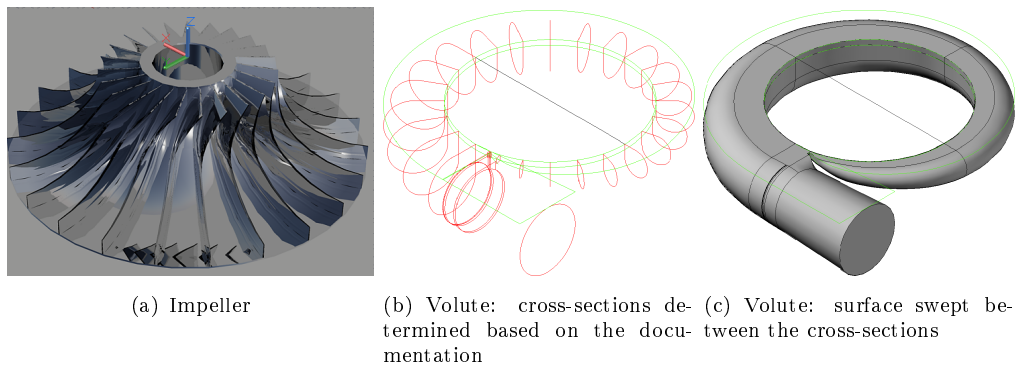


FIGURE 3.2: Selected elements of the CAD geometry of the experimental stand

3.1.2 Computational mesh

3.1.2.1 Mesh design criteria

Based on the initial calculations (performed in ANSYS CFX), Fluent user guide [4] and analytical calculations of y^+ [2], the following mesh criteria were specified in order to assure reaching stable solution and satisfactory level of convergence:

- Aspect Ratio ≤ 125
- Equiangular skewness ≥ 0.3
- Volume change ≤ 8
- Thickness of the first inflation layer = 0.2 mm (this value corresponded to y^+ in the range 20 – 40)
- Inflation layer expansion ratio = 1.25

where the first parameter refers to stretching of mesh elements, the second to their angular deformation, the third to changes of size of elements in contact, the fourth to

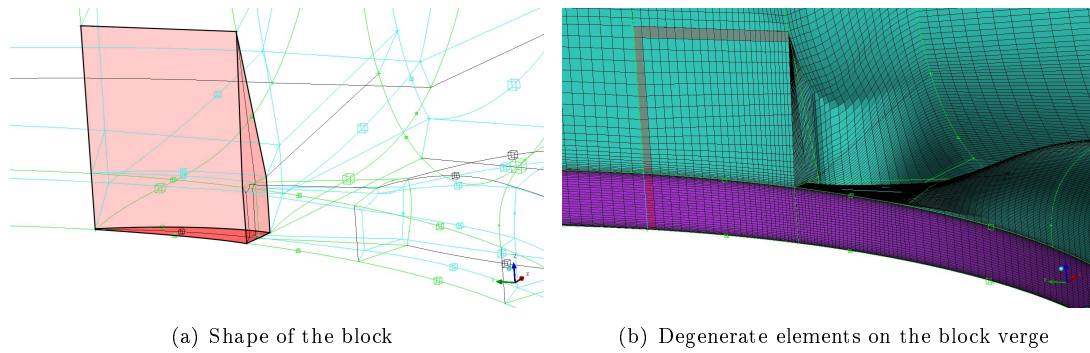


FIGURE 3.3: Wedge-shaped block resulting from the necessity of joining block vertices

thickness of the first elements at the wall and the last to the factor of growth of thickness of elements in the boundary layer. Precise definitions of aforementioned parameters can be found in numerous books devoted to Computational Fluid Dynamics [4, 126].

There were two exceptions, where mesh design criteria were loosen:

1. Region in the vicinity of the volute tongue, where the geometry forced use of a wedge-shaped block created by joining the vertices. Generation of structured grid for a volute was a real challenge. As a consequence, degenerate mesh elements appeared. However, much effort was undertaken to keep their number as small as possible, and to locate them further from the tongue, where pressure gradients were the highest. The wedge-shaped block is shown in figure 3.3(a) and degenerate elements are marked in figure 3.3(b).
2. Inlet and outlet pipe sections. Due to large volumes and lack of significant pressure gradients in the axial direction, the design parameters were reformulated in this region to:
 - Aspect Ratio ≤ 250
 - Equiangular skewness ≥ 0.3
 - Volume change ≤ 8
 - Thickness of the first inflation layer = 0.4 mm
 - Inflation layer expansion ratio = 1.25

The condition of higher thickness of the first inflation layer did not result in higher values of y^+ as the flow velocity within the pipes was much lower than in the impeller.

3.1.2.2 Description of the computational domain

Due to mesh generation procedure the system was divided into 3 domains: the inlet, the rotor and the outlet domains. Below, each of them is described shortly.

1. Inlet domain (figure 3.4) - included the straight pipe section 1000 mm long and Witoszyński nozzle. A mesh was generated in ICEM CFD.

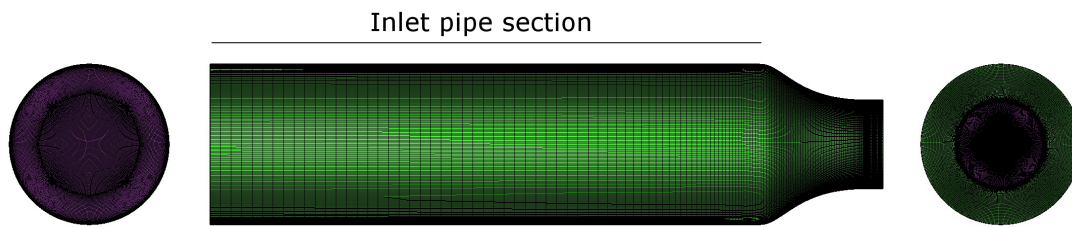


FIGURE 3.4: Inlet domain

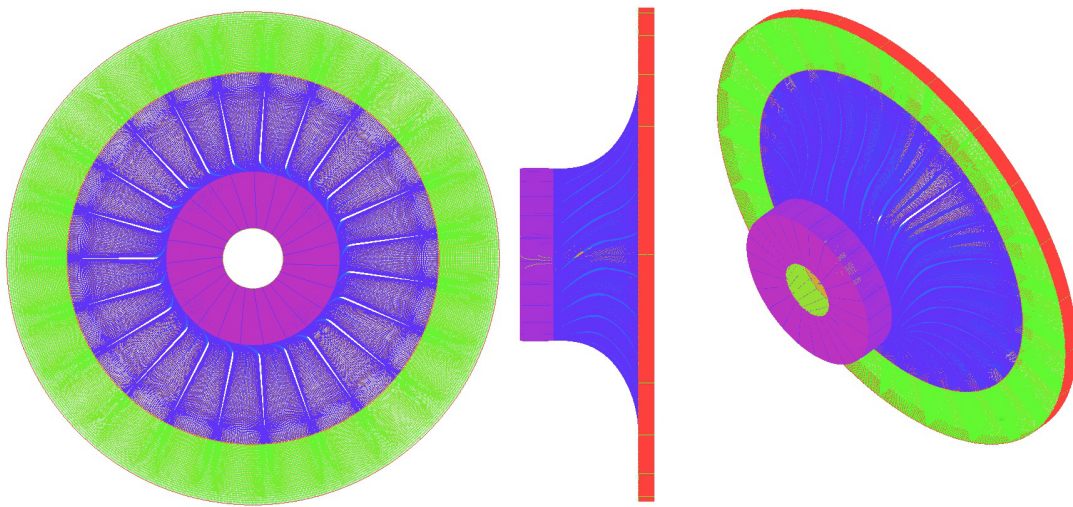


FIGURE 3.5: Rotor domain

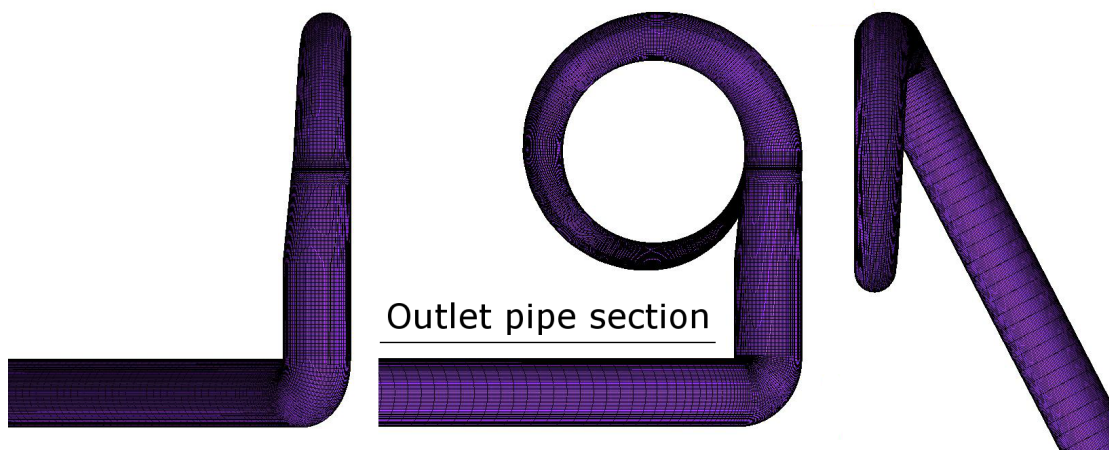


FIGURE 3.6: Outlet domain (not full outlet pipe section is shown)

2. Blower domain (figure 3.5) - included three sub-domains: the inblock (pink), the impeller passage (violet) and the diffuser (green). A mesh was generated in ANSYS Turbogrid for a single blade and was confined by periodic surfaces located in the middle of neighbouring blade passages. The mesh included a gap over the blade tip with adequate element size refinement. The complete rotor mesh was obtained as a multiplication of this mesh (23 copies of this grid rotated around Z axis by an appropriate angle).
3. Outlet domain (figure 3.6) - included the volute, the straight pipe section (250 mm), the right-angle elbow and the straight pipe section (3750 mm).

Application of ICEM CFD and ANSYS Turbogrid allowed to generate good quality hexagonal meshes (block structured) in the majority of elements. Generation of such grids was much more laborious than automatic generation of tetrahedral meshes. However, it allowed to take advantage of the hexagonal mesh stretching, due to the fact that it was aligned with the flow direction. Therefore, elements could be much longer in the flow direction in comparison to element size in the normal-to-wall direction due to smaller velocity gradients. Such a mesh is known to produce smaller numerical diffusion [4]. Hence, for the same number of elements hexahedral mesh can give higher precision solution.

All grids were combined in ICEM CFD into a single mesh containing all domains and exported into *.msh* format accepted by FLUENT. Table 3.1 presents mesh parameters attained at different domains and globally within the whole computational mesh. The size of computational grid used in this study was around 8 million elements. This was much more compared to mesh sizes used in another studies of surge in centrifugal compressors mentioned in section 1.6:

- T. Turunen-Saaresti and J. Larjola used 600000 elements [120].
- W. Huang et al. used 2000000 elements [54].
- R. Hunziker et al. used 350000 elements [55].

3.1.3 Simulation definition

All simulations were conducted in Ansys FLUENT 14.0. As the maximum Mach number for a given setting constituted $M_a = 0.33$ a choice of pressure-based coupled solver was justified. All simulations were conducted in a transient mode. Air was treated as an ideal gas, another parameters were specified explicitly (specific heat $C_p = 1006.43 \frac{\text{J}}{\text{kg}\cdot\text{K}}$, thermal conductivity $\lambda = 0.0242 \frac{\text{W}}{\text{m}\cdot\text{K}}$, viscosity $\mu = 1.7894 \cdot 10^{-5} \frac{\text{kg}}{\text{m}\cdot\text{s}}$, molecular mass $\hat{m} = 28.966 \frac{\text{kg}}{\text{kmol}}$). Aside from mass and momentum conservation equations the numerical model included energy transfer equations. Reynolds Averaged Navier Stokes (RANS) method was applied. Use of more advanced methods: Large Eddy Simulations (LES) or Detached Eddy Simulation (DES) was beyond the computational power available in the project. Therefore, RANS simulations with turbulent viscosity models were considered. Choice of turbulence model was preceded with study of 4 models presented in section 3.1.6. As a result of this analysis 2-equation realizable $k-\epsilon$ turbulence model was applied in form given by Shih et al. [109]. Default model constants were applied ($C_{1e} = 1.44$, $C_2 = 1.9$, $\sigma_k = 1.0$, $\sigma_\epsilon = 1.2$). Also the default pressure interpolation scheme formulated

TABLE 3.1: Parameters of the computational mesh used in this study

Inlet		
	inlet pipe section	elsewhere
Aspect ratio	250	125
Volume change	8	3.5
Skewness	0.5	0.5
Boundary Layer	0.4/1.25	0.2/1.25
y^+ average	13.6	14.7
y^+ max	226.8	226.8
Number of elements	529920	
Rotor		
Aspect Ratio	47	
Volume change	3.5	
Skewness	0.3	
Boundary Layer	$\approx 0.2/1.25$	
y^+ average	12.9	
y^+ max	239.4	
Number of elements	5884391	
Outlet		
	outlet pipe section	elsewhere
Aspect ratio	250	125
Volume change	8	2
Skewness	0.35	0.3
Boundary Layer	0.4/1.25	0.2/1.25
y^+ average	31.2	26.8
y^+ max	86.3	445.1
Number of elements	1546482	
Total		
	in & out pipe sections	elsewhere
Aspect ratio	250	125
Volume change	8	8
Skewness	0.3	0.3
Boundary Layer	0.4/1.25	0.2/1.25
y^+ average	23.2	21.9
y^+ max	226.8	445.1
Number of elements	7960793	

by Rhie and Chow [101] was used. This method is known to perform well if there are no sudden pressure jumps, momentum sources or high convection. Possible errors could be detected by presence of the normal velocity component at the walls, which was not observed in results. SIMPLE pressure-velocity coupling algorithm was used and resulted in satisfactory convergence. The default FLUENT convergence criteria were chosen, ie. 10^{-3} for scaled residuals except energy equation for which the convergence criterion was set to 10^{-6} . This choice is widely accepted standard applied by default in FLUENT. The convergence criteria were satisfied during the simulation. In each time step, residuals decreased by about three orders of magnitude.

Default FLUENT spatial discretization schemes were used:

- Density: second order upwind

- Momentum: second order upwind
- Turbulent kinetic energy: first order upwind
- Turbulent dissipation rate: first order upwind
- Energy: second order upwind

Application of the second order scheme for solution parameters was chosen to assure good quality of the solution. The only exception was done for turbulent kinetic energy and turbulent dissipation rate, where the first order discretization was applied. This method is satisfactory in most cases with exception of situation of large local fluctuations over single mesh elements. In presented case variations were mainly present in the boundary layer which was covered by the inflation layer that was very refined, hence this setting was applied. Gradients were computed by Least Squares Cell-Based method. This algorithm assumes linear variation of parameters between neighbouring cells which is multiplied by a matrix of weights computed for each cell depending on its geometrical relation to adjacent cells. This method is superior to cell-based gradient and produces results similar to node-based gradient. However, it requires less computational time than node-based gradient which made it a preferable choice [3].

The inlet and outlet domains were stationary in the global frame of reference. The rotor domain was rotating around z axis with angular velocity $\omega = 6000$ rpm and was connected with another domains by the sliding mesh interfaces. The time step t_s was adjusted in such a way, that n time steps were required for the rotation of the impeller by one blade passage. By setting $t_s = 4.4 \cdot 10^{-5}$ one obtains:

$$n = \frac{1}{f_{BP} \cdot t_s} = 9.88$$

which was satisfactory for modelling of local flow structures appearing in separate impeller channels. The number of iterations per time step was specified to 20 or smaller if the convergence criteria were attained earlier. The implicit time discretization was applied due to its known feature of unconditional stability with respect to the size of time step. This was important in analysed case, where element size range was varying to high extent.

3.1.3.1 Boundary Conditions

Figure 3.7 presents the computational domain with the main boundary conditions and the interfaces between three sub-domains listed in section 3.1.2.2. Special care was taken to make the boundary conditions as close to the test stand conditions as possible. At the test stand the machine operating conditions were determined for different positions of the throttling valve which generated resistance for fluid flow and, therefore, controlled the mass flow rate. This kind of conditions are usually reproduced in simulations by setting fixed mass flow rate at the inlet and pressure at the outlet or vice versa. Such combinations were proven to be a reliable reproduction of physical conditions at the stable machine operation range [4]. However, at unstable flow neither mass flow rate nor pressure are constant at the outlet and none of presented steady boundary conditions

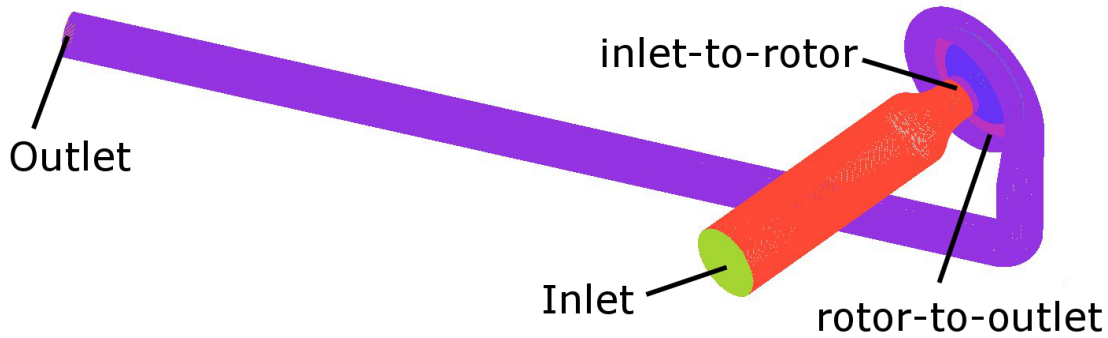


FIGURE 3.7: Computational domain used in the study with the main boundary conditions and interfaces outlined

would fully correspond to the real situation. On the other hand, specification of unsteady conditions would require detailed data which could not be gathered by available equipment at the test stand under study. Therefore, in order to limit the discrepancy with test stand, large inlet and outlet volumes were included in computational domains. In presented study a combination of the inlet mass flow rate and the outlet pressure was chosen. It was possible to use the option 'target mass flow rate' at the outlet, however, its application would require much bigger number of iterations per time step and therefore, was not efficient in practice. Results showed that in spite of small quantitative differences with the experiment, simulation provided a good solution of unstable phenomena at low mass flow rates. Details are presented in section 3.2.

In this section each boundary condition is described one by one (names of the conditions as in FLUENT):

Mass-flow Inlet The boundary condition **mass-flow-inlet** specified the global value of the mass flow rate at the inlet. Details of the boundary condition were as follows:

- Mass flow rate $\in [0.1, 0.3, 0.5, 0.8, 1.0, 1.2] \frac{\text{kg}}{\text{s}}$;
- Initial value of pressure 101325 Pa;
- Flow direction normal to the boundary;
- Total temperature 300 K;
- Turbulence specification method: Intensity and Hydraulic Diameter;
 - Intensity 1%;
 - Hydraulic diameter 0.3 m.

The machine operating point was set by the value of mass flow rate. The turbulence intensity at the inlet was determined on the basis of the following formula [4]:

$$I \approx \frac{u'}{u_{avg}} = 0.16(Re)^{-\frac{1}{8}}$$

where u_{avg} is the average flow velocity and u' is the velocity fluctuation. The length scale was given by the empirical formula, which can be approximated by the pipe diameter D :

$$\mathcal{L} = 0.07 D$$

At the experimental stand the inlet pipe was much longer than the length of inlet domain. Therefore, it was assumed, that the velocity profile at the inlet boundary condition location was fully developed. The factor of 0.07 was based on the maximum value of mixing length in a fully-developed turbulent pipe flow. Based on that, FLUENT approximated the values of turbulent kinetic energy k and turbulent dissipation rate ϵ at the boundary in the following manner:

$$k = \frac{3}{2}(u_{avg}I)^2$$

$$\epsilon = C_\mu^{\frac{3}{4}} \frac{k^{\frac{3}{2}}}{\mathcal{L}}$$

C_μ was the empirical parameter characteristic for the turbulence model (in this case 0.09).

The boundary condition fixed the total mass flow rate at the inlet, however, it was important to know whether the velocity profile was also reproduced in the simulation. Figure 3.8 presents velocity profile at the control surface, where experimental velocity profile was measured (see section 2.1.1.1), which was about 750 mm downstream of the inlet to the computational domain. Both profiles corresponded to $\dot{m} = 0.8 \frac{\text{kg}}{\text{s}}$. One can observe that the profiles obtained in both methods were reasonably close, which confirmed that the flow in the inlet pipe was a good representation of flow conditions present at the test stand.

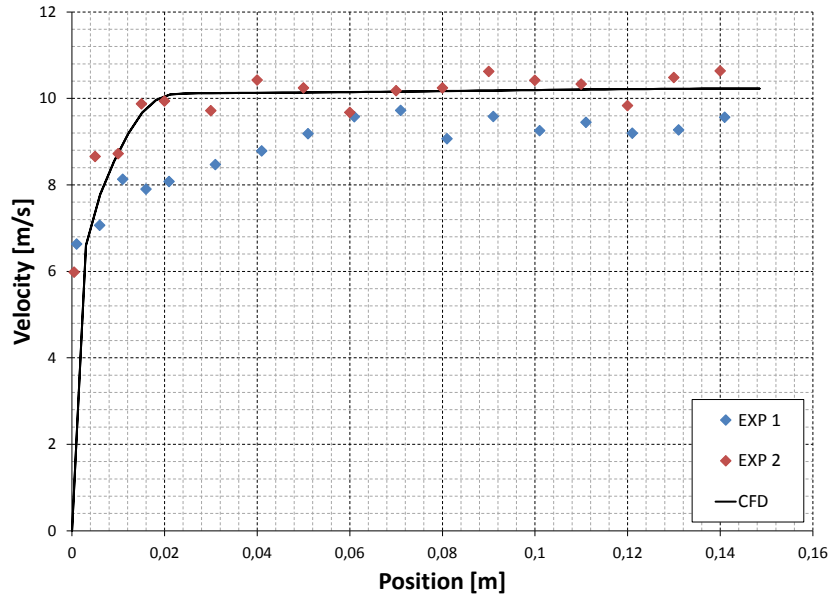


FIGURE 3.8: Comparison of velocity profiles obtained in the simulation and in the experiment at the pipe cross-section containing gauges p_{s-in} , p_{t-in1} and p_{t-in2} ($\dot{m} = 0.8 \frac{\text{kg}}{\text{s}}$)

Pressure Outlet The boundary condition **outlet-vent** specified the average value of pressure at the outlet surface. It did not constrain the value of mass flow rate. Therefore, in this condition, the reverse flow was allowed. The value of pressure at the outlet was set based on the experimental performance curve. Details of the outlet boundary condition are listed below:

- Gauge pressure was determined from the empirical formula obtained during the experimental part of study (with pressure in Pa and mass flow rate in $\frac{\text{kg}}{\text{s}}$):

$$p_{out} = (-11170\dot{m}^2 \frac{\text{s}^2}{\text{kg}^2} + 11764\dot{m} \frac{\text{s}}{\text{kg}} + 105652) \text{ Pa} \quad (3.1)$$

The derivation of the formula is provided below.

- Flow direction normal to the boundary;
- Total temperature 300 K;
- Turbulence specification method: Intensity and Hydraulic Diameter;
 - Intensity 1%;
 - Hydraulic diameter 0.16 m.

Turbulence intensity was calculated in the same manner as at the inlet.

Figure 2.13 in section 2.2.1 presented the compressor performance curve obtained in the experiment which was approximated by the equation:

$$\frac{p_{out}}{p_{in}} = (-0.092131\dot{m}^2 \frac{\text{s}^2}{\text{kg}^2} + 0.11613\dot{m} \frac{\text{s}}{\text{kg}} + 1.0427) \quad (3.2)$$

However, the outlet control point in the experiment was located at the volute outlet which was much before the outlet boundary condition in the computational domain. Pressure at this cross-section was smaller due to [127]:

- friction pressure losses at both pipe segments (Darcy–Weisbach equation) $\Delta p_f = \lambda \frac{l}{D} \frac{\rho u^2}{2}$;
- pressure loss at the pipe elbow $\Delta p_e = \zeta \frac{\rho u^2}{2}$;

where λ is friction factor that can be obtained from Moody chart [21]. In the examined case it was assumed that in the range of Re attained in the study, friction factor was constant and equal to $\lambda = 0.018$. Therefore Darcy-Weisbach equation yielded:

$$\Delta p_f = 891 \cdot \dot{m}^2 \frac{\text{Pa}}{\frac{\text{kg}^2}{\text{s}^2}}$$

The ζ parameter for the right angle elbow equals to 0.7 [21]. This allowed to estimate the value of losses in the elbow:

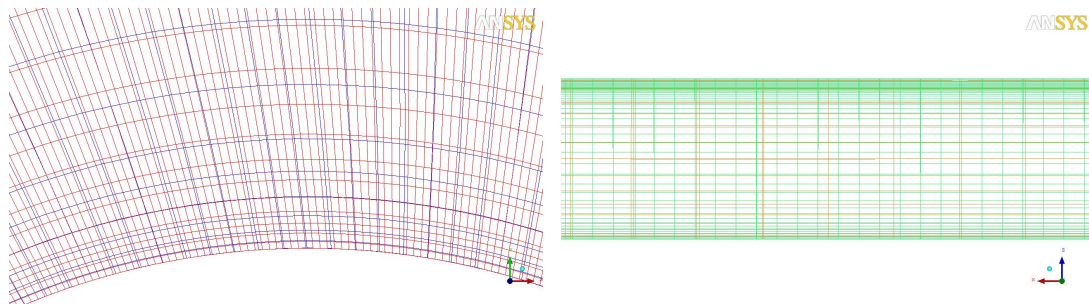
$$\Delta p_e = 947 \cdot \dot{m}^2 \frac{\text{Pa}}{\frac{\text{kg}^2}{\text{s}^2}}$$

Both estimates depended on the second power of mass flow rate. After subtracting losses from the experimental performance curve described by equation 3.2 and assuming that $p_{in} = p_{atm} = 101325$ Pa equation 3.1 was obtained.

Walls The boundary condition **wall** was defined at all other locations:

- Non-slip;
- Adiabatic;
- Smooth;
- Wall motion defined in the absolute frame of reference:
 - Zero (inlet domain, outlet domain, diffuser walls, impeller shroud);
 - f_{rot} (impeller hub, impeller blades)

Mesh interfaces Four interfaces were defined in the simulation. Two of them were defined as sliding mesh interfaces between the rotor and another domains. Two other interfaces were defined in places where geometrical constraints made creation of continuous mesh impossible.

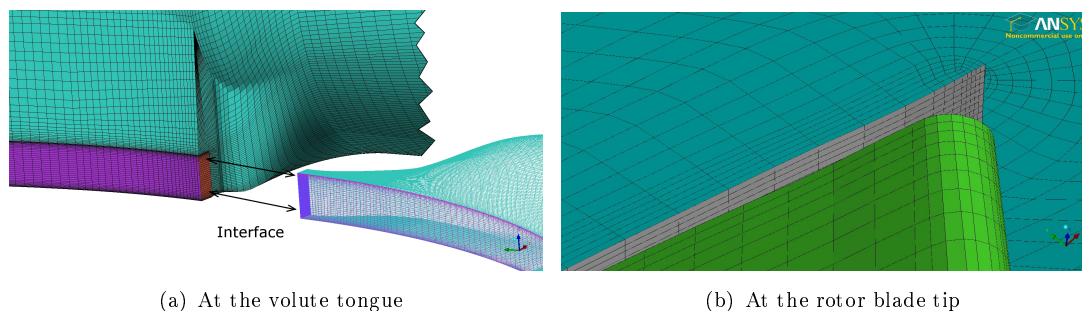


(a) Sliding mesh interface between the inlet and the rotor domains (b) Sliding mesh interface between the rotor and the outlet domains

FIGURE 3.9: Interfaces defined in the study between two domains

Figure 3.9(a) presents the surface elements at both sides of the interface between the inlet and the rotor domains at the hub boundary layer region. Due to rotational motion of the rotor domain this interface was defined as sliding mesh interface. The element size in the rotor domain was smaller due to mesh refinement associated with the blade boundary layers. Much care was taken to keep ratio of element sizes at both sides of the interface not bigger than 3 to limit interpolation errors. In tangential direction, the difference was equal to 3, while in the radial direction, it was possible to keep it smaller than 3. The only exception was the shroud boundary layer, where due to mesh refinement at the blade tip clearance the difference was bigger.

Figure 3.9(b) presents both grids at the sliding mesh interface between the rotor and the outlet domains (diffuser and volute). The ratio of the tangential dimension at both sides of the interface was equal to 3 along the whole circumference. Along height it equalled 2 at the hub and around 4 at the shroud. As previously, bigger difference in this region was caused by the mesh refinement in the blade tip clearance.



(a) At the volute tongue

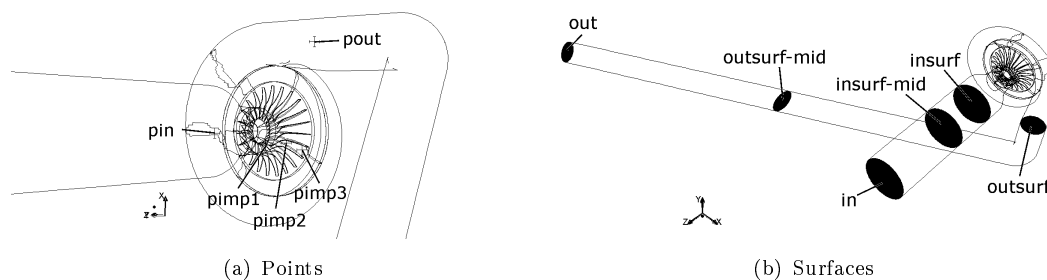
(b) At the rotor blade tip

FIGURE 3.10: Interfaces defined in the study in particular domains

Another two interfaces were created due to difficulties in construction of continuous grids in regions of complex geometry. The volute mesh interface is presented in figure 3.10(a). The region of the tongue was the most difficult for meshing. In fact it was impossible to create a continuous hexahedral mesh that fitted to such a geometry. This was caused by a fact, that due to structural mesh arrangement the same number of elements was maintained along the contracting cross-section of the volute. Therefore, the average element size decreased noticeably and the use of the interface became inevitable. Another region, where the use of the interface was applied was the tip shroud clearance presented in figure 3.10(b). This approach is a predefined method in Turbogrid [5].

3.1.4 Solver monitoring

About half of the computations were conducted in Archie-West supercomputer centre. Each node contained Dual Intel Xeon X5650 2.66 GHz units with 6 cores (detailed specification can be found in [1]). Each computation was conducted on 2 nodes, i.e. on 12 cores. Total recorded CPU usage reached 57470 CPU. Another part of the computations was done on local machines available at the Strathclyde University and Lodz University of Technology. Therefore, the total computational time for the project can be estimated to 120000 CPU hours. Such a substantial number resulted from the fact, that each simulation required many iterations to reach stability. It was caused by the fact, that the domain size was big and included large volumes of the inlet and the outlet pipe. The pressure waves needed certain amount of time steps to reflect several times from boundaries and damp the fluctuations out.



(a) Points

(b) Surfaces

FIGURE 3.11: Positions and labels of the monitoring points and surfaces

During the simulation, pressure and mass flow rate signals were monitored at several control points and surfaces. Positions of the points was analogous to the positions of the

pressure tappings in the experimental study (see figure 3.11(a)). Additionally, a set of control surfaces was used to monitor the mass flow averaged values of the parameters. Figure 3.11(b) presents the control surfaces and their labels. At the moment when the monitors reflected that the dynamic stability of the task was considered to be reached, the final result was specified as the average from last four rotations of the impeller. Figure 3.12(a) presents pressure in the last 4 rotations for one of simulations together with the average value which was treated as the final result (p-insurf-fin). Figure 3.12(b) presents mass flow rate in the last 4 rotations determined for the same simulation at all control surfaces. The final (m-fin) result was calculated from the average of all signals with exception of the inlet surface, where it was fixed by the boundary condition. In the case of mass flow rates smaller than $0.5 \frac{\text{kg}}{\text{s}}$ the interval corresponding to 20 rotations was used for calculation of the final results due to much longer period of the fluctuations.

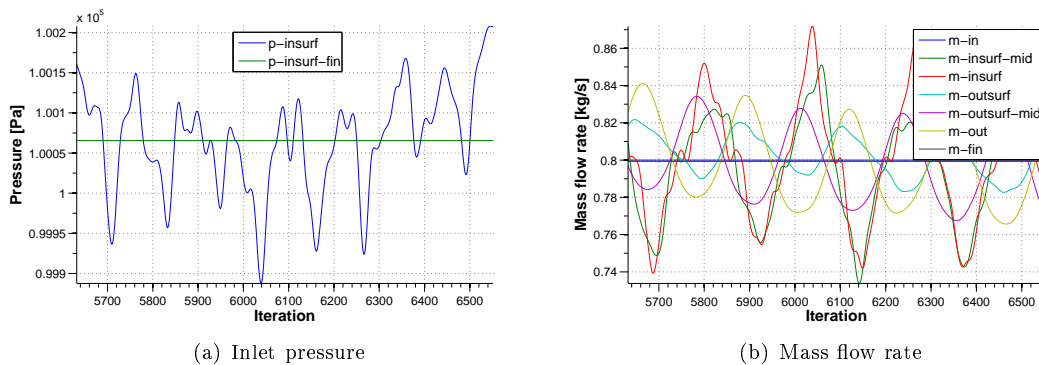


FIGURE 3.12: Example of the simulation final result establishment

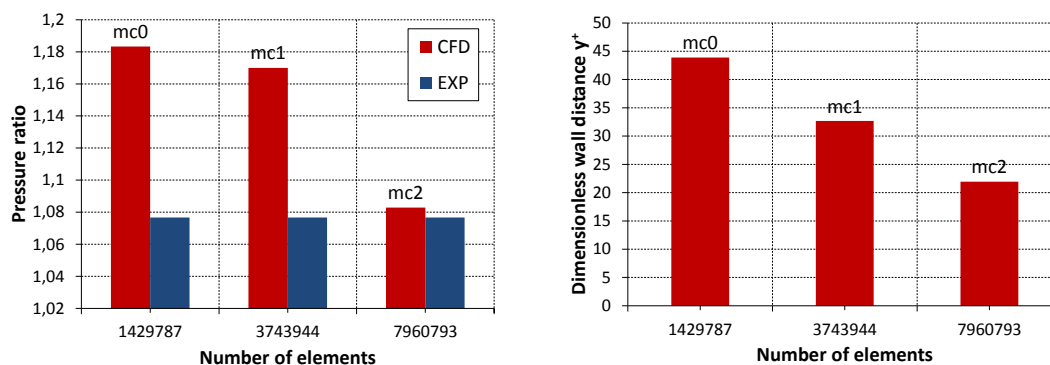
3.1.5 Mesh size study

TABLE 3.2: Meshes used in the mesh size study

Label	Size change factor	Timestep	Number of elements
<i>mc0</i>	1	$8.8 \cdot 10^{-5}$ s	1429787
<i>mc1</i>	1.5	$6.6 \cdot 10^{-5}$ s	3743944
<i>mc2</i>	2	$4.4 \cdot 10^{-5}$ s	7960793
<i>mc3</i>	2.5	$3.5 \cdot 10^{-5}$ s	17586215

This section shortly describes the procedure that was undertaken to justify the choice of the mesh size applied in the study. Table 3.2 presents the list of meshes applied in the mesh size study. Grids labelled as *mc0* – *mc3* were obtained by successive decrement of element sizes in each direction by the factors 1.5, 2, 2.5 starting from the base mesh *mc0*. The physical time step was decreased by the same value as the size change factor. It can be observed, that in each case the number of elements between consecutive meshes changed more than twice. Comparison was done for the mass flow rate $\dot{m} = 0.8 \frac{\text{kg}}{\text{s}}$, i.e. close to the design conditions. The pressure ratio was treated as the output parameter and was monitored during the simulation. At the moment of sufficient stabilization, the average from 20 rotations was treated as the final result. The main problem came from the fact that interpolation of solutions between meshes *mc0* - *mc3* was not possible.

Usually, to decrease the computational cost, simulation is first conducted on the smallest mesh and then the final result is interpolated as initial condition for computations conducted on finer grid. However, each solution initialized from interpolated flow field resulted in solver divergence and floating point exception. This brought the necessity of use of the automatic initialization at each mesh. This method was connected with substantial increase of time required by the solution to stabilize. In the case of the biggest mesh - *mc3*, it was estimated that the number of CPU hours needed for stabilisation could have exceeded 12000. This caused that mesh *mc3* was excluded from this study. After the initial part of the solution it exhibited very similar results to *mc2*.



(a) Pressure ratio compared to the experimental result (b) Average values of the dimensionless wall distance

FIGURE 3.13: Results of the mesh size study conducted close to the design conditions ($\dot{m} = 0.8 \frac{\text{kg}}{\text{s}}$)

Figure 3.13(a) presents result of the mesh size study compared to the value of the pressure ratio obtained from the experimental performance curve presented in figure 2.13. As expected, coarser meshes resulted in significant over-prediction of the pressure ratio generated by the blower. Surprisingly, difference in the output between *mc0* and *mc1* was quite low and both values were over-predicting the pressure ratio by a large factor of around 10% (*mc0*) and around 8% (*mc1*). However, further refinement to *mc2* provided substantial reduction in the output and the over-prediction decreased to the value smaller than 1%. This showed that the refinement between *mc1* and *mc2* was crucial for physical model of losses which were under-estimated on coarser meshes. Considering very long period of computations for *mc3*, *mc2* appeared to be a good compromise between the quality and the computational cost.

The tendency of *RANS* simulations to over-predict the machine performance is a well known phenomenon and was observed in various simulations of turbomachines [63]. This is coming from the fact, that *RANS* equations incorporate the time-averaged velocity component \bar{u} which means that small local fluctuations are not simulated. In fact, this problem cannot be removed completely and mesh refinement could only reduce its range by improving the turbulence modelling, prediction of the boundary layer and its point of separation. Small error in pressure ratio could be believed to result from a sum of small local effects which did not affect the global character of the flow. However, the change from *mc1* to *mc2* resulted in very significant difference of the generated pressure head. This suggested some change of the global character of the flow. However, at this point there was not much room for improvement and it was expected that further refinements would not have such a big influence on the overall machine performance.

Another factor, which was considered during choice of the mesh refinement level was the y^+ parameter. Figure 3.13(b) presents the average values of y^+ obtained for examined

grids. As expected, the trend observed followed the relations of the dimension change factor, since the ratios between y^+ for consecutive meshes were close to 1.5. Following this trend, the value of y^+ at *mc3* would be close to 16. Both values: 22 and 16 were lying outside of the viscous sub layer in a region known as the Log-law layer [126] and there would be no significant difference from the point of view of the quality of the solution of the boundary layer. In fact, the FLUENT user guide [4] recommends that 'each wall-adjacent cell's centroid should be located within the log-law layer, $30 < y^+ < 300$. A y^+ value close to the lower bound $y^+ = 30$ is most desirable'. The mesh *mc2* fulfilled this recommendation very well since y^+ was close or even smaller than $y^+ = 30$ at most locations. The highest values did not exceed the value of $y^+ = 300$ with the only exception of the surface at the volute tongue. However, this region was in the separation bubble and no regular boundary layer was formed therein. This was another argument confirming, that further refinement of the *mc2* would not bring benefits proportional to increment of the computational time.

3.1.6 Turbulence model study

TABLE 3.3: Models of turbulence used in the study

Model name	Remarks
Realizable $k-\epsilon$	Standard wall function
Realizable $k-\epsilon$	Enhanced wall function
$k-\omega$	Standard version
$k-\omega$	SST

This section summarizes the procedure that was conducted in order to choose the most adequate turbulence model which close the set of *RANS* equations. Table 3.3 presents the list of analysed models. Each of them was represented by set of two equations. Due to the fact, that all models resulted in similar outputs under nominal working conditions, the test was conducted for two another values of the mass flow rate $\dot{m} = 1.0 \frac{\text{kg}}{\text{s}}$ and $\dot{m} = 1.2 \frac{\text{kg}}{\text{s}}$ in order to approximate the performance curve.

The most obvious choice for the model was the $k-\epsilon$ one, since it was used in all previous studies of the surge in centrifugal impeller [54, 55, 120]. Model formulation proposed by Shih et al. [109], named in FLUENT as the realizable $k-\epsilon$, was applied. This model is known to perform well in the case of flow in rotating channels and backward recirculating flows. This well implied to the conditions met in unstable range of the blower operation. One has to take into account that, as it was described above, for attained range of y^+ the boundary layer was not fully resolved and the wall function was applied. This approach is valid for well attached flow. In the case of separated flows it could be a source of error or at least uncertainty. Separation regions can be over or under predicted depends on the turbulence models and local flow conditions. Unfortunately, full solution of the boundary layer ($y^+ < 1$) was far beyond available computational resources.

The version of $k-\epsilon$ turbulence model with so-called enhanced wall treatment was also analysed. This model is recommended if y^+ values in the simulation correspond to the buffer region $3 < y^+ < 30$. Normally $k-\epsilon$ chooses appropriate wall function based on the value of y^+ . This can be a source of errors for meshes with values of y^+ oscillating in between $y^+ = 3$ and $y^+ = 30$. In this range neither the laminar sublayer profile nor the

turbulent Log-law wall function provides appropriate description. In the enhanced wall function approach the law-of-the wall function is described by the function suggested by Kader [64]:

$$\frac{u}{u_\tau} = e^\Gamma \left(\frac{u}{u_\tau} \right)_{lam} + e^{\frac{1}{\Gamma}} \left(\frac{u}{u_\tau} \right)_{turb}$$

where:

$$\Gamma = -\frac{a(y^+)^4}{1 + by^+}$$

Blending function smoothly shifts between two formulas:

$$\left(\frac{u}{u_\tau} \right)_{lam} = y^+ \left(1 + \frac{\alpha}{2} y^+ \right), \quad y^+ < 3$$

$$\left(\frac{u}{u_\tau} \right)_{turb} = \frac{1}{\kappa} \ln(y^+), \quad y^+ > 30$$

In above equations u stands for the velocity component parallel to the wall, u_τ - the shear velocity, y^+ - the dimensionless wall distance, κ - the von Karman constant, α - constant describing the influence of pressure gradients and $a = 0.01$, $b = 5$. Such a formulation assures asymptotic behaviour at $y^+ < 3$ and $y^+ > 30$, but also reasonable representation of the velocity profile inside the buffer region $3 < y^+ < 30$. Choice of this model was motivated by the fact, that the average value of y^+ for the mesh *mc2* was within the buffer region, and smooth transition between the laminar sublayer and the Log-law wall functions could improve the solution.

The third model was the standard formulation of the $k-\omega$ model proposed by Wilcox [128]. The difference between $k-\epsilon$ and $k-\omega$ lies in the fact, that instead of the transport equation for the dissipation rate (ϵ), the transport equation for the specific dissipation ($\omega = \frac{\epsilon}{k}$) was used [126]. Change of variables allows to exclude the problem of near-wall treatment as the $\omega \rightarrow \infty$ at the wall. In the case of free-stream flows ω attains values close to zero. In this condition, the eddy viscosity $\mu_t \sim \rho \frac{k}{\omega}$ becomes very sensitive to the specific dissipation. Therefore $k-\omega$ is known to perform worse in free stream flows than $k-\epsilon$.

The last analysed model was the SST $k-\omega$ model developed by Menter [85]. This is a hybrid model that combines $k-\omega$ model and $k-\epsilon$ after substitution $\epsilon = \omega k$. After such a transformation, the obtained ω equation contains additional element known as cross-diffusion term. Both models are multiplied by a blending function $0 \leq F \leq 1$ and added together. The blending function is designed to be equal to one in the near-wall region which activates the standard $k-\omega$ model and zero away from the surface which activates the transformed $k-\epsilon$ [3]. Some of the model constants are also blended between values used by default in $k-\epsilon$ and $k-\omega$. These modifications allow to merge known strong points of near-wall performance of $k-\omega$ and high accuracy of $k-\epsilon$ in far-field zones.

Figure 3.14 presents results of the pressure ratio obtained with the use of described turbulence models. One can observe that the over-prediction was present at all circumstances, which could be at least partially associated with the mesh size effects described in the previous section. In general, differences between values obtained from different models were smaller than the difference between them and the experimental investigation results. Difference between results of two versions of $k-\epsilon$ turbulence model were very small which could results from the fact that the mesh was not refined so much to take advantage of the enhanced wall treatment. Higher differences were observed for models which base on the $k-\omega$ equations. At $\dot{m} = 1.2 \frac{\text{kg}}{\text{s}}$ $k-\omega$ performed slightly better than $k-\epsilon$. $k-\omega$ in Menter variant provided solution lying between those two. $k-\epsilon$ with

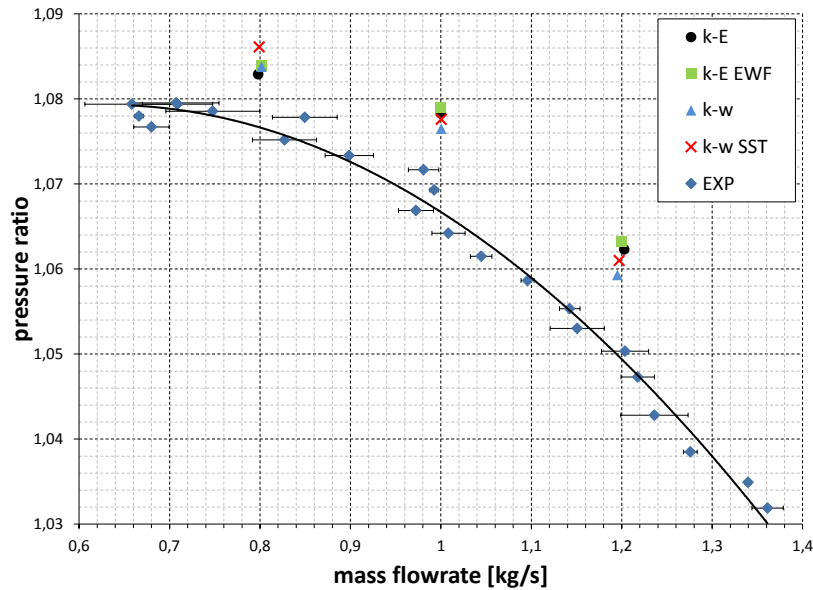


FIGURE 3.14: Results of the turbulence model study

wall enhanced function gave the highest over-prediction. At $\dot{m} = 1.0 \frac{\text{kg}}{\text{s}}$ the differences between data obtained from all models were the lowest. The lowest pressure ratio was obtained with $k-\omega$, then $k-\omega SST$ and $k-\epsilon$. The highest value was attained with $k-\epsilon$ with wall enhanced treatment. Situation changed at $\dot{m} = 0.8 \frac{\text{kg}}{\text{s}}$. At this mass flow rate, SST provided the highest pressure ratio. $k-\omega$ provided smaller output, which was very close to $k-\epsilon$ with enhanced wall function. Realizable $k-\epsilon$ gave the result which was the closest to the experimental curve.

All turbulence models provided similar results and all the differences could be considered as small from the point of view of the global parameter such as the pressure ratio of the simulated machine. The final choice of the realizable $k-\epsilon$ without wall enhanced treatment was motivated by the following arguments:

- This model gave results closer to the experimental performance curve at the point $\dot{m} = 0.8 \frac{\text{kg}}{\text{s}}$ which was the closest to the surge margin. At other points it behave reasonably well.
- This model, or very similar formulations of $k-\epsilon$, was applied in another papers considering surge phenomenon in the centrifugal impeller.
- This model has the lowest computational power requirements. All other models required more algebraic operations per iteration.

3.1.7 Method of comparison with the experimental data

Comparison of signals was conducted in several ways including: the performance curve, frequency spectra, phase portraits and source signals. In each method comparison required certain actions or signal pre-processing. This section briefly describes methods applied in this study.

3.1.7.1 Pressure signals

Figure 2.12 shows relation between the mass flow rate and the throttle opening area (named as TOA therein) that was obtained in the experiment. This curve is presented again in figure 3.15 which indicates the values of mass flow rates used in the numerical part of this study and their corresponding values of TOA . Marked points correspond to all cases that were included in the numerical study. At $\dot{m} = 0.1 \frac{\text{kg}}{\text{s}}$ the experimental signal was taken from $TOA = 5\%$ case, which was the smallest value at which the measurements were conducted.

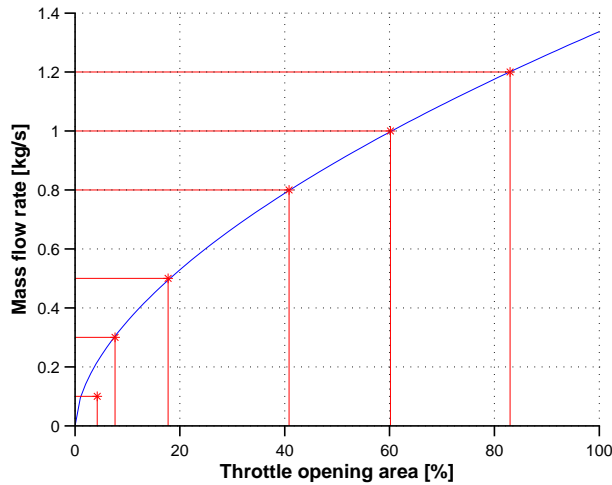


FIGURE 3.15: TOA values in quasi dynamic analysis that were chosen for comparison with the mass flow rate applied in the simulation

Comparison of the pressure signals presented in section 3.3 concerned the control points p_{s-in} , p_{s-out} , p_{s-imp1} , p_{s-imp2} and p_{s-imp3} . The only exception is presented in section 3.2.1, where pressure ratio was computed based on the mass flow averaged pressures attained at the surfaces *insurf* and *outsurf*. As presented in figure 3.11(b), these surfaces were positioned exactly at the cross-sections containing the points p_{s-in} (*insurf*) and p_{s-out} (*outsurf*).

3.1.7.2 Pressure spectra

According to section 2.1.1.3 in the experimental quasi-dynamic procedure each signal contained $2^{21} = 2097152$ samples gathered with a frequency of $f_{EXP} = 100$ kHz. This implied an effective frequency band equal to 0.05 Hz – 50 kHz with resolution of 0.05 Hz. The time step applied in the simulation equalled to $T_{CFD} = 44 \mu\text{s}$. Therefore the sampling frequency was equal to $f_{CFD} = 22.7$ kHz. The number of samples used to generate the numerical frequency spectrum was equal to 2900 (150000 at the deep surge). This implied an effective frequency band 7.8 Hz – 11.4 kHz with resolution of 7.8 Hz (1.5 Hz – 11.4 kHz with resolution of 1.5 Hz at the deep surge).

Presented spectra can be distorted by the phenomenon known as the Spectral leakage [45, 53]. It appears if the signal contains a fractional number of periods of any signal harmonics. As a result the amplitudes of these harmonics are blurred in the spectrum graph and surrounded by smaller false peaks. The phenomenon becomes less significant

if the signal contains many periods of the signal harmonic. Length of the experimental signal was equal to 20.97 s, while the length of the numerical signal was much smaller: 0.13 s (0.66 s at the deep surge). This caused that both spectra were affected by the spectral leakage at different rate and comparison of both signals was difficult. Therefore, for the sake of clarity the experimental signal was cut to length of the numerical signal before applying the FFT analysis to both of them. Figure 3.16 presents spectrum of the same experimental signal before and after trimming into proper length. One can observe, that the spectrum obtained from shorter signal was affected by stronger noise as a result of the spectral leakage. Also, the peaks at lower frequency were represented with smaller accuracy which was caused by smaller resolution. However, the shorter version of signal represented the level of accuracy of the frequency spectrum obtained from the simulation signal and was, therefore, more suitable for comprehensive comparison.

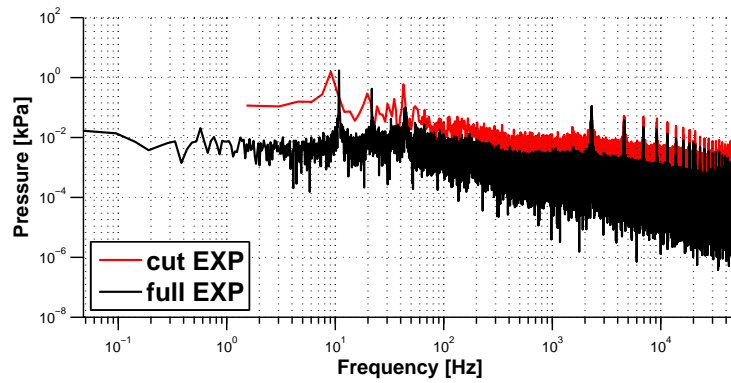


FIGURE 3.16: Frequency spectra obtained from full experimental signal ($2^{21} = 2097152$ samples) and experimental signal after trimming (65995 samples)

3.1.7.3 Representation of signals in the phase space

In order to assure the same signal processing before plotting the phase portrait, the Gaussian filter was applied to signals obtained in simulation similarly to how it was done in the experimental case. As mentioned in section 2.2.3.4, the value of σ for the Gaussian filter used in the experiment was equal to $\sigma_{EXP} = 50$ samples. The difference in sampling periods between the experiment and the simulation was $\frac{T_{CFD}}{T_{EXP}} = \frac{4.4 \cdot 10^{-5}}{10^{-5}} = 4.4$. Therefore, the value of $\sigma_{CFD} = 11.36$ provided the same time-window of the filter ($\sigma_{CFD} \cdot T_{CFD}$) as in the experimental case ($\sigma_{EXP} \cdot T_{EXP}$).

3.2 Results

3.2.1 Blower performance curve

Some of the operating points were already presented during the mesh size and turbulence model studies in sections 3.1.5 and 3.1.6. However, the analysis of unstable phenomena included three other mass flow rates $\dot{m} = 0.5 \frac{\text{kg}}{\text{s}}$, $\dot{m} = 0.3 \frac{\text{kg}}{\text{s}}$ and $\dot{m} = 0.1 \frac{\text{kg}}{\text{s}}$. Figure 3.17 presents a full set of the operational points. The performance curve obtained in the simulation lied above the experimental curve. Section 3.1.5 showed that the potential

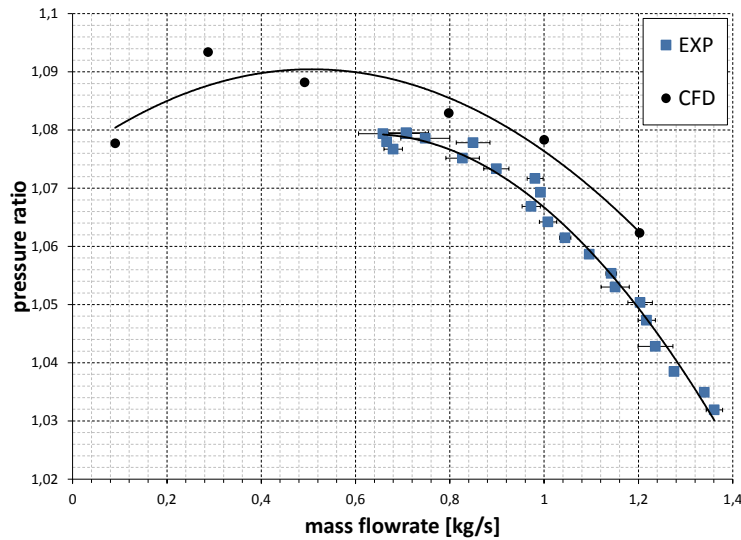


FIGURE 3.17: Compressor performance curve $PR(\dot{m})$ obtained in the experiment and the numerical study

reason of this tendency originated from the mesh refinement, however it could be also influenced by another factors, such as: geometrical simplifications, boundary conditions, turbulence modelling, assumed air parameters or solver settings. Nevertheless, the shape of the curve under stable working conditions was reproduced very well and simulation approximated the machine performance quite well. Figure 3.18 presents non-dimensional performance curve.

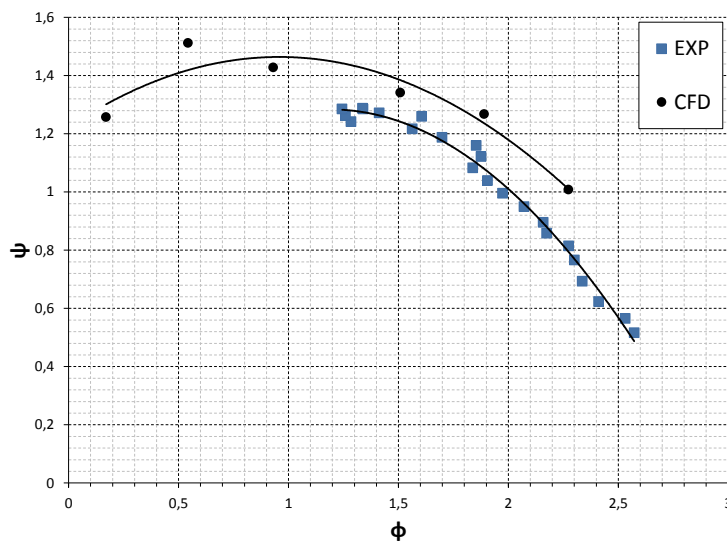


FIGURE 3.18: Compressor performance curve $\psi(\phi)$ obtained in the experiment and the numerical study

Figure 3.19 demonstrates the trajectories of the operational points drawn on the basis of the values of mass flow rate and pressure ratio at the successive time steps of each simulation. The mass flow rate at the inlet was set by the boundary conditions and remained constant. Presented mass flow variations were taken from the rotor inlet. At

$\dot{m} = 1.2 \frac{\text{kg}}{\text{s}}$ the operating point fluctuated slightly around the average. Since the range of fluctuations was limited, the global machine working conditions were fully stable. At $\dot{m} = 1.0 \frac{\text{kg}}{\text{s}}$ the rate of fluctuation was similar or even smaller. At $\dot{m} = 0.8 \frac{\text{kg}}{\text{s}}$ it raised, indicating slight instabilities. Below $\dot{m} = 0.6 \frac{\text{kg}}{\text{s}}$ experimental measurements were not possible due pressure fluctuations. Also in the simulations all points at these mass flow rates were affected by large fluctuations. At $\dot{m} = 0.5 \frac{\text{kg}}{\text{s}}$ and $\dot{m} = 0.3 \frac{\text{kg}}{\text{s}}$ the pressure ratios and the mass flow rates started to oscillate to much higher extent and these conditions cannot be regarded as fully stable. This region was named as the pre-surge stage. It revealed several similarities to the intermediate state and the inlet recirculation identified in the experimental part of the study. At $\dot{m} = 0.1 \frac{\text{kg}}{\text{s}}$ the operating point started to move along the closed limit cycle. It can be noticed that during certain moment of the cycle the flow attained negative mass flow rate, which allowed to claim that observed phenomenon fulfilled the definition of the deep surge [98]. Table 3.4 presents the postulated working regimes observed in simulations. Section 3.3 contains more detailed comparison of the numerical and the experimental results.

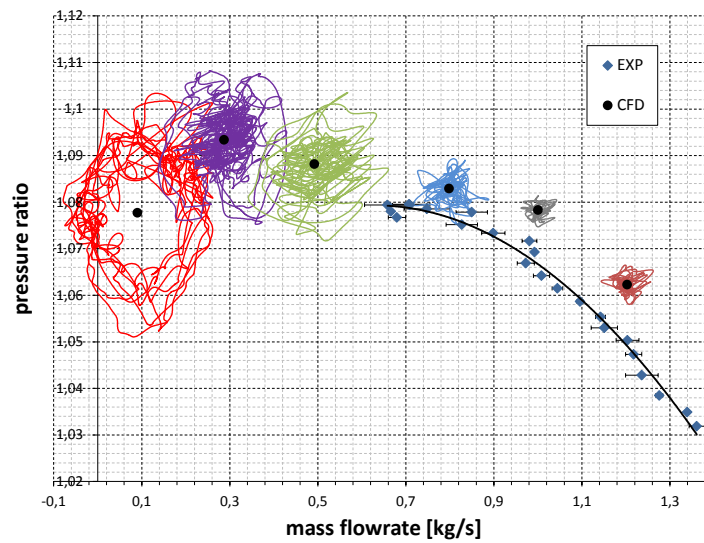


FIGURE 3.19: Operational point traces obtained in the simulation compared to the experimental performance curve

TABLE 3.4: Working regimes identified during the simulations

mass flow rate physical $\left[\frac{\text{kg}}{\text{s}} \right]$	throttling coefficient	Stability	Name	
$\dot{m} = 0.1$	$\phi = 0.19$	$TOA \approx 5\%$	unstable	Deep surge
$\dot{m} = 0.3$	$\phi = 0.57$	$TOA \approx 8\%$	unstable	Pre-surge
$\dot{m} = 0.5$	$\phi = 0.95$	$TOA \approx 18\%$	unstable	Pre-surge
$\dot{m} \geq 0.8$	$\phi \geq 0.51$	$TOA \geq 41\%$	stable	Stable work

3.2.2 Representation of the flow structures - stable working conditions and pre-surge

This section is devoted to description of flow structures observed in the study. Numerical simulations provided a large amount of data that allowed to extract values of flow parameters in any point within domain. Therefore, it was crucial to post-process the data in a way allowing comprehensive study. The method of flow visualization was specified individually for each phenomenon depending on its character. First, the overview on flow structure observed at all mass flow rates is presented. Section 3.2.2.2 is devoted to flow instabilities observed at $\dot{m} = 0.5 \frac{\text{kg}}{\text{s}}$. Section 3.2.2.3 is devoted to the phenomenon of the inlet recirculation present at $\dot{m} = 0.3 \frac{\text{kg}}{\text{s}}$. Section 3.2.3 provides a step-by-step description of consecutive phases of the deep surge cycle observed at $\dot{m} = 0.1 \frac{\text{kg}}{\text{s}}$.

3.2.2.1 Overview of stable and pre-surge flow conditions

Figure 3.20 presents an overview on flow structures present at all examined cases with the exception of $\dot{m} = 0.1 \frac{\text{kg}}{\text{s}}$. This flow rate is analysed thoroughly in section 3.2.3. Each figure contains three different forms of visualization of the instantaneous flow conditions. Colour maps in the inlet presents the axial velocity component scaled with the legend located at the right hand side. Blue regions in the impeller correspond to regions, where velocity was smaller than $5 \frac{\text{m}}{\text{s}}$, which are referred to as **stagnation zones** henceforth. For the sake of clarity, the hub was presented in grey colour. Colour maps at the diffuser present the static pressure at mid-height scaled according to the legend located at the left hand side. Black streamlines represent the flow in global frame of reference projected on this surface. However, at lower flow rates the flow angle depended also on spanwise location of the control surface. This can be observed in figure 3.21 showing the circumferentially mass flow averaged velocity in the diffuser and figure 3.22 showing the circumferentially mass flow averaged diffuser flow angle. Pressure rise in the diffuser is presented in figure 3.23. Figure 3.24 presents the velocity distribution in the volute cross-section located opposite to the tongue.

At $\dot{m} = 1.2 \frac{\text{kg}}{\text{s}}$ one can observe in figure 3.20 that the inlet velocity profile was almost perfectly uniform. Stagnation zones in the impeller were very small and appeared due to the blade tip vortices only. Large mass flow rate was associated with big difference of pressures between two sides of blades that induced substantial air flow over the blade tips. According to figure 3.23 pressure difference between the diffuser outlet and inlet was close to 2800 Pa. Velocity distribution within the diffuser was not uniform. At the back wall, it was significantly higher (figure 3.21) and angle was slightly lower (figure 3.22). Therefore, the boundary layer at the front wall was thicker while the boundary layer at the back wall was much more narrow which is typical for mass flow rates higher than nominal [77]. Such a velocity distribution meant higher risk of separation at the front wall and higher friction losses at the back wall [122]. Velocity was gradually decreasing towards the outlet. The angle maintained values close to the inlet throughout whole diffuser. Figure 3.24 presents flow structure in the volute cross-section located opposite to the tongue. One can observe, that velocity of jet leaving the diffuser was relatively high and was decreasing gradually after entering the volute. The velocity tangential component was circulating around the volute centre with relatively constant value. The velocity in swirl centre dropped which stayed in agreement with theory of volute flow formulated by Van den Braembussche and Hande [123]. Normal velocity component exhibited shape typical for bent channels. It was higher at the volute inner wall and

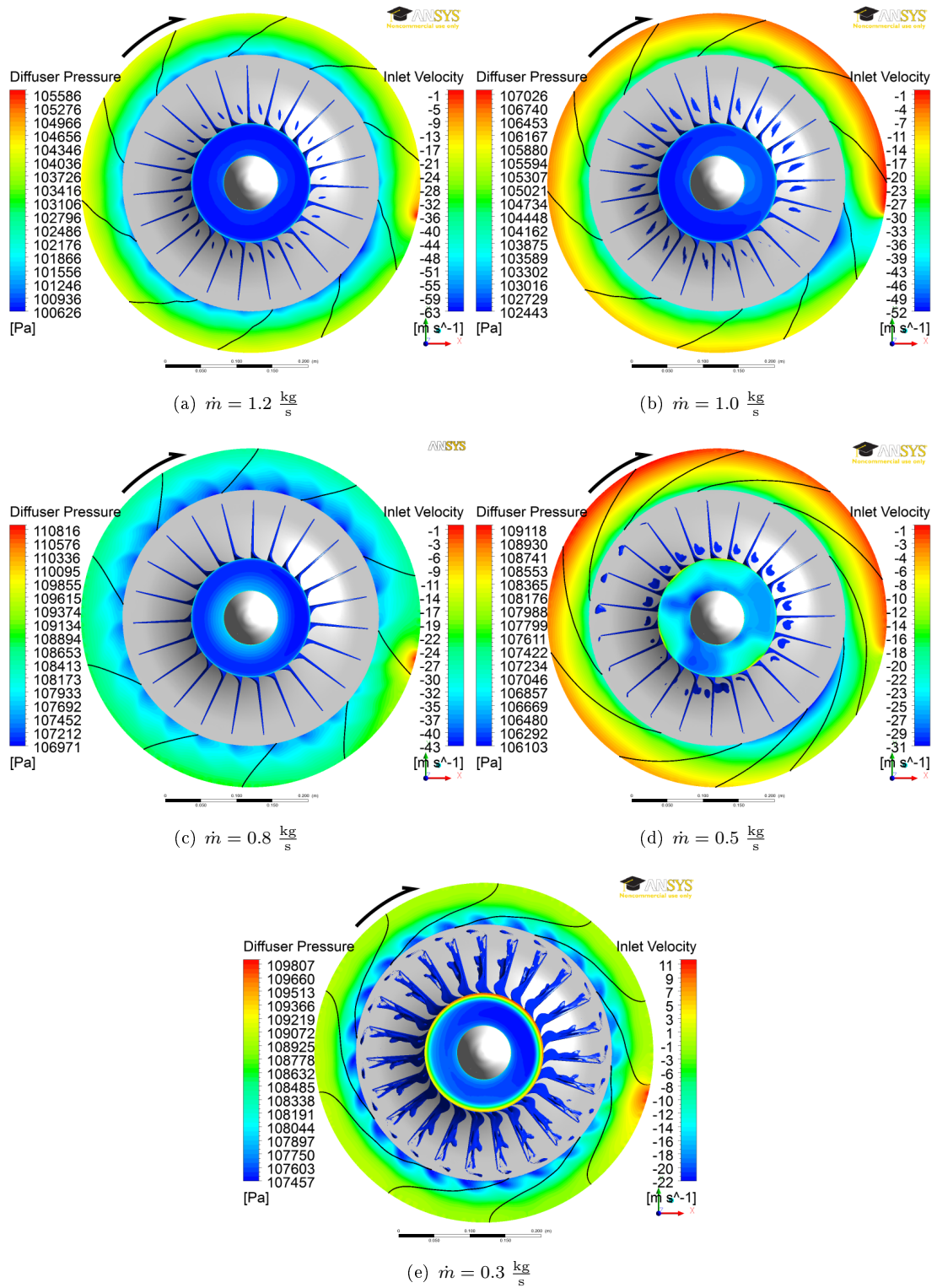


FIGURE 3.20: Flow within impeller and diffuser

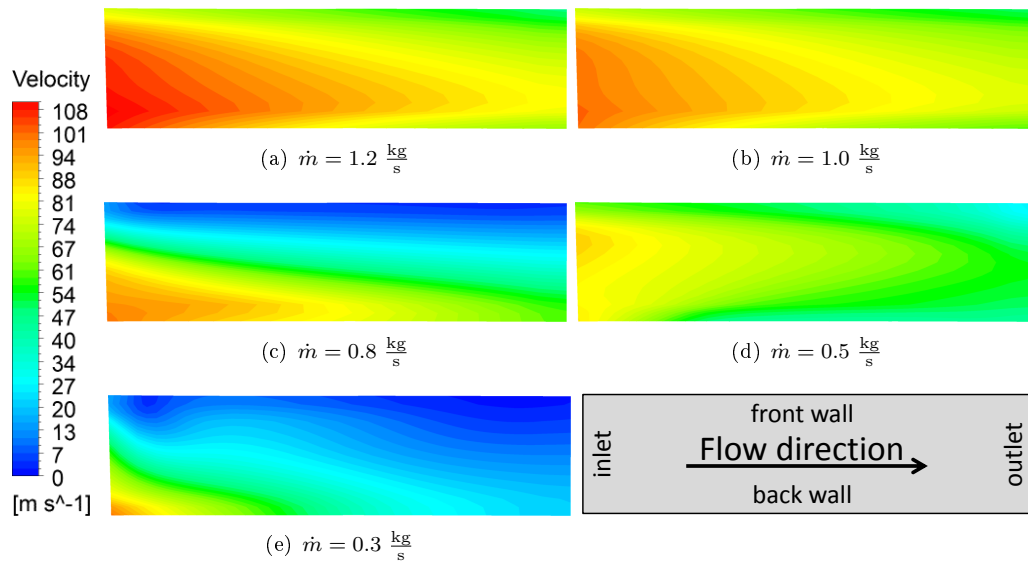


FIGURE 3.21: Circumferentially mass flow averaged velocity in the meridional cross-section of the vaneless diffuser

lower in the vicinity of the outer wall. Just above jet a triangular stagnation zone was formed.

At $\dot{m} = 1.0 \frac{\text{kg}}{\text{s}}$ stagnation zones appeared within the impeller in analogous locations but were a little bigger. Pressure rise in the diffuser was smaller and equalled to 2300 Pa. The pressure in neighbourhood of the volute tongue noted much more significant drop than in the previous setting. This caused higher pressure gradient along neighbouring impeller channels and less uniform flow therein. It was confirmed by disappearance of stagnation zones and caused circumferential non-uniformity observed at the impeller inlet. The fact that presence of the volute can cause circumferential instability even upstream of the impeller was in agreement with results presented by Sorokes et al. [111]. Velocity in

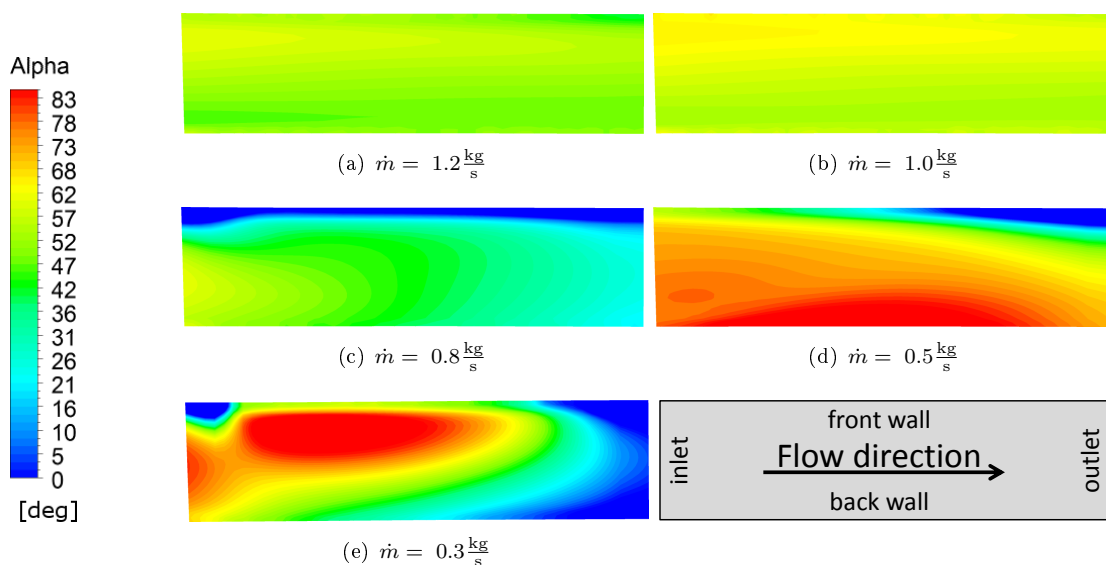


FIGURE 3.22: Circumferentially mass flow averaged flow angle from the normal direction in the meridional cross-section of the vaneless diffuser

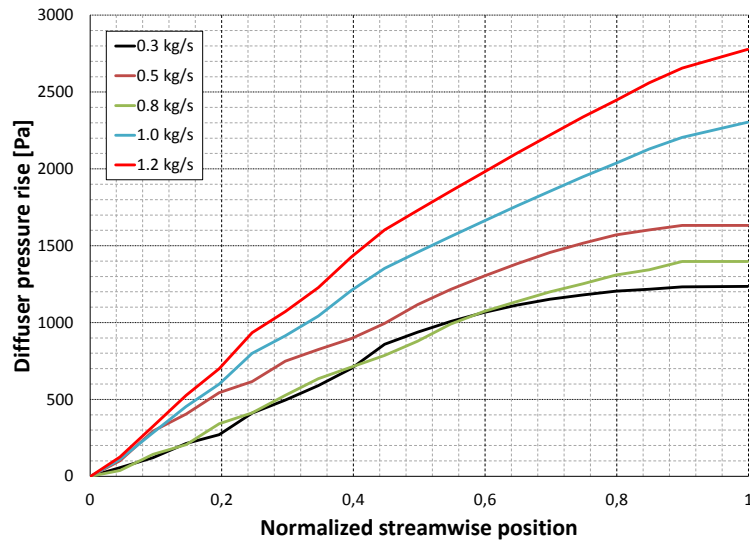


FIGURE 3.23: Mass flow averaged pressure rise along the diffuser

the diffuser behaved very similarly to the previous case, but was slightly smaller. The diffuser flow angle was a bit higher, but its distribution was even more uniform and almost perfectly constant spanwise and streamwise. The tangential velocity component in the volute cross-section presented circulation similar to the previous case. The normal component was much more uniform than at $\dot{m} = 1.2 \frac{\text{kg}}{\text{s}}$. The triangular stagnation zone above the diffuser outlet was also observed above the volute inlet.

Figure 3.20 shows that at $\dot{m} = 0.8 \frac{\text{kg}}{\text{s}}$ the flow in the impeller was free from stagnation zones. Circumferential non-uniformity at the inlet was hardly noticeable. This flow rate is regarded as the nominal one. The pressure rise in the diffuser dropped to around 1400 Pa. The reason of this can be observed in figure 3.21. The diffuser was affected by stagnation that appeared close to the front wall while the core flow was concentrated in vicinity of the back wall. Appearance of stagnation at this side was caused by much thicker boundary layer which was more likely to separate. According to Rebernik [100], the stagnation zones are typical for conditions close to the design mass flow rate and below it. Very small velocity resulted in a zero-angle layer observed in figure 3.22. Below it, the angle of the core flow was equal to 60° at the diffuser inlet and was two times smaller at the outlet. Figure 3.24 shows, that the diffuser stagnation zone merged with the stagnation triangular region in the volute. Naturally, the overall flow velocity in the volute was smaller than in the previous case. The slowest normal velocity component at the volute cross-section was present close to the volute outer wall. Described analysis suggested that the source of high pressure rise lied in undisturbed flow within the impeller. Pressure rise in the diffuser was significantly reduced by the separation. Nevertheless, observation of different time steps allowed to conclude that observed flow field could be regarded as constant in time. Therefore the overall machine operation which can be regarded as stable.

At $\dot{m} = 0.5 \frac{\text{kg}}{\text{s}}$ the impeller inlet velocity profile became clearly non-regular. This irregularity was also reflected in the size of impeller stagnation zones that differed from channel to channel. Flow in the diffuser was very different from what was observed in the previous case. Pressure rise in the diffuser was equal to 1600 Pa, however, it was oscillating in time. The velocity profile at the diffuser inlet changed (figure 3.21). Boundary layer at the back wall became thicker, while the boundary layer at the front

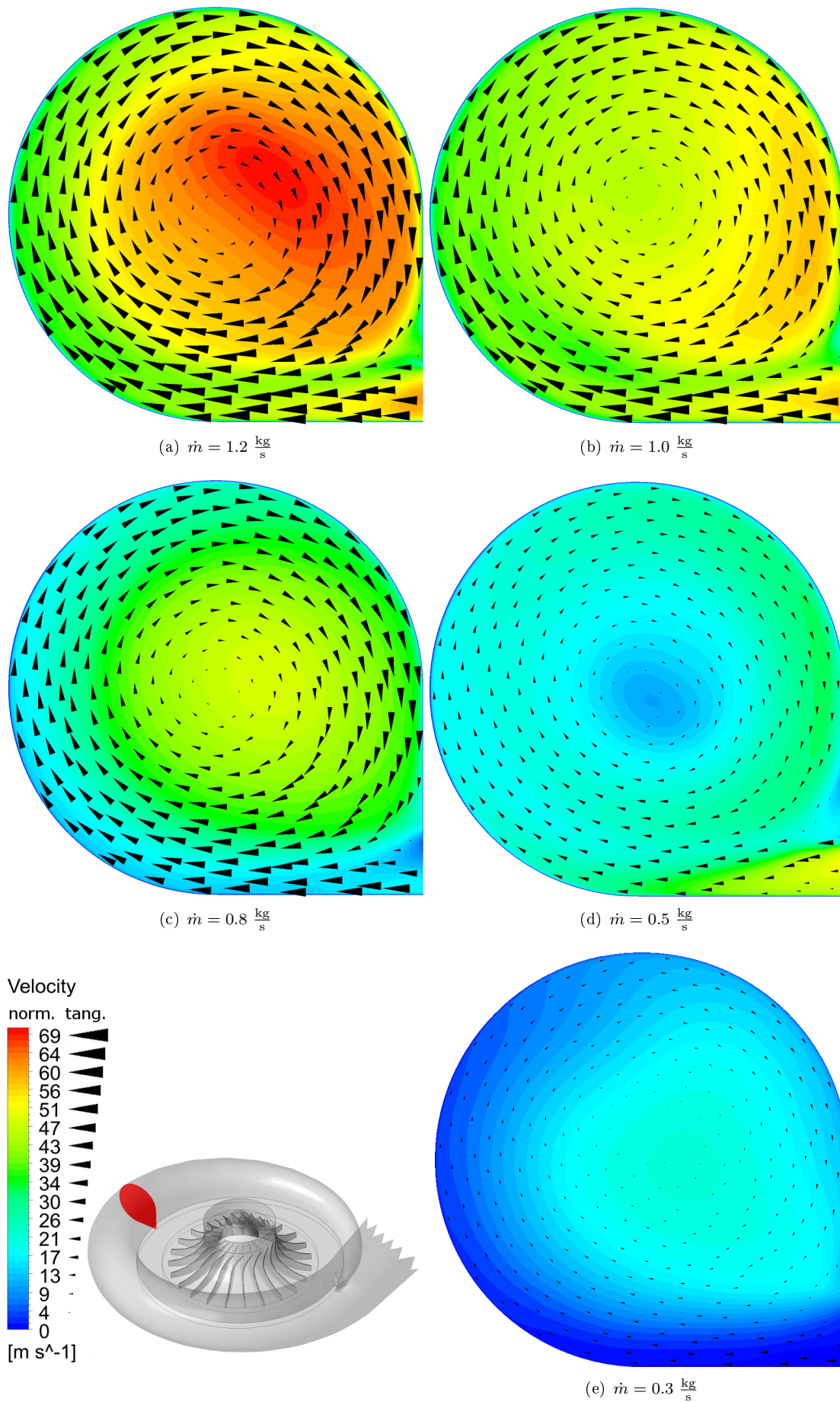


FIGURE 3.24: Velocity distribution in the volute cross-section located opposite to the tongue; arrows correspond to the velocity component tangential to the surface, color map corresponds to the velocity component normal to the surface

wall became thinner, which is typical for under-design mass flow rate [77]. Flow angle distribution presented in figure 3.22 revealed that flow close to the front wall was mainly radial and close to the back wall- circumferential. Such a flow structure is known to be a source of the instability [105]. Indeed, in this case a weak circumferential instability was observed which is described in section 3.2.2.2. Figure 3.24 shows that the stagnation zone above the volute inlet decreased in size and did not interfere with jet leaving the diffuser. Very small velocity in the volute explained high value of the pressure ratio obtained in this configuration. Small normal velocity meant that the energy conversion was done efficiently before the volute. At $\dot{m} = 0.8 \frac{\text{kg}}{\text{s}}$ the air was slowing down mostly in the volute and the outlet pipe downstream of the control surface *outsurf* that was used to determine the pressure ratio.

At $\dot{m} = 0.3 \frac{\text{kg}}{\text{s}}$ the inlet velocity profile showed a clear sign of the inlet recirculation. This structure is fully described in section 3.2.2.3. Stagnation zones occupied large volume of each impeller channel. Large stagnation was also observed in the diffuser at the front wall (figure 3.21). Figure 3.22 shows that flow recirculated in this region. Below recirculation, flow velocity was decreasing very quickly together with substantial change of the flow angle from very close to circumferential at the inlet to nearly radial at the outlet. Shape of streamlines in the mid-span can be observed in figure 3.20. As a consequence of diffuser velocity distribution, flow at the volute inlet presented in figure 3.24 was almost perfectly tangential. Then, tangential velocity component formed a weak swirl with centre located above the volute geometrical centre. This phenomenon is typical for volutes operating at mass flow rates much smaller than optimal [122]. Flow pulsations were observed in this configuration. Nevertheless, their size did not affect the global pressure ratio which was slightly higher than at $\dot{m} = 0.5 \frac{\text{kg}}{\text{s}}$.

3.2.2.2 Flow instability at $\dot{m} = 0.5 \frac{\text{kg}}{\text{s}}$

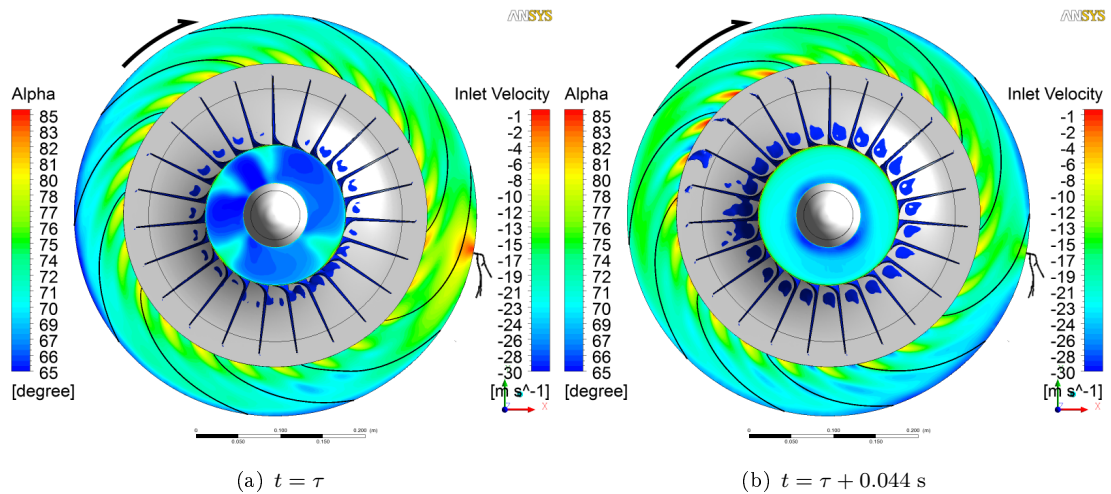
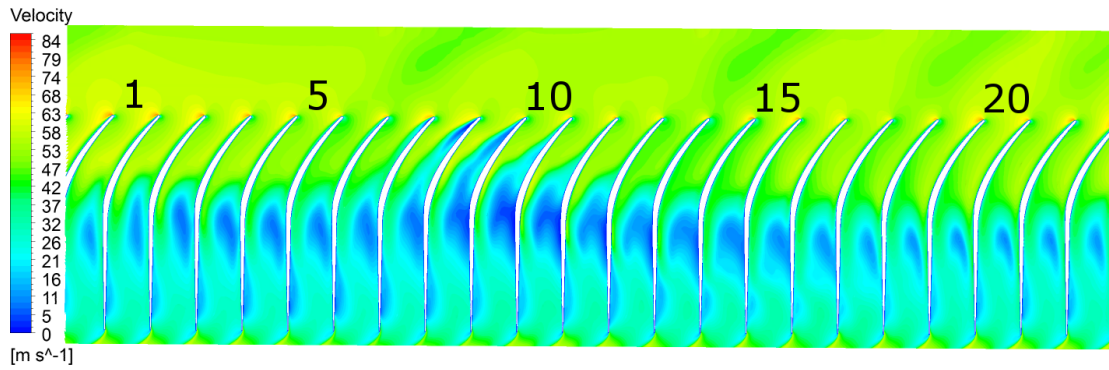
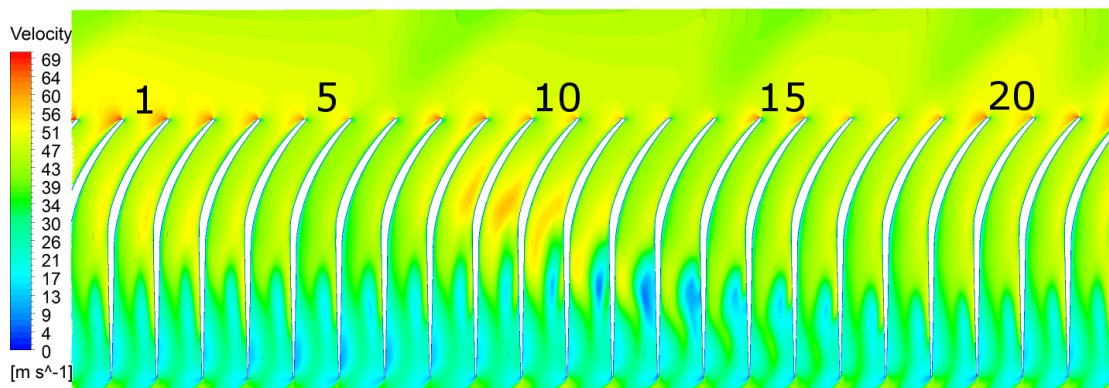


FIGURE 3.25: Overview on flow at $\dot{m} = 0.5 \frac{\text{kg}}{\text{s}}$

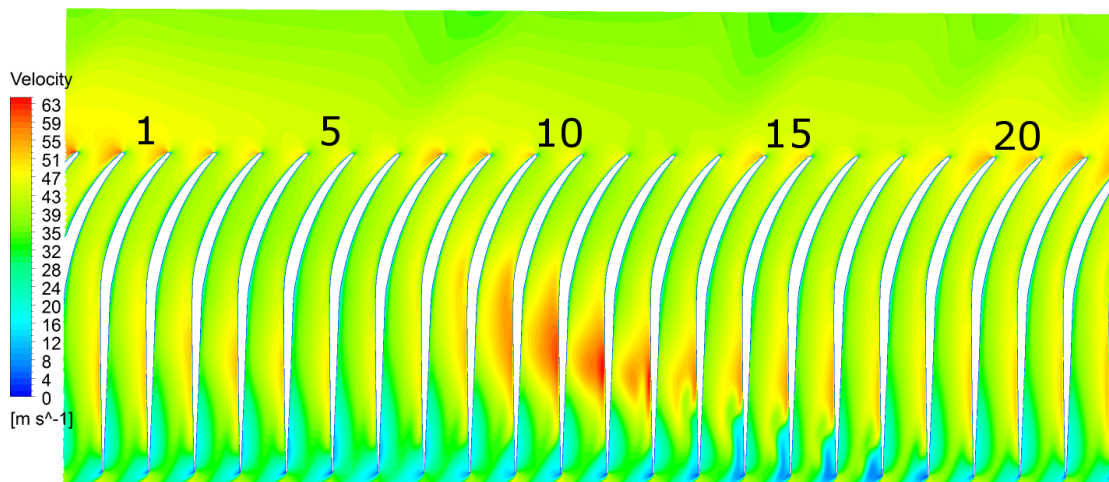
Figure 3.25 presents the flow overview depicted in similar manner as in figure 3.20. The only difference lies in the fact that the diffuser color map presents flow angle instead of pressure. Two plots correspond to different time steps separated by 0.044 s. One can observe that jet and wake were entering the diffuser at different angles and mixed at half of its length. After mixing the angle was oscillating circumferentially. At $t = \tau$ a region



(a) 80% of span



(b) 50% of span



(c) 20% of span

FIGURE 3.26: Velocity color maps at $t = \tau$ on blade to blade surfaces located at different spanwise positions, where 0% corresponds to the hub and 100% to the shroud

of higher flow angle was observed in the vicinity of the tongue, while at $t = \tau + 0.044$ s it appeared at the opposite side of the diffuser.

Flow instability was also observed in the impeller. The sequence described below was appearing recurrently. Figure 3.26 shows blade to blade velocity color maps located at 80%, 50% and 20% of the span respectively. For the sake of clarity channels were numbered. At 80% of the span the stagnation zones were present in all channels at the straight part of the blade suction side as a result of flow over blade tips. In channels

20 – 23 and 1 – 5 growth of another stagnation zone was observed close to the trailing edge. This structure was induced by non-uniform distribution of the diffuser flow angle. As a result, the stability of flow within channels was lost and two stagnation zones were growing concurrently (channels 5 – 8). This also influenced the angle of attack which in channel 8 exceeded critical value causing the stagnation at the leading edge. Channels 9 – 11 were fully occupied by both stagnations. One was present close to the leading edge suction side, the other one close to the trailing edge pressure side. Afterwards stagnation zones started decaying till channel 18. At this point the trailing edge stagnation started building up and the cycle was repeated.

At 50% of the span, trailing edge stagnation zone was much less noticeable than in the previous case. Higher flow velocity was noted in channels 9 – 11, i.e. in places where the leading edge stagnation was observed at 80% of the span. Therefore, the region of stagnation was co-existing with the region of higher velocity at lower spanwise positions. At 50% of the span, stagnation zones appeared in channels 12 – 14. Hence, it can be believed that the stagnation initiated at the shroud tip was progressing towards the hub. Blade to blade color map drawn close to the hub at 20% of the span, confirmed this scenario. At this location, separation zone was observed in channels 15 – 18 near the trailing edge. After reaching the trailing edge, the stagnation separated from the blade causing increment of the diffuser flow angle. This created a room for generation of separation at the pressure side of the blade.

The mechanism of migration of the stagnation zones from shroud to hub can be explained following the simplified model of flow in centrifugal channel presented by Balje [10]. This model described the meridional flow as a result of three forces

- centrifugal force caused by rotation of the impeller $\rho(2\pi f_{rot})^2 R$, where R is the distance from impeller axis
- centrifugal force caused by curvature of the channel $\frac{\rho V^2}{R_m}$, where R_m is the curvature of the streamline at meridional cross section
- the spanwise pressure gradient $\frac{\delta p}{\delta n}$, where n is the distance measured from the hub

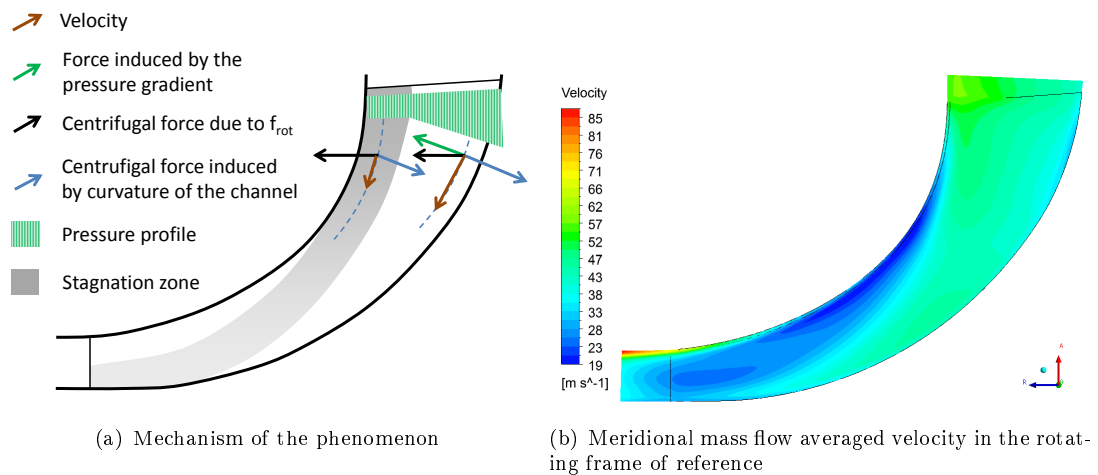


FIGURE 3.27: Migration of stagnation cells from shroud to hub

Figure 3.27(a) presents schematically forces acting on the fluid located within the stagnation zone and outside of it. In non-stagnated regions balance of three forces provided

fluid acceleration along the channel. In stagnated region, the pressure profile was close to constant and the third force became negligible. This disturbed the balance and caused the tendency of low energy stagnation zones to migrate towards the hub. This phenomenon could be also observed in figure 3.27(b) demonstrating the mass flow averaged distribution of velocity in the rotating frame of reference. As a result of flow stagnations in some channels, the average value dropped at the shroud close to mid-chord. The shape of contours reflects the migration of low-velocity zones towards the hub.

Presented cycle of stagnation that included separation initiated at the impeller leading edge exhibited some similarities with phenomenon of the Progressive Impeller Rotating Stall (PIRS). There is no clear definition of stability criteria for this phenomenon. Some researchers claim that the PIRS begins in the moment, when the tip separation reaches the pressure side of another blade [122], which results in significant channel blockage. Such a situation was observed in figure 3.26. According to Frigne and Van den Braembussche [33] the PIRS can lead to Abrupt Impeller Rotating Stall (AIRS) in the case, when it is triggered by the Difusser Rotating Stall (in this case Vaneless Difusser Rotating Stall- VDRS). In the presented instance the diffuser was not at stall. However, certain circumferential instability of the angle was observed (figure 3.25).

According to state of the art the VDRS phenomenon appears as a result of exceeding the critical diffuser inlet flow angle α_{cr} [59]. In these conditions the flow becomes almost aligned with the pressure gradient and the boundary layer does not have sufficient velocity to compensate the adverse pressure gradient. As a result, the reverse flow appears in the boundary layer which interacts with the core flow and pressure pulsates circumferentially [34, 76].

Senoo and Kinoshita [105] derived theoretical model in which α_{cr} was a function of the relative diffuser length $\frac{b}{R_2}$. According to notation introduced in this study the relative diffuser length equalled $\frac{b}{R_2} = \frac{2b_2}{D_2} = 0.087$. In this condition Senoo theorem yielded $\alpha_{cr} \approx 79^\circ$. However, figures 3.22 and 3.25 showed that in examined study the average flow angle at the diffuser inlet was smaller $\alpha \approx 70^\circ$.

Another method can be applied to specify the critical conditions. Abdelmahid and Bertrand stated that the stall onset can be determined by the critical mass flow rate coefficient ϕ_{cr} [7]. They found that ϕ_{cr} decreased with $\frac{b}{R_2}$. Otugen et al. conducted analysis of stall cells appearing in diffusers with different relative lengths $\frac{b}{R_2}$ [117]. One of them was equal to $\frac{b}{R_2} = 0.09$, which was very close to diffuser applied in this study ($\frac{b}{R_2} = 0.087$). Otugen et al. observed the rotating stall at mass flow coefficient $\phi_{cr} = \frac{\dot{m}}{2\pi R_2 b \rho u_{tip}} = 0.11$. Recalculating this value to the blower applied in this study resulted in $\dot{m}_{cr} = 0.2 \frac{\text{kg}}{\text{s}}$ which was much smaller than $\dot{m} = 0.5 \frac{\text{kg}}{\text{s}}$ in the case analysed in this point.

Both considerations lead to conclusion that conditions met at this mass flow rate were not satisfactory for appearance of the fully-developed VDRS. This, however, did not exclude weak fluctuations in the diffuser that were synchronized with the PIRS. At lower mass flow rate the flow angle/mass flow rate were much closer to the critical conditions. However, at $\dot{m} = 0.3 \frac{\text{kg}}{\text{s}}$ circumferential fluctuations were not observed. This can be connected with presence of the inlet recirculation (IR). IR initiated at the leading edge was propagated downstream and, therefore PIRS disappeared. If this observation is valid, then two interesting conclusions can be made:

- Flow oscillations in the diffuser were triggered by the PIRS.
- Appearance of the inlet recirculation decreased the chances of propagation of another instabilities in the impeller and the diffuser. This statement was also supported by experimental results. Spectral maps in section 2.2.3.2 shown that as

long as the inlet recirculation was present, pressure in another zones was relatively stable. Moreover, the inlet recirculation disappearance was concurrent with appearance of instabilities in another zones. Detailed analysis of the inlet recirculation observed in the simulation is presented in section 3.2.2.3.

3.2.2.3 Inlet recirculation

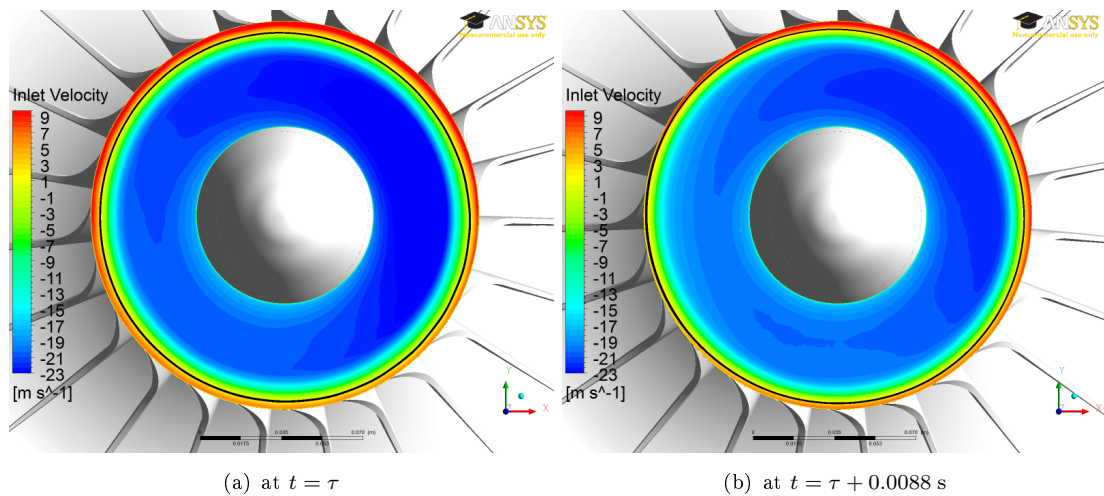


FIGURE 3.28: Axial velocity component at cross-section containing point p_{s-imp1} at $\dot{m} = 0.3 \frac{\text{kg}}{\text{s}}$

The inlet recirculation (IR) was observed in the case $\dot{m} \leq 0.3 \frac{\text{kg}}{\text{s}}$ and at some stages of the deep surge cycle $\dot{m} \leq 0.1 \frac{\text{kg}}{\text{s}}$. Figure 3.28 presents the color maps showing the axial velocity component at cross-section containing point p_{s-imp1} at two different moments of time. The positive values of velocity represent the backflow. The change in flow direction was marked with a black line. This allowed to observe thickness of the inlet recirculation. It can be noticed that it was present at whole circumference during all time. However, for a given angular position the recirculation zone thickness was slightly changing with time. It depended on the velocity distribution in the core flow. At the angular position, where the core flow velocity was higher, the IR layer was thicker. On the other hand, smaller core velocity was usually connected with thinner layer of the IR.

The flow structure in this zone is illustrated in figure 3.29(a). Plot 3.29(b) presents streamlines initiated in two regions. Streamlines scaled with the rainbow colormap are initiated at the impeller leading edge at a distance from the shroud not higher than 10% of the channel span. The core flow is presented in figure in form of black streamlines. One can clearly see the flow recirculation in this region. According to Breugelmans and Sen, it was most likely initiated by flow separation at the blade suction side [15]. As indicated in their study the recirculating flow was carrying much energy that was transferred into static pressure at the walls of the suction pipe. Figure 3.29(a) clearly confirmed this statement. One can observe that the pressure values were higher at the suction pipe wall at both sides of analysed cross-section. Higher pressure at the pipe wall in presence of the recirculation zone was also observed in the experimental study as it was described in section 2.2.3.3. On the other hand, figure 3.28 showed that the recirculation zone thickness was varying with time. This explained possible reason of large pressure drops registered in the experiment.

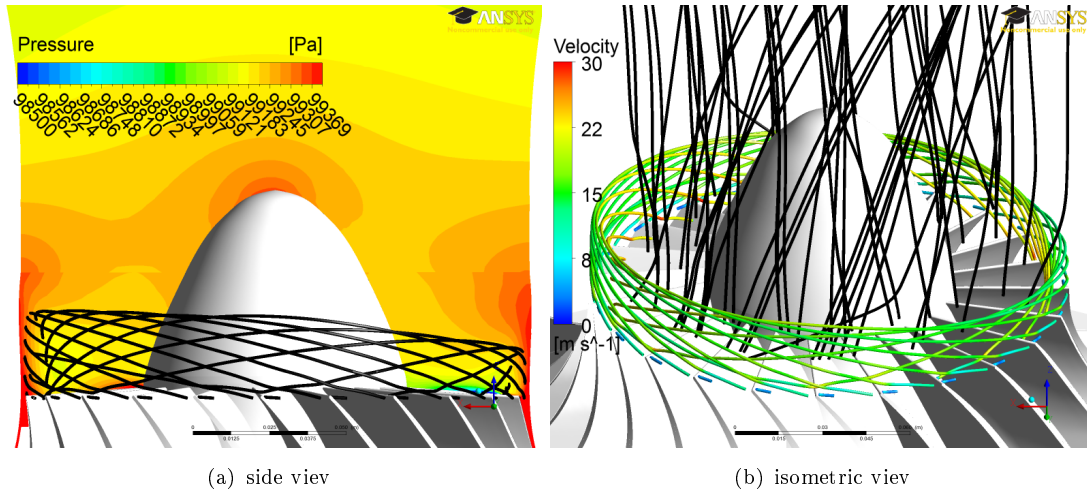


FIGURE 3.29: Region affected by the inlet recirculation at $\dot{m} = 0.3 \frac{\text{kg}}{\text{s}}$

As mentioned above, a probable source of the IR lied in separation at the blade leading edge, close to the shroud tip. In fact, this separation was also present as a part of the rotating stall cycle described in section 3.2.2.2 and identified as one of possible regions of its onset. Therefore, it can be postulated that these two flow structures could have been initiated at the same place. The difference lied in the direction of propagation of the recirculation. At $\dot{m} = 0.5 \frac{\text{kg}}{\text{s}}$ it propagated downstream, then disappeared and reappeared periodically as a part of the full rotating stall cycle. At $\dot{m} = 0.3 \frac{\text{kg}}{\text{s}}$ separation became present at whole circumference and propagated upstream. The most likely source of this difference lied in pressure distribution in this region. Figure 3.30 illustrates pressure color maps in the case, when the IR appeared ($\dot{m} = 0.3 \frac{\text{kg}}{\text{s}}$) and in the case when the rotating stall was observed ($\dot{m} = 0.5 \frac{\text{kg}}{\text{s}}$). Obviously, higher pressures were observed in region close to the shroud affected by the IR. However, in vicinity of the hub, difference was also evident. At $\dot{m} = 0.5 \frac{\text{kg}}{\text{s}}$ pressure difference in axial direction from the top to the bottom of plot was close to 700 Pa while at $\dot{m} = 0.3 \frac{\text{kg}}{\text{s}}$ it was not higher than 100 – 200 Pa. This is not clear, however, whether this observation pointed out source of the IR, or its result. Therefore, the onset of the IR will be subject to further analysis.

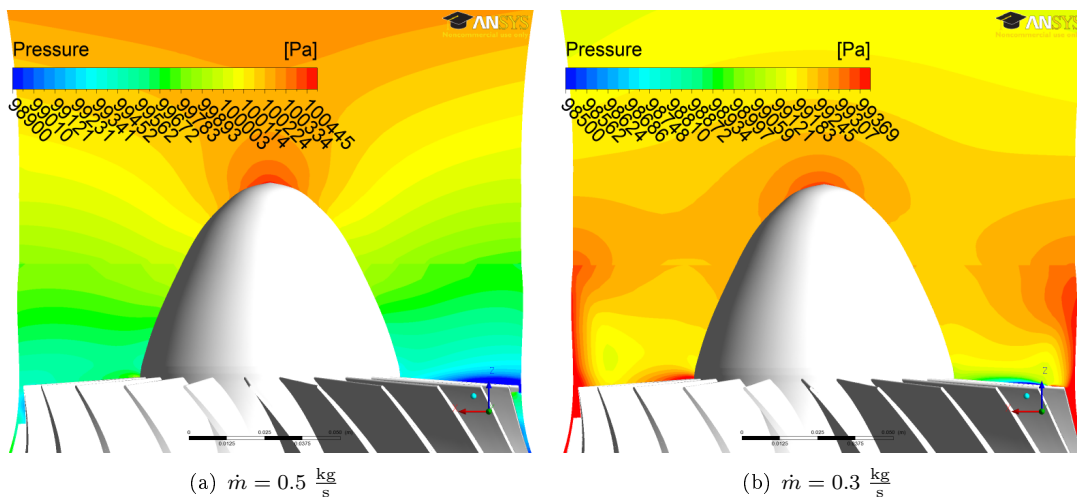
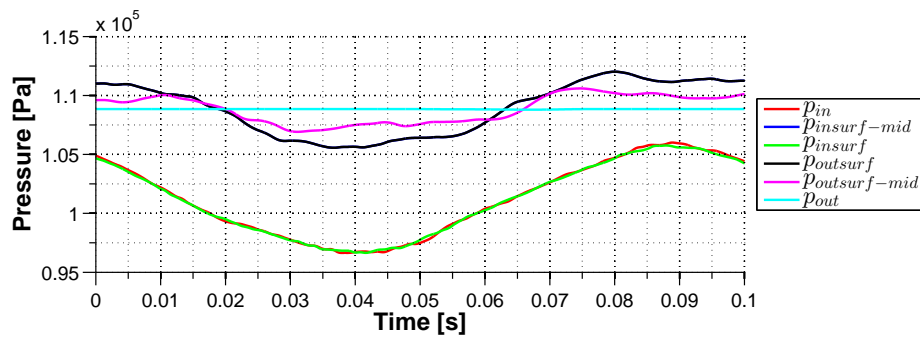


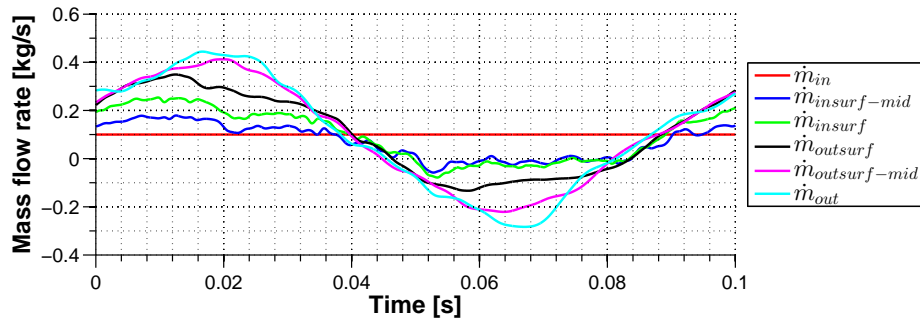
FIGURE 3.30: Pressure color map of inlet zone at different mass flow rates

In the experimental study the IR was clearly noticed. The mechanism of the IR was proven to be of great use for early detection of unstable phenomena. Presented work was the second example of obtaining the IR in numerical analysis conducted in IOT. The first successful attempt was conducted by Chodkiewicz et al. [20]. Present work could be treated as continuation of this work. Due to higher computational resources it introduced much more detailed model of this phenomenon. The main difference between the numerical and the experimental study lied in order of appearance of different unstable phenomena. In experimental study the inlet recirculation was first instability, in numerical study it was preceded by instabilities of the form similar to the progressive impeller rotating stall.

3.2.3 Representation of the flow structures - the deep surge



(a) mass flow averaged pressure



(b) mass flow

FIGURE 3.31: Time-variation of flow parameters at the control surfaces during the surge cycle

As mentioned earlier, the deep surge was observed in the simulation conducted for $\dot{m} = 0.1 \frac{\text{kg}}{\text{s}}$. Figure 3.31 shows the values of mass flow averaged pressure and mass flow rate at control surfaces during a single surge cycle. The pressure characteristics at the inlet and at the impeller inlet had shapes very close to purely harmonic which indicated linear character of oscillations in this region. At the outlet the presence of higher frequency modes was observed, which was partially caused by the fact, that the outlet pressure was fixed by the boundary condition. There was a critical value of pressure head that caused immediate backflow of the fluid. This can be confirmed by figure 3.32. It presents the value of pressure ratio during the surge cycle computed from mass flow averaged pressures at surfaces *outsurf* and *insurf*. One can observe, that its drop appeared around 0.025 s

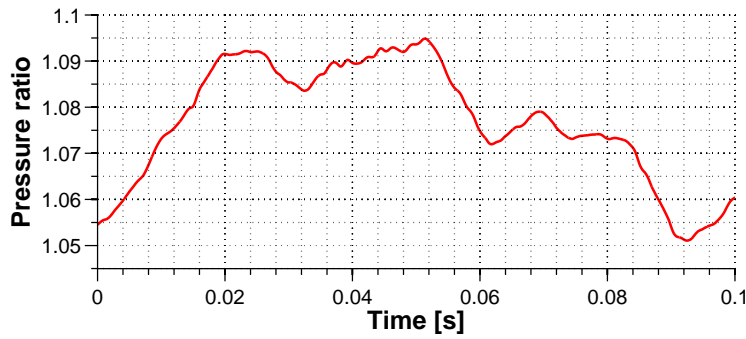


FIGURE 3.32: Pressure ratio during the surge cycle

and again around 0.05 s. This corresponded to the situation when the pressure head generated by the blower was not sufficient to overcome the pressure difference between the outlet and the inlet. The mass flow rate plots revealed dominating harmonic of the signal that oscillated around the value fixed by the inlet boundary condition. The further the monitor was located from inlet, the higher its amplitude was. Another issue was that the monitors located closer to the inlet exhibited more high-frequency fluctuations.

3.2.3.1 Overview

Figure 3.33 presents the pressure color maps at different stages of the single surge cycle. Additionally, each plot was supplemented with streamlines starting from the impeller (black) and the outlet (grey). The streamlines were added in order to visualise direction of the fluid flow.

The surge cycle observed in the simulation was analysed step by step similarly as it was presented by Bloch [12]. At the beginning of the surge cycle ($t = 0$ s), the blower operated as during machine start up, when pressure head is gradually increasing together with mass flow rate. Figure 3.33 shows that the air flew smoothly from the impeller towards the outlet. All monitored mass flow rates were slightly higher than the inlet boundary condition $\dot{m} = 0.1 \frac{\text{kg}}{\text{s}}$. The pressure ratio was below its nominal value $\frac{p_{out}}{p_{in}} = 1.055$. The blower did not reach its maximum capacity, therefore, the pressure head was increasing with time at a constant rate which is confirmed by figure 3.32. At this moment pressure just behind the volute was higher than at the pipe outlet by 3 kPa. This value of pressure difference between two ends of the outlet pipe is never exceeded and can be regarded as maximal. On the other hand, mass flow rate through the blower was higher than at the inlet which caused pressure decrement within the inlet pipe.

At $t = 0.0176$ s pressure within the inlet pipe was uniform as it can be observed in figure 3.33. High mass flow rate in the outlet pipe caused decrement in pressure gradient between its both ends. The maximum value of the pressure head that was generated by the blower was attained around $t = 0.02$ s (figure 3.32). Mass flow rate at all sections was much higher than at the inlet and the flow started decelerating, which was observed as decreasing mass flow rate. As long as it remained higher than $\dot{m} = 0.1 \frac{\text{kg}}{\text{s}}$ the inlet pipe pressure continued to decrease but at slower rate.

Figure 3.33 presents flow at $t = 0.0352$ s, when mass flow rate was very close to $\dot{m} = 0.1 \frac{\text{kg}}{\text{s}}$. Just after that, around $t = 0.04$ s stagnation appeared almost simultaneously within the whole system which was indicated in figure 3.31. This was also the moment, when the inlet pipe pressure attained the smallest value. From this point all pressures

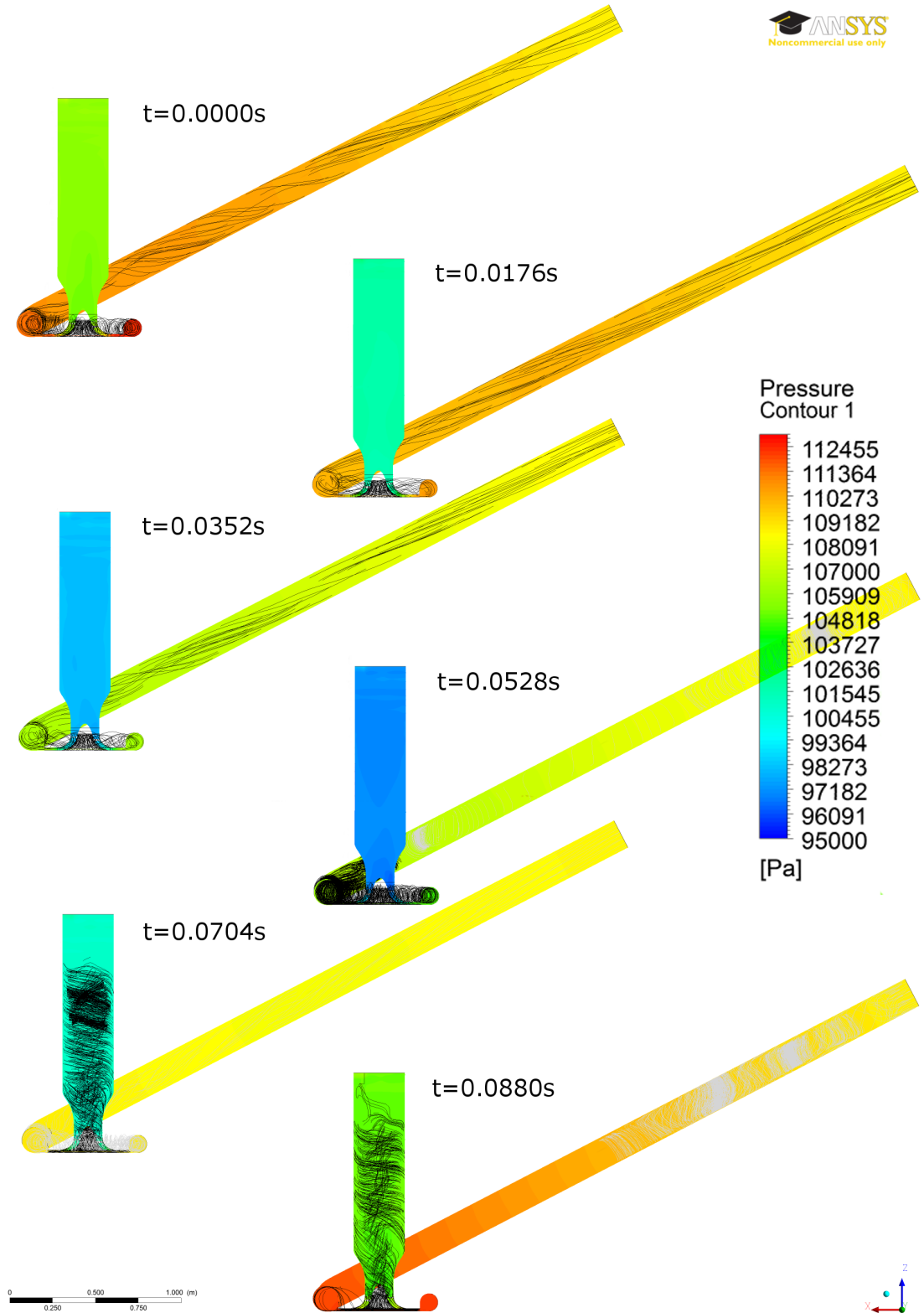
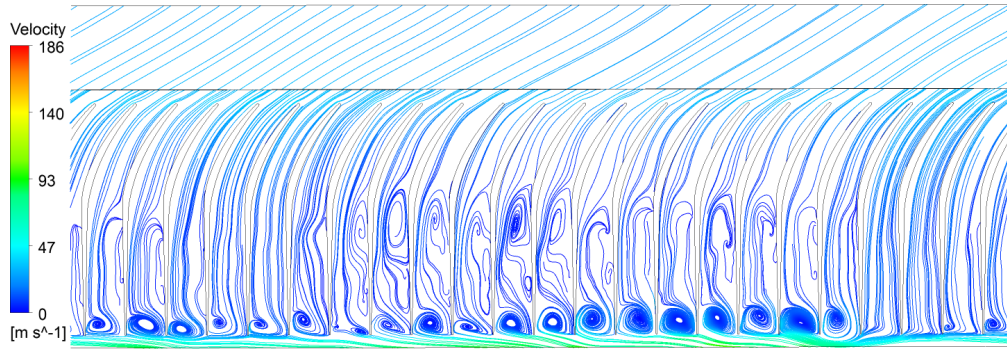


FIGURE 3.33: Pressure distribution at consecutive moments of the surge cycle

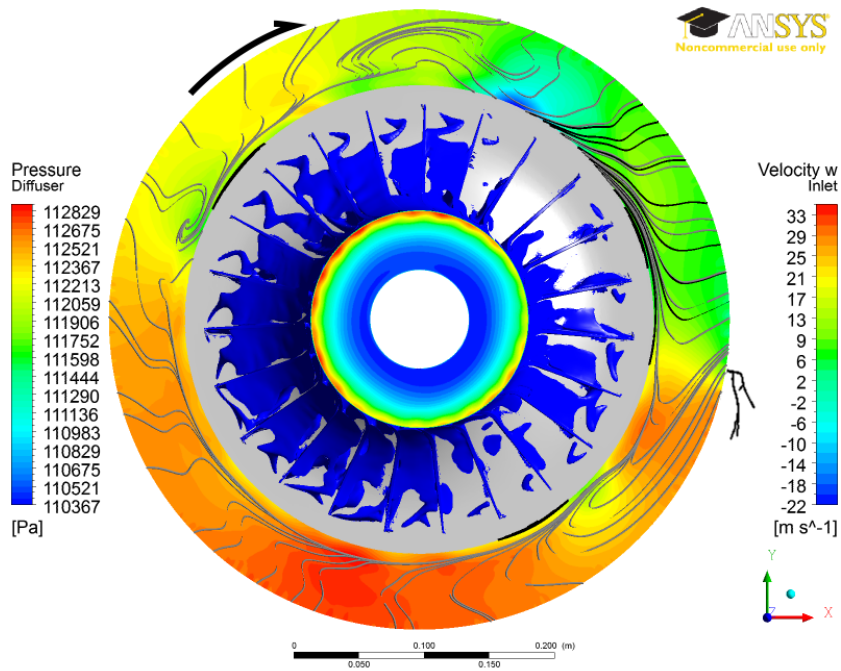
at whole domain were increasing. This took place at slower rate at the blower inlet than at the blower outlet and, consequently its pressure head was increasing very slowly.

At $t = 0.04$ s, inlet mass flow rate at all control surfaces became lower than the inlet boundary condition $\dot{m} = 0.1 \frac{\text{kg}}{\text{s}}$ (figure 3.31). Pressure in the inlet pipe started to increase at a very slow rate. Meanwhile, pressure in the outlet pipe just behind the blower was increasing a bit faster due to the fact, that its value was smaller than at the outlet boundary condition and backflow started to appear within the plenum. Figure 3.32 shows that the pressure head was increasing very slowly till $t = 0.0528$ s. Increment rate was much lower than during initial phase $0 \text{ s} < t < 0.02 \text{ s}$ and included weak high frequency oscillations. This suggests very short phases of subsequent regular work and de-pressurization. Figure 3.33 presents the system at the very end of this phase ($t = 0.0528$ s). One can observe the stagnation region in the outlet pipe (located just behind the inlet pipe) where fronts of the air streams flowing from blower and outlet met. Just after that, the backflow propagated towards the inlet and occupied the whole system. The de-pressurization phase was initiated and pressure head started decreasing. At $t = 0.0704$ s pressure stabilized in the middle of the pipe and just behind the impeller it continued slow increment. This moment is presented in figure 3.33. One can observe that the air that coming back from the impeller was observed in the inlet pipe. At $t = 0.0880$ s the pressure distribution in the outlet pipe stabilized. Figure 3.33 shows the moment when pressure in the inlet pipe attained maximum. The last traces of the backflow were observed in the inlet pipe and in the outlet pipe. A very small value of pressure difference between the impeller inlet and outlet leaved room for phase of normal blower operation that initiated this description of the surge cycle.

Obtained surge model is not a perfect representation of the real phenomenon. The most important discrepancies are coming from the assumed boundary conditions. The choice of combination of boundary conditions applied in analysed case was presented in section 3.1.3.1. It was motivated by the fact, that the specification of the outlet mass flow rate would be possible only for the 'pressure-vent' condition with the additional option 'target mass flow rate' [4]. Such a solution would be ineffective in transient case where large pressure and mass flow rate fluctuations are present. Even if that was possible, such a set of boundary conditions would still not represent the physics of the real flow. The problem lies mainly in the outlet boundary condition which in reality is realized by a throttling valve. Such a valve in the case of large flow fluctuations influences both parameters: \dot{m} and p in a very complex way. Therefore, the further improvement of the model should be concentrated on better definition of the boundary conditions mainly. In presented study, the problem was partially solved by application of large volumes of the inlet and the outlet pipes. However, some non-physical effects were observed. The most significant of them is the fact, that the pressure oscillation amplitude observed at the inlet was larger than at the outlet. This finding is opposite to what was registered in the experiment and is a well known fact resulting from the Greitzer model [38–40].



(a) Streamlines at the rotor mid-span (blade-to-blade)

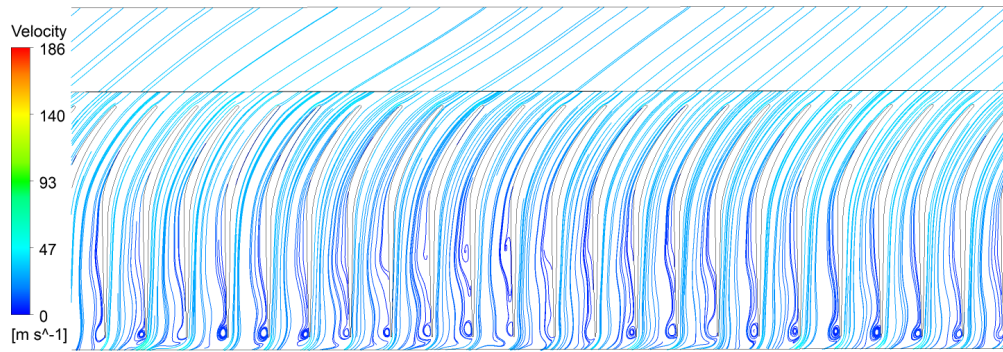


(b) Axial velocity component at the inlet; stagnation zones in the impeller; pressure distribution and streamlines in the diffuser

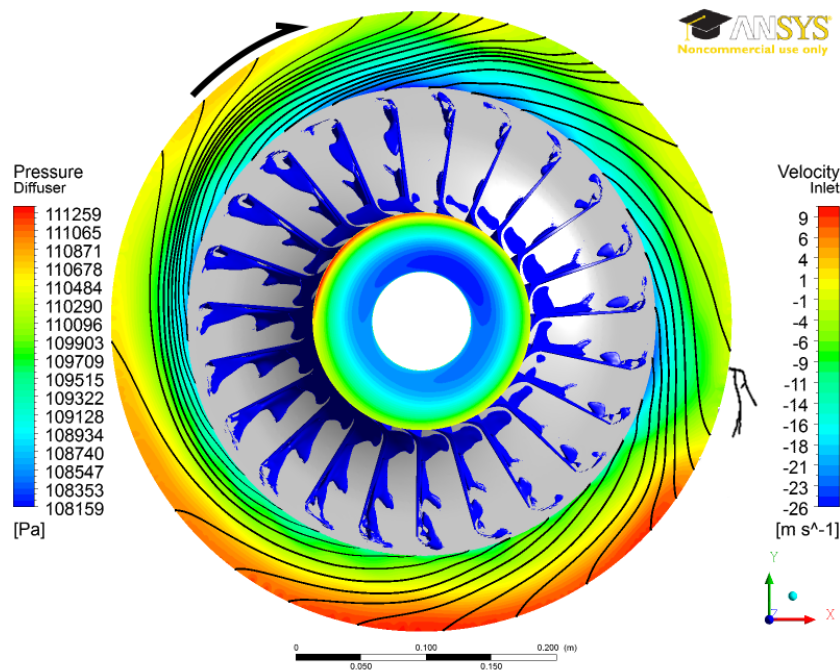
FIGURE 3.34: Surge cycle at $t = 0.0000$ s

3.2.3.2 Impeller and diffuser flows

Figures 3.34-3.39 present visualizations of the flow in the impeller and the diffuser. Each of them contains two subfigures. Subfigures 3.34(a)-3.39(a) show a streamline in blade to blade view of the impeller and a region upstream of the impeller at the mid-span. Figures 3.34(b)-3.39(b) show a combination of several post processing methods that allow to understand the flow at given moment. The impeller inlet contains color map showing distribution of the axial velocity component. Regions marked in blue in the impeller represent places, where relative velocity in the frame of reference rotating with the impeller was smaller than $5 \frac{m}{s}$. These zones are referred to as stagnation regions henceforth. Pressure in the diffuser mid-span is presented by means of color map. Attention was focused on local pressure fluctuation, therefore, scale limits were set locally for each timestep. Additionally, streamlines were drawn in the diffuser in order to show the air flow direction in the stationary frame of reference. The color of streamlines depends



(a) Streamlines at the rotor mid-span (blade-to-blade)

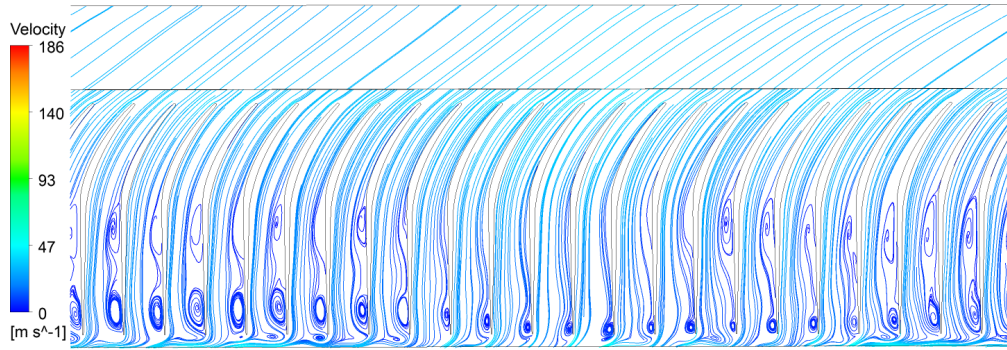


(b) Axial velocity component at the inlet; stagnation zones in the impeller; pressure distribution and streamlines in the diffuser

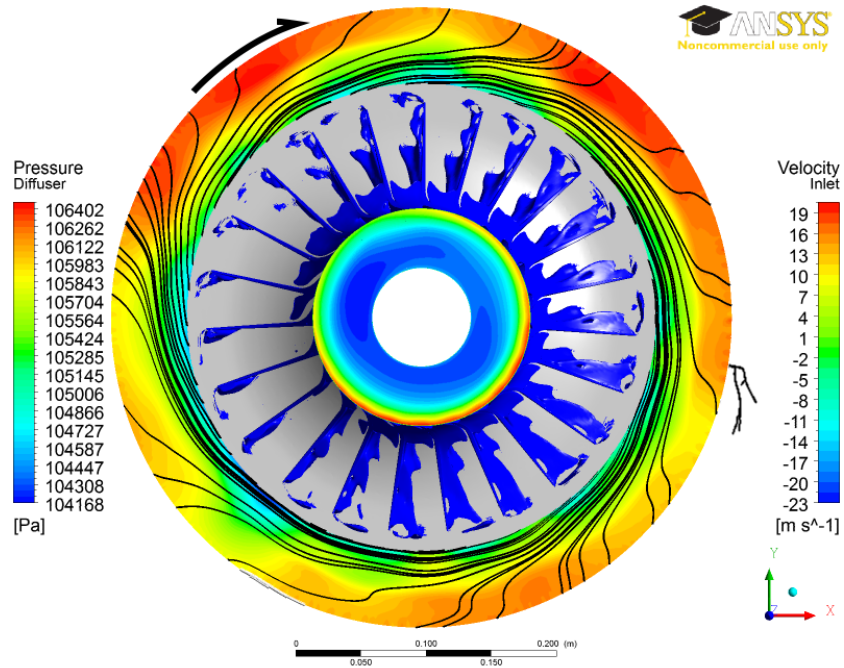
FIGURE 3.35: Surge cycle at $t = 0.0176$ s

on their starting point: black streamlines were initiated at the diffuser inlet and correspond to flow downstream. White streamlines were initiated at the diffuser outlet and correspond to reverse flow. Grey streamlines were initialized within the diffuser and were added only in cases of flow stagnation when none of previous methods of initialization were successful. For the sake of consistence, the choice of times at which the flow was visualized was analogous to the previous section.

Figure 3.34 shows flow in the impeller at $t = 0$ s. One can observe that only a small part of the diffuser circumference was occupied by flow passing directly from inlet to outlet represented by black streamlines. It corresponded to 3 – 4 channels of the impeller where stagnation was not observed. Air leaving these channels flew directly towards the volute. All other channels were fully blocked and the diffuser was dominated by the air circulating around. Figure 3.34(a) shows the structure of flow in the impeller. One can distinguish two types of swirls:



(a) Streamlines at the rotor mid-span (blade-to-blade)

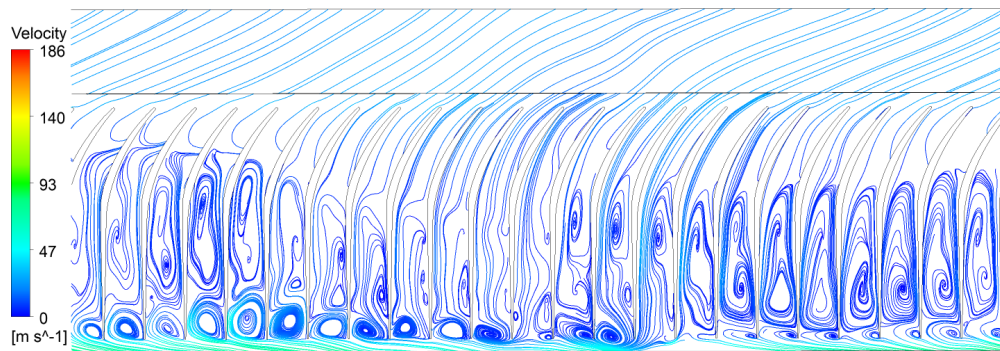


(b) Axial velocity component at the inlet; stagnation zones in the impeller; pressure distribution and streamlines in the diffuser

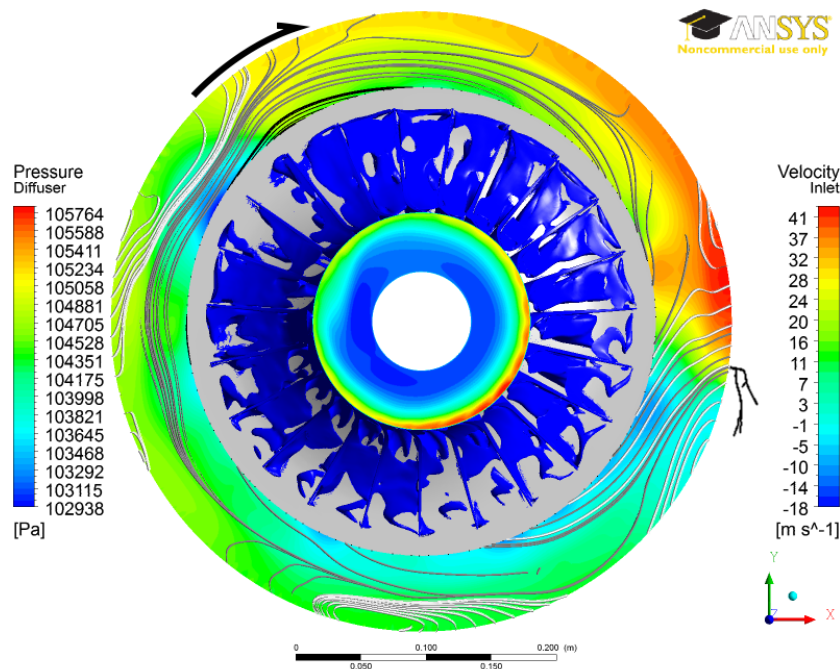
FIGURE 3.36: Surge cycle at $t = 0.0352$ s

- Large swirls occupying around half of the channels. These cells can be also observed as stagnation zones in figure 3.34(b). These structures had a form similar to the the stagnation zones presented in section 3.2.2.2. Temporary appearance and disappearance of this type of structures during the surge was observed by numerous researchers including [38, 71, 96]. At this moment two stagnation cells were observed (figure 3.37(b)). Cells were irregular, one of them contained around 11 channels, another only 3.
- Near the outlet of the impeller much smaller swirls were observed. The reason of them was the same as it was described in section 3.2.2.2 for $\dot{m} = 0.5 \frac{\text{kg}}{\text{s}}$. The only channels not affected by this phenomenon were the ones, where a significant radial velocity component was observed in the diffuser.

Figure 3.34(b) shows that also the inlet recirculation was present at the impeller inlet. In fact, all phenomena characteristic for the pre-surge stage and described in sections



(a) Streamlines at the rotor mid-span (blade-to-blade)

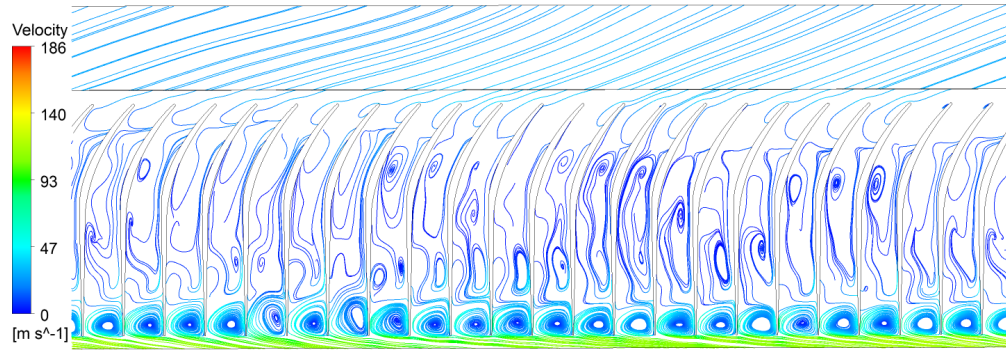


(b) Axial velocity component at the inlet; stagnation zones in the impeller; pressure distribution and streamlines in the diffuser

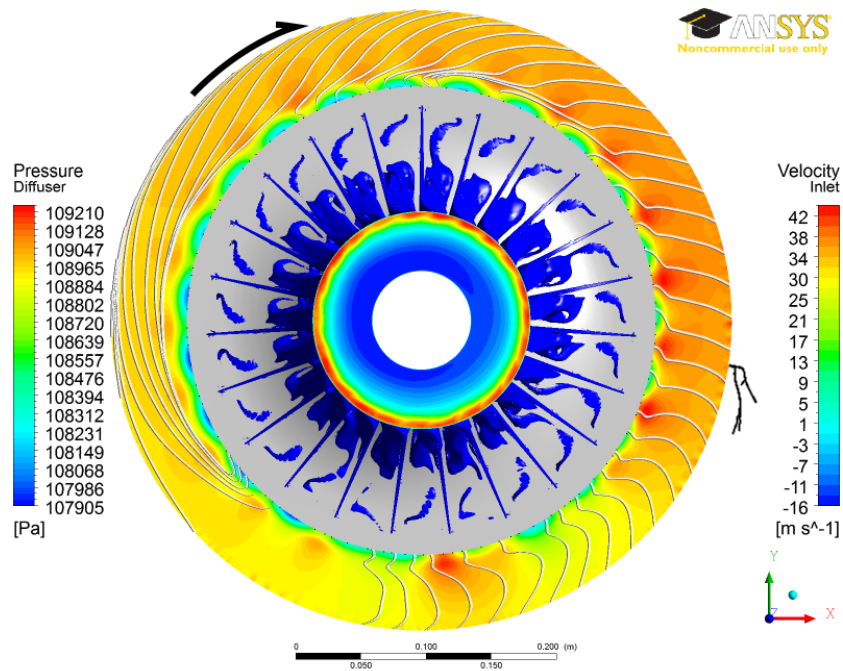
FIGURE 3.37: Surge cycle at $t = 0.0528$ s

3.2.2.2 and 3.2.2.3 were appearing and disappearing at different stages of the surge cycle. After $t = 0$ s the blower was gradually entering the phase of regular operation. This was clearly reflected in the shape of flow presented in figure 3.35 for $t = 0.0176$ s. Flow in the impeller was almost free from stagnation, however, small vortices were still present. These were caused by low mass flow rate in the diffuser. In figure 3.35(b) one can observe that the flow in the diffuser had a form of undisturbed spirals. This moment corresponded to the highest positive mass flow rate and the observed flow can be regarded as the closest to the one present close to the design working conditions. The pressure rise of 3 kPa was noted across diffuser which confirmed, that the transformation of kinetic energy into potential one took place in the diffuser.

At $t = 0.0352$ s figure 3.36(b) presents that the value of pressure rise in the diffuser dropped to around 2 kPa and particle tracks just behind the impeller had a shape of spirals with smaller radial component. This time corresponds to a moment when the blower was working closely to its maximal pressure head, but the mass flow rate was already dropping. Smaller mass flow rate started inducing appearance of bigger



(a) Streamlines at the rotor mid-span (blade-to-blade)



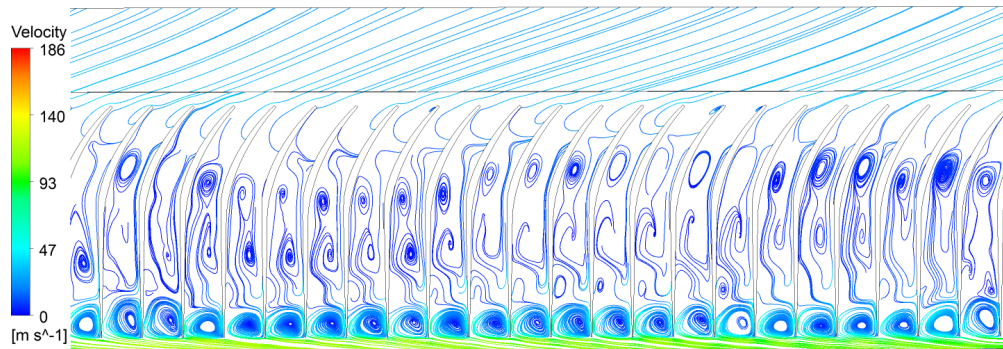
(b) Axial velocity component at the inlet; stagnation zones in the impeller; pressure distribution and streamlines in the diffuser

FIGURE 3.38: Surge cycle at $t = 0.0704$ s

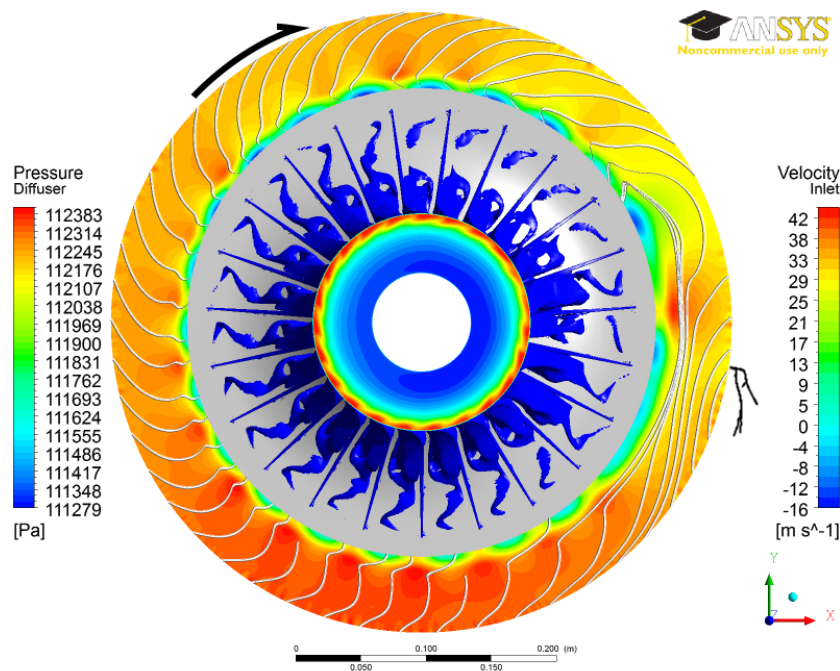
stagnation zones in the impeller. This influenced about 15 channels.

Disturbances were growing and at $t = 0.0528$ s (figure 3.37(a)) only one or two channels could have been considered as partly free from recirculation. According to figure 3.31 at this instance the mass flow rate through the blower was close to zero. This explained the fact, that stagnation region covered almost whole impeller. Streamlines in the diffuser had a form of closed circles as there was no room for the air to leave it. This explained the grey color of streamlines as most of air was neither entering nor leaving the diffuser. Figure 3.33 shows that at this moment the de-pressurization stage was initiated. Looking at the inlet one can observe, that the inlet recirculation grew significantly. Considering figure 3.31 one can see that at this time, the mass flow at this control surface (*insurf*) was already negative. Hence, the backflow was present in the inlet recirculation zone while the core flow remained positive. This fact can be regarded as one of the most interesting findings of this part of the study as it was not reported before.

In figure 3.38 the backflow is clearly visible. The direction of flow in the diffuser observed in figure 3.38(b) was reversed as air was coming from the volute towards the impeller.



(a) Streamlines at the rotor mid-span (blade-to-blade)



(b) Axial velocity component at the inlet; stagnation zones in the impeller; pressure distribution and streamlines in the diffuser

FIGURE 3.39: Surge cycle at $t = 0.0880$ s

The phenomenon appeared at almost whole circumference. Flow in the impeller was very disturbed and exhibited no regular structure with the only exception of swirls at the blade trailing edge. The inlet velocity map shows that the backflow was still taking place only in the recirculation zone while the core flow kept flowing downstream. Similarly, at the impeller outlet two flow directions were detected. Figure 3.40(a) presents the velocity component perpendicular to the surface at the impeller outlet. Black line separates the upper part of the channel which was occupied by the recirculating flow with velocity reaching $45 \frac{\text{m}}{\text{s}}$. The lower part was occupied by flow directed downstream with velocity of $32 \frac{\text{m}}{\text{s}}$. Nevertheless, as it can be observed in figure 3.40(b) air coming in normal direction immediately recirculated back towards the inlet. At $t = 0.0880$ s (figure 3.39) the shape of the diffuser streamlines suggests slower flow which is also confirmed by the size of stagnation bubbles in the impeller. Also the pressure rise in the diffuser became smaller. All these factors indicated, that the backflow was about to disappear. Just after that the flow started to stabilize and the system started the surge cycle from the beginning.

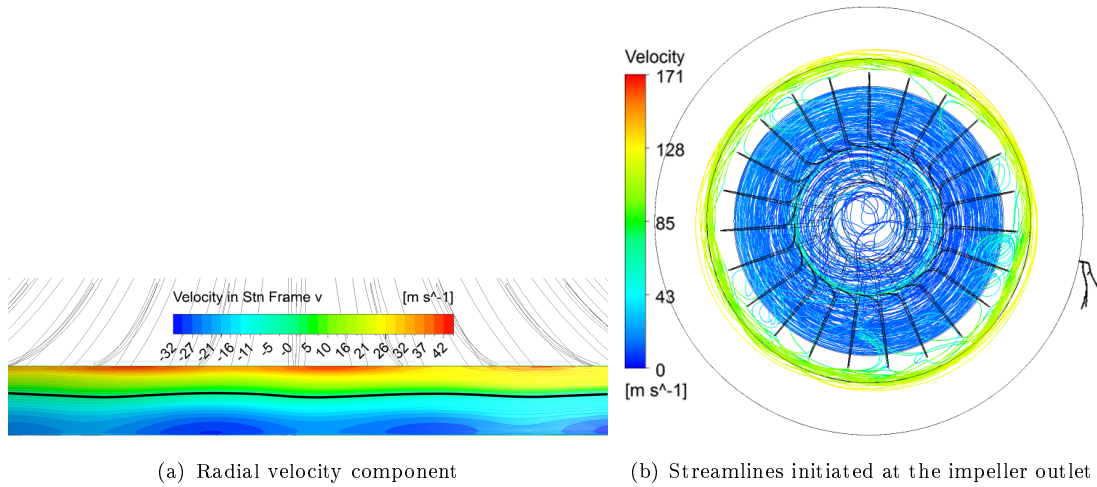


FIGURE 3.40: Recirculation at the impeller outlet at $t = 0.0704$ s

3.3 Comparison with experimental results

3.3.1 Spectral analysis

Similarly to experimental tests conducted in the quasi-dynamic procedure (presented in section 2.2.3) the frequency spectra were computed from the pressure signals gathered at the control points: p_{s-in} , p_{s-out} , p_{s-imp1} , p_{s-imp2} and p_{s-imp3} . The corresponding signals from quasi-dynamic experiment and the simulation were selected according to the procedure described in section 3.1.7. Afterwards both signals were subject to the Fourier analysis in order to obtain their frequency spectra. The limit of the highest frequency present in the simulation spectra came from the the time step and constituted:

$$f_{max} = \frac{1}{2 \cdot t_s} = 11363 \text{ Hz}.$$

The smallest frequency was different for each signal depending on the time of the simulation that was used for the calculation of the spectrum. The time of simulation was controlled manually depending on the values of key parameters monitored during the solution. The computations were carried on to cover at least 3 periods of any significant oscillation that was observed. The only exception was at $\dot{m} = 0.1 \frac{\text{kg}}{\text{s}}$ where single surge cycle required about two weeks to be computed and its amplitude was slightly increasing with each iteration. Therefore, the simulation was conducted till the moment when difference between consecutive minima/maxima was in the range of several pascals. Complete comparison of all monitoring points at all mass flow rates required analysis of 30 plots. Therefore, selection of representative plots is presented. Full set of plots can be found in appendix B. Most important frequencies observed in the simulation are listed in table 3.5.

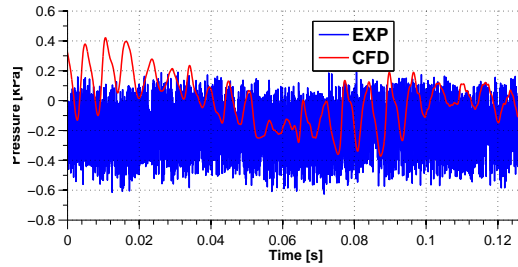
3.3.1.1 Stable working conditions

The frequency spectra under stable working conditions did not exhibit many peaks that could be related to particular flow phenomena. Therefore, this section contains selected

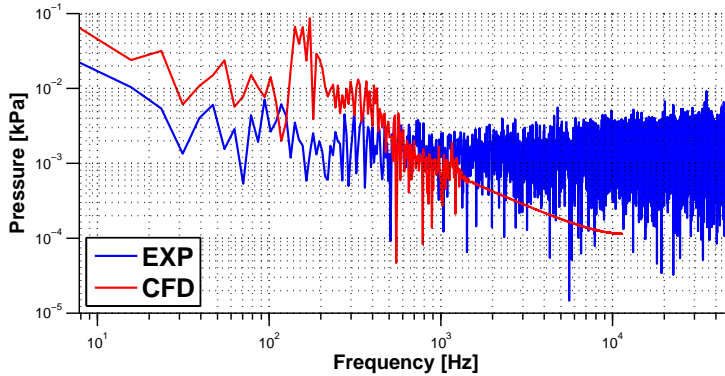
TABLE 3.5: Characteristic frequencies observed in the numerical study; abbreviations: S-present at the stable regime ($\dot{m} \geq 0.8 \frac{\text{kg}}{\text{s}}$); N-present at the pre-surge and the surge regime ($\dot{m} \leq 0.5 \frac{\text{kg}}{\text{s}}$), B-present under both: stable and unstable conditions

notation	frequency Hz	Type	Points	Amplitude kPa	Name
f_{rot}	100	B	all	various	impeller frequency
f_{BP}	2300	B	$p_{s-imp2-3}$	various	blade passing frequency
f_{BP_h}	4600	B	$p_{s-imp2-3}$	various	blade passing frequency (second harm.)
f_{ns1}	≈ 172	S	$p_{s-in}, p_{s-out}, p_{s-imp2-3}$	$\approx 10^{-1}$	
f_{nn1}	9.8	N	all	≈ 1	main surge frequency
f_{nn2}	61	N	p_{s-out}	$\approx 10^{-1}$	

plots registered at $\dot{m} = 0.8 \frac{\text{kg}}{\text{s}}$ only. A full set of frequency spectra registered at all monitoring points at all analysed mass flow rates were included in appendix B.



(a) signals



(b) frequency spectra

FIGURE 3.41: Comparison of signals obtained at p_{s-in} in the quasi dynamic experiment conducted at $TOA = 41\%$ and in the simulation at $\dot{m} = 0.8 \frac{\text{kg}}{\text{s}}$

Figure 3.41 presents signals and frequency spectra obtained at p_{s-in} . Looking at the signals one can observe, that oscillation noted in the simulation was characterized by much smaller presence of high frequency components. Consequently the frequency spectrum obtained in the simulation was much weaker at high frequencies. This discrepancy had two sources. The first was the high frequency noise being an inevitable part of experimental measurement. Second reason lied in known feature of URANS simulations, which poorly reproduce high frequency flow field fluctuations, especially when compared to LES methods [104]. The experimental signal was characterized by quite uniform distribution

of the fluctuation amplitude spectrum. In the numerical signal spectrum, group of three peaks was observed at 141 Hz, 156 Hz and $f_{ns1} = 172$ Hz.

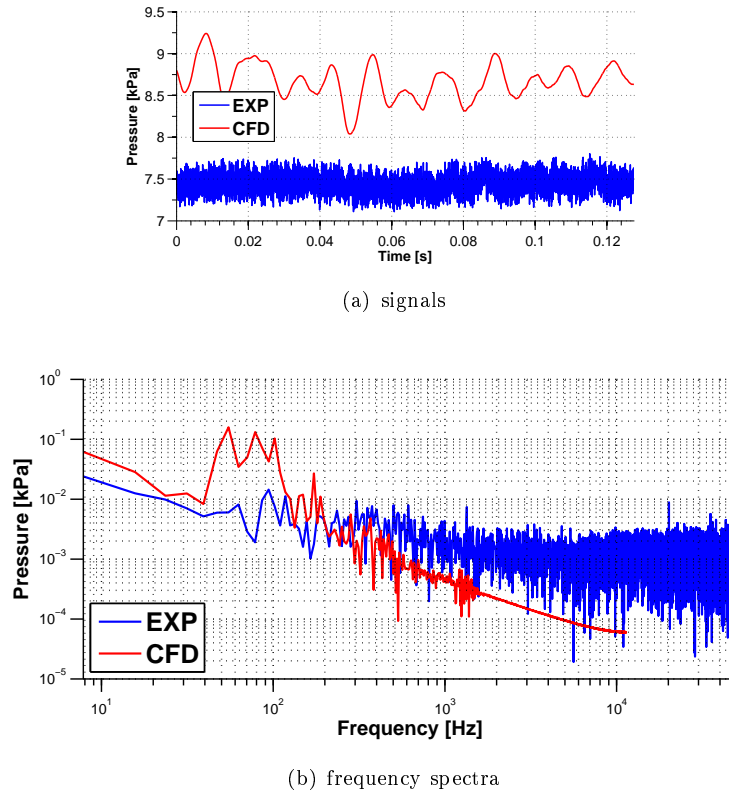


FIGURE 3.42: Comparison of signals obtained at p_{s-out} in the quasi dynamic experiment conducted at $TOA = 41\%$ and in the simulation at $\dot{m} = 0.8 \frac{\text{kg}}{\text{s}}$

Figure 3.42 demonstrates signal and spectrum attained at p_{s-out} . As a result of over-prediction of the pressure ratio the average component was much higher in the simulation. Similarly to p_{s-in} the CFD signal had higher amplitudes at low frequency components and much lower at high frequency components. The experimental spectrum was relatively flat, numerical spectrum contained peaks at 55 Hz, 78 Hz and $f_{rot} = 100$ Hz. Lower peak at $f_{ns1} = 172$ Hz was also noticeable.

As it was observed in analysed cases, the amplitude of low frequency pressure oscillations was at considerable level, however, much lower than at the non-stationary regimes. The source of this phenomenon can be explained based on plots shown in figure 3.43. It presents the behaviour of the inlet pressure signal in two cases: stable ($\dot{m} = 0.8 \frac{\text{kg}}{\text{s}}$) and unstable ($\dot{m} = 0.1 \frac{\text{kg}}{\text{s}}$). The oscillations in both cases had almost the same frequency which was close to the surge frequency $f_{nm1} \approx 10$ Hz. Nevertheless, the difference lied in damping factor. At unstable working regime (figure 3.43(a)) the amplitude rose with time, while at the stationary working regime (figure 3.43(b)) the fluctuations were going to disappear within several seconds. This finding was very interesting and confirmed the fundamental hypothesis formulated by Greitzer in his compressor surge theorem [38, 39]. In this model surge is understood as the natural frequency of the air oscillations within the system where damping depends on the mass flow rate. At the surge limit damping attains the critical value and the system transforms into unstable. In the case of examined machine, figure 3.43(b) represents the damped case and figure 3.43(a) - amplified case. One can observe also a slight difference in frequency of the pressure oscillations. It

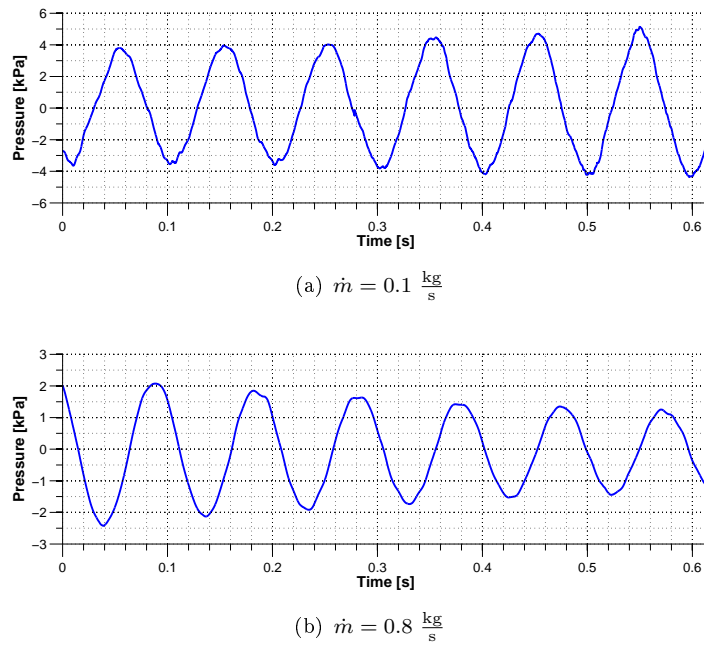


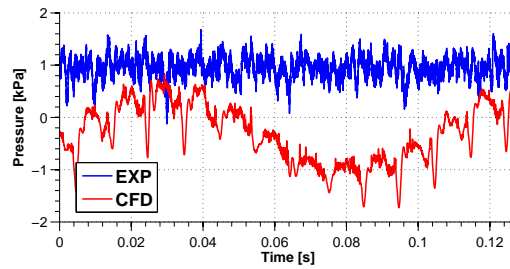
FIGURE 3.43: Variation of the mass flow averaged pressure signals at the surface *insurf* for different boundary conditions

may be caused by the fact, that damping factor is known to reduce the natural frequency of the system.

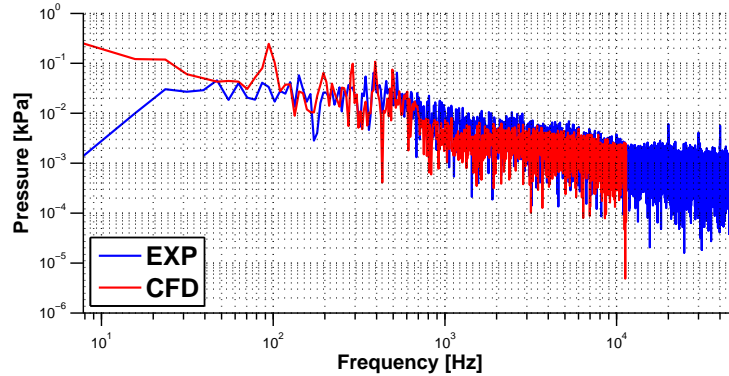
The time scale of damping was in the range of seconds, which made this phenomenon very difficult to be recorded in the experimental analysis. Such an experiment requires very precise data acquisition system and throttling valve that can be closed instantaneously. Nevertheless, in the experimental study presented in section 2.2.3 due to high precision of the quasi-dynamic analysis some symptoms of damped surge peaks were observed in the stable working regime. On the other hand, in the case of numerical simulations the time scale of a few seconds can be regarded as very large, especially if one considers the amount of time necessary to compute a single time step. In the presented study, the simulations were solved up to one second. This included as many as 23000 iterations, but it was still not enough for the low frequency oscillations to fully disappear. This caused their high amplitude at the stable frequency spectra which, however, represented the component that was decreasing with time and could not be regarded as characteristic for this regime of the blower operation.

3.3.1.2 Pre-surge

As it was stated before, simulation for two mass flow rates $\dot{m} = 0.3 \frac{\text{kg}}{\text{s}}$ and $\dot{m} = 0.5 \frac{\text{kg}}{\text{s}}$ were characterized by local instabilities and were labelled as pre-surge conditions. In this section these two cases are described and compared to the experimental data by means of the spectral analysis. As it was stated in section 3.2.2 the inlet recirculation and the progressive impeller rotating stall were believed to be initiated at the impeller leading edge. Therefore, the most crucial position for analysis of both instabilities was located in point p_{s-imp1} . Figures 3.44 and 3.45 present signals and spectra obtained at this point at $\dot{m} = 0.5 \frac{\text{kg}}{\text{s}}$ and $\dot{m} = 0.3 \frac{\text{kg}}{\text{s}}$ respectively.



(a) signals



(b) frequency spectra

FIGURE 3.44: Comparison of pressure signals obtained at p_{s-imp1} in the quasi dynamic experiment conducted at $TOA = 18\%$ and in the simulation at $\dot{m} = 0.5 \frac{\text{kg}}{\text{s}}$

The nature of differences between two working conditions can be revealed by the analysis of the source signals. At $\dot{m} = 0.5 \frac{\text{kg}}{\text{s}}$ the numerical curve exhibited long period oscillations while the experimental curve was affected by a high frequency fluctuations only. At $\dot{m} = 0.3 \frac{\text{kg}}{\text{s}}$ the situation was opposite: the experimental curve exhibited a long period oscillations with minor influence of high frequencies. The numerical curve was characterised by a high frequency oscillations only, but of much higher amplitude.

Frequency spectrum of signal obtained in the simulation at $\dot{m} = 0.5 \frac{\text{kg}}{\text{s}}$ (figure 3.44) showed two dominating peaks. One of them was close to the surge frequency 9.8 Hz. This peak was not observed explicitly in the spectrum due to limited resolution and spectral leakage (see section 3.1.7.2), hence the frequency was measured directly from the signal. Second strong component had an impeller rotational frequency $f_{rot} = 100$ Hz. One can observe that weaker peaks appeared also at its harmonic frequencies up to $5 \cdot f_{rot} = 500$ Hz. The experimental signal at this mass flow rate was affected by a broadband noise caused by the inlet recirculation (see section 2.2.3.2). Frequency spectrum of the signal obtained in the simulation at $\dot{m} = 0.3 \frac{\text{kg}}{\text{s}}$ (figure 3.45) contained group of numerous peaks enclosed between 78 Hz and wide peak at ≈ 1100 Hz. As mentioned, this kind of broadband noise was characteristic for the inlet recirculation.

It could be stated that in the simulation and the experiment the blower was affected by several modes of air fluctuations which could be damped or amplified depending on the machine operating point. Each of these modes corresponded to different phenomenon. In this case it is believed that different combinations of surge ($f \approx 10$ Hz), inlet recirculation (broadband noise) and progressive impeller rotating stall ($10 \text{ Hz} < f < 100 \text{ Hz}$)

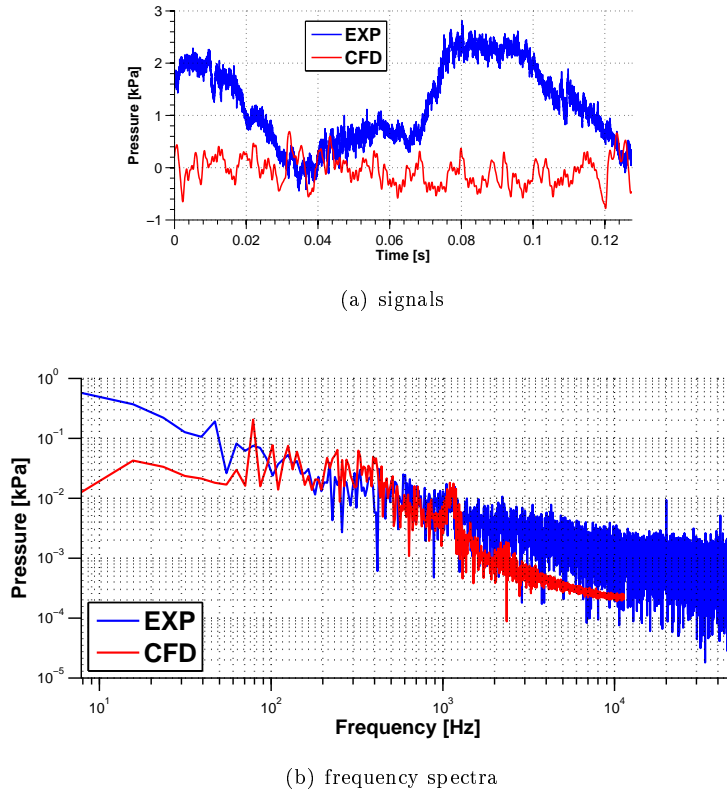


FIGURE 3.45: Comparison of pressure signals obtained at p_{s-imp1} in the quasi dynamic experiment conducted at $TOA = 8\%$ and in the simulation at $\dot{m} = 0.3 \frac{\text{kg}}{\text{s}}$

was observed. The difference lied in the fact, that the inlet recirculation in the experiment appeared as the first instability, while in the simulation it was preceded by the progressive impeller rotating stall.

3.3.1.3 Deep surge

All plots included in this section were computed from signals registered at $\dot{m} = 0.1 \frac{\text{kg}}{\text{s}}$. Figure 3.46 presents pressure signal and frequency spectra obtained in the experiment and the simulation at the inlet control point. Both signals contained strong low frequency component representing the main surge oscillations. According to table 2.4 presented in section 2.2.3.2 the frequency of experimental surge cycle equalled to $f_{sn1} = 10.8 \text{ Hz}$. Signal plot showed that in the simulation it was slightly lower $f_{nm1} = 9.8 \text{ Hz}$. The oscillation amplitude observed in the numerical results was much higher than in the experiment. The observed difference most likely resulted from discrepancy between outlet boundary condition and its numerical representation. Also factors such as turbulence model and mesh refinement could have contributed to this difference to some extent (see section 3.2.3). Moreover, one can observe that amplitude was increasing with time. The computations were conducted till the moment when subsequent minima/maxima differed by no more than fraction of kPa. As presented, this criterion was achieved after 0.6 s. The numerical analysis revealed structure of the signal which was close to linear. In the case of experiment, presence of higher frequency components was clearly visible in the signal. In both frequency spectra a very strong peak was observed at the surge ($f_{nm1} = 9.8 \text{ Hz}$

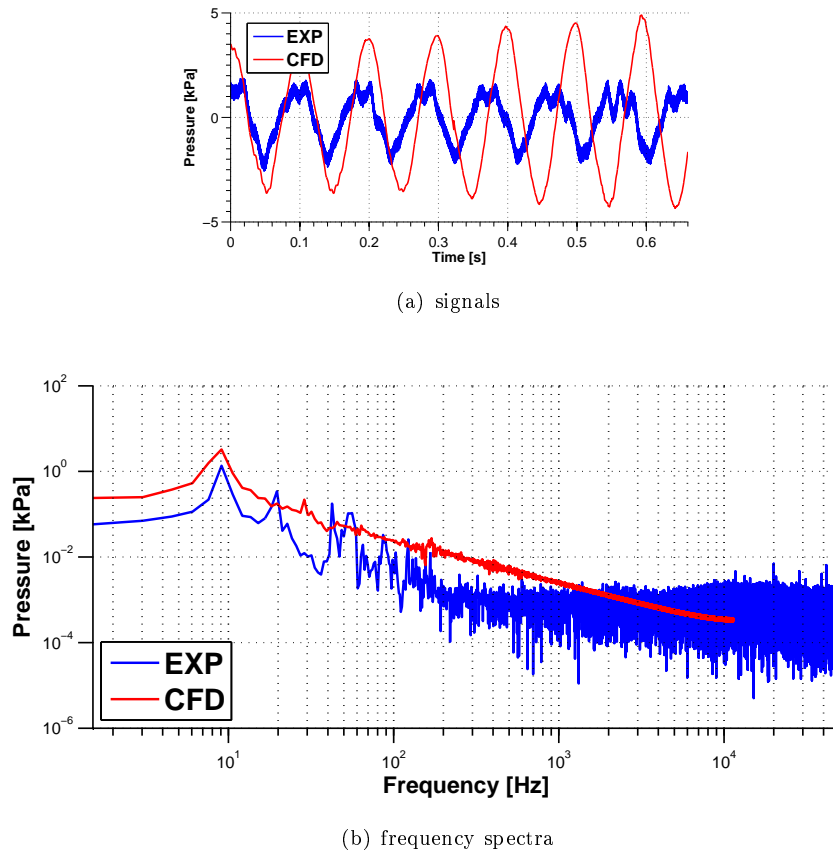


FIGURE 3.46: Comparison of signals obtained at p_{s-in} in the quasi dynamic experiment conducted at $TOA = 5\%$ and in the simulation at $\dot{m} = 0.1 \frac{\text{kg}}{\text{s}}$

and $f_{sn1} = 10.8 \text{ Hz}$). The difference in frequencies was not observed in the spectrum due to its limited resolution. Then, as the frequency rose, the amplitude of the signal harmonics decreased gradually. In fact, spectrum obtained from signal gathered in the simulation was almost totally free from another peaks which confirmed statement presented in section 3.2.3 that in the inlet pipe CFD surge model was almost perfectly linear.

At the outlet control point p_{s-out} (figure 3.47) signal obtained in the simulation revealed presence of higher order components. At this location the average value of the CFD signal was higher. This tendency was constant for all regimes due to over-prediction of the numerical results described in section 3.1.5. Contrary to the inlet signal the amplitude at the outlet was higher in the experiment than in the simulation. Both frequency spectra were dominated by the deep surge peak ($f_{nn1} = 9.8 \text{ Hz}$ and $f_{sn1} = 10.8 \text{ Hz}$, difference not observed in spectrum due to limited resolution) which attained exactly the same amplitude in both signals. Therefore, it can be concluded that apart from discrepancies in the inlet domain, the amplitude of the surge cycle in the outlet plenum was modelled accurately. Experimental spectrum contained also a peak at $f_{sn3} = 43.5 \text{ Hz}$. In the case of CFD weaker peaks were observed at 19 Hz, 29 Hz, 33 Hz and $f_{nn2} = 61 \text{ Hz}$. After that, the spectrum continued to decrease.

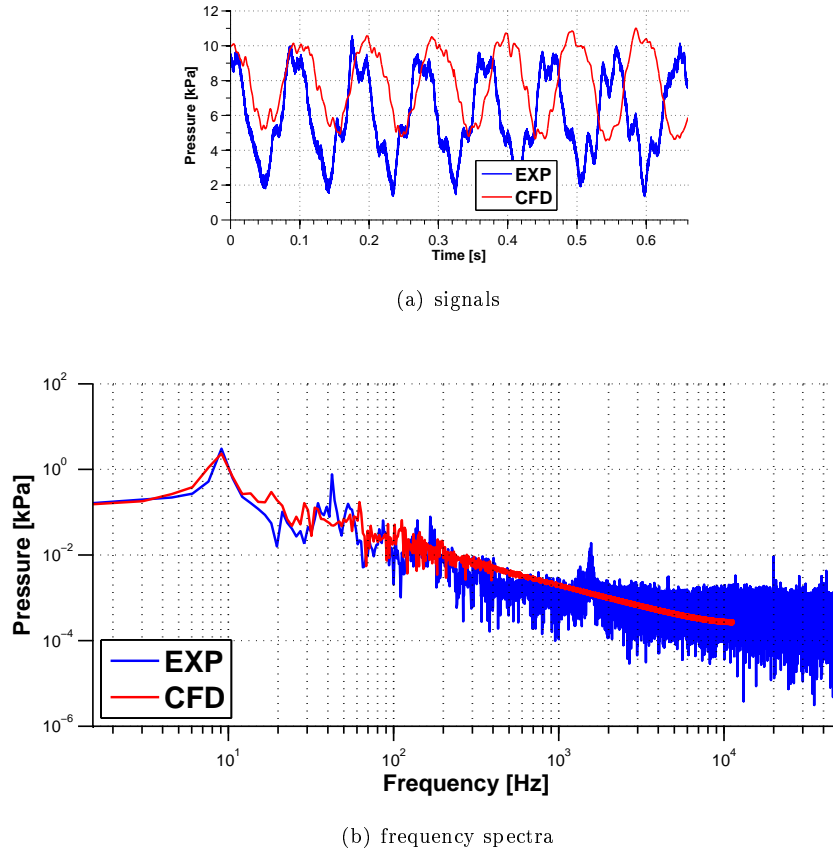


FIGURE 3.47: Comparison of pressure signals obtained at p_{s-out} in the quasi dynamic experiment conducted at $TOA = 5\%$ and in the simulation at $\dot{m} = 0.1 \frac{\text{kg}}{\text{s}}$

3.3.2 Influence of the outlet plenum volume

3.3.2.1 Spectral analysis of the numerical surge with reduced plenum volume

TABLE 3.6: Characteristic frequencies observed at the deep surge in the numerical study with the reduced plenum volume

notation	frequency Hz	Points	Amplitude kPa	Comments
f_{BP}	2300	$P_{s-in}, p_{s-imp1-3}$	various	blade passing frequency
f_{BP_h}	4600	$p_{s-imp2-3}$	various	blade passing frequency (second harm.)
f_{nn1}^{SP}	14	all	≈ 10	deep surge
f_{nn4}^{SP}	≈ 65	$p_{s-out}, p_{s-imp2-3}$	≈ 1	impeller-diffuser instability

The experimental study included examination of the blower $DP1.12$ with reduced length of the outlet pipe (named as the SP case compared to the LP case with large plenum volume). Results presented in section 2.2.4 confirmed the influence of the plenum volume on surge characteristics. This section is devoted to the analogous numerical analysis. The volume of the outlet domain was reduced to $V_{SP} = 0.0435 \text{ m}^3$ and a new simulation was run with the same boundary conditions. Figures 3.48 and 3.49 present the frequency spectra obtained at $\dot{m} = 0.1 \frac{\text{kg}}{\text{s}}$ with the reduced plenum volume at p_{s-in} and p_{s-out}

respectively. Main frequencies observed in this part of the study are summarized in table 3.6.

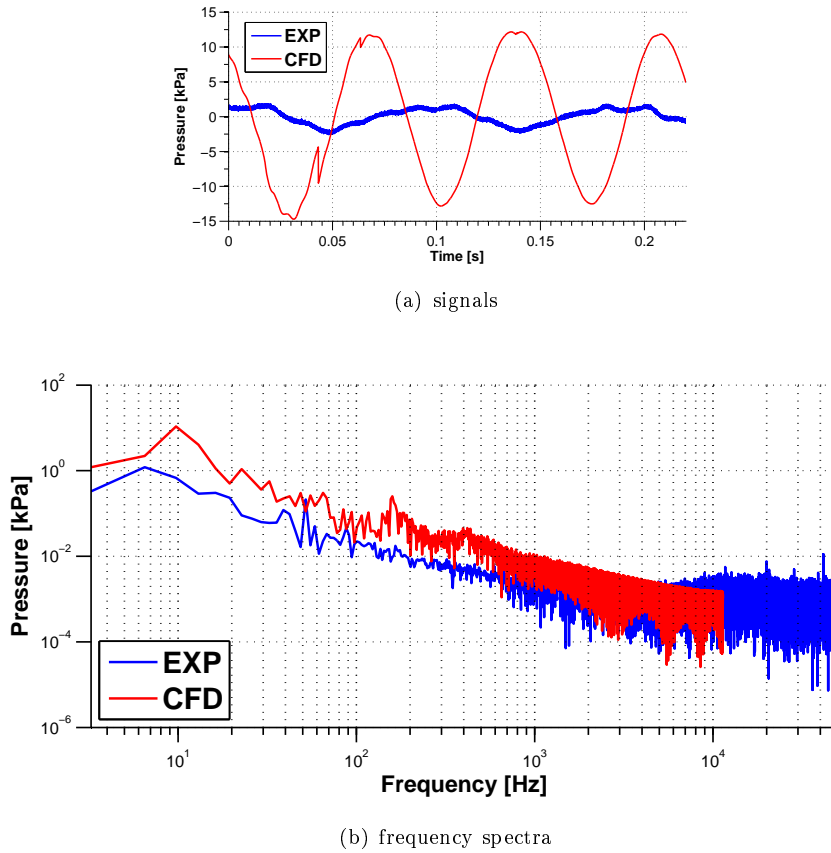


FIGURE 3.48: Comparison of pressure signals obtained at p_{s-in} in the quasi dynamic experiment conducted at $TOA = 5\%$ and in the simulation at $\dot{m} = 0.1 \frac{\text{kg}}{\text{s}}$ with reduced plenum volume

Figure 3.48 presents p_{s-in} pressure signals gathered in the experiment and simulation and their spectra. The most apparent difference lied in the amplitude of oscillations. At the experimental stand with reduced plenum it was much smaller than in the LP case, while CFD signal amplitude was even higher. The CFD oscillation was also very close to linear which resulted in nearly flat frequency spectrum dominated by the surge peak. Due to limited resolution, value of the surge frequency was computed directly from signal plot and equalled $f_{nn1}^{SP} = 14 \text{ Hz}$.

Similarly to the LP case, oscillations at the outlet were much better reproduced by the numerical model. Figure 3.49 presents p_{s-out} pressure signals gathered in the experiment and simulation and their spectra. One can observe, that the amplitude of CFD oscillations was only slightly over-predicted by the simulation and both signals had comparable shape. The frequency spectrum revealed that each spectrum was dominated by two peaks. In case of the experiment it was the surge peak $f_{sn1}^{SP} = 11 \text{ Hz}$ and $f_{sn2}^{SP} = 41 \text{ Hz}$. In the numerical model it was the surge peak $f_{nn1}^{SP} = 14 \text{ Hz}$ and $f_{nn4}^{SP} \approx 65 \text{ Hz}$.

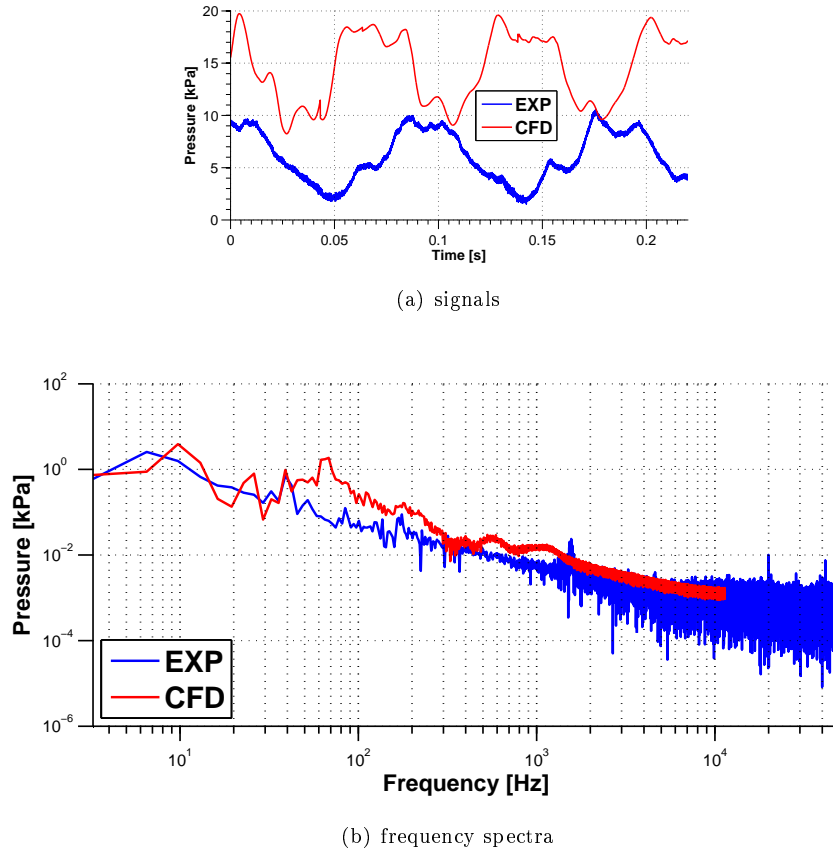


FIGURE 3.49: Comparison of pressure signals obtained at p_{s-out} in the quasi dynamic experiment conducted at $TOA = 5\%$ and in the simulation at $\dot{m} = 0.1 \frac{\text{kg}}{\text{s}}$ with reduced plenum volume

3.3.2.2 Analysis of the deep surge dominating frequencies

In section 2.2.4.3, comparison of dominating surge frequencies of the LP case and SP case were provided. Study of frequency spectra revealed existence of two peaks $[f_{sn1}, f_{sn1}^{SP}] \approx 12 \text{ Hz}$ and $[f_{sn3}, f_{sn2}^{SP}] \approx 41 \text{ Hz}$ named as f_A and f_B respectively. Both peaks were present in the SP and the LP configurations. f_A had the strongest amplitude in the LP case, while in the SP case f_B dominated. It was also shown that the f_A frequency was closely associated with frequency of the Helmholtzian resonator. The f_B frequency was suspected to be caused by an instability located in the vicinity of p_{s-imp3} control point. Table 3.7 contains data presented in table 2.6 supplemented with results of the numerical study. Values of the experimental peaks were updated based on transformed spectra used for the sake of comparison (see section 3.1.7.2).

In both cases of the plenum volume, frequency of the main surge frequency was very close to the experiment and slightly lower than frequency of the Helmholtz resonator. Peak A in the experimental analysis was much stronger in the LP case. In the simulation, situation was opposite. The oscillations p_{s-out} stayed on comparable level to the experimental signal. The difference was much stronger in the case of p_{s-in} . This resulted in ratio $\frac{p_{s-out}}{p_{s-in}} = 0.7$ in the LP case. In SP case this ratio was even smaller $\frac{p_{s-out}}{p_{s-in}} = 0.4$. This confirmed that positioning of the boundary conditions closer to the impeller increased discrepancy between the model and the experimental rig.

TABLE 3.7: Surge amplitudes and frequencies in the SP and the LP cases

SP case ($1.98 \cdot 10^{-2} \text{ m}^3$)				
		Experiment	Simulation	Helmholtz resonator
Peak A	Frequency	14 Hz	14 Hz	17 Hz
	Amplitude p_{s-in}	1000 Pa	12000 Pa	
	Amplitude p_{s-out}	1900 Pa	4300 Pa	
	Ratio $\frac{p_{s-out}}{p_{s-in}}$	1.9	0.4	
Peak B	Frequency	41 Hz	60 – 70 Hz	–
	Amplitude p_{s-in}	220 Pa	–	
	Amplitude p_{s-imp3}	400 Pa	1000 Pa	
	Ratio $\frac{p_{s-imp3}}{p_{s-in}}$	1.8	–	
LP case ($7.31 \cdot 10^{-2} \text{ m}^3$)				
		Experiment	Simulation	Helmholtz resonator
Peak A	Frequency	10.8 Hz	9.8 Hz	12 Hz
	Amplitude p_{s-in}	1400 Pa	3300 Pa	
	Amplitude p_{s-out}	3000 Pa	2300 Pa	
	Ratio $\frac{p_{s-out}}{p_{s-in}}$	2.1	0.7	
Peak B	Frequency	44 Hz	61 Hz	–
	Amplitude p_{s-in}	180 Pa	–	
	Amplitude p_{s-imp3}	590 Pa	110 Pa	
	Ratio $\frac{p_{s-imp3}}{p_{s-in}}$	3.2	–	

It is not certain whether peak B was observed in the numerical model. The closest noticeable amplification noted in the simulation was located in the region 60 – 70 Hz. In the SP case it was relatively strong and equalled 1 kPa in p_{s-imp3} . In the LP case it was hardly visible and equalled 110 Pa. This frequency is typical for PIRS [33] and, therefore it could be suspected that this peak is associated with this phenomenon (see section 3.2.2.2). However, presented data did not allow to support or negate this hypothesis and this matter should be addressed to further studies.

3.3.3 Representation of signals in the phase space

Phase portrait of each signal is presented in two figures. First contains comparison of phase portraits obtained from the simulation signals at different flow regimes. In the second, the comparison between phase portraits obtained from numerical and experimental analysis is provided. Signals p_{s-imp2} and p_{s-imp3} were not presented due to the fact, that the phase portraits were strongly affected by pressure oscillations due to passing blades.

3.3.3.1 Inlet

Figure 3.50 demonstrates the phase trajectory of the signal in point p_{s-in} . Plot includes the phase portrait obtained at the deep surge and its projections onto three planes. Projections contain also the signals attained at different mass flow rates in the same way as it was done in section 2.2.3.4 with TOA values. Under stable conditions the plot exhibits large rate of fluctuations of the second derivative which was common for all points in the

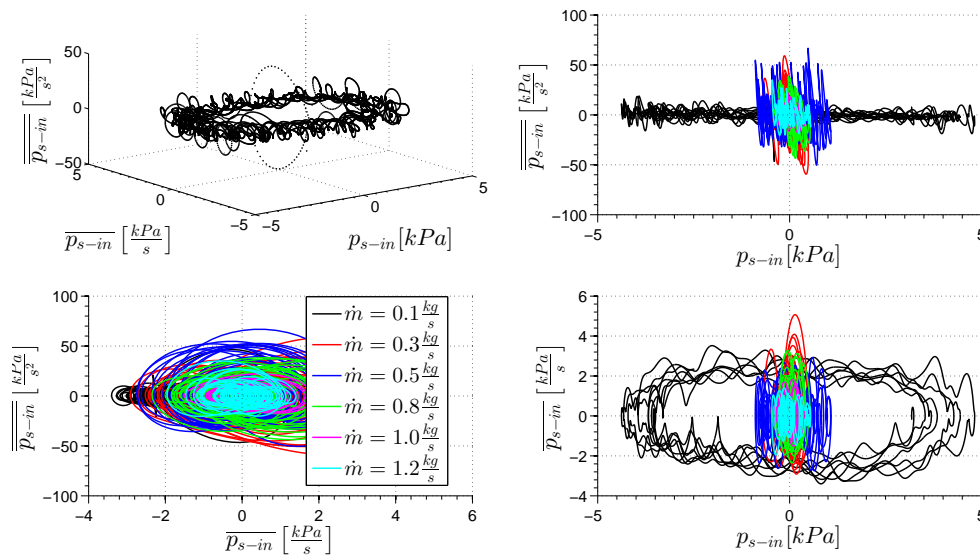


FIGURE 3.50: Phase portrait of the pressure signals in the control point p_{s-in} at \dot{m} values corresponding to different working regimes

inlet domain. The first derivatives behaved analogously to how it was observed in the experiment. The surge limit cycle had a clear toroidal structure circulating around the point $(0, 0, 0)$. Almost elliptical character of the phase portrait suggested that the oscillations had a form very close to linear harmonic oscillations. The simulation reconstructed a pure version of the surge which was only slightly perturbed by higher order phenomena. The projection $\overline{\overline{p_{s-in}}} - p_{s-in}$ showed that the fluctuations of the second derivative at the surge were small compared to the fluctuations observed at the pre-surge. This is why the shape of the surge limit cycle, which had a form of an ellipse, was not clearly distinguishable at this projection. On the other hand, projection $\overline{\overline{p_{s-in}}} - p_{s-in}$ exhibited similar range of fluctuations of the first derivative at all non-stationary regimes.

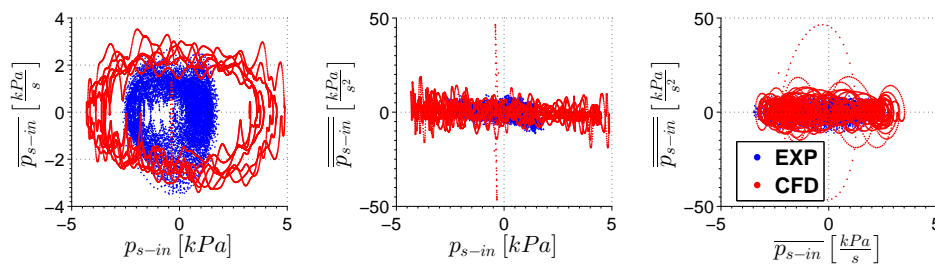


FIGURE 3.51: Comparison of the phase portrait projections of the pressure signals in the control point p_{s-in} at $\dot{m} = 0.1 \frac{\text{kg}}{\text{s}}$ and $TOA = 5\%$

Comparison between numerical and experimental surge cycle is presented in figure 3.51. 3-dimensional plot of both signals drawn together was not readable and was omitted. One can observe that shape of the limit cycle had a very similar character at all projections. However, the experimental phase portrait had more complex shape reflecting presence of non-linear effects in the deep surge cycle. The character of oscillations in the simulation was close to harmonic compared to the experimental surge affected by higher order disturbances. This conclusion could be also confirmed by analysis of the pressure

signals presented in figure 3.46, where the numerical signal at the inlet was almost purely harmonic.

3.3.3.2 Outlet

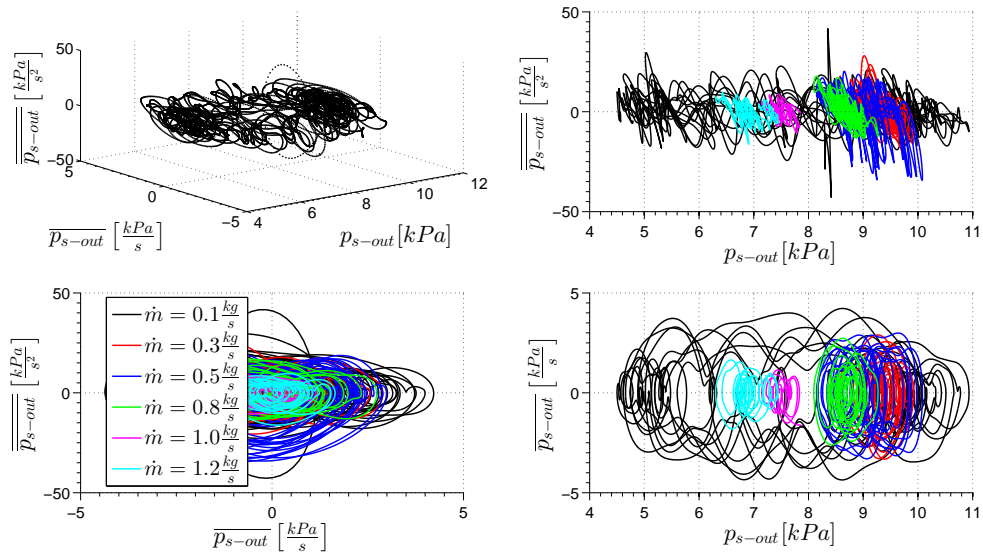


FIGURE 3.52: Phase portrait of the pressure signals obtained in the simulation in the control point p_{s-out} at \dot{m} values corresponding to different working regimes

The phase portrait of the outlet pressure p_{s-out} is shown in figure 3.52. At stable regime the rate of derivative fluctuation and the rate of pressure fluctuation was much lower than at the unstable regime. However, it was higher than it was observed at the experimental stand. Then at $\dot{m} = 0.5 \frac{\text{kg}}{\text{s}}$ and $\dot{m} = 0.3 \frac{\text{kg}}{\text{s}}$ the phase portrait had a form similar to the experimental transient phase. At the deep surge, the limit cycle had a toroidal shape, with smaller gap in the middle of the torus. This resulted from presence of non-linear fluctuations that were also observed in figure 3.47. Figure 3.53 shows comparison of the surge cycle with its experimental representation. Contrary to the situation observed at the inlet, at this location the pressure amplitude was smaller than in the experiment. The rate of derivative fluctuation was comparable in both cases.

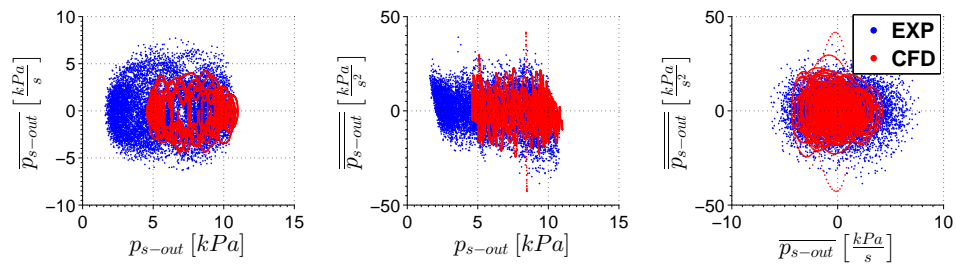


FIGURE 3.53: Comparison of the phase portrait projections of the pressure signals in the control point p_{s-out} at $\dot{m} = 0.1 \frac{\text{kg}}{\text{s}}$ and $TOA = 5\%$

3.3.3.3 Impeller inlet

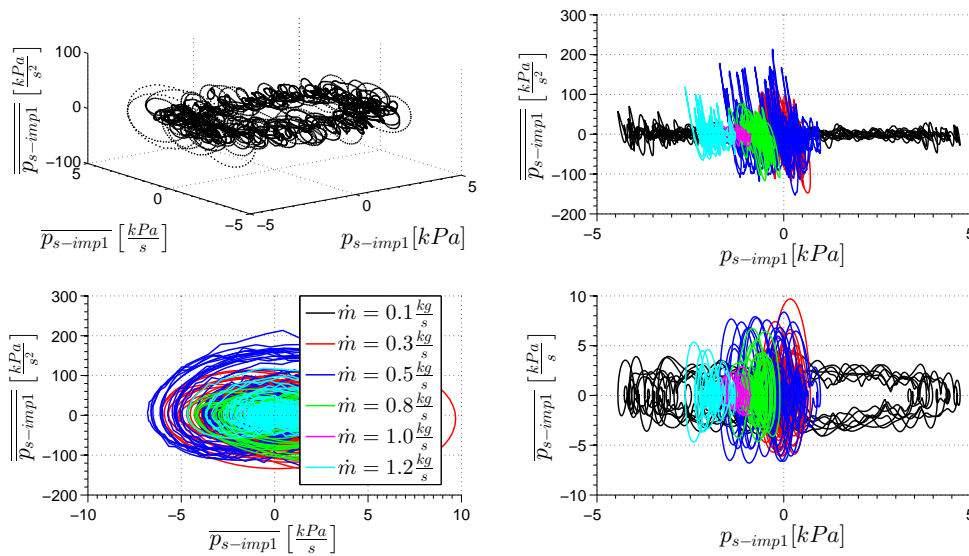


FIGURE 3.54: Phase portrait of the pressure signals obtained in the simulation in the control point p_{s-imp1} at \dot{m} values corresponding to different working regimes

The phase portrait at the impeller inlet looked very similar to the one noted at the inlet. The surge phase cycle shown in figure 3.54 had a toroidal shape with less apparent gap that indicated stronger presence of non-linear fluctuations. The main difference between inlet and p_{s-imp1} was noted at the pre-surge regime ($\dot{m} = 0.3 \frac{\text{kg}}{\text{s}}$ and $\dot{m} = 0.5 \frac{\text{kg}}{\text{s}}$). Similarly to p_{s-in} , under stable conditions the rate of second derivative fluctuations was much higher than it was noted in the stable regime. However, in this case the rate of first derivative fluctuation was much higher than in the case of the surge or than at any other point analysed so far. Similarly to the experimental analysis, this phenomenon could be associated with appearance of boundary layer separation at the impeller leading edge associated with the inlet recirculation or the flow instability observed at $\dot{m} = 0.5 \frac{\text{kg}}{\text{s}}$. Comparison with the experimental surge phase portrait is plotted in figure 3.55. It showed tendency of over-prediction of the pressure amplitude similarly to p_{s-in} . Rate of derivative fluctuation was comparable at both methods which can be observed in projection $\overline{\overline{p_{s-imp1}}} - \overline{p_{s-imp1}}$.

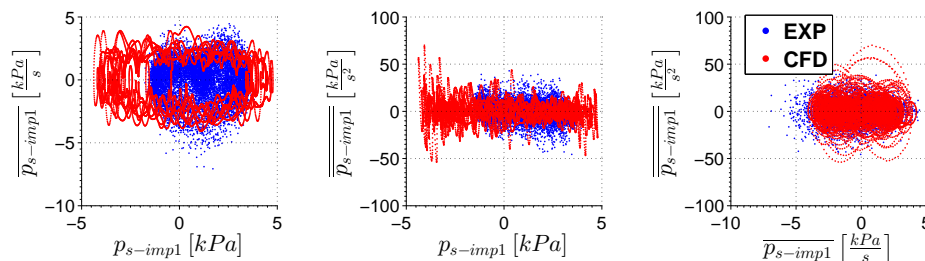


FIGURE 3.55: Comparison of the phase portrait projections of the pressure signals in the control point p_{s-imp1} at $\dot{m} = 0.1 \frac{\text{kg}}{\text{s}}$ and $TOA = 5\%$

3.4 Summary

In the numerical study the blower was found to operate in four regimes. Numerical simulation allowed to analyse the structures in detail and draw several conclusions about the flow structures present in each of them. List presented below contains four working regimes and the most noticeable findings regarding each of them:

1. stable working regime ($\dot{m} \in [0.8 \frac{\text{kg}}{\text{s}}, 1.0 \frac{\text{kg}}{\text{s}}, 1.2 \frac{\text{kg}}{\text{s}}]$) - the flow field was reasonably constant in time with the exception of the secondary flows over the impeller blade tips. Simulation reproduced shape of the blower performance curve with tendency to over-predict the machine pressure ratio (section 3.2.1).
 - Stagnation zones in the impeller caused by the secondary flows over the blade tip were present at higher mass flow rates $\dot{m} \in [1.0 \frac{\text{kg}}{\text{s}}, 1.2 \frac{\text{kg}}{\text{s}}]$. At $0.8 \frac{\text{kg}}{\text{s}}$ these structures did not appear confirming that under nominal conditions the impeller was operating optimally. The pressure ratio obtained in the simulation slightly over-predicted the experimental data (section 3.2.2.1).
 - At all considered conditions the stagnation zone appeared in the volute above the diffuser outlet. At $0.8 \frac{\text{kg}}{\text{s}}$ a thin layer of stagnation was observed at the diffuser front wall along its whole length (section 3.2.2.1).
2. pre-surge ($\dot{m} = 0.5 \frac{\text{kg}}{\text{s}}$) - recurrent flow instability was detected in the impeller and the diffuser. Due to the fact, that instability was very weak, the overall machine operation was regarded as stable (section 3.2.2.2).
 - Diffuser was affected by circumferential fluctuations of the flow angle. In the impeller, migration of the stagnation zone was observed from the inlet leading edge towards the trailing edge. It was observed that it also had a tendency to move from the shroud towards the hub (section 3.2.2.2).
 - Fluctuations in the diffuser could be induced by fluctuations in the impeller and vice versa (section 3.2.2.2).
 - Impeller instability can be classified as the progressive impeller rotating stall (section 3.2.2.2).
3. pre-surge ($\dot{m} = 0.3 \frac{\text{kg}}{\text{s}}$) - inlet recirculation (IR) appeared upstream of the impeller leading edge. The structure was permanent, however its thickness was fluctuating. Due to local character of the instability the overall machine operation was regarded as stable (section 3.2.2.3).
 - Instability was initiated at the impeller blade leading edge close to the shroud. Flow recirculated creating flow structure in a shape of a torus (section 3.2.2.3).
 - Recirculating flow was characterized by high energy, which resulted in increased average pressure within the recirculation zone. This finding was in agreement with the experimental results and state of the art (section 3.2.2.3).
 - As it was mentioned, pressure was higher in very thin IR layer. The fact, that its thickness was varying in time can be a possible explanation of pressure jumps registered in the experiment (section 3.2.2.3).
 - Presented study was the first documented instance of describing the IR in detail by means of the numerical simulation (section 3.2.2.3).

- Analysis of $\dot{m} = 0.5 \frac{\text{kg}}{\text{s}}$ shown that instability present at this mass flow rate could be triggered by the same phenomenon as IR: flow separation at the impeller leading edge (section 3.2.2.2). Therefore, it could be concluded that appearance of the IR decreased the chances of propagation of another instabilities in the impeller and the diffuser. This statement was also supported by experimental results. Spectral maps in section 2.2.3.2 showed that as long as the IR was present, pressure in another zones was relatively stable. IR disappearance was concurrent with appearance of instabilities in another zones.
4. deep surge ($\dot{m} = 0.1 \frac{\text{kg}}{\text{s}}$) - a low frequency cycle of flow fluctuations of high amplitude. Oscillations influenced whole domain. The surge cycle included a phase of flow in normal direction and phase of the reversed flow. Similarly to the experiment, this regime was regarded as very unstable and dangerous (section 3.2.3).
- Numerical model of the deep surge had a character of periodical oscillations with frequency of 9.8 Hz. Pressure and mass flow-rate signals had a shape of the surge cycle sinusoidal oscillation with limited presence of the higher order terms. Phase shift between \dot{m} and p signals was close to 90° . Full cycle included two phases: regular work, and de-pressurization (section 3.2.3.1).
 - At regular work phase, the machine pressure ratio was gradually increasing till the moment or reaching the highest value that can be generated by the machine. During this phase, the mass flow rate was increasing, reached the maximum and started to decrease. At the very end of this phase, the flow direction was reversed (section 3.2.3.1).
 - De-pressurization phase was characterized by quick drop of the pressure ratio. During de-pressurization mass flow rate started to increase (section 3.2.3.1).
 - At de-pressurization phase structure similar to the inlet recirculation was observed at the impeller outlet (section 3.2.3.2).
 - The backflow in the inlet pipe, if present, was always occupying part of the cross-section in close vicinity of the pipe wall. It co-existed with the core flow going in the regular direction in the central part of the cross-section (section 3.2.3.2).

Comparison between the numerical and the experimental data included several methods: spectral analysis, phase portraits and raw signal analysis. The main conclusions from spectral analysis and comparison of the raw signal are presented below:

- Each simulation was started with certain initial conditions and considerable amount of iterations was needed to obtain stabilised flow field. During stabilisation a low-frequency fluctuations were observed with frequency very close to frequency of the deep surge cycle. This confirmed the fundamental assumption formulated by Greitzer [38, 39], that the deep surge corresponds to a natural frequency of the flow which is damped in the stable working conditions (section 3.3.1.1).
- Numerical model very well reproduced the main surge cycle. Surge frequency obtained in the numerical study was in close agreement with the experimental result. Blade passing and impeller frequencies were well reproduced by the simulation. Another high frequency peaks were usually not observed in the numerical study or their size was much smaller than in the experiment (section 3.3.1.3).

- Surge cycle obtained in the numerical study was characterized by over-estimated fluctuations in the inlet pipe. This discrepancy was caused by the outlet boundary condition. Under unstable working conditions, the valve characteristics was non-linear. Creation of such a characteristics would require another experimental rig which was far beyond means and scope of this study. The problem was partially solved by use of large volumes of the inlet and the outlet pipe sections which allowed to obtain reasonable numerical model of the surge cycle, which was not met in state of the art. However, one has to be aware of its limitations (section 3.3.1.3).
- Spectral characteristics obtained in the numerical analysis in the case of the reduced plenum volume was relatively flat and only some peaks were observed. Flow was dominated by the deep surge peak which was much stronger than in the experiment. Its frequency was very close to the experimental result. Close proximity of the boundary condition increased over-prediction of pressure variation in the inlet pipe (section 3.3.2).

Main conclusions drawn from analysis of the phase portraits:

- Phase portraits obtained in the simulation under stable conditions had very similar shape to the experimental ones. The main difference lied in over-predicted rate of fluctuation of pressure and its derivatives, especially the second derivative (section 3.3.3).
- At the impeller inlet zone at the pre-surge conditions ($\dot{m} \in [0.5 \frac{\text{kg}}{\text{s}}, 0.3 \frac{\text{kg}}{\text{s}}]$) rate of derivatives fluctuation was much higher and indicated appearance of the first local instabilities. This was mostly visible in the point located close to the impeller leading edge (section 3.3.3).
- Surge limit cycle drawn from signals obtained in the numerical analysis had elliptical shape. At all analysed locations the numerical limit cycles were in good agreement with the experimental ones. The limit cycle obtained from numerical data had shape closer to elliptical which is usually resulting from purely harmonic oscillations. This confirmed that the numerical surge cycle was less perturbed by the higher order phenomena (section 3.3.3).

Acknowledgments

Results of the numerical study were obtained using the EPSRC funded ARCHIE-WeSt High Performance Computer (www.archie-west.ac.uk). EPSRC grant no. EP/K000586/1



Closing remarks

4.1 Main achievements of the present study

The experimental and numerical investigations included a wide range of data collection and analysis methods that allowed for drawing several conclusions regarding the unstable phenomena. Sections 2.3 and 3.4 summarized the main outcomes that were given for each part separately. The list below provides only the most important points that can be considered as a valuable contribution to the contemporary state of knowledge on these phenomena, namely:

Quasi-dynamic analysis - a novel method developed in the experimental analysis. It allowed one to obtain spectral maps of very high resolution. These maps provided a clear distinction between different phases of blower operation and illustrated a spectral structure of each of them. Very low and blurred frequency peaks at the stable working regime in the close proximity of frequencies that are characteristic of pressure oscillations in the unstable operation were observed. This confirmed the fundamental claim of Greitzer lumped parameter model and could be an interesting method of predicting possible frequencies of unstable oscillations in different machines.

RDF factor - The analysis of trajectories of pressure signals in the phase space resulted in a proposal of the RDF (rate of derivative fluctuation) factor that can be applied to real-time monitoring of flow instabilities. Values higher than 3 indicate danger of the unstable blower operation. This observation can be used to design a new type of anti-surge device based on detection of local instabilities.

Numerical simulation of the inlet recirculation - The CFD study included simulations of accuracy that was not present in the state of the art. Thus, a structure of the inlet recirculation was modelled in detail. Results confirmed that the inlet recirculation zone was characterized by higher average pressure. Its thickness was varying in time and this possibly explains short pressure drops obtained in the experiment. These conclusions can be a starting point for creation of a mathematical model of the inlet recirculation and formulation of the stability criteria.

Numerical simulation of the deep surge - The numerical simulation of the deep surge was conducted with a very small time step and, as a result, a detailed analysis of the deep surge cycle was possible. The surge frequency was in close agreement with the experiment, especially in the case of the large outlet plenum volume. The surge cycle consisted of a phase of regular work and de-pressurization that appeared after reaching the machine maximum pressure ratio. Short periods of appearance and disappearance of the inlet recirculation and impeller instabilities were also observed. The reversed flow in the inlet pipe was present in close vicinity of the pipe wall, whereas the region close to its axis was occupied by air flowing in the normal direction.

4.2 Answer to the thesis

As a result of the exhaustive experimental and numerical studies, the main advantages and limitations of CFD simulations of unstable flow phenomena in centrifugal compressing units were revealed. It provided complementary data that decently complied with the experiment. The performance curves from the numerical and experimental analyses were following a similar trend with slight over-prediction of pressure ratio obtained with CFD. The frequency spectra and phase trajectories also confirmed close behaviour of the CFD signal and the experimental data.

There was a reasonable correspondence between different phases of unstable work of the machine obtained in the simulation and in the experiment. The most clear similarity was observed at the deep surge and at the inlet recirculation. The transient phase also revealed certain similarities, however, the experimental data neither confirmed nor denied the flow structures observed in corresponding simulation. In all cases the CFD data provided a description of the flow field with a level of information that was far beyond classic experimental method.

The observed discrepancies concerned mainly a sequence of unstable flow structures that appeared in the experiment and the simulation with a decreasing mass flow rate. In the simulation, the first instability had a form of flow separations that were propagating downstream of the impeller leading edge, whereas in the experiment, the inlet recirculation was observed first. This showed that at given level of the mesh refinement the CFD methods are not fully reliable in predicting the moment of appearance of particular flow structures. Another important disagreement between the experiment and the simulation was observed in the inlet pipe during deep surge cycle and revealed a clear need of further studies on boundary conditions that are a better representation of the physical conditions on the test stand.

In section 1.7.2 the main thesis of the dissertation was formulated as follows:

CFD methods can provide description of surge and pre-surge flow phenomena in the centrifugal blower. In further perspective, it can lead to construction of efficient anti-surge devices.

The aforementioned summary fully justifies a positive answer to the first sentence. The latter one can be also considered as true. As mentioned in section 4.1, one of the main achievements of this work consisted in a level of detail in which the unstable flow structures were modelled with the simulations. This allows one to develop the anti-surge devices in two ways:

- Numerical simulations provide detailed data about the flow field that can be used to develop a surge model to better understand local flow instabilities which, in turn, can lead to development of anti-surge devices.
- The anti-surge device can be directly introduced into the simulation in order to analyse its efficiency before building a prototype. This can include programmable boundary conditions based on values of pressure at the given control point.

One has to remember that the presented simulations of unstable phenomena in the centrifugal blower required much computational power. This is the main limitation of CFD methods for this purpose. However, continuous progress of computing units decreases the scale of this problem. On the other hand, the main advantage of CFD simulations lies in full freedom of conducting simulations of the deep surge, whereas in the case of machines of higher power, the experimental investigation methods are strictly limited for safety reasons.

4.3 Future work

The list below gives a short outline of possible ways in which the presented research can be continued in the future:

- development of a CFD model of the blower at surge and pre-surge:
 - different definition of the outlet boundary condition,
 - * from the analytical valve resistance curve,
 - * by including the valve in the simulation domain,
 - * by obtaining the valve resistance curve from the experiment,
 - numerical simulations of different geometries to establish guidelines how to choose the Greitzer model parameters (L_c and S_c),
 - simulation of the blower with a *RDF*-based anti-surge scheme,
 - simulation including the inlet bleeding system,
- study of the inlet recirculation:
 - study of the inlet recirculation for different inlet configurations,
 - approximation of the stability limit for the inlet recirculation,
- development of the experimental test stand:
 - design of controllers for real-time *RDF* monitoring,
 - application of transparent machine components for PIV measurements,
 - detailed measurements of the diffuser flow.

Bibliography

- [1] Archie-west: Simulation of surge onset in centrifugal compressors. <http://www.archie-west.ac.uk/projects/computational-fluid-dynamics/simulation-of-compressor-surge/>. Accessed: 2013-11-05.
- [2] Cfd-online wiki. <http://www.cfd-online.com/Wiki/>. Accessed: 2012-05-12.
- [3] *Ansys Fluent 14.0 Theory Guide*. ANSYS Inc, 2011.
- [4] *Ansys Fluent 14.0 User's Guide*. ANSYS Inc, 2011.
- [5] *Ansys TurboGrid 14.0 User's Guide*. ANSYS Inc, 2011.
- [6] A.N. Abdelhamid. Analysis of rotating stall in vaneless diffusers of centrifugal compressors. In *Proceedings of Turbo Expo*, New Orleans, 1980. ASME.
- [7] A.N. Abdelhamid and J. Bertrand. Distinctions between two types of self excited gas oscillations in vaneless radial diffusers. In *Proceedings of Turbo Expo*, San Diego, 1979. ASME.
- [8] E.H. Abed, P.K. Houpt, and W.M. Hosny. Bifurcation analysis of surge and rotating stall in axial flow compressors. *Journal of Turbomachinery*, 115(4):817–824, 1993.
- [9] O.O. Badmus, K.M. Eveker, and C.N. Nett. Control-oriented high-frequency turbomachinery modeling: General one-dimensional model development. *Journal of Turbomachinery*, 117(3):320–335, 1995.
- [10] O.E. Balje. *Turbomachines: a guide to design selection and theory*. Wiley and sons, New York, 1981.
- [11] D. Bently, P. Goldman, and J. Yuan. Rotor Dynamics of Centrifugal Compressors in Rotating Stall. *Orbit*, pages 40–50, 2001.
- [12] H.P. Bloch. *A practical guide to compressor technology*. Wiley-Interscience, 2006.
- [13] K.K. Botros. Transient phenomena in compressor stations during surge. *Journal of Engineering for Gas Turbines and Power*, 116(1):133–142, 1994.
- [14] K.K. Botros and J.F. Henderson. Developments in centrifugal compressor surge control—a technology assessment. *Journal of Turbomachinery*, 116(2):240–249, 1994.
- [15] F.A. Breugelmans and M. Sen. Prerotation and fluid recirculation in the suction pipe of centrifugal pumps. In *Proceedings of 11th International Pump Symposium*, Texas, 1982. A&M University.
- [16] I.N. Bronshtein and K.A. Semydayev. *Handbook of mathematics*. Springer, 2007.

-
- [17] N. Bulot, X. Ottavy, and I. Trebinjac. Unsteady pressure measurements in a high-speed centrifugal compressor. *Journal of Thermal Science*, 19(1):34–41, 2010.
- [18] J. Chen. Numerical simulation of stall and stall control in axial and radial compressors. Technical report, Mississippi State University, 2006.
- [19] J. Chen and J. Barter. Comparison of time-accurate calculations for the unsteady interaction in turbomachinery stage. In *Proceedings of 34th Joint Propulsion Conference & Exhibit*, Cleveland, 1998. AIAA/ASME/SAE/ASEE.
- [20] R. Chodkiewicz, K. Sobczak, Z. Kazimierski, and W. Kryłowicz. Numeryczne badania zjawisk związanych z niestateczną pracą jednostopniowej sprężarki promieniowej za pomocą programu tascflow. cz. i identyfikacja zjawisk. *Ciepłne Maszyny Przepływowe - Turbomachinery*, pages 145–160, 2000.
- [21] J.M. Cimbala and Y.A. Çengel. *Essentials of fluid mechanics: fundamentals and applications*. McGraw-Hill Higher Education, 2008.
- [22] N.A. Cumpsty. *Compressor aerodynamics*. Halsted Press, 1989.
- [23] B. de Jager. Rotating stall and surge control: A survey. In *Proceedings of the 34th Conference on Decision and Control*. IEEE, 1995.
- [24] R.C. Dean and Y. Senoo. Rotating wakes in vaneless diffusers. *Journal of Basic Engineering*, 82(3):563–570, 1960.
- [25] R.L. Elder and M. E. Gill. A discussion of the factors affecting surge in centrifugal compressors. *Journal of Engineering for Gas Turbines and Power*, 107(2):499–506, 1985.
- [26] H.W. Emmons, C.E. Pearson, and H.P. Grant. Compressor surge and stall propagation. *Transactions of ASME*, 77(4):455–467, 1955.
- [27] M.R. Feulner, J.D. Paduano, and G.J. Hendricks. Modeling for control of rotating stall in high-speed multistage axial compressors. *Journal of Turbomachinery*, 118(1):1–10, 1996.
- [28] R.P. Feynman, R.B. Leighton, and M. Sands. *The Feynman Lectures on Physics, Desktop Edition Volume I*, volume 1. Basic Books, 2013.
- [29] D.A. Fink, N.A. Cumpsty, and E.M. Greitzer. Surge dynamics in a free-spool centrifugal compressor system. *Journal of Turbomachinery*, 114(2):321–332, 1992.
- [30] А. Лебедев. Исследование нестационарных процессов в центробежном компрессоре с применением вейвлет преобразования. 2008.
- [31] W.H. Fraser. Recirculation in centrifugal pumps. *Materials of Construction of Fluid Machinery and Their Relationship to Design and Performance*, pages 65–86, 1981.
- [32] W.H. Fraser. *Recirculation in Centrifugal Pumps*. World Pumps, 1982.
- [33] P. Frigne and R. Van den Braembussche. Distinction between different types of impeller and diffuser rotating stall in a centrifugal compressor with vaneless diffuser. *Journal of Engineering for Gas Turbines and Power*, 106(2):468–474, 1984.

- [34] P. Frigne and R. Van den Braembussche. A theoretical model for rotating stall in the vaneless diffuser of a centrifugal compressor. *Journal of Engineering for Gas Turbines and Power*, 107(2):507–513, 1985.
- [35] R.W. Graham and V.D. Prian. Experimental and theoretical investigation of rotating-stall characteristics of single-stage axial-flow compressor with hub-tip ratio of 0.76. Technical report, National Advisory Committee for Aeronautics, 1953.
- [36] J.T. Gravdahl and O. Egeland. A moore-greitzer axial compressor model with spool dynamics. In *Proceedings of the 36th Conference on Decision and Control*, San Diego, 1997. IEEE.
- [37] J.T. Gravdahl and O. Egeland. Speed and surge control for a low order centrifugal compressor model. In *Proceedings of the 36th International Conference on Control Applications*, San Diego, 1997. IEEE.
- [38] E.M. Greitzer. Surge and rotating stall in axial flow compressors—part i: Theoretical compression system model. *Journal of Engineering for Power*, 98(2):190–198, 1976.
- [39] E.M. Greitzer. Surge and rotating stall in axial flow compressors—part ii: Experimental results and comparison with theory. *Journal of Engineering for Power*, 98(2):199–211, 1976.
- [40] E.M. Greitzer. Review—axial compressor stall phenomena. *Journal of Fluids Engineering*, 102(2):134–151, 1980.
- [41] E.M. Greitzer. The stability of pumping systems—the 1980 freeman scholar lecture. *Journal of Fluids Engineering*, 103(2):193–242, 1981.
- [42] C. Gu, K. Yamaguchi, T. Nagashima, and H. Higashimori. Observation of centrifugal compressor stall and surge in phase portraits of pressure time traces at impeller and diffuser wall. *Journal of Fluids Engineering*, 129(6):773–779, 2007.
- [43] Q. Guo, H. Chen, X.C. Zhu, Z.H. Du, and Y. Zhao. Numerical simulations of stall inside a centrifugal compressor. *Journal of Power and Energy*, 221(5):683–693, 2007.
- [44] K.E. Hansen, P. Jorgensen, and P.S. Larsen. Experimental and theoretical study of surge in a small centrifugal compressor. *Journal of Fluids Engineering*, 103(3):391–395, 1981.
- [45] F.J. Harris. On the use of windows for harmonic analysis with the discrete fourier transform. *Proceedings of the IEEE*, 66(1):51–83, 1978.
- [46] U. Haupt, N. Kaemmer, M. Rautenberg, and A.N. Abdelhamid. Excitation of blade vibration by flow instability in centrifugal compressors. In *Proceedings of Turbo Expo*, Düsseldorf, 1986. ASME.
- [47] B. Hellmich and J.R. Seume. Causes of acoustic resonance in a high-speed axial compressor. *Journal of Turbomachinery*, 130(3):031003, 2008.
- [48] L. Horodko. Investigation of centrifugal compressor surge with wavelet methods. In *Proceedings of 6-th European Conference on Turbomachinery, Fluid Dynamics and Thermodynamics*, Lile, 2005. VKI.

- [49] L. Horodko. Identification of rotating pressure waves in a centrifugal compressor diffuser by means of the wavelet cross-correlation. *International Journal of Wavelets, Multiresolution and Information Processing*, 4(02):373–382, 2006.
- [50] L. Horodko. Zastosowanie czasowo-częstotliwościowej analizy sygnałów do badania niestatecznej pracy sprężarki promieniowej. Technical Report 990, Łódź University of Technology, 2006.
- [51] L. Horodko. Badania eksperymentalne zjawisk poprzedzających pompowanie sprężarki promieniowej i ich identyfikacja za pomocą falkowej analizy sygnałów ciśnień. Technical report, Łódź University of Technology, 2007.
- [52] L. Horodko. Detection of surge precursors in a centrifugal compressor with a wavelet method. In *Proceedings of 7th European Conference on Turbomachinery, Fluid Dynamics and Thermodynamics*, Athens, 2007. VKI.
- [53] L. Horodko. *Systemy pomiarowe i podstawy analizy sygnałów*. Łódź University of Technology, 2013.
- [54] W. Huang, S. Geng, J. Zhu, and H. Zhang. Numerical simulation of rotating stall in a centrifugal compressor with vaned diffuser. *Journal of Thermal Science*, 16(2):115–120, 2007.
- [55] R. Hunziker, H.P. Dickmann, and R. Emmrich. Numerical and experimental investigation of a centrifugal compressor with an inducer casing bleed system. *Proceedings of the Institution of Mechanical Engineers, Part A: Journal of Power and Energy*, 215(6):783–791, 2001.
- [56] M.C. Huppert, E.L. Costilow, and D.F. Johnson. Preliminary investigation of compressor blade vibration excited by rotating stall. Technical report, 1952.
- [57] H. Ishii and Y. Kashiwabara. Study on surge and rotating stall in axial compressors: A numerical model and parametric study for multiblade-row compressors. *JSME International Journal. Series B: Fluids and Thermal Engineering*, 39(3):621–631, 1996.
- [58] R.A. Izmaylov. Unsteady flow phenomena in centrifugal compressor: rotating stall and beyond. In *Proceedings of 12th International Symposium on Unsteady Aerodynamics*, London, 2009. Imperial College.
- [59] W. Jansen. Rotating stall in a radial vaneless diffuser. *Journal of Basic Engineering*, 86(4):750–758, 1964.
- [60] D. Japikse. Stall, stage stall, and surge. In *Proceedings of the Tenth Turbomachinery Symposium*, 1981.
- [61] D. Japikse. *Centrifugal compressor design and performance*. Concepts Eti, 1988.
- [62] K. Kabalyk, G. Liśkiewicz, L. Horodko, M. Stickland, and W. Kryłłowicz. Use of pressure spectral maps for analysis of influence of the plenum volume on the surge in centrifugal blower. In *Proceedings of Turbo Expo (in press)*, Düsseldorf, 2014. ASME.
- [63] K. Kacprzak, G. Liśkiewicz, and K. Sobczak. Numerical investigation of conventional and modified savonius wind turbines. *Renewable Energy*, 60:578–585, 2013.

- [64] B.A. Kader. Temperature and concentration profiles in fully turbulent boundary layers. *International Journal of Heat and Mass Transfer*, 24(9):1541 – 1544, 1981.
- [65] N. Kämmer and M. Rautenberg. A distinction between different types of stall in a centrifugal compressor stage. *Journal of Engineering for Gas Turbines and Power*, 108(1):83–92, 1986.
- [66] Y. Komatsubara and S. Mizuki. Dynamical system analysis of unsteady phenomena in centrifugal compressor. *Journal of Thermal Science*, 6(1):14–20, 1997.
- [67] W. Kryłłowicz. Badania niestatecznej pracy jednostopniowej sprężarki promieniowej. Technical Report 889, Łódź University of Technology, 2001.
- [68] W. Kryłłowicz. Sprężarki Przepływowe. Materiały 6 edycji kursu IMP PŁ, 2007.
- [69] T. Kubo and S. Murata. Unsteady flow phenomena in centrifugal fans: 1st report, rotating flow patterns in an inlet duct. *Bulletin of JSME*, 19(135):1039–1046, 1976.
- [70] V.A. Kuz'min and V.N. Khazhiev. Measurement of liquid or gas flow (flow velocity) using convergent channels with a witoszynski profile. *Measurement Techniques*, 36(3):288–296, 1993.
- [71] P.B. Lawless and S. Fleeter. Rotating stall acoustic signature in a low-speed centrifugal compressor: Part 1—vaneless diffuser. *Journal of Turbomachinery*, 117(1):87–96, 1995.
- [72] E. Lennemann and J.H.G. Howard. Unsteady flow phenomena in rotating centrifugal impeller passages. *Journal for Engineering for Power*, 92(1):65–71, 1970.
- [73] Y. Levy and J. Pismenny. The number and speed of stall cells during rotating stall. In *Proceedings of Turbo Expo*, Atlanta, 2003. ASME.
- [74] D.C. Liaw and S.T. Chang. Bifurcation analysis of a centrifugal compressor. In *Proceedings of International Conference on Systems, Man, and Cybernetics*. IEEE, 2011.
- [75] G. Liškiewicz, L. Horodko, M. Stickland, and W. Kryłłowicz. Identification of phenomena preceding blower surge by means of pressure spectral maps. *Experimental Thermal and Fluid Science*, 54:267–278, 2014.
- [76] S. Ljevar. *Rotating stall in wide vaneless diffusers*. Technische Universiteit Eindhoven, 2007.
- [77] S. Ljevar, H.C. de Lange, and A.A. van Steenhoven. Rotating stall characteristics in a wide vaneless diffuser. Reno, 2005. ASME.
- [78] S. Ljevar, H.C. de Lange, and A.A. Van Steenhoven. Two-dimensional rotating stall analysis in a wide vaneless diffuser. *International Journal of Rotating Machinery*, 2006, 2006.
- [79] A.M. Lyapunov. The general problem of the stability of motion. *International Journal of Control*, 55(3):531–534, 1992.
- [80] R. Magiera. Kompleksowe badania eksperymentalne i numeryczne układów wlotowych dmuchawy promieniowej wyposażonej w nastawną kierownicę wstępną. Technical report, Łódź University of Technology, 2010.

-
- [81] I. McDougal and R.L. Elder. Simulation of centrifugal compressor transient performance for process plant applications. *Journal for Engineering for Power*, 105(4):885–890, 1983.
- [82] N.M. McDougall, N.A. Cumpsty, and T.P. Hynes. Stall inception in axial compressors. *Journal of Turbomachinery*, 112(1):116–123, 1990.
- [83] R.J. McKee and C.E. Edlund. Method and apparatus for detecting the occurrence of surge in a centrifugal compressor, 2006. US Patent 6,981,838.
- [84] R.J. McKee, S. Siebanaler, and D.M. Deffenbaugh. Increased flexibility of turbo-compressors in natural gas transmission through direct surge control. Technical report, Southwest Research Institute, USA, 2004.
- [85] F.R. Menter. Two-equation eddy-viscosity turbulence models for engineering applications. *American Institute of Aeronautics and Astronautics*, 32(8):1598–1605, 1994.
- [86] A. Mertins. *Signal Analysis: Wavelets, Filter Banks, Time-Frequency Transforms and Applications*. Wiley Press, 1999.
- [87] C. Meuleman. *Measurement and unsteady flow modelling of centrifugal compressor surge*. PhD thesis, 2002.
- [88] C. Meuleman, F. Willems, R. de Lange, and B. de Jager. Surge in a low-speed radial compressor. In *Proceedings of 43rd International Gas Turbine and Aeroengine Congress*, Stockholm, 1998. ASME.
- [89] S. Mizuki, Y. Kawashima, and I. Ariga. Investigation concerning rotating stall and surge phenomena within centrifugal compressor channels. In *Proceedings of International Gas Turbine Conference*, London, 1978. ASME.
- [90] S. Mizuki and Y. Oosawa. Unsteady flow within centrifugal compressor channels under rotating stall and surge. *Journal of Turbomachinery*, 114(2):312–320, 1992.
- [91] F.K. Moore and E.M. Greitzer. A theory of post-stall transients in axial compression systems: Part i—development of equations. *Journal of Engineering for Gas Turbines and Power*, 108(1):68–76, 1986.
- [92] F.K. Moore and E.M. Greitzer. A theory of post-stall transients in axial compression systems: Part ii—application. *Journal of Engineering for Gas Turbines and Power*, 108(2):231–239, 1986.
- [93] B.R. Munson, A.P. Rothmayer, T.H. Okiishi, and W.W. Huebsch. *Fundamentals of Fluid Mechanics, Student Solutions Manual and Student Study Guide*. Wiley, 2012.
- [94] A. Mutou, S. Mizuki, Y. Komatsubara, and H. Tsujita. Behavior of attractors during surge in centrifugal compression system. In *Proceedings of Turbo Expo*, Stockholm, 1998.
- [95] B.R. Noack, F. Ohle, and H. Eckelmann. Construction and analysis of differential equations from experimental time series of oscillatory systems. *Physica D: Nonlinear Phenomena*, 56(4):389–405, 1992.

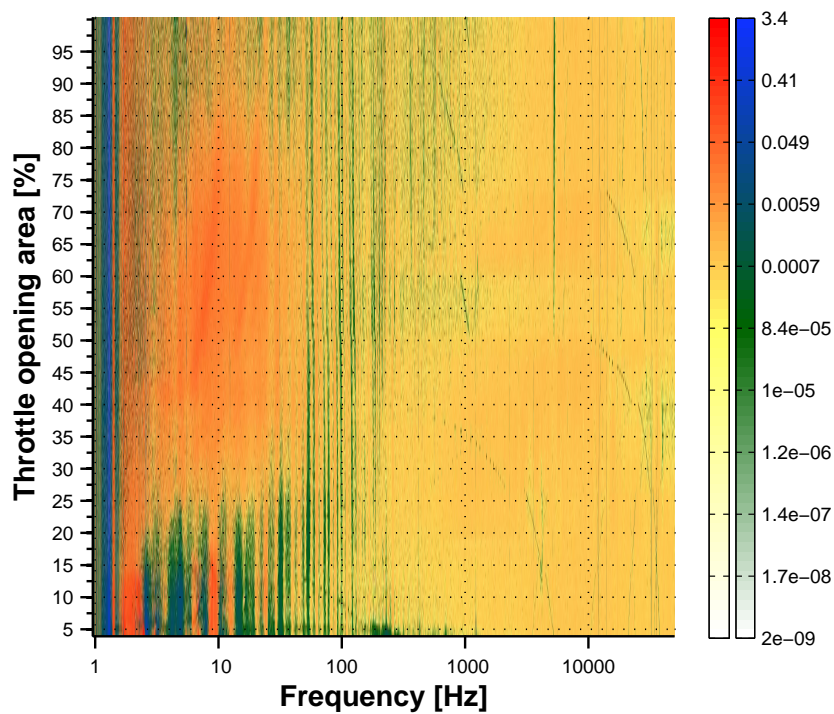
- [96] W.C. Oakes, P.B. Lawless, and S. Fleeter. A characterization of rotating stall behaviors in high and low speed centrifugal compressors. In *Proceedings of International Compressor Engineering Conference*, Indiana, 1998. Purdue University.
- [97] N.H. Packard, J.P. Crutchfield, J.D. Farmer, and R.S. Shaw. Geometry from a time series. *Physical Review Letters*, 45(9):712, 1980.
- [98] R.C. Pamphreen. *Compressor surge and stall*. Concepts Eti, 1993.
- [99] T. Raitor and W. Neise. Sound generation in centrifugal compressors. *Journal of Sound and Vibration*, 314(3):738–756, 2008.
- [100] B. Rebernik. Investigation on induced vorticity in vaneless diffusers of radial flow pumps. In *Proceedings of 4th Conference on Fluid Machinery*, Budapest, 1972. Akadémiai Kiadó.
- [101] C.M. Rhie and W.L. Chow. Numerical study of the turbulent flow past an airfoil with trailing edge separation. In *Proceedings of 3rd Joint Thermophysics, Fluids, Plasma and Heat Transfer Conference*, Louis, 1983.
- [102] C. Rodgers. Typical performance characteristics of gas turbine radial compressors. *Journal for Engineering for Power*, 86(2):161–170, 1964.
- [103] P.H. Rothe and P.W. Runstadler. First-order pump surge behavior. *Journal of Fluids Engineering*, 100(4):459–466, 1978.
- [104] S.M. Salim, R. Buccolieri, A. Chan, and S. di Sabatino. Numerical simulation of atmospheric pollutant dispersion in an urban street canyon: Comparison between rans and les. *Journal of Wind Engineering and Industrial Aerodynamics*, 99(2):103–113, 2011.
- [105] Y. Senoo, M. Ishida, and Y. Kinoshita. Asymmetric flow in vaneless diffusers of centrifugal blowers. *Journal of Fluids Engineering*, 99(1):104–111, 1977.
- [106] Y. Senoo and Y. Kinoshita. Influence of inlet flow conditions and geometries of centrifugal vaneless diffusers on critical flow angle for reverse flow. *Journal of Fluids Engineering*, 99(1):98–102, 1977.
- [107] J. Shabbir, A. and Zhu and M. Celestina. Assessment of three turbulence models in a compressor rotor. In *Proceedings of International Gas Turbine and Aeroengine Congress*, Birmingham, 1996. ASME.
- [108] F. Shen, H. Chen, and X.C. Zhu. A three-dimensional vaneless diffuser stall model. *Proceedings of the Institution of Mechanical Engineers, Part C: Journal of Mechanical Engineering Science*, 224(9):1933–1945, 2010.
- [109] T.H. Shih, W. Liou, A. Shabbir, Z. Yang, and J. Zhu. A new $k - \epsilon$ eddy viscosity model for high reynolds number turbulent flows. *Computers and Fluids*, 24(3):227 – 238, 1995.
- [110] M.T. Sideris and R. Van den Braembussche. Influence of a circumferential exit pressure distortion on the flow in an impeller and diffuser. *Journal of Turbomachinery*, 109(1):48–54, 1987.

- [111] J.M. Sorokes, C.J. Borer, and J.M. Koch. Investigation of the circumferential static pressure non-uniformity caused by a centrifugal compressor discharge volute. In *Proceedings of Turbo Expo*, Stockholm, 1998. ASME.
- [112] Z.S. Spakovszky. *Applications of axial and radial compressor dynamic system modeling*. PhD thesis, 2001.
- [113] T. Steglich, R. Van den Braembussche, J. Prinsier, J. Kitzinger, and J.R. Seume. Improved diffuser/volute combinations for centrifugal compressors. *Journal of Turbomachinery*, 130(1):11–14, 2008.
- [114] A. Stein. *Computational analysis of stall and separation control in centrifugal compressors*. PhD thesis, Georgia Institute of Technology, 2000.
- [115] H. Tamaki. Experimental study on surge inception in a centrifugal compressor. *International Journal of Fluid Machinery and Systems*, 2(4):409–417, 2009.
- [116] H. Tamaki, H. Nakao, and T. Aizawa. Experimental study on surge inception in a centrifugal compressor. *Journal of Turbomachinery*, 32(8):466–472, 2004.
- [117] M.V. Ötügen, R.M.C. So, and B.C. Hwang. Diffuser stall and rotating zones of separated boundary layer. *Experiments in Fluids*, 6(8):521–533, 1988.
- [118] K. Toyama, P.W. Runstadler, and R.C. Dean. An experimental study of surge in centrifugal compressors. *Journal of Fluids Engineering*, 99(1):115–124, 1977.
- [119] Y. Tsujimoto, Y. Mori, and Y. Yoshida. Study of vaneless diffuser rotating stall based on two-dimensional inviscid flow analysis. *Journal of Fluids Engineering*, 118(1):123–127, 1996.
- [120] T. Turunen-Saaresti and J. Larjola. Unsteady pressure field in a vaneless diffuser of a centrifugal compressor: An experimental and computational analysis. *Journal of Thermal Science*, 13(4):302–309, 2004.
- [121] H. Uchida, M. Inayoshi, and K. Sugiyama. Effect of a circumferential static pressure distortion on small-sized centrifugal compressor performance. In *Proceedings of International Gas Turbine Congress*, Tokyo, 1987. GTSJ.
- [122] R. Van den Braembussche. Centrifugal compressors analysis & design. Course note 192, 2014.
- [123] R. Van den Braembussche and B.M. Hande. Experimental and theoretical study of the swirling flow in centrifugal compressor volutes. *Journal of Turbomachinery*, 112(1):38–43, 1990.
- [124] J. van Helvoirt. *Centrifugal compressor surge: Modeling and identification for control*. PhD thesis, 2007.
- [125] J. van Helvoirt and B. de Jager. Dynamic model including piping acoustics of a centrifugal compression system. *Journal of Sound and Vibration*, 302(1–2):361 – 378, 2007.
- [126] H.K. Versteeg. *An introduction to computational fluid dynamics the finite volume method*. Pearson Education, 1995.
- [127] F.M. White. *Fluid mechanics*. McGraw-Hill, 1999.

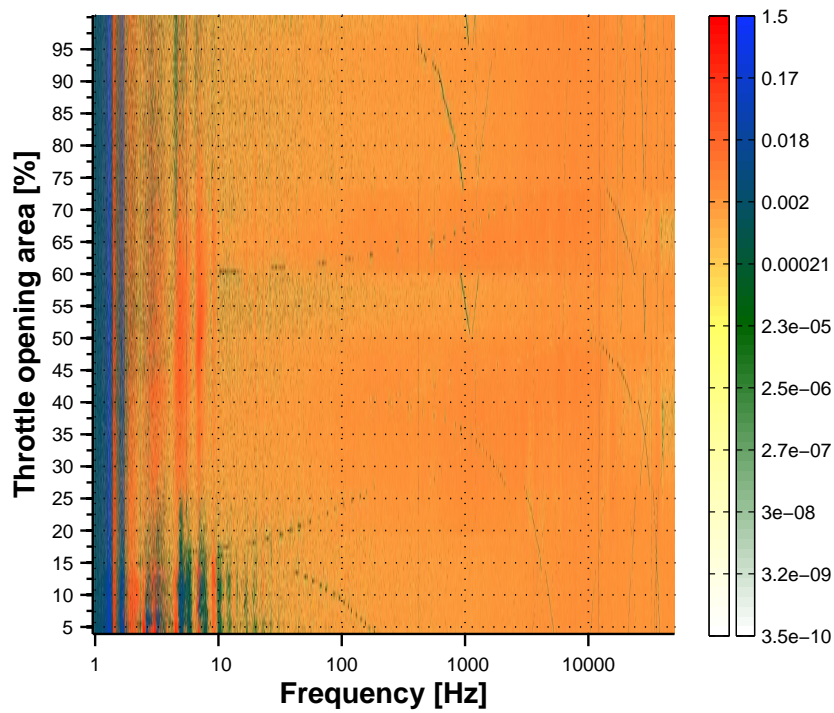
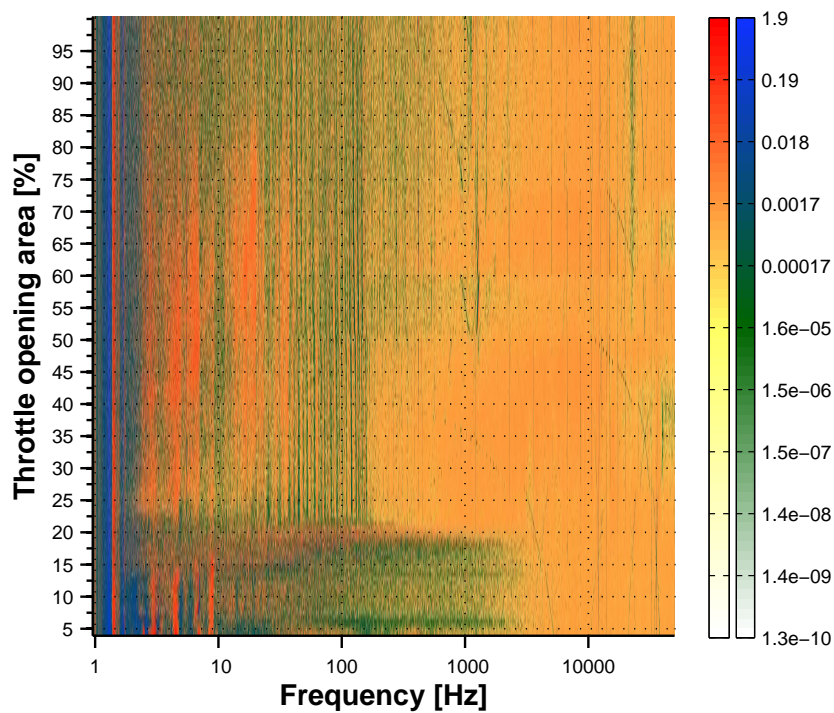
-
- [128] D.C. Wilcox. *Turbulence modeling for CFD*. DCW industries, 1998.
- [129] F. Willems. *Modeling and Bounded Feedback Stabilization of Centrifugal Compressor Surge*. Technische Universiteit Eindhoven, 2000.
- [130] F. Willems and B. de Jager. Modeling and control of compressor flow instabilities. *Control Systems*, 19(5):8–18, 1999.
- [131] S.Y. Yoon, Z. Lin, C. Goyne, and P.E. Allaire. An enhanced greitzer compressor model with pipeline dynamics included. In *Proceedings of American Control Conference*, San Francisco, 2011. IEEE.

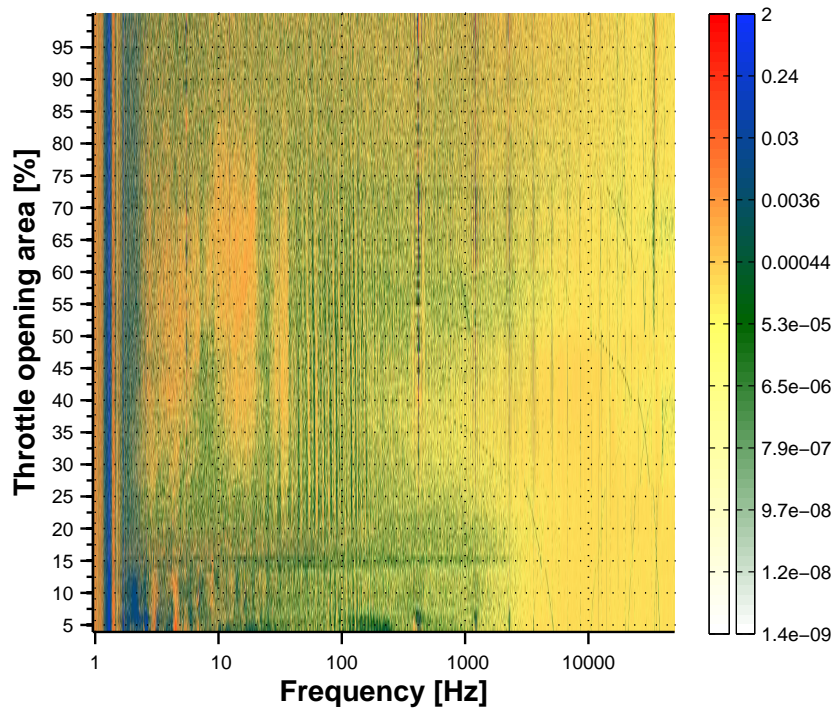
Differential spectral maps

Section 2.2.3 contains spectral maps obtained at different gauges in case of the large plenum volume and the small plenum volume. The differential spectral maps presented herein allow to compare both cases on the same plot. Each of them was obtained from subtraction of the SP amplitudes from LP amplitudes or the other way round. If the amplitude in LP case is higher, the difference is represented with the colorbar consisting of cold colors. In the amplitude in SP case is higher, the difference is represented with the colorbar consisting of warm colors.

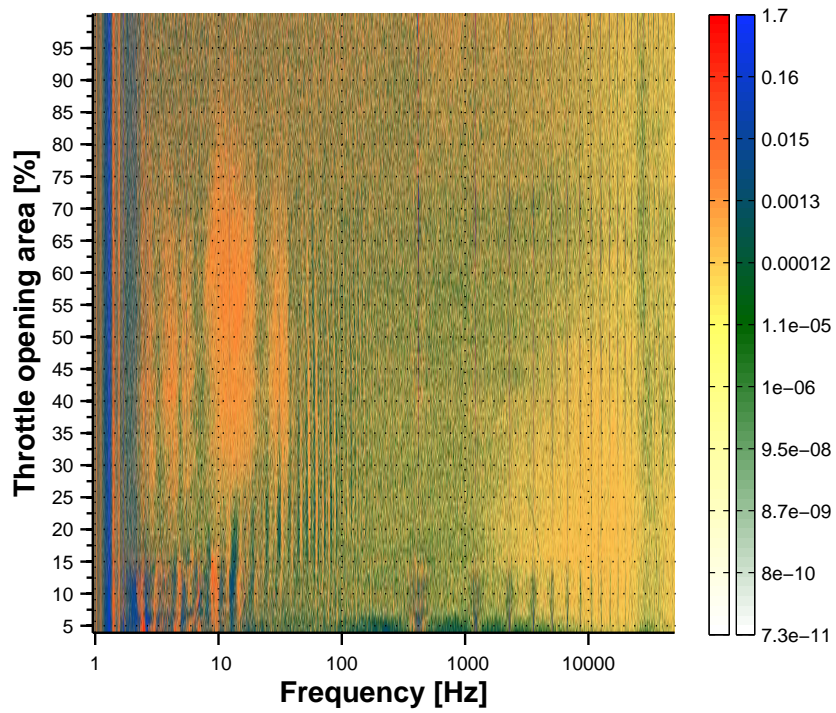


Differential spectral map of the signals p_{s-in}

Differential spectral map of the signals p_{s-out} Differential spectral map of the signals p_{s-imp1}



Differential spectral map of the signals p_{s-imp2}

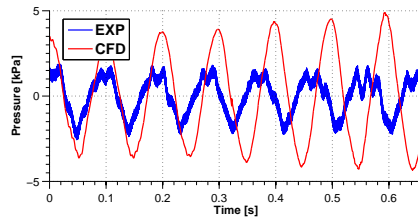


Differential spectral map of the signals p_{s-imp3}

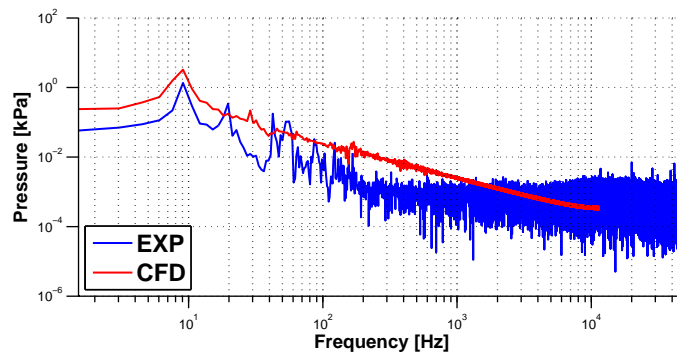
Frequency spectra

Section 3.3.1 is devoted to description of signals collected at the selected control points and their frequency spectra. Appendix contains full list of signals gathered at the all control points at all analysed mass flow rates.

B.1 $\dot{m} = 0.1 \frac{kg}{s}$

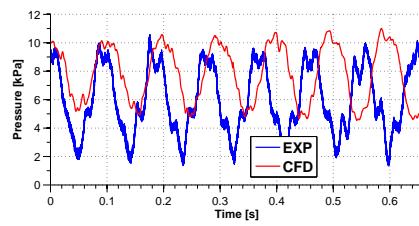


(a) signals

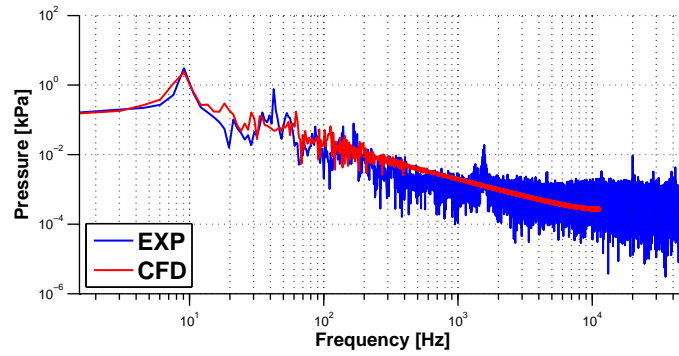


(b) frequency spectra

Comparison of pressure signals obtained at p_{s-in} in the quasi dynamic experiment conducted at $TOA = 4\%$ and in the simulation at $\dot{m} = 0.1 \frac{kg}{s}$ ($\phi = 0.19$)

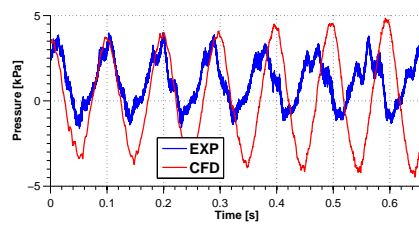


(a) signals

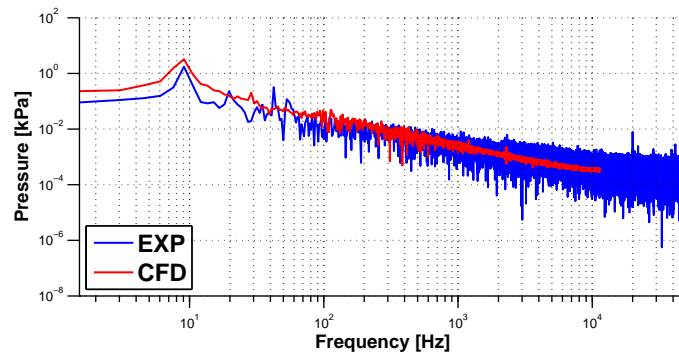


(b) frequency spectra

Comparison of pressure signals obtained at p_{s-out} in the quasi dynamic experiment conducted at $TOA = 4\%$ and in the simulation at $\dot{m} = 0.1 \frac{\text{kg}}{\text{s}}$ ($\phi = 0.19$)

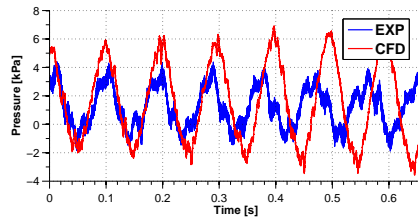


(a) signals

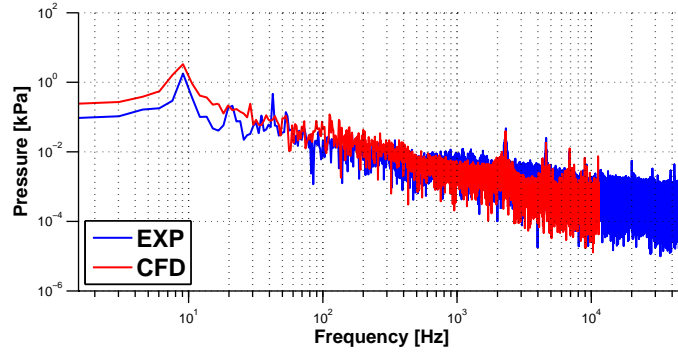


(b) frequency spectra

Comparison of pressure signals obtained at p_{s-imp1} in the quasi dynamic experiment conducted at $TOA = 4\%$ and in the simulation at $\dot{m} = 0.1 \frac{\text{kg}}{\text{s}}$ ($\phi = 0.19$)

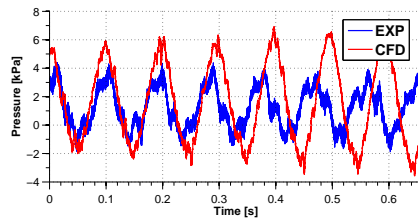


(a) signals

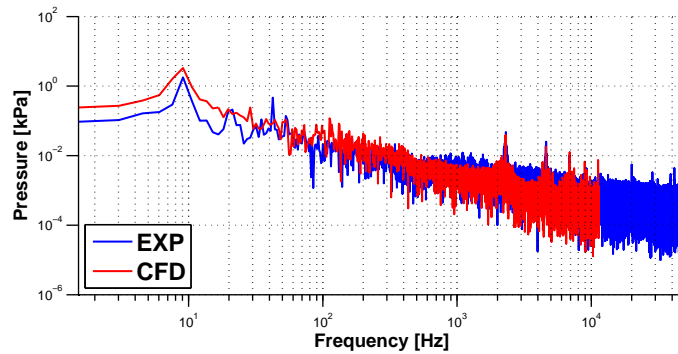


(b) frequency spectra

Comparison of pressure signals obtained at p_{s-imp2} in the quasi dynamic experiment conducted at $TOA = 4\%$ and in the simulation at $\dot{m} = 0.1 \frac{\text{kg}}{\text{s}}$ ($\phi = 0.19$)



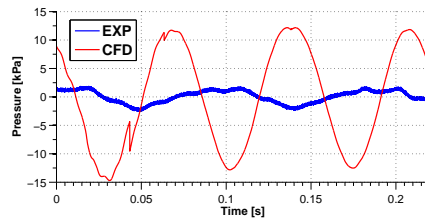
(a) signals



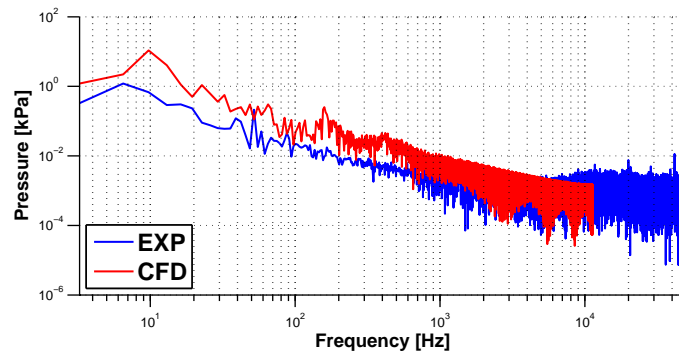
(b) frequency spectra

Comparison of pressure signals obtained at p_{s-imp2} in the quasi dynamic experiment conducted at $TOA = 4\%$ and in the simulation at $\dot{m} = 0.1 \frac{\text{kg}}{\text{s}}$ ($\phi = 0.19$)

B.2 $\dot{m} = 0.1 \frac{kg}{s}$ with reduced plenum

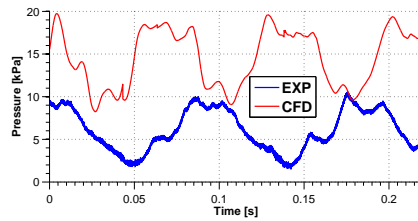


(a) signals

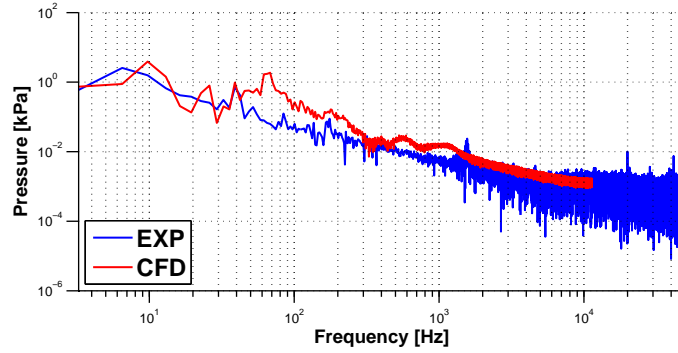


(b) frequency spectra

Comparison of pressure signals obtained at p_{s-in} in the quasi dynamic experiment conducted at $TOA = 4\%$ and in the simulation at $\dot{m} = 0.1 \frac{kg}{s}$ ($\phi = 0.19$) with reduced plenum volume

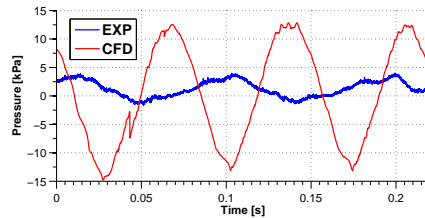


(a) signals

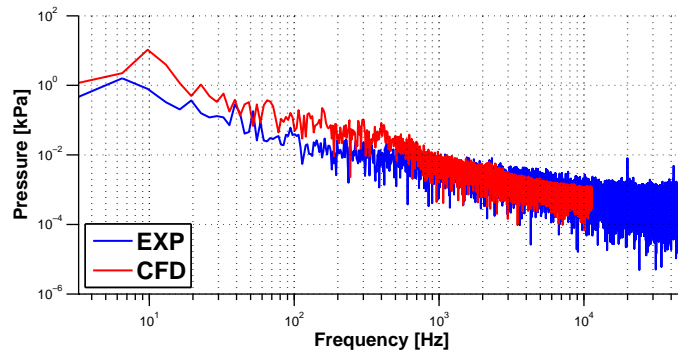


(b) frequency spectra

Comparison of pressure signals obtained at p_{s-out} in the quasi dynamic experiment conducted at $TOA = 4\%$ and in the simulation at $\dot{m} = 0.1 \frac{\text{kg}}{\text{s}}$ ($\phi = 0.19$) with reduced plenum volume

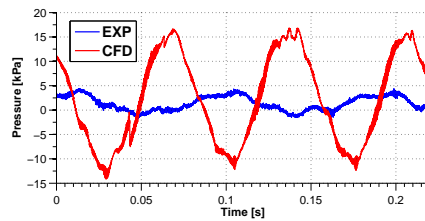


(a) signals

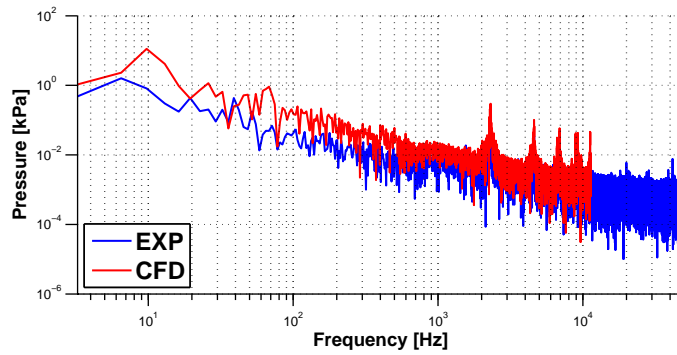


(b) frequency spectra

Comparison of pressure signals obtained at p_{s-imp1} in the quasi dynamic experiment conducted at $TOA = 4\%$ and in the simulation at $\dot{m} = 0.1 \frac{\text{kg}}{\text{s}}$ ($\phi = 0.19$) with reduced plenum volume

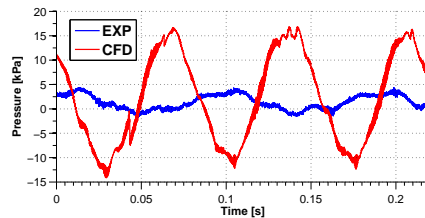


(a) signals

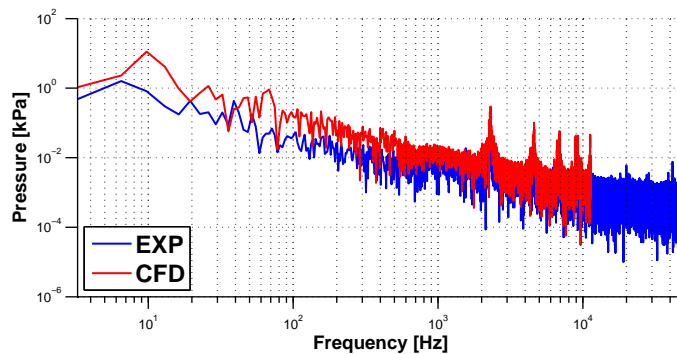


(b) frequency spectra

Comparison of pressure signals obtained at p_{s-imp2} in the quasi dynamic experiment conducted at $TOA = 4\%$ and in the simulation at $\dot{m} = 0.1 \frac{\text{kg}}{\text{s}}$ ($\phi = 0.19$) with reduced plenum volume



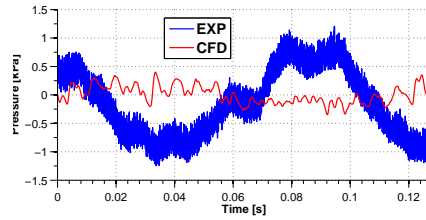
(a) signals



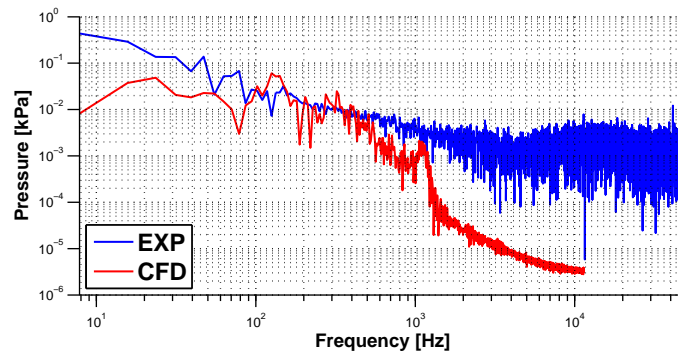
(b) frequency spectra

Comparison of pressure signals obtained at p_{s-imp2} in the quasi dynamic experiment conducted at $TOA = 4\%$ and in the simulation at $\dot{m} = 0.1 \frac{\text{kg}}{\text{s}}$ ($\phi = 0.19$) with reduced plenum volume

B.3 $\dot{m} = 0.3 \frac{kg}{s}$

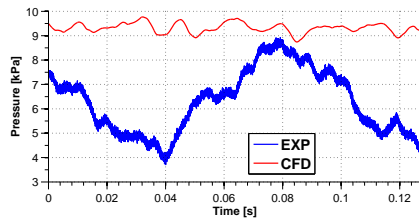


(a) signals

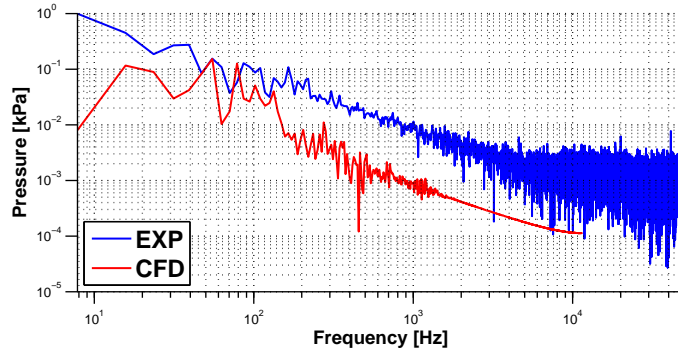


(b) frequency spectra

Comparison of pressure signals obtained at p_{s-in} in the quasi dynamic experiment conducted at $TOA = 8\%$ and in the simulation at $\dot{m} = 0.3 \frac{kg}{s}$ ($\phi = 0.57$)

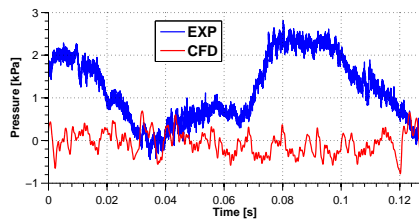


(a) signals

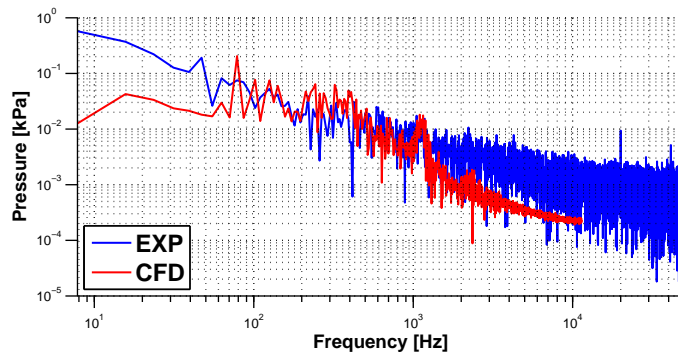


(b) frequency spectra

Comparison of pressure signals obtained at p_{s-out} in the quasi dynamic experiment conducted at $TOA = 8\%$ and in the simulation at $\dot{m} = 0.3 \frac{kg}{s}$ ($\phi = 0.57$)

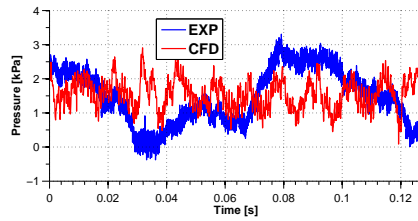


(a) signals

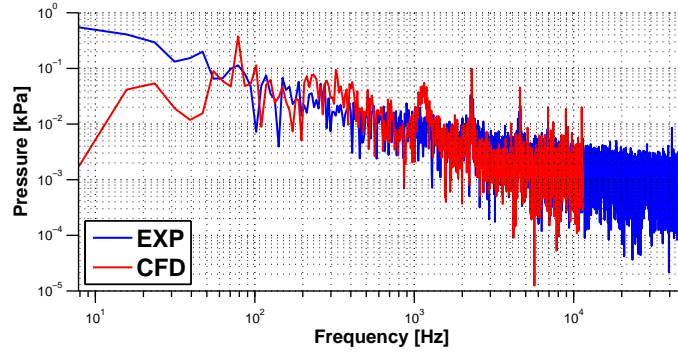


(b) frequency spectra

Comparison of pressure signals obtained at p_{s-imp1} in the quasi dynamic experiment conducted at $TOA = 8\%$ and in the simulation at $\dot{m} = 0.3 \frac{kg}{s}$ ($\phi = 0.57$)

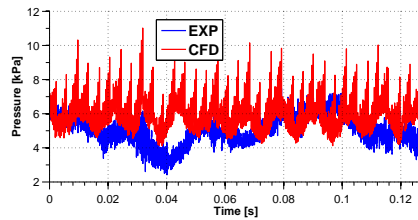


(a) signals

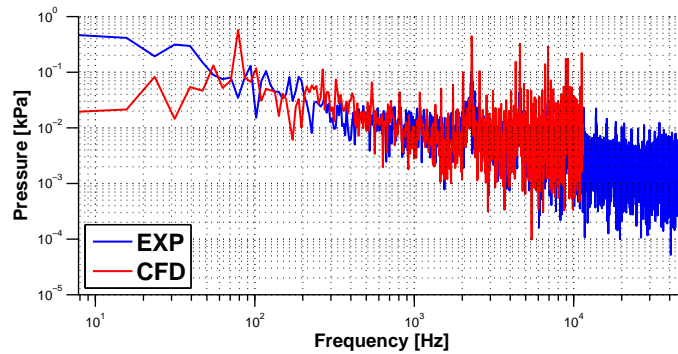


(b) frequency spectra

Comparison of pressure signals obtained at p_{s-imp2} in the quasi dynamic experiment conducted at $TOA = 8\%$ and in the simulation at $\dot{m} = 0.3 \frac{\text{kg}}{\text{s}}$ ($\phi = 0.57$)

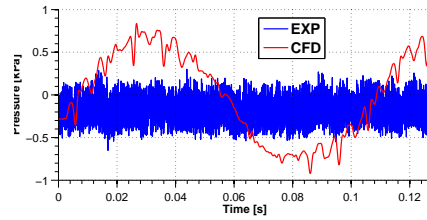


(a) signals

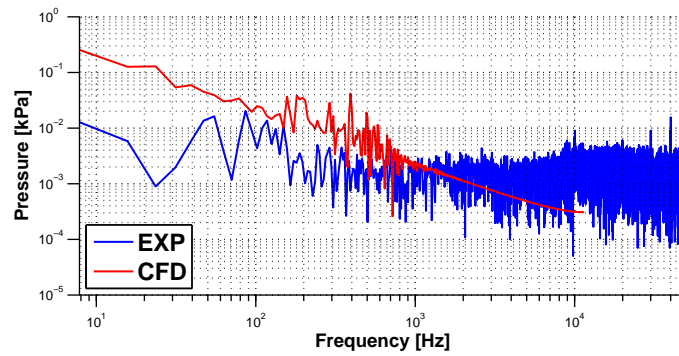


(b) frequency spectra

Comparison of pressure signals obtained at p_{s-imp3} in the quasi dynamic experiment conducted at $TOA = 8\%$ and in the simulation at $\dot{m} = 0.3 \frac{\text{kg}}{\text{s}}$ ($\phi = 0.57$)

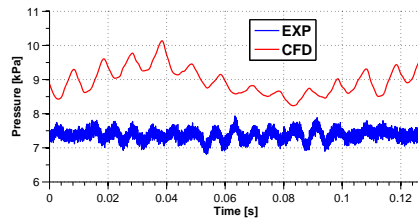
B.4 $\dot{m} = 0.5 \frac{kg}{s}$ 

(a) signals

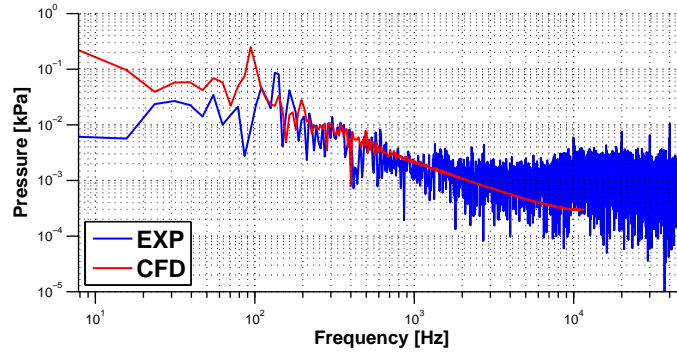


(b) frequency spectra

Comparison of pressure signals obtained at p_{s-in} in the quasi dynamic experiment conducted at $TOA = 18\%$ and in the simulation at $\dot{m} = 0.5 \frac{kg}{s}$ ($\phi = 0.95$)

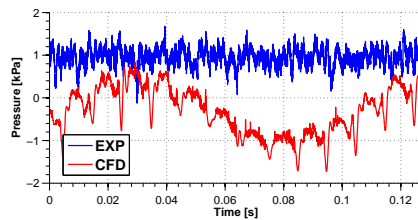


(a) signals

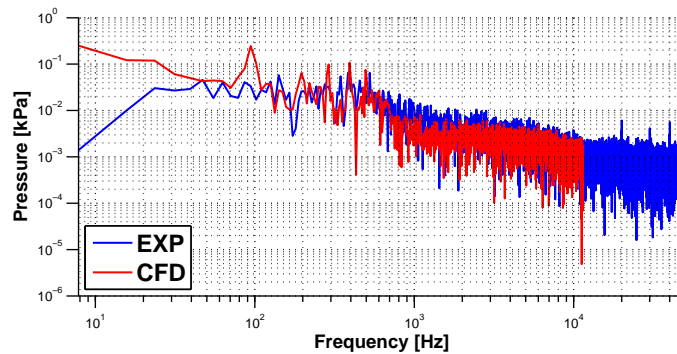


(b) frequency spectra

Comparison of pressure signals obtained at p_{s-out} in the quasi dynamic experiment conducted at $TOA = 18\%$ and in the simulation at $\dot{m} = 0.5 \frac{kg}{s}$ ($\phi = 0.95$)

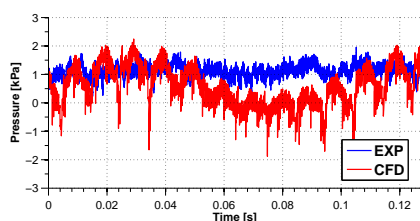


(a) signals

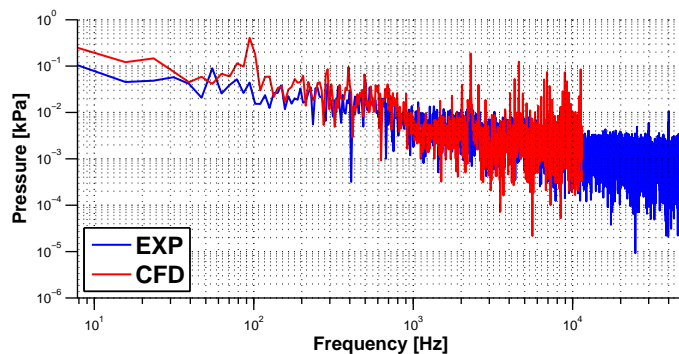


(b) frequency spectra

Comparison of pressure signals obtained at p_{s-imp1} in the quasi dynamic experiment conducted at $TOA = 18\%$ and in the simulation at $\dot{m} = 0.5 \frac{kg}{s}$ ($\phi = 0.95$)

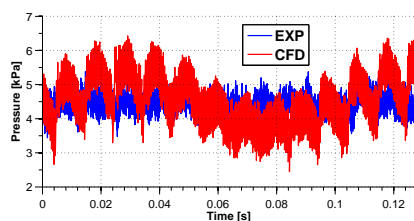


(a) signals

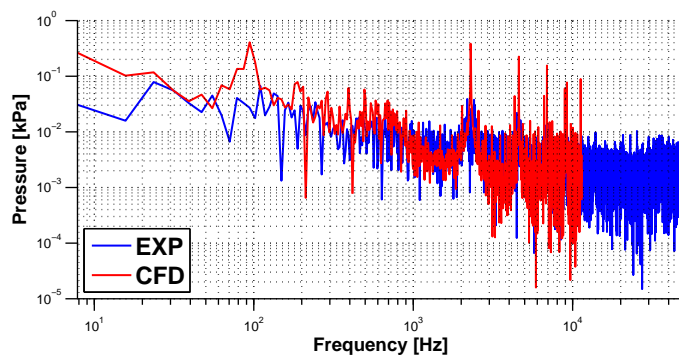


(b) frequency spectra

Comparison of pressure signals obtained at p_{s-imp2} in the quasi dynamic experiment conducted at $TOA = 18\%$ and in the simulation at $\dot{m} = 0.5 \frac{\text{kg}}{\text{s}}$ ($\phi = 0.95$)

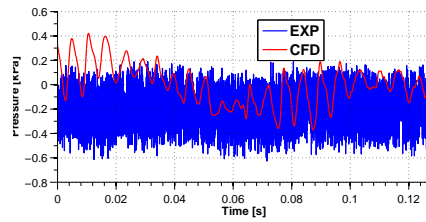


(a) signals

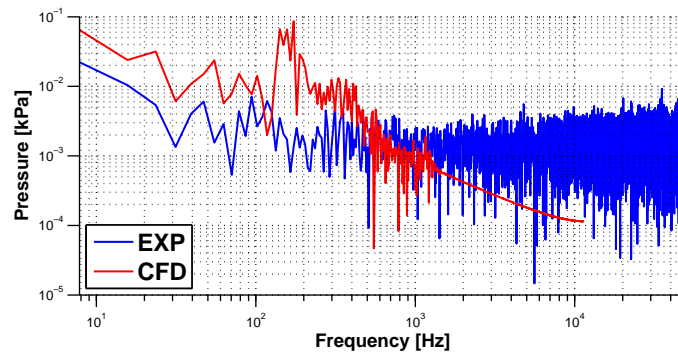


(b) frequency spectra

Comparison of pressure signals obtained at p_{s-imp3} in the quasi dynamic experiment conducted at $TOA = 18\%$ and in the simulation at $\dot{m} = 0.5 \frac{\text{kg}}{\text{s}}$ ($\phi = 0.95$)

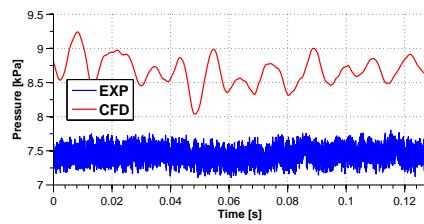
B.5 $\dot{m} = 0.8 \frac{kg}{s}$ 

(a) signals

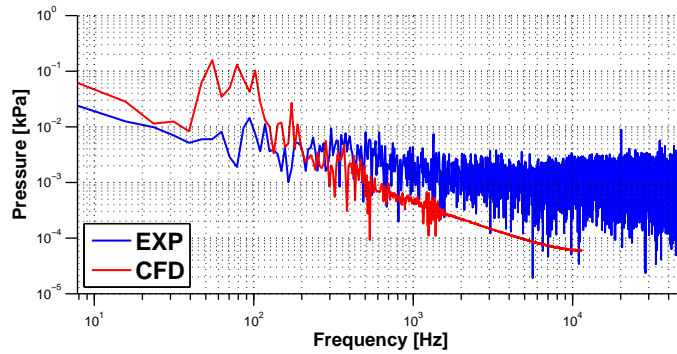


(b) frequency spectra

Comparison of pressure signals obtained at p_{s-in} in the quasi dynamic experiment conducted at $TOA = 41\%$ and in the simulation at $\dot{m} = 0.8 \frac{kg}{s}$ ($\phi = 1.51$)

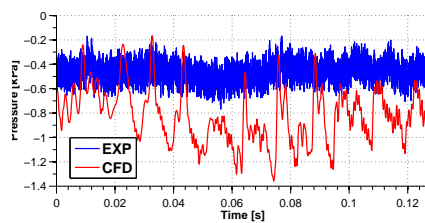


(a) signals

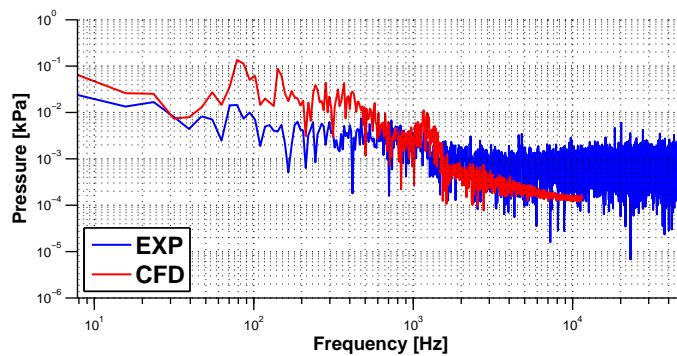


(b) frequency spectra

Comparison of pressure signals obtained at p_{s-out} in the quasi dynamic experiment conducted at $TOA = 41\%$ and in the simulation at $\dot{m} = 0.8 \frac{\text{kg}}{\text{s}}$ ($\phi = 1.51$)

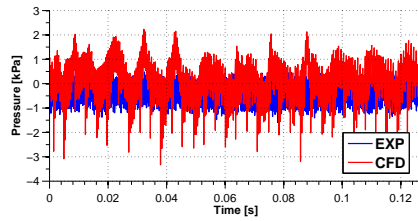


(a) signals

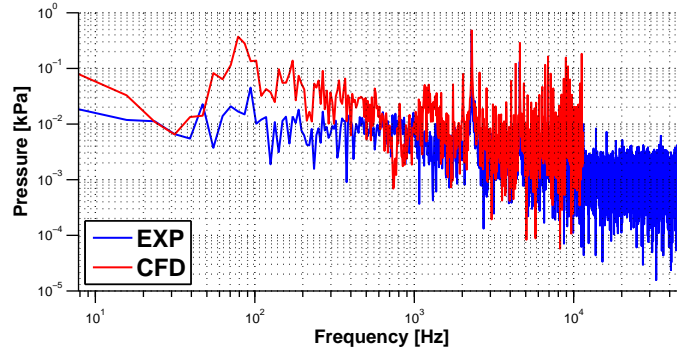


(b) frequency spectra

Comparison of pressure signals obtained at p_{s-imp1} in the quasi dynamic experiment conducted at $TOA = 41\%$ and in the simulation at $\dot{m} = 0.8 \frac{\text{kg}}{\text{s}}$ ($\phi = 1.51$)

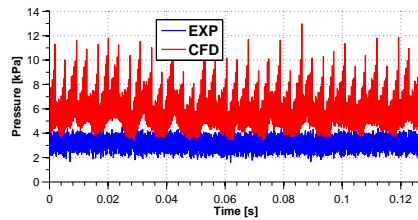


(a) signals

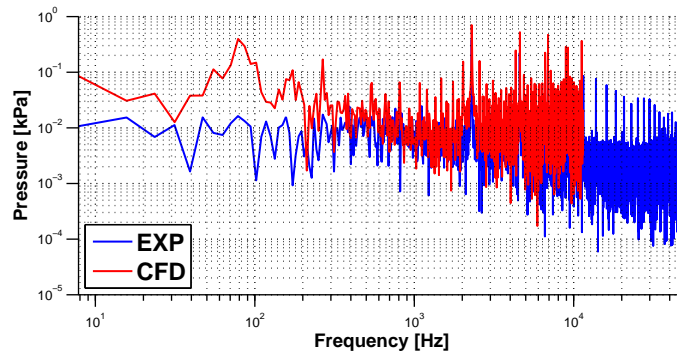


(b) frequency spectra

Comparison of pressure signals obtained at p_{s-imp2} in the quasi dynamic experiment conducted at $TOA = 41\%$ and in the simulation at $\dot{m} = 0.8 \frac{\text{kg}}{\text{s}}$ ($\phi = 1.51$)



(a) signals



(b) frequency spectra

Comparison of pressure signals obtained at p_{s-imp3} in the quasi dynamic experiment conducted at $TOA = 41\%$ and in the simulation at $\dot{m} = 0.8 \frac{\text{kg}}{\text{s}}$ ($\phi = 1.51$)